# ADVANCED DETECTOR TECHNOLOGIES FOR THE CUORE EXPERIMENT

**Samuele Sangiorgio**

A Thesis submitted
for the degree of
Doctor of Philosophy in Physics

Supervisor:
Prof. Andrea Giuliani

Coordinator:
Prof. Philip Ratcliffe

**UNIVERSITÀ DEGLI STUDI DELL'INSUBRIA**
**Faculty of Mathematical, Physical and Natural Science**
**Department of Physics and Mathematics**

XIX ciclo
2006

*To Caterina*

Se anche conoscessi tutti i misteri e tutta la scienza
ma non avessi la carità non sono nulla.

[S. Paolo, Corinti 1, 13-2]

# Short Table of Contents

# Detailed Table of Contents

# Abstract

In the past 50 years low temperature detectors have undergone a remarkable growth, and are now widely used in many physics research experiments. Bolometers are successful because their essence is incredibly simple (conversion of energy into a temperature signal), and at the same time very versatile and powerful. Moreover, many fields of physics contribute to describe their behavior and operation: thermodynamics, particle interaction, low temperatures physics and solid state physics.

Bolometers are interesting also for another important reason: they are very sensitive tools that could mark a turning point in one of the most challenging research topics of the last years: neutrinoless double beta decay ($\beta\beta0\nu$). The Dirac or Majorana nature of the neutrinos and their absolute masses could be finally unveiled if this decay will be observed.

The bolometric technique is extensively employed for $\beta\beta0\nu$ research in the Cuoricino experiment, which constitutes the stimulating environment of this work. Cuoricino serves two purposes: on one hand, it is a standalone project that is providing important results on the limit of the $^{130}$Te $\beta\beta0\nu$ half-life (and therefore on the effective neutrino Majorana mass); on the other hand, it is the prototype of a next–generation, 1–ton scale experiment named CUORE (Cryogenic Underground Observatory for Rare Events), aiming at reaching the inverted hierarchy region of neutrino masses.

Despite Cuoricino's good performance, the goal of CUORE will not be reached without important R&D efforts aiming at enhancing the performance of the single CUORE bolometer and of the whole detector. This thesis documents part of these efforts.

In particular, this Ph.D. activity focuses on three main issues: from the perspective of the single bolometer, we faced (1) detector optimization and (2) background reduction; we also (3) studied the behavior, performances and noise of a new generation of cryostats to be used in CUORE.

**Bolometer optimization** The optimization aims at improving the detector performance and increasing the reproducibility and the serialization of the construction procedure.

The first item addressed is the temperature sensor of CUORE bolometer; at present Neutron Transmutation Doped thermistors play this role.

We started investigating the effect of the $T_0$ thermistor parameter on the pulse amplitude. Our test showed that values of $T_0$ higher than the present one

are not suitable, due to the increased electron–phonon decoupling.

In an effort to simplify the thermistors wiring, we also studied thermistors where two notches in the usual parallepipedal shape allow wire bonding from the top. Our simulations indicate that a small performance reduction is likely to be expected due to different distribution of thermal power in the thermistor. This effect is however limited and should not cause concern. Samples of such thermistors have already been acquired and will be tested soon to confirm this result.

Finally, we designed and tested a capacitive sensor that does not suffer the dissipative read–out and Johnson noise of thermistors. Unfortunately, positive (but not particularly remarkable) results were obtained only with AC excitation. Since we aimed at static DC operation of the sensor, we decided to abandon the project.

Bolometers couplings were the subject of a subsequent optimization. The spread of the values of thermal and mechanical connections between the different parts are one of the origins of the scarce reproducibility of our bolometers. Moreover, thermal contractions must be carefully considered. Finally, we have to keep in mind that CUORE is made out of $\sim 1000$ detectors and therefore standard, easy and batch–able mounting procedures are to be preferred. We proposed and tested several solutions for the two main couplings: absorber to heat sink and absorber to thermistor. We achieved promising results, but none of them proved significantly better than the current setup.

**Background reduction** One of the main drawbacks of calorimetric bolometers is their lack of identification of particle interaction sites. As a consequence, external particles reaching the detector can mimic internal events. This is especially dangerous for surface contaminations: degraded $\alpha$ and $\beta$ events produce a continuum background that extends down into the $\beta\beta0\nu$ region. Currently, we believe that this is the real obstacle to the CUORE sensitivity.

I substantially contributed to the development of a new and innovative kind of bolometers, which we named *Surface Sensitive Bolometers* (SSB). These detectors have a partial ability to recognize the events' origin, thus overcoming a common disadvantage of these devices.

The idea that lies behind this technique is to thermally couple thin slab–bolometers on the surfaces of the main bolometer to create a single composite device. The thermal dynamics of this device can be used to identify events from the external surface and distinguish them from those in the bulk of the main absorber. Comparison of pulse amplitudes, decay and rise times proved to be effective in background reduction.

Several tests were performed both with small–size prototypes and CUORE–like bolometers, to completely characterize and understand their behaviour, highlighting advantages of this technique (e.g. powerful discrimination with different rejection methods) and addressing drawbacks (e.g. detector complexity, read–out channels proliferation).

Another method to obtain event discrimination is to couple the light signal of a scintillator to the phonon signal of a normal bolometer. In this way, a double independent read–out (heat and scintillation) will allow the required suppression of the background, thanks to the different Quenching Factor (QF) between $\alpha$ and $\gamma$. The scintillation light was measured through a second independent bolometer made of a thin pure Ge absorber.

In our specific case, we wanted to verify the possibility of operating pure and doped $TeO_2$ crystals as bolometers and check their scintillating properties (if any). A $PbMoO_4$ crystal was also used to compare previous positive results. Due to low sensitivity we were only able to put limits to the light yield of $TeO_2$ crystals; however, we obtained a clear cross–check of the results on $PbMoO_4$ scintillation.

**Cryogenic free dilution refrigerator** The tests and experimental activities were carried out mainly at the *Low Temperature Detector Laboratory* (LTD) of the Insubria University in Como. When underground measurements were required, the CUORE R&D setup at the *Laboratori Nazionali del GranSasso* was used.

The LTD laboratory at Como was especially appealing because of the presence of a dilution refrigerator cryostat that works without cryogenic LHe bath, with the aid of a Pulse Tube cryocooler, like the one planned for CUORE. In this thesis, I will report the knowledge gained on this system. We measured its performance and reliability; special attention was also paid to the study of the vibration induced on the bolometers. We conclude that such system performs very well, but there are indications that Pulse Tubes vibrations in the low frequency region could affect large size bolometers.

# · Chapter 1 ·

# Bolometric detectors

## 1.1 Introduction

Starting from the very first idea of F. Simon [1] back in 1935, the field of low–temperature detectors (LTD) has been continuously growing and reaching many areas of research. LTDs feature excellent energy resolution, sensitivity to all kind of particles, low energy threshold and a wide choice of construction materials, and are therefore suitable for many different applications.

It is not our aim to review here the status of art of LTD physics and technology. There are indeed excellent review articles on the subject [2–5] and recent advancements can be found in the proceedings of specific LTD conferences [6,7].

LTDs were first proposed as perfect calorimeters i.e. all the energy released by a particle interaction is thoroughly thermalized. As a consequence, the temperature of the absorber element of the device increases. This temperature variation corresponds simply to the ratio between the energy released and the heat capacity of the absorber.

Many fields of physics have taken advantage of the great versatility and potentiality of these detectors: dark matter, double and single beta decay, X– and Gamma–ray astronomy, and others. As we will see, they find their best applications in rare events physics, particularly in double beta decay and dark matter searches.

LTDs can be classified according to the type of elementary excitations (phonons, quasi-particles, ...) which mediate the detection of particles. In the following, the attention is focused on the LTDs that are sensitive to phonons. In particular, the expression *bolometer* was introduced to identify LTD used to measure power fluxes but is now commonly used to indicate a LTD that is sensitive to single particle interactions.

In this chapter, after a brief review of the basic operation principles and an introduction to the main bolometers components, we will describe a way to model and simulate their behavior. We will use these simulations in the following chapters.

## 1.2 Bolometers: what they are

### 1.2.1 Operation principles

A bolometer consists normally of two main components: the *energy absorber*, where the particles to be detected deposit their energy, and the *sensor*, which collects the excitations produced by the particle interactions in the energy absorber and develops a signal.

As the elementary excitation energy is very low, less than 10 meV, the bolometers have to work at low temperatures, so as to prevent the thermal generation of excitations that could hide the particle signals. Therefore, the detector is coupled to a heat bath that is usually maintained at a temperature in the range between 10 and 100 mK.

When a particle interaction occurs in the energy absorber, the phonons produced are out of equilibrium; in fact they have about the Debye energy, of the order of tens of meV, while the thermal energy is orders of magnitude lower, given the very low operation temperature. So these phonons are named athermal phonons.

Normally the athermal phonons degrade their energy and relax onto a new equilibrium distribution by interacting with the surface of the crystal absorber, with the defects of the crystal lattice and with the different isotopes present in the absorber.

According to the type of phonon sensor used, the PMDs can be fast or slow, of course in the context of bolometric detectors. In the first case they have a response time of the order of microseconds and can be sensitive to athermal phonons. If the phonon sensor's response time is slow and longer than the thermalization time of the non-equilibrium phonons produced by the particle interaction, it will be sensitive mainly to thermal phonons. In the latter case the sensor measures the temperature of the detector and is a thermometer. The detector works then as a perfect calorimeter. In many experimental situations it is difficult to distinguish between these two extreme cases, also because the nature of the detection mechanism is still poorly known.

### 1.2.2 Absorber

A scheme of a very simple thermal model for a PMD is reported in fig. 1.1. When operated as a perfect calorimeter, the height of the bolometer's thermal signal corresponds to the ratio between the energy $E$ deposited by the particle and the heat capacity $C$ of the detector, $E/C$. The time constant of the signal is equal to the ratio between the heat capacity and the thermal conductance $G$ to the bath, $C/G$. The most important parameter of the detector is then the heat capacity, that has to be small to achieve large and fast signals.

At low temperatures the specific heat of a crystal can be expressed as:

$$c(T) = c_r(T) + c_e(T) \tag{1.1}$$

where $c_r$ represents the lattice contribution to the specific heat and $c_e$ the electron one. Dielectric diamagnetic materials are preferred as energy absorbers

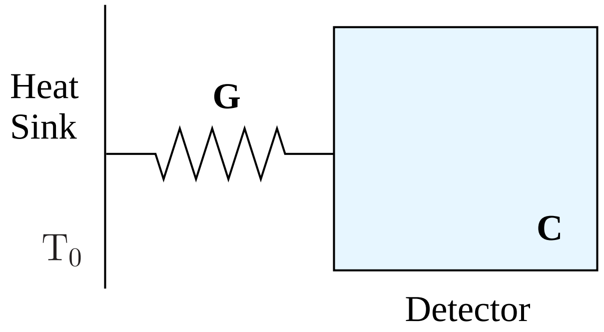


**Figure 1.1** - Monolithic thermal model of a bolometer. Here the detector is modeled as a unique system weakly coupled to the heat sink.

because

$$c_e(T) = 0; \qquad c_r(T) = \frac{12}{5}\pi^4 k_B N_A \left(\frac{T}{\Theta_D}\right)^3; \tag{1.2}$$

where $k_B$, $N_A$ and $\Theta_D$ are the Boltzmann constant, the Avogadro number and the Debye temperature respectively.

In metals the specific heat is dominated by the electron contribution that is proportional to $T$. However, if the metal is in superconductive state, then the electron contribution to the specific heat at $T \ll T_c$ is

$$c_e(T) = K_s e^{-2(\frac{T_c}{T})} \tag{1.3}$$

where $K_s$ is a constant depending on the material characteristics.

The above considerations lead to prefer diamagnetic or superconductors as energy absorber materials.

Absorber dimensions usually depend on the type of applications and can range from micrograms, as in the case of X-ray spectroscopy, to kilograms, as in the case of Gamma-ray spectroscopy, Double Beta Decay and Dark Matter searches.

**Thermalization processes of the deposited energy**

The processes that allow the conversion of the deposited particle energy into thermal phonons are complex and we will provide here only a brief summary. The main thermalization processes occur through the nuclear and electronic channels [8].

In the *nuclear channel*, the particle interactions with the crystal lattice produce vibrational excitations thanks to the nuclear scattering. Damages of the lattice are also likely to occur, depending on the particle energy. In this case the energy is not converted into phonons and the statistical fluctuation of the number of the produced defects can worsen energy resolution. Thermalization through nuclear interaction is important only for charged massive particles.

Electron–hole pairs are created from the interaction through the *electronic channel*. At the beginning these carriers have very high spatial density and energy but they soon interact with each other and then spread very quickly in the crystal. As a quasi–equilibrium situation is reached, they undergo their final degradation via direct interaction with the lattice site and produce phonons.

Radiative (with photon escape), non–radiative recombination of e–h pairs, and trapping into impurity sites and lattice defects could reduce the fraction of the initial energy that is transferred to the lattice as phonons.

The nuclear and electronic processes lead to a population of phonons having energy much higher than the energy of thermal phonons at the bolometer working temperature. At this point new phenomena of phonon energy degradation occur, so that phonons thermalize. These processes can be classified in three channels: phonon–phonon interaction, scattering on impurities, and reflection on crystal surfaces. The conversion towards low energies is a very slow process, and it is difficult to make a quantitative estimation due to the complication of the involved mechanisms.

After a certain number of the phonon decays, the mean free path becomes larger than crystal dimensions. At this point in pure crystals, there is a ballistic propagation of phonons until they reach the crystal surfaces [9]. Using several fast sensors (able to detect athermal phonons) it is possible in principle to determine the particle interaction point using the phonon signal relative time [10]. Phonons that are not absorbed by a sensor will be reflected by surfaces and therefore they can undergo decay processes and at the end they thermalize.

For superconductor materials, the thermalization processes could be longer. This happens in particular when the Debye temperature $\theta_D$ for the material is large and the critical temperature $T_c$ is low. In fact, in this case, phonons that are generated by particle interactions easily break the Cooper pairs and cause an energy storage in the quasi–particle system. For this reason, even in the case when superconductive materials present lower heat capacity at the same temperature, the diamagnetic dielectric materials are to be preferred.

**Intrinsic energy resolution**

By thermodynamic considerations that will be explained in §1.2.4 it is possible to express the intrinsic energy resolution ΔE for a bolometric detector sensitive to thermal phonons as

$$\Delta E = \sqrt{k_B C(T) T^2} \tag{1.4}$$

where $k_B$ and C are the Boltzmann constant and the energy absorber heat capacity respectively.

According to this equation, ΔE is independent of E.

To give an idea of the potentiality of these devices, we can calculate that for 1 kg of $TeO_2$ working at 10 mK the intrinsic energy resolution is about 10 eV. Once again we see that a crucial parameter of the energy absorber is its Debye temperature, $\theta_D$, which has to be as high as possible in order to reduce the specific heat. For this reason, light materials with a small mass number are better energy absorbers in terms of heat capacity. Even superconductors are in principle suitable, since the electronic contribution to the specific heat vanishes exponentially below the critical temperature.

It is possible to see the advantage of bolometers over conventional devices for radiation spectroscopy as the energy resolution is concerned. In fact the energy interaction generates a number of elementary excitations, N, equal to

$$N = \frac{E}{\epsilon}$$

where $\epsilon$ is the energy to produce an elementary excitation. The intrinsic energy resolution is limited by the statistic fluctuation of the produced elementary excitation number. So the theoretic energy resolution $\Delta$E is

$$\frac{\Delta E}{E} = 2.35 \cdot \frac{\Delta N}{N} \tag{1.5}$$

that is proportional to the $\sqrt{\epsilon}$. In a scintillator detector $\epsilon$ is about 100 eV, in a gas detector $\epsilon$ is about 30 eV, whereas in a solid state detector $\epsilon$ is around 3 eV. As already said, in a PMD the energy of an elementary excitation is less than 0.01 eV even in the case of athermal phonons, so, at least in principle, energy resolutions more than an order of magnitude better than to conventional devices are possible.

### 1.2.3 Phonon Sensor

In order to achieve good signal-to-noise ratio, a bolometer neeeds a high sensitivity phonon sensor. The phonon sensor is a device that collects the phonons produced in the absorber and generates an electrical signal, usually proportional to the energy contained in the collected phonons. A simple realization of this device can be accomplished through the use of a thermistor, whose resistance, as a function of the temperature, has a steep slope. In practical devices, there are two main classes of thermistors which give the best results: semiconductor thermistors (STs) and transition edge sensors (TESs).

Thermistors are usually characterized by their "logarithmic sensitivity" A, defined as

$$A = \left| \frac{d \log R(T)}{d \log T} \right| \tag{1.6}$$

The value of the sensitivity is usually in the range 1÷10 for STs and in the range $10^2$–$10^3$ for TESs.

Here the two most common approaches are introduced, but in the rest of this work, we will focus on STs. Other techniques (e.g. measure of the change of magnetisation of a proper paramagnetic material) which are less common but quite interesting are reported elsewere [6].

#### 1.2.3.1 Transition edge sensors

The TESs are superconductive films kept around the critical temperature ($T_C$). They are intrinsically fast, and so they can detect athermal phonons. Their working point lies in a narrow range of temperature. A typical example of a resistance-temperature curve for a TES is shown in fig. 1.2. The superconductive film is deposited on the absorber crystal, with typical thickness of a few

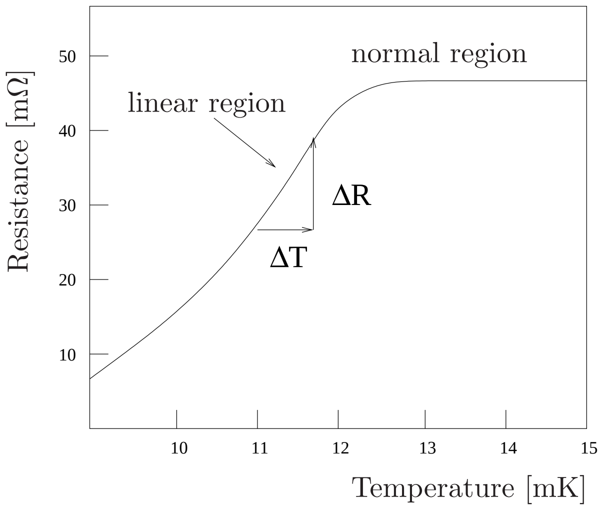


**Figure 1.2** - Resistance of a Tungsten TES thermistor as a function of the temperature.

hundred nanometers [11]. This technique can take advantage of the SQUID technology as read-out. TESs are made normally only of a single superconductor, but it is possible also to use a bilayer film formed by a normal metal and a superconductor. In the latter case, because of the proximity effect, the normal metal is driven superconductive and the resulting $T_C$ can be much lower than that of the pure superconductor. In this way it is possible to tune the $T_C$ by adjusting the thickness of the layer.

#### 1.2.3.2 Semiconductor thermistors

As the STs are intrinsically slow, they are probably sensitive mainly to thermal phonons in a PMD. In this context, they give information about systems in thermal equilibrium, and could be thought as temperature sensors. However, it must be remarked that there are clear indications that also athermal phonons can be detected by STs; in this case the collected pulses contain non thermal components.

STs consist normally of Ge or Si small crystals with a doped region. The doping process must be chosen to provide a uniform concentration of dopants in the thermistor volume. Neutron Transmutation Doping (NTD) is usually the best choice for Ge. Standard planar Si technology (ion implantation) works also well.

The typical steep dependence of the sensor resistance on the temperature is:

$$\rho \simeq \rho_0 \cdot \exp\left(\frac{\epsilon(T)}{k_B T}\right)^{1/2} \tag{1.7}$$

where $k_B$ is the Boltzmann constant, $\epsilon(T)$ is the activation energy and $\rho_0$ is a parameter depending on the doping conditions.

Semiconductors are covalent solids that may be regarded as insulators because the valence band is completely full and the conduction band is completely empty at the absolute zero. They present an energy gap between the valence and conduction bands of no more than 2 eV. For silicon the energy gap is 1.14 eV and for germanium the gap is 0.67 eV. So, for intrinsic semiconductors, i.e. for a semiconductor without impurities, the conduction can happen only with an activation energy equal or larger than the energy gap. This mechanism is possible at high working temperature, since $kT \simeq 0.025$ eV at room temperature.

If impurities are present in the semiconductor lattice (extrinsic or doped semiconductors) then it is possible to have electronic conduction also at lower temperatures. In this case in fact, the impurities introduce discrete levels slightly above the top of the valence band or under the bottom of the conduction band, depending on the type of atoms inserted in the semiconductor. For low impurity concentrations, the localized energy levels of dopant atoms are not broadened into bands because these atoms are many lattice spacings apart and they interact with each other very weakly. The energy difference, $\Delta\epsilon$, between the donor impurity energy levels and the conduction band and between the acceptor impurity energy levels and the valence band, is small; for instance if a small amount of arsenic impurities is introduced in a germanium crystal, a energy activation equal to $\Delta\epsilon = 0.0127$ eV is obtained. So the conduction mechanism due to dopant sites dominates the conduction at room and lower temperatures. Depending on the number of dopant atoms, the semiconductor, also near the zero temperature, can behave as an insulator or a metal. So, there exists a critical concentration $\mathrm{N}_c$ that characterizes the transition from the insulator to the metallic behavior of the semiconductor. The region near this concentration is named metal-insulator transition region (MIT) [12].

At temperatures lower than 10 K, the conduction is due to the migration of charge carriers from an impurity site to another. When the donor concentration is increased, the wave function of the external electron of the donor atom overlaps with the external electron wave function of the neighboring atoms. In this situation the electrons are not localized and the conduction happens when electrons jump from a donor site to another (*hopping mechanism*) [13] without using the conduction band. This migration is due to quantum-mechanical tunneling through the potential barrier which separates the two dopant sites. The conduction is activated by phonon mediation as schematically described in fig. 1.3, in which the tunnelling process is also shown.

If $\mathrm{T} \ll 10$ K and if the net doping atom concentration is slightly lower than $N_c$, then the resistivity is strongly dependent on the temperature. For this reason, usually, it is chosen to operate semiconductor thermistors slightly below the MIT region. The dominant conduction mechanism in these conditions of temperature and dopant level is named "Variable Range Hopping" (VRH) and the carriers can migrate also on far sites if their energy levels are located in a narrow range around the Fermi energy. As the state density near the Fermi energy in the semiconductor is determined by compensation level K, it plays a fundamental role in the VRH process. Let's recall that K is equal to the ratio between the acceptor concentration $N_A$ and the donor concentration $N_D$.

For VRH, the resistivity depends on the temperature in the following way [14]:

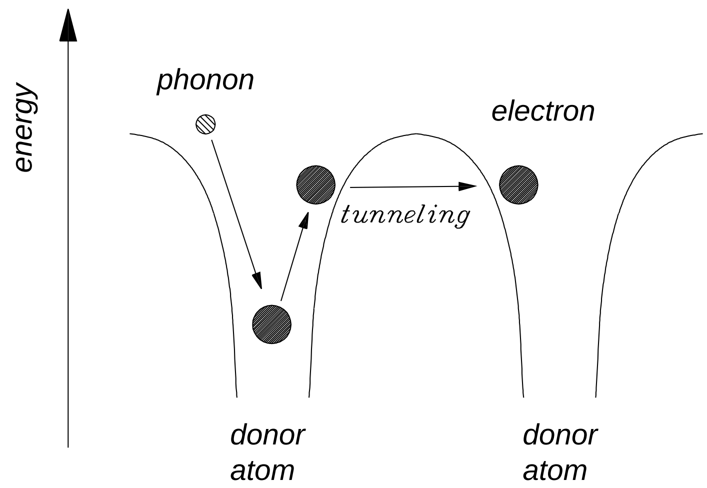


**Figure 1.3** - Schematic representation of hopping conduction mechanism.

$$\rho = \rho_0 \cdot \exp\left(\frac{T_0}{T}\right)^{\gamma} \tag{1.8}$$

where $\rho_0$ and $T_0$ are parameters depending on the doping and compensation levels. The exponent $\gamma$ in the Mott model, for a three-dimensional system, is equal to $\frac{1}{4}$ for low compensation levels. For larger values of K, the Coulomb repulsion among the electrons leads to the formation of a gap (Coulomb gap) in the electron state density near the Fermi energy. The value of $\gamma$ in this case becomes $\frac{1}{2}$.

### 1.2.4 Detector noise

In this section the principal noise sources of a bolometric detector using a ST sensor will be presented. These sources can be classified as generating intrinsic and extrinsic noise. The latter will be discussed in §4.1.2.

It is not possible to totally eliminate **intrinsic noise** sources that provide energy resolution limit of the detector. As these sources depend on detector parameters, they have to be carefully analyzed to achieve the optimal experimental configuration. The two main sources of intrinsic noise are:

**Johnson Noise:** Every resistance R working at a temperature $T_b$ generates a white noise having a power spectrum equal to:

$$e_R = \sqrt{4k_B R T_b} \tag{1.9}$$

The sensor is visually biased using a $R_L$ load resistance that in general is at a temperature $T_L$ different from $T_b$ (for instance, at room temperature, as in most of the devices described in the following chapters). So also the Johnson noise of the load resistance $R_L$ has to be taken into account, but it is possible to demonstrate that this can be made negligible with respect to the detector noise; in fact the load resistance contribution to the detector noise $e_{det}$ is

$$e_{det} = e_{R_L} \left( \frac{R}{R_L + R} \right)^2 \tag{1.10}$$

This contribution can therefore be reduced by choosing a large enough value for $R_L$.

$$\frac{e_{det}}{e_R} = \frac{e_R}{e_{R_L}} \left( \frac{R}{R_L} \right)^2 = \frac{R}{R_L} \cdot \frac{T_L}{T} \tag{1.11}$$

**Thermodynamic Noise:** As already anticipated in §1.2.2, in case of complete energy thermalization, the intrinsic energy resolution is limited by the thermodynamic fluctuations of the number of thermal phonons exchanged with the heat bath through the thermal connection $G$. This produces energy fluctuations and therefore an intrinsic detector noise. An estimate of this noise can be obtained by the following simplified argument. The number of phonons contained in the absorber at thermal equilibrium can be estimated as

$$N = \frac{E}{\epsilon_a} = \frac{C(T) \cdot T}{k_B \cdot T} = \frac{C(T)}{k_B} \tag{1.12}$$

where the mean phonon energy $\epsilon_a$ is equal to $k_B \cdot T$ and $E$ is the internal energy of the absorber [15]. If Poisson statistics is assumed then it is possible to estimate the fluctuations of the internal energy of the absorber in the following way:

$$\Delta E = \Delta N \cdot k_B T = \sqrt{N} \cdot k_B T = \sqrt{\frac{C(T)}{k_B}} \cdot k_B T = \sqrt{k_B C(T) T^2} \tag{1.13}$$

that is the expression already presented in §(1.4). In the monolithic bolometer model case, a detailed calculation of noise due to intrinsic sources shows that a dimensionless factor $\xi$ has to be introduced as a multiplier for eq. 1.13. The $\xi$ value depends on the details of the temperature sensor, of the thermal conductance and of the heat capacity temperature dependences, and can be made of the order of unity with a proper optimization work.

## 1.3 Bolometers: the thermal model

### 1.3.1 Introduction

In this section we will introduce the thermal model that we developed to explain and simulate the bolometers thermal behavior. We will start from a very raw model and we will add more details and generalization later on.

This model gives the possibility to write the equations that rule the static and dynamic behavior of the bolometers. That means, essentially, that we will be able to determine the temperatures and heat powers of the different part of the detectors and their time change when a particle heats up the absorber.

The system of equations that we will present in the next sections cannot be solved analytically. We developed numerical codes for this purpose but we will not go into their details. It is however possible to solve analytically the systems by introducing proper approximations as in section 1.3.6.

In chapter 3 we will use the model drawn here to simulate real Cuoricino bolometers. We will show there that this model can be of great use in the design and optimization of the detectors. Moreover, in chapter 7, the model will be applied to a new kind of bolometers with surface sensitivity and it will predict their behavior correctly.

### 1.3.2 Assumptions of the model

Our model is based on two basic hypotheses:

· In the pure calorimeter approach, all the energy is converted into phonons in a time which is negligible compared to the pulse evolution. The final phonons are completely thermalized.

· At every instant the thermal distribution of each component of the system is in thermal equilibrium. In other words, the phonon distribution is thermal at every time. For this reason it is meaningful to assign a specific temperature to each detector component at every times.

We shall note that these assumptions are not always completely true. For example, we already mention the possibility of using out–of–equilibrium phonons. However, as you will see, the model we develop here is not too rigid and can be adapted to different situations.

### 1.3.3 A thermal network

From a thermal point of view, every system can be thought to be made of *nodes* with a given heat capacity that are connected by *links* characterized by their thermal conductivity. To be honest, this is a sort of simplification because links can have their heat capacity but in most cases (at least in ours) is negligible. In such a system, we will have thermal powers at nodes and they flow trough the network towards the heat bath.

A very simplified model for a bolometer is shown in figure 1.4. Here an absorber is connected to the heat sink trough the conductace $G_{ab}$. A sensor is also linked to the absorber via $G_{as}$. The heat sink is kept at a constant temperature $T_b$. Absorber and sensor have heat capacity $C_a$ and $C_s$ and temperature $T_a$ and $T_s$ respectively.

The model we are developing must predict the bolometer behavior for both static and dynamic conditions.

In ideal **static conditions** all the temperatures are equal to the heat bath temperature. This is the thermal equilibrium situation whitout any external thermal power. Actually, it is very likely that a thermal power acts on absorber or on the sensor. We will assume them constant and indicate them as $P_f$. For example, these background powers can be due to microvibration in the absorber

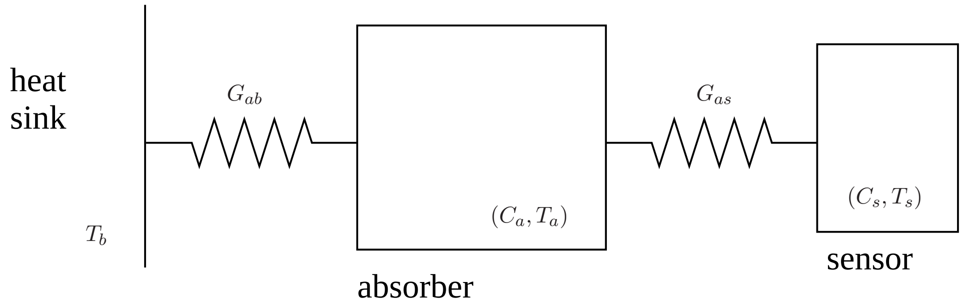


**Figure 1.4** - Sketch of a basic bolometric detector of 2 stages.

or to parasitic currents into the sensor.The output of the static model is thus the unknown temperatures $T_a$ and $T_s$ once the conductances, the background powers and the heat sink temperature are known or estimated.

Concerning the **dynamic behavior**, we have discussed previously how the heat is produced after the interaction of a particle in the absorber.This heat is transferred to the sensor increasing its temperature. Finally, the heat is brought away by the heat sink trough $G_{ab}$ and the temperature comes back to its initial value. In other words, from the initial static situation, a thermal pulse is produced into the absorber and measured by the sensor. The model should then reproduce this behavior and determine the time evolution of the temperatures $T_a(t)$ and $T_s(t)$ given the thermal parameters and the static bolometer conditions.

Since we want also to introduce the sensor details into our model and reproduce its real output, we will focus our attention on bolometers with neutron transmutation doped (NTD) Ge thermistors as phonon sensors. Their resistance changes steeply with temperature as in (1.8).

In §3.2 we will also see that semiconductor thermistors are characterized by an electron–phonon decoupling explained by the *hot electron model*. In our model, this can be taken into account by assuming a finite thermal conductance between the lattice phonons and the *hopping* electrons. The detector model changes accordingly as in figure 1.5 where $G_{ep}$ is the electron–phonon conductance and $G_{rb}$ is the conductance of the read-out wires of the thermistor. You might have noticed that no coupling exists between the electrons and the heat sink even if in principle, electrons in the wires are connected to the outside. However, this conductance has never been seen experimentally.

It is easy to show that the thermal network of figure 1.5 can be converted into an equivalent electrical circuit and solved by making use of this analogy. Thermal powers become current generators, electric potential plays the role of the temperatures and so on. Recently even the diagram algebra of electronics has been successfully used with success to simulate similar systems [16]. However, all this approach relies on several approximations of the real system. On the contrary, the model we derived here try to minimize the hypotheses on the system and we will be able to add terms which otherwise could not be taken into account.

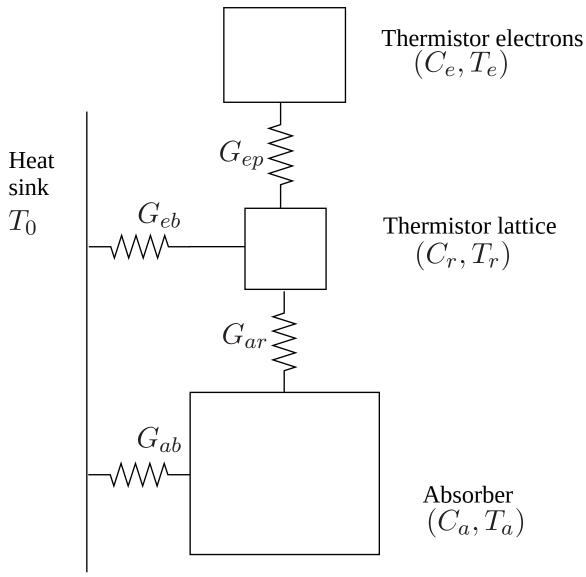


**Figure 1.5** - Sketch of a 3–stages bolometric detector.

### 1.3.4 Static behavior

We already explained that the solution of the static problem consists in the determination of the equilibrium configuration of the thermal network of figure 1.6 which is the same as of figure 1.5 but with explicit indication of the thermal powers flowing into the network. In fact, the equilibrium is reached when all the thermal power balance at each node is equal to zero. In our model, $P_{f,a}$ and $P_{f,e}$ are parasitic powers while $P_e$ is the Joule power induced into the thermistor's electron system by the polarization circuit:

$$P_e = I^2 \cdot R(T_e) \tag{1.14}$$

where the resistance-temperature relationship is given by 1.8.

From elementary thermodynamics, we know that the power flowing between two point at temperature $T_1$ and $T_2$ with $T_1 > T_2$ trough a conductance $G$ is:

$$P_{12} = \int_{T_2}^{T_1} G(T)dT \tag{1.15}$$

where the conductance can be expressed in our case in the power form:

$$G(T) = g_0 \cdot T^{\alpha}, \tag{1.16}$$

. The latter equation can be inserted into (1.15) and integrated:

$$P_{12} = \frac{g_{0,12}}{\alpha_{12}+1}\left[T_1^{\alpha_{12}+1} - T_2^{\alpha_{12}+1}\right] \tag{1.17}$$

The power balance at the three nodes of the thermal network of figure 1.6 is therefore:

$$\begin{cases} P_e + P_{f,e} = P_{er} \\ P_{er} = P_{rb} + P_{ra} \\ P_{ra} + P_{f,a} = P_{ab} \end{cases} \tag{1.18}$$

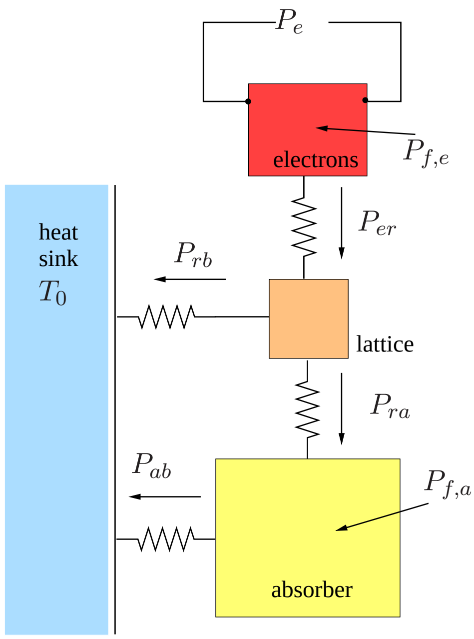


**Figure 1.6** - Power fluxes between each element of the bolometer of 3 thermal stages. A priori, the direction of the thermal fluxes are unknown, but it is not necessary once an assumption is established.

which can be written explicitly by using (1.17) as a function of the three unknown temperatures $T_e, T_a, T_r$ ad of the parameters $g_0$ and $\alpha$ of each thermal conductance. The parasitic power $P_f$ and the heat bath temperature are treated as known constants.

The system that we obtain is unfortunately strongly non linear. Infact power law terms are present in the equations. An exponential term is also present in the equation for the electron part of the thermistors due to $R(T_e)$. For this reason, we decided to solve numerically the system (1.18). We underline that the interest is focused in finding the temperature $T_e$ from which we can calculate the thermistors resistance with (1.8). This is infact the quantity that is measured experimentally for different biasing values.

### 1.3.5 Dynamic behavior

Static detector conditions are the necessary starting point for the analysis of its dynamical behavior. We are facing the problem of determining the time evolution of the temperatures of the system in figure 1.6 after the instantaneous injection of an energy $E$ in the absorber at $t = 0$.

It is easier and meaningful to try to solve this problem for the simplest possible thermal network i.e. a bolometer with total (absorber + sensor) heat capacity $C$ linked to a thermal bath at temperature $T_0$ by means of a thermal conductance $G$. Let's also assume we can treat $C$ and $G$ as costants (no temperature dependence). On the bolometer we will also inject a costant power $P$ (e.g. due to the biasing of the sensor). From the previous section it is straightforward to write the equation for the static condition of this simplified bolometer as:

$$P = \int_{T_0}^{T_s} G dt = G \cdot (T_s - T_0) \tag{1.19}$$

where $T_s$ is the static bolometer temperature when equilibrium with the heat sink holds. Let's move now to determine $T(t)$. Taking care not to forget the bolometer internal energy, it's trivial to show that conservation of energy for an infinitesimal time $dT$ leads to the differential equation:

$$P dt - C dT = G \cdot (T(t) - T_0) dt$$

or

$$P - C\dot{T} = G \cdot (T(t) - T_0) \tag{1.20}$$

Since at $t = 0$ we were at thermal equilibrium we can write

$$P - C\dot{T} = G \cdot (T(t) - T_s) + G \cdot (T_s - T_0)$$

From (1.19) and defining $\Delta T(t) = T(t) - T_s$ we can rewrite once more this equation in the form:

$$- C\dot{\Delta T} = G \cdot \Delta T\,. \tag{1.21}$$

From the initial condition

$$\Delta T(t = 0) = \frac{E}{C}\,, \tag{1.22}$$

we have the trivial exponential solution:

$$\Delta T(t) = \frac{E}{C} \cdot e^{-t/\tau} \quad \text{con} \quad \tau = \frac{C}{G}\,. \tag{1.23}$$

Even if we worked on an extremely simplified model, we would like to point out few aspects of the problem which have more general validity.

· Dynamic behavior of a thermal network is described mathematically by a set of differential equations that translate the conservation of energy at each node.

· The static conditions of the system are the unavoidable starting point time evolution. After the pulse, the system come back to those initial conditions.

· Relaxation time towards equilibrium is generally ruled by exponential decay with a time constant $\tau = C/G$.

It is now simple to come back to the more complex thermal system of an absorber and a thermistor split into lattice and electron system. Let $T_e(t)$, $T_r(t)$ and $T_a(t)$ the three unknown temperatures and $C_e$, $C_r$ and $C_a$ the related heat capacity. Power fluxes are still those of (1.17). As before, conservation of energy leads to this set of differential equations:

$$\begin{cases} -C_e\dot{T}_e = -P_e - P_{f,e} + P_{er} \\ -C_r\dot{T}_r = +P_{re} + P_{rb} + P_{ra} \\ -C_a\dot{T}_a = +P_{ar} - P_{f,a} + P_{ab} \end{cases} \tag{1.24}$$

which can be written more explicitly:

$$\begin{cases} -C_e\dot{T}_e + P_e + P_{f,e} = \dfrac{g_{er}}{\alpha_{er}+1}\left[T_e^{\alpha_{er}+1} - T_r^{\alpha_{er}+1}\right] \\ -C_r\dot{T}_r = \dfrac{g_{er}}{\alpha_{er}+1}\left[T_r^{\alpha_{er}+1} - T_e^{\alpha_{er}+1}\right] + \\ \qquad + \dfrac{g_{rb}}{\alpha_{rb}+1}\left[T_r^{\alpha_{rb}+1} - T_b^{\alpha_{rb}+1}\right] + \dfrac{g_{ra}}{\alpha_{ra}+1}\left[T_r^{\alpha_{ra}+1} - T_a^{\alpha_{ra}+1}\right] \\ -C_a\dot{T}_a + P_{f,a} = \dfrac{g_{ra}}{\alpha_{ra}+1}\left[T_a^{\alpha_{ra}+1} - T_r^{\alpha_{ra}+1}\right] + \dfrac{g_{ab}}{\alpha_{ab}+1}\left[T_a^{\alpha_{ra}+1} - T_b^{\alpha_{ra}+1}\right] \end{cases} \tag{1.25}$$

This is a system of 3 ordinary differential equations that must be solved with the initial conditions given by

$$\begin{cases} T_e(0) = T_{e,s} \\ T_r(0) = T_{r,s} \\ T_a(0) = T_{a,s} + \Delta T_a \end{cases} \tag{1.26}$$

where the indexes '$s$' refers to the temperatures of the nodes at static equilibrium.

Since we wanted to keep a compact notation, the heat capacities that appear in the previous equations has not been written explicitly as temperature dependent. However, we remind that generally

$$C(T) = c \cdot T^\beta \left[{}^{\text{Joule}}/_{\text{K}}\right] \tag{1.27}$$

where $c$ is an experimentally measured coefficient and $\beta$ can be 3 or 1 depending on the material (dielectric or conductor). For the same reason, the expression

$$\Delta T_a = \frac{E}{C_a}$$

is valid only if $\Delta T \ll T$. More appropriately we should write

$$\Delta T = \left[\frac{\beta+1}{c}E + T_s^{\beta+1}\right]^{1/\beta+1} - T_s \tag{1.28}$$

### 1.3.6 The analytical approximation

We clearly need numerical algorithms to solve the systems of equations (1.18) and (1.24). These algorithms will be briefly discussed in the next section. Here we want to show that it is possible to linearize (1.24) by means of some reasonable approximations and derive the pulse evolution analytically.

Let us assume that the thermal pulse which is produced inside the absorber is only a small perturbation of the working point provided by the solution of the static problem. This is our main hypothesis. For example, the integral that describes the power flowing towards the heat bath in dynamic condition is:

$$\int_{T_b}^{T_s+\Delta T} G(T)dT$$

where $T_s$ is the temperature of the current node in static conditions and $\Delta T$ is the temperature variation during the pulse evolution. In the *small signal approximation* stated above, this integral can be rewritten as a sum of two terms:

$$\int_{T_b}^{T_s} G(T)dT + \int_{T_s}^{T_s+\Delta T} G(T)dT \simeq \int_{T_b}^{T_s} G(T)dT + G(T_s) \cdot \Delta T$$

The same consideration holds for all the power fluxes. If we then assume that the thermistor lattice heat capacity is negligible, we determine a set of linear coupled equations with constant coefficients. Even the *electrothermal feedback*, which is an effect of the dependence of the thermistor resistance from the temperature (§3.2.2), can be included in the equations. An effective heat conductance, greater than the real one, between the lattice and the electrons of the thermistors will do the job.

At this point it easy to show that the solution of the dynamic problem can be derived analytically as a difference of exponential terms:

$$\Delta T_e(t) = \frac{E}{C_a} \cdot K \cdot (e^{\lambda_1 t} - e^{\lambda_2 t})$$

where $K$, $\lambda_1$ and $\lambda_2$ are constant which are related to the heat capacities and conductances of the system at the static temperature $T_s$.

### 1.3.7 The numerical algorithms

We developed two numerical `C` codes to solve numerically the two systems of equations (1.18) and (1.24). Without going into much details, we will briefly discuss here the algorithm used and their implementation.

#### 1.3.7.1 Non-linear system of equations for the static bolometer behavior

The linear system of equations that describe the static bolometer equation (1.18) can be rewritten using vectors as:

$$\mathbf{f}(\mathbf{x}) = \mathbf{0} \tag{1.29}$$

Several (but not many) algorithms exist to solve numerically this system and they all need some knowledge on the behavior of $\mathbf{f}$. We decided to use the *Newton–Raphson method* as described in [17]. Other more sophisticated algorithms exist but our problem is far too simple to ask for such complex methods.

The Newton–Raphson algorithm gives an easy way to determine the solution of the problem when a good initial guess of the solution is available. One of the steps involve the use of the Jacobian matrix of $\mathbf{f}(\mathbf{x})$.This is not a problem in our case because the functions that appear in (1.18) can be easily differentiated. We will thus use the analytical expression for the Jacobian in order to reduce computation time and increase precisions.

The theoretical limit of this method consists in the limited global convergence, i.e. the algorithm is not guaranteed to converge with the wrong choice of the initial guess. In our case, the function **f** has a clear physical origin and it must have a uniform behavior. Moreover, the physical problem itself allow for only one equilibrium point for the static condition i.e. a unique solution of the equations. Nevertheless, a careful choice of the starting guessed solution will reduce substantially the computation time.

Our method to guess a first estimation of the temperatures of the nodes starts with a linearization of the system (1.18). A good linear approximation consist in the evaluation of the thermal conductances at a fixed constant temperature $\tilde{T}$.

#### 1.3.7.2 Differential system of equations for the dynamic bolometer behavior

The equations (1.24) which is the mathematical description of the dynamic behavior of the bolometers, can be easily reduced to the classic structure of a system of 4 coupled differential equations:

$$\begin{cases} \dot{T}_e = f_e(T_e, T_r, T_a, V) \\ \dot{T}_r = f_r(T_e, T_r, T_a) \\ \dot{T}_a = f_a(T_e, T_r, T_a) \end{cases} \tag{1.30}$$

where the functions $f_i$ on the right side are known function of the thermal and electrical parameters of the system. The initial conditions are given by (1.26) + (1.28).

Two improvements of the well–known *Eulero's method of finite increments* have been taken into considerations: the *Runge–Kutta method* and the *Burlish–Stoer method*. The decision fall on the latter. More details on the two methods can be found either in the [17] or in [18] with a brief explanations on pros and cons.

# · Chapter 2 ·

# Scientific Framework and Motivations

In the first chapter, we have introduced phonon mediated detectors and their interesting features which make them very attractive in many fields of particle and radiation detection. In particular, we focused our attention on low temperature PMDs (bolometers) as they are the central topic of this Ph.D. research activity.

We already pointed out that bolometers are succesfully used for rare event search. From this point of view, bolometers play an important role in one of the most attractive field of physics: the search for neutrinoless double beta decay ($\beta\beta0\nu$ ). Recently, members of the American Physical Society Multidivisional Neutrino Study published a critical review of the neutrino situation [19] where they recommend to pursue the search for neutrinoless double beta decay with high priority because of its importance in our understanding of neutrinos and the origin of mass through the solution of the Dirac–Majorana puzzle.

In this chapter we briefly review the reasons for this strong interest in $\beta\beta0\nu$ for astro–particle physics; we also underline the peculiarity of this phenomenon and the present status of its experimental search.

## 2.1 The Quest for the Neutrinos Truth

### 2.1.1 An elusive particle

The existence of the neutrino dates back to 1930 when W. Pauli postulated its presence to reconcile the data on the $\beta$–decay with energy conservation. Since then, big improvements have been made in the comprehension of neutrinos and their mysterious properties.

The first theory on beta decay comes in 1934 from E. Fermi [20]; further progress was made in the '50s, thanks to Lee and Yang's hypothesis on the parity violation, experimentally proved in 1956 by Wu. In 1959 F. Reines and C. Cowan performed the first direct observation of the electron antineutrino from a nuclear reactor. In 1962 muon neutrinos were discovered at the Brookhaven National Laboratories. In the 60's the interest on neutrino was renewed by the possibility of using this particle to study astrophysical sources. In those years, neutrinos produced in the sun and in the atmosphere were observed. In 1987, neutrinos from a supernova in the Large Magellanic Cloud were also detected.

In the Standard Model (SM) of electroweak interactions, neutrinos are described as the left–handed massless partners of the charged leptons. This description is incomplete as it cannot account for the finite neutrino masses which were recently discovered in neutrino oscillation experiments that have been clearly demonstrated.

### 2.1.2 Mixing and masses

The unexpected behavior of the neutrinos from the sun (discrepancy between the measured and the expected flux) was the first hint that something was missing in our comprehension of $\nu$ physics. The solution of this problem relies on the attribution of non–conventional properties to neutrino particles: mixing and oscillations.

The hypothesis of neutrino mixing was proposed for the first time by B. Pontecorvo [21] in 1957. Similarly to what happens in the hadronic sector for the CKM matrix, neutrino flavor eigenstates $\nu_l$ $(l = e, \mu, \tau)$ can differ from their mass eigenstates $\nu_i$ $(i = 1, 2, 3)$. A unitary mixing matrix $U$ is therefore introduced to express the flavour states as linear combination of the mass states. This matrix is named after Pontecorvo, Maki, Nakagawa and Sakata [22, 23] and can be parametrized by three mixing angles and two complex phases:

$$\begin{pmatrix} \nu_e \\ \nu_\mu \\ \nu_\tau \end{pmatrix} = UV \begin{pmatrix} \nu_1 \\ \nu_2 \\ \nu_3 \end{pmatrix} =$$
$$\begin{pmatrix} c_{12}c13 & s_{12}c13 & s_{13}e^{i\delta} \\ -s_{12}c_{23} - c_{12}s_{23}s_{13}e^{i\delta} & c_{12}c_{23} - s_{12}s_{23}s_{13}e^{i\delta} & s_{23}c_{13} \\ -s_{12}c_{23} - c_{12}s_{23}s_{13}e^{i\delta} & -c_{12}s_{23} - s_{12}c_{23}s_{13}e^{i\delta} & c_{23}c_{13} \end{pmatrix} \times \tag{2.1}$$
$$\begin{pmatrix} 1 & 0 & 0 \\ 0 & e^{i\Phi_2/2} & 0 \\ 0 & 0 & e^{i\Phi_3/2+delta} \end{pmatrix} \begin{pmatrix} \nu_1 \\ \nu_2 \\ \nu_3 \end{pmatrix}$$

where $c_{ij} \equiv \cos\theta_{ij}$ and $s_{ij} \equiv \sin\theta_{ij}$; $\theta_{ij}$ are the mixing angles measured with the neutrino oscillations; $\delta$ is the Dirac CP phase. $V$ is a diagonal matrix containing the Majorana CP phases ($\Phi_2$ and $\Phi_3$) that do not exist in the case of Dirac neutrinos and that, in any case, cancel in neutrino oscillations.

As a consequence of (2.1), neutrinos oscillate between flavor states with a non vanishing probability which depends on the energy, the traveled distance and the difference $\Delta m^2$ of the square of the masses.

Several experimental observation on solar, atmospheric and reactor neutrinos (Homestake, Super–Kamiokande, SAGE, GALLEX/GNO, SNO, KamLAND, ...) confirmed clearly this picture. This exciting result (neutrinos do have masses!) is one of the most important discoveries of the last few years and widens particle physics horizons.

Oscillation experiments are unfortunately unable to provide the absolute value of the $\nu$ masses as they are sensible only on $\Delta m^2$. The “best fit” values [24]

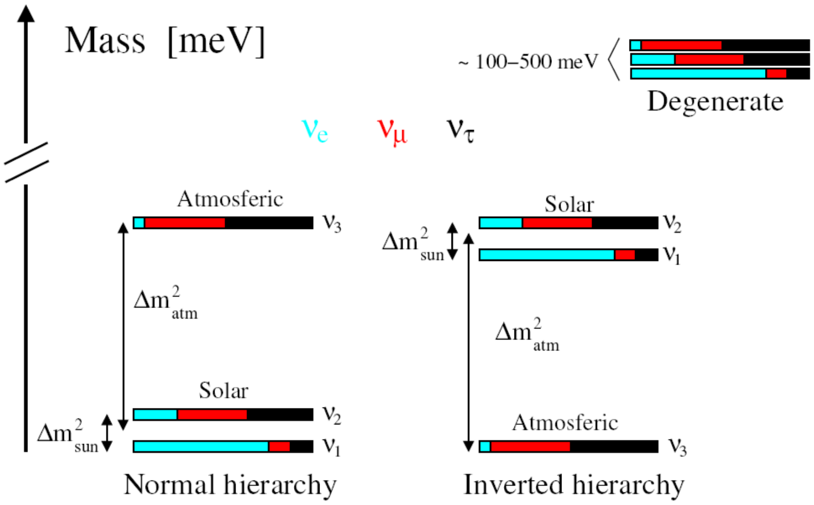


**Figure 2.1** - Neutrino mass pattern based on the experimental relation $\Delta m^2_{\text{sol}} \ll \Delta m^2_{\text{atm}}$

for $\Delta m^2$ are:

$$\begin{aligned} \Delta m^2_{\text{sol}} &= \Delta m^2_{21} = (7.0 \pm 0.3) \times 10^{-5} \quad \text{eV}^2 \\ \Delta m^2_{\text{atm}} &= \Delta m^2_{31} = (2.5^{+0.20}_{-0.25}) \times 10^{-3} \quad \text{eV}^2 \end{aligned} \tag{2.2}$$

This experimental scenario is compatible with three mass patterns, as shown in fig. 2.1:

- Quasi degenerate (QD) : $m_1 \sim m_2 \sim m_3$, $m^2_{1,2,3} \gg |\delta m^2_{\text{atm}}|$
- Normal hierarchy (NH) : $m_1 \lesssim m_2 < m_3$
- Inverted hierarchy (IH) : $m_3 < m_2 \lesssim m_1$

Which of these schemes is correct is still an open question, together with the related issue on the absolute values of neutrino masses.

### 2.1.3 The Dirac–Majorana puzzle

Another open question concern the nature of neutrinos. The distinction between particle and antiparticle is related to the presence of a conserved quantity (charge). This happens for all charged particles, were the antiparticles have opposite electric charge. However, any other charge can distinguish particles from antiparticles in the same way (e.g., neutron or the $\Lambda^0$ differ from their antiparticles since they have opposite baryon number). The possibility that a particle do not differ from its own antiparticle was first suggested by Majorana in 1937 [25]. Neutrinos came out to be the best candidate to be Majorana particles.

In the framework of the Standard Model, massive Dirac neutrinos consist of four different states, assuming a neutrino with negative helicity (left handed) $\nu_L$;

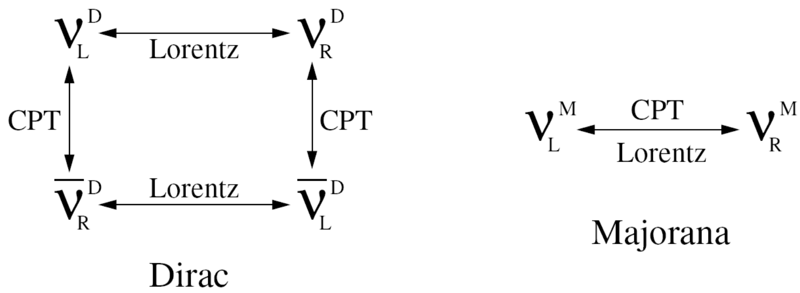


**Figure 2.2** - Transformations among neutrinos: Dirac neutrinos (left) and Majorana neutrinos (right).

if CPT theorem holds, then there will be the corresponding CPT–transformed state, i.e. an antineutrino with positive helicity (right handed), $\bar{\nu}_{\mathrm{R}}$. If the neutrino has a mass then a Lorentz boost exists that allow the helicity flip. Thus if the neutrino has a charge (lepton number) and a mass, it consists of four different states and is called a Dirac neutrino. If, on the contrary, the neutrino do not have charge, only the two helicity states are defined; this is called a Majorana neutrino (see fig. 2.2). Due to the V–A structure of the Standard Model the right handed neutrinos are sterile. Thus only two neutrinos are able to interact, as in the Majorana case. The difference is that in the Standard Model, Dirac–$\nu$s interaction follows from charge conservation while in the Majorana case the interaction is ruled by helicity.

From a theoretical point of view, the possibility that neutrinos are Majorana particles is particularly appealing. The fact that neutrinos and charged leptons, belonging to the same weak doublet, have an extremely different mass (at least a factor $10^5$) cannot be explained in the Dirac theory. Such an anomaly can, on the contrary, be explained in a natural way (without adding any exotic symmetry or property) through the *see–saw mechanism* [26]: in the Majorana case, the mass of the neutrino naturally satisfies the relation

$$M_\nu M \approx M_{q,l}^2 \tag{2.3}$$

where $M_{q,l}$ represent the mass of a lepton or a quark, and $M$ a mass scale.

Due to their tiny mass, the Dirac neutrinos are practically produced in nature, always left–handed, while anti–neutrinos are right handed. It is therefore impossible to discriminate whether they interact due to the lepton charge or due to their helicity. In this scenario, the observation of neutrinoless double beta decay would be the most clear way to state the Majorana nature of neutrinos.

### 2.1.4 Standard Model escape paths

Neutrino physics is strongly related to many fields of physics and a deeper comprehension of some neutrino characteristics could help solving some puzzles of nature. Determination of masses and nature of neutrinos is especially important.

For example, in the context of Grand Unified Theories (GUTs) it is possible to develop predictive models for the fermion masses in general and for the neutrino masses in particular. The smallness of the neutrino masses is explained by means of the see–saw mechanism, which is often incorporated in GUTs in various forms. In this context, neutrino is naturally a Majorana particle. Therefore, the experimental determinations of the neutrino mass scale, pattern and nature are crucial bench tests for predictive GUTs and for the improvement of our understanding of the basic theory of fundamental interactions.

In parallel, the understanding of Big-Bang Nucleosynthesis and the features of the Cosmic Microwave Background (CMB) illustrate the important role of neutrinos in the history of the early universe. Neutrino flavor oscillations and other bounds tell us that the heaviest neutrino mass is in the range 0.04 - 0.6 eV. Therefore, neutrinos are a component of dark matter, but their total mass, although it outweighs the stars, gives only a minor contribution to invisible matter density. Neutrinos are so light and they had streamed freely away from developing aggregations of matter until quite recently (in cosmological terms), when they eventually cooled and their speed has decreased to significantly less than the speed of light. What is then the neutrino role in shaping the universe? Do neutrinos allow to understand the matter-antimatter asymmetry of the universe, via leptogenesis? The answer to these questions requires the precise knowledge of the neutrino mass values.

It is clear, therefore, that the neutrino mass scale is crucial over two fronts: progress in the comprehension of elementary particles and solution of hot astroparticle problems.

Three complementary approaches are currently pursued:

· Cosmology: from the CMB and LSS (Large Scale Structure) studies, it is possible to place limit on the absolute value of neutrino masses. It must be noted however that a considerable spread is present in recently published result (see for example [27]); moreover, the result are very sensitive to even small changes of the input data and might depend on priors (and sometimes degenerate) cosmological parameters.

· Single beta decay: it consist on the direct observation of the $\beta$ decay spectrum at the endpoint; it is based on the pure kinematics of the decay via the so called Kurie plot; the present sensitivity is unfortunately quite limited ($m_\nu \lesssim 2eV$).

· Neutrinoless double beta decay: as it will be clear in the next section, if neutrinos are Majorana particles, double beta decay could happen without emission of neutrinos; the most stringent bounds on $m_\nu$ come from this kind of measurements but with uncertainties from nuclear physics and the possible presence of other mechanism (different from massive neutrinos) that could mediate the process.

These three approaches are truly complementary because they measure different combinations of the neutrino mass eigenvalues and therefore an international research program should purse them simultaneously.

In the following, we will focus our attention only on the neutrinoless double beta decay. The studies of neutrinoless double beta decay are essential and unique in their potential to fix the neutrino masses and to answer key–questions beyond neutrino physics itself.

## 2.2 Double Beta Decay

### 2.2.1 What is it?

The Double Beta Decay (DBD) is a rare spontaneous nuclear transition [28,29]. The existence of this decay was proposed for the first time by Maria Goeppert–Mayer [30] in 1935. In this transition a nucleus ($A$,$Z$) changes the nuclear charge of two units maintaining the same mass number, so it becomes ($A$,$Z\pm2$) nucleus. Let's focus our attention on the case in which a ($A$,$Z$+2) nucleus appears in the final state. Normally DBD is not favored with respect to the single beta decay, and it is possible to observe this transition only for those nuclei for which the single $\beta$ decay is either energetically forbidden (this occurs when the intermediate ($A$,$Z$+1) nucleus has a binding energy greater than the ($A$,$Z$) and ($A$,$Z$+2) nuclei) or suppressed by a large change of the nuclear spin–parity state.

This situation can be understood by looking at the Weizsäcker expression for the atomic mass as a function of the mass number $A$ and the number of neutrons $N$ and protons $Z$. In particular the Weizsäcker formula contains the "pairing" term that takes into account that the binding energy of the nucleus increases if protons or neutrons are coupled to give an angular momentum equal to zero:

$$\delta = \begin{cases} +12/A^{1/2} & \text{for even A and odd Z,N} \\ -12/A^{1/2} & \text{for even A and even Z,N} \\ 0 & \text{for odd A} \end{cases} \tag{2.4}$$

If isobaric nuclei are considered and their atomic masses are plotted as function of $Z$ it is easy to find that, for odd $A$, the nuclei are positioned as described in fig. 2.3(left). If even $A$ nuclei are considered, it is found that the nuclear masses are disposed as shown in fig. 2.3(right).

Two different DBD modes are usually considered: first, the decay with two neutrinos, where lepton number is conserved and so it is allowed by the SM described by the reaction

$$\beta\beta2\nu: \quad (A,Z) \rightarrow (A,Z+2) + 2e^- + 2\bar{\nu}_e \tag{2.5}$$

and, second, the neutrinoless decay given by

$$\beta\beta0\nu: \quad (A,Z) \rightarrow (A,Z+2) + 2e^- \tag{2.6}$$

where it is evident that lepton number is violated. An experimental confirmation of this decay mode will thus constitute an important step in the study of elementary particle physics beyond the SM. The Feynman diagrams for both decay modes are shown in fig. 2.4.

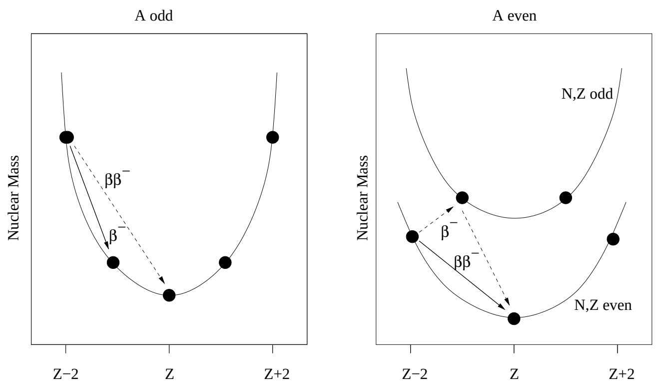


**Figure 2.3** - Nuclear mass as function of the proton number.

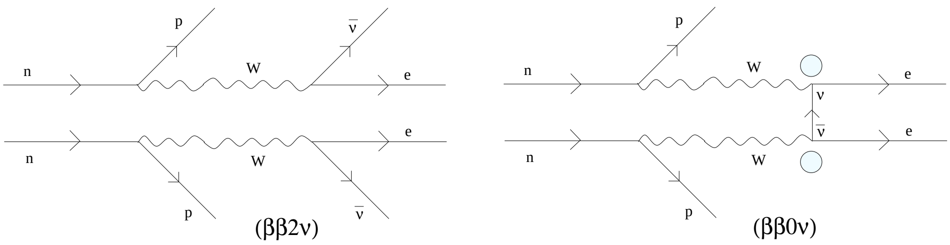


**Figure 2.4** - Feynman diagrams for double beta decay with two neutrinos (left) and with no neutrino emission (right). In this second case, an antineutrino is produced at vertex 1 and a neutrino is absorbed at vertex 2. This process is allowed only for Majorana neutrinos.

The discrimination between these decay modes is, in principle, very simple and is based on the shape of the spectrum of the sum of the energy of the two emitted electrons. In fact, this spectrum is determined by the phase space of the other emitted particles. As shown in fig. 2.5, the $\beta\beta 2\nu$ is a four body decay and so the spectrum is a continuum with a maximum value around one third of the $Q$ value. On the contrary, in $\beta\beta 0\nu$ , the two electrons retain all the available kinetic energy (neglecting the nuclear recoil). For this reason, the spectrum is a spike at the transition energy, enlarged only by detector resolution.

In both cases, the DBD is a semileptonic second–order weak interaction and thus is characterized by a very long lifetime: $\tau_{\beta\beta} \sim 10^{18} - 10^{22}$ years for the 2 neutrino channel. Thus, the experimental observation of this decay turns out to be a great challenge because very rare events have to be detected in the presence of unavoidable traces from other radioisotopes with similar transition energies but with decay times that are even 10 orders of magnitude shorter. Presently, $\beta\beta 2\nu$ has been observed for $\sim 10$ nuclei [31].

### 2.2.2 Extraction of neutrino properties

Neutrinoless DBD probability is usually expressed using the general relation derived from Fermi's golden rule:

$$\left[T^{0\nu}_{1/2}\right]^{-1} = G^{0\nu} \left|M^{0\nu}\right|^2 \langle m_\nu \rangle^2 \tag{2.7}$$

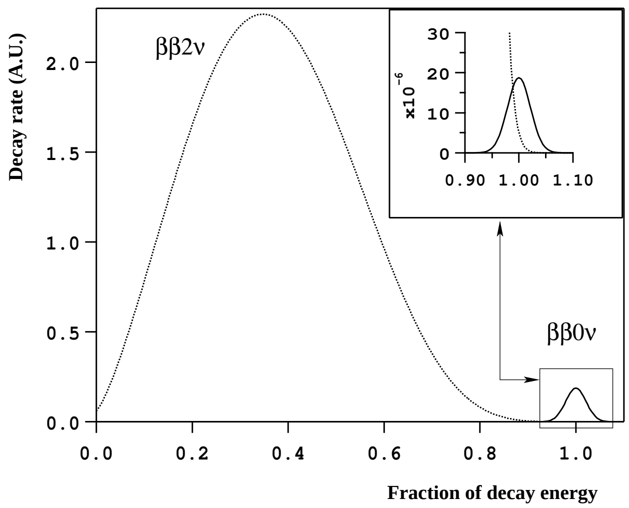


**Figure 2.5** - Schematic representation of the spectrum of the sum of the energy of the electrons for $\beta\beta 2\nu$ (dashed line) and $\beta\beta 0\nu$ (solid line). In the inset the relative intensity of the two neutrinos decay is overestimated in order to underline its contribution to the DDB0$\nu$ background. All spectra are obtained with the convolution of a 5% energy resolution that is common to many experiments.

where $G^{0\nu}$ is the phase space integral and can be estimated exactly, $\left|M^{0\nu}\right|^2$ is the decay matrix element and $\langle m_\nu \rangle$ the effective neutrino mass:

$$\langle m_\nu \rangle = \sum_k \phi_k m_k |U_{ek}|^2 \qquad (k = 1, 2, 3) \tag{2.8}$$

Stressing again the fact that $\beta\beta 0\nu$ is possible only for Majorana's neutrinos, let's observe that the $\phi_k$ phases that appear in the last equation are the CP intrinsic neutrino parities. Their presence implies that cancellations are possible. When neutrino is a Dirac particle then cancellation is total (it is equivalent to a couple of degenerate Majorana neutrinos with opposite phases). Therefore, $\beta\beta 0\nu$ could take place only through the exchange of Majorana neutrinos. Since DBD is sensitive to neutrinos of a given nature, it can solve the puzzle about it. Observation of $\beta\beta 0\nu$ would clearly means that neutrinos are Majorana particles. However, if we are unable to obtain a positive indication of $\beta\beta 0\nu$ because of lack of sensitivity, neutrinos may still be Majorana particles. In fact, only direct neutrino mass measurements can demonstrate the Diract nature of neutrinos.

Eq. (2.8) points out also the importance of $\beta\beta 0\nu$ in mass hierarchy discovery. In fact, even if $\langle m_\nu \rangle$ depends on $\phi_k$, their upper and lower limits depend on the absolute values of the mixing matrix elements. Thus, if it could be possible to measure $\langle m_\nu \rangle$ from oscillation experiments, it would mean that a range for the absolute neutrino mass can be gained, as shown in fig. 2.6 and 2.7. For this reason the $\beta\beta 0\nu$ could help to solve the questions on the absolute value of neutrino masses and to disentangle the hierarchy scheme of the neutrino mass eigenvalues.

In particular a sensitivity of $\sim 10 - 50$ meV on $\langle m_\nu \rangle$ could definitely exclude the inverse and quasi–degenerate hierarchy [37].

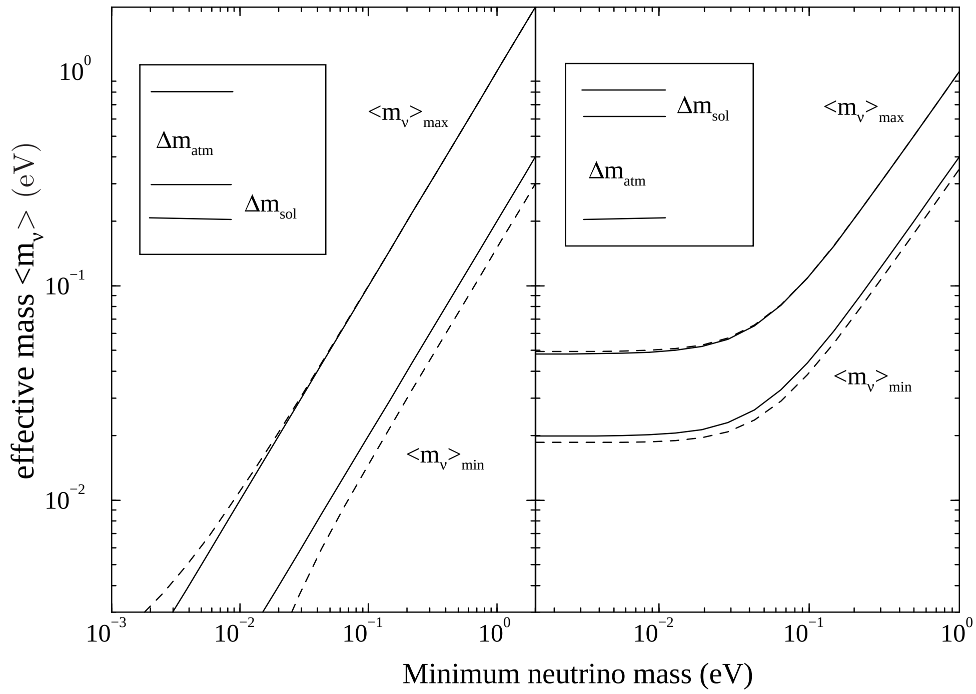


**Figure 2.6** - Plot of the effective mass $\langle m_\nu \rangle$ as a function of the lightest neutrino mass (on a log-log scale) [32]. In the left side direct mass hierarchy has been supposed while on the right the inverse one. Both curves have been evaluated for the LMA solution with $\delta m^2_{\text{atm}} = 2.4 \times 10^{-3}$ eV$^2$, $\delta m^2_{\text{sol}} = 4.5 \times 10^{-5}$ eV$^2$ e $|U_{e,2}|^2 = 0.3$. Solid lines have been calculated for $U_{e,3} = 0$ while dashed line uses the latest limit obtained from the CHOOZ and Palo Verde experiments: $|U_{e,3}|^2 = 0.025$ [33, 34].

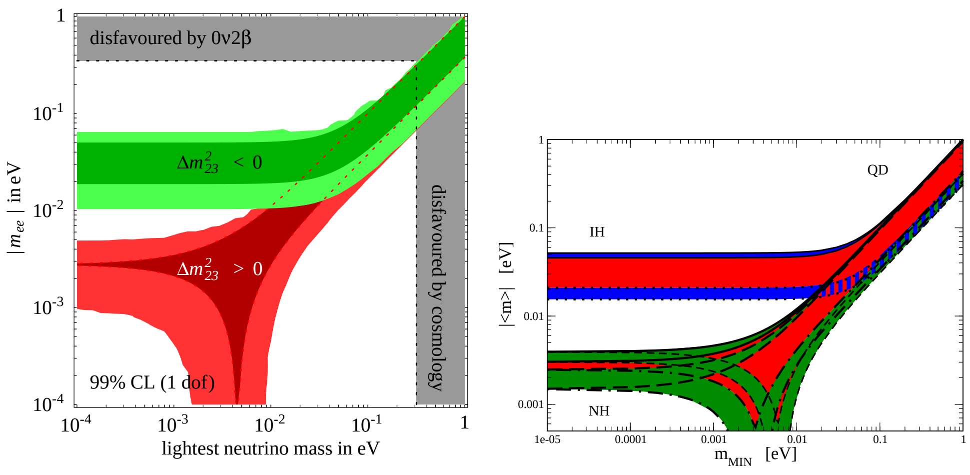


**Figure 2.7** - The possibility to distinguish between the three neutrino mass hierarchies depends on the allowed values of $|\langle m_\nu \rangle|$ in each case. (left) Plot the $99\%$ CL range for $m_{ee}$ as function of the lightest neutrino mass from [35]. (right) The predicted value of $|\langle m_\nu \rangle|$ (including a prospective $2\sigma$ uncertainty) as a function of of the lightest neutrino mass for $\sin^2\theta_{13} = 0.015 - -0.006$, including the latest MINOS results (see [36]).

| Nuclide | i.a. [%] | Q–value [keV] |
|---|---|---|
| $^{48}$Ca | 0.0187 | 4272 |
| $^{76}$Ge | 7.44 | 2038.7 |
| $^{100}$Mo | 9.63 | 3034 |
| $^{116}$Cd | 7.49 | 2804 |
| $^{130}$Te | 33.9 | 2528 |
| $^{150}$Nd | 5.64 | 3367 |
| $^{150}$Nd | 5.64 | 3367 |

**Table 2.1** - Properties of $\beta\beta0\nu$ candidates nuclides

From eq. (2.7), it is also clear that the evaluation of $\langle m_\nu \rangle$ from an experimental measure of $T^{0\nu}_{1/2}$ will require the exact knowledge of the nuclear matrix elements. From a theoretical point of view, this is the main limit when describing $\beta\beta0\nu$ . Several models have been proposed and is not simple to evaluate their correctness and accuracy, especially because they are not connected with other nuclear processes for easy cross–check. Even the comparison with the two neutrino decay presents unclear points, mostly because of the different neutrino role in the two processes. More references and the results of the matrix elements calculation can be found in [38]. Recent efforts have been devoted to give an estimation of the uncertainties of the NME calculations [39].

### 2.2.3 Candidate nuclides

Several nuclides are $\beta\beta0\nu$ candidates. They are reported in tab. 2.1 along with their most relevant properties: the isotopic abundance and the energy of the expected transition. As we will discuss later, the isotopic abundance is an important because very big active mass are needed by $\beta\beta0\nu$ experiments. The transition Q–value is relevant because the phase–space factor $G^{0\nu}$ that appears in (2.7) goes like $Q^5$. Moreover, it is better if the $\beta\beta0\nu$ Q–value falls in a region of the spectrum were the background from other radioactive events is as low as possible.

## 2.3 Experimental efforts for DBD search

### 2.3.1 Experimental approach and requirements

As described in fig. 2.5, the shape of the two electrons' summed energy spectrum enables us to distinguish among the two different decay modes discussed. In particular, the $\beta\beta0\nu$ signal is very clear: a peak at the transition $Q$-value, enlarged only by the detector energy resolution. Additional signatures may come from the single electrons energy and angular distribution.

Two experimental strategies are possible:

**Indirect techniques:** an approach that was important at the beginning of the DBD era and consists in the detection and identification of the daughter nuclide (A,Z+2) in a sample containing a high concentration of the DBD candidate (A,Z). The sample must be untouched for a long time. These geochemical and radiochemical experiments are no more pursued nowadays because it is not possible to distinguish the decay channel (zero o two neutrinos decay).

**Direct techniques:** an approach based on the development and operation of specific detectors with the aim to detect the two electrons emitted and therefore reconstruct the energy spectrum of fig. 2.5. In some cases, it is possible to measure additional information like the energy of each electron or their momentum.

The properties of the DBD set many strong constrains and requirements on the experimental techniques:

**High energy resolution:** a small peak must be revealed over background.

**Low background:** it is necessary to work deep underground, to use radioclean materials and proper shields.

**Big sources:** to increase the number of candidates nuclides under measurement in order to have sensitivity on the decay time up to $10^{25}$–$10^{28}$ years.

**Event reconstruction ability:** the $\beta\beta0\nu$ has a very characteristic decay with the two electrons that share the whole decay energy; electrons tracking can therefore help in background rejection.

Unfortunately there are up to now no detectors that can fulfill these four requirements at the same time.

Two are, substantially, the techniques used:

**homogenous detectors:** (or active source detectors), whose main advantage is to have the active $\beta\beta0\nu$ candidate nuclide inside the detector material;

**non–homogeneous detectors:** (or passive source detectors), in which the source and the detector are distinct.

Several conventional detectors have been used so far in DBD direct searches: solid state devices (Germanium spectrometers and Silicon detector stacks), gas counters (time projection chambers, ionization and multiwire drift chambers) and scintillators (crystal scintillators and stacks of plastic scintillators). Techniques based on the use of low temperature calorimeters have been, on the other hand, proposed and developed in order to improve the experimental sensitivity and enlarge the choice of suitable candidates for DBD searches, with an active source approach.

A common feature of all DBD experiments has been the constant work against backgrounds. Further suppression of such backgrounds will be the challenge for future projects whose main goal will be to maximize the $\beta\beta0\nu$ rate while minimizing background contributions.

### 2.3.2 Sensitivity

In order to compare different experiments and point out the advantages and the disadvantages of the different detecting techniques, it is convenient to introduce a very important parameter, called sensitivity $S$. It is defined as the lifetime corresponding to the minimum number of detectable events above background at a given confidence level. Let $t$ be the measurement time, $M$ the "active" mass (i.e. the mass of the $\beta\beta0\nu$ decay nuclides present in the source), $B$ the background counting rate (expressed in number of counts per unit energy per unit time per unit mass) in the energy region where the decay peak is expected, $\Gamma$ the FWHM energy resolution and $\varepsilon$ the efficiency of the detector. If the background is not null, we can express the sensitivity as

$$S(T_{1/2}) = K \cdot \frac{i.a.}{A}\sqrt{\frac{M \cdot t}{\Gamma \cdot B}} \cdot \varepsilon \qquad (1\sigma) \tag{2.9}$$

where $A$ is the compound molecolar mass, $i.a.$ the candidate nuclide isotopic abundance and $K$ is a constant factor. In addition to its simplicity, eq. (2.9) has the advantage of emphasizing the role of the essential experimental parameters: mass, measuring time, isotopic abundance, background level, energy resolution and detection efficiency.

Therefore, to improve the experimental results, it is possible by "brute force" increase $(M \cdot t)$ and to enhance the detector technology $(\Gamma \cdot B)$.

Strong background reduction is one of the most critical issue in $\beta\beta0\nu$ experiment. Several kinds of background source are usually present: internal to the active source due to natural decay chain elements or cosmogenic activation; external from cosmic rays, neutrons and contamination of surrounding materials; surface contamination of the detectors. An unavoidable/unrejectable source of background for the $\beta\beta0\nu$ mode is constituted by the $\beta\beta2\nu$ decay close to the endpoint and high energy resolution is therefore extremely important.

As far as the non–homogeneous detectors experiments are concerned, they are mostly performed with gas detectors (TPC, DC) in which the source is introduced into the volume of the detector as very thin sheets (of about 50 $\mu m$), to reduce the energy loss of the electrons emitted in the decay. The detection efficiency associated with this kind of measure is of the order of 30%. The great advantage of these experiments lies in the reduction of the background: the clear trace, which is peculiar in a drift chamber, for a 2 electrons event, guarantees a very good capability of background discrimination. The energy resolution, on the other hand, cannot be as good as $\sim$ 7–10% FWHM.

On the other side, homogeneous detectors can have detection efficiencies of the order of $\sim$ 90%, and energy resolution of the order of $\sim$ 0.2% FWHM (for Ge diodes and bolometers), while the background (mainly arising from the surrounding setup) cannot be easily rejected.

### 2.3.3 The present: first generation experiments

Impressive progress has been obtained during the last few years in improving $\beta\beta0\nu$ half–life limits for several isotopes and in systematically updating the

$\beta\beta2\nu$ rates. In particular, good $\beta\beta0\nu$ sensitivities have been achieved in few experiments that we will very briefly summarize here.

**Heideleberg–Moscow**

The best limit on $\beta\beta0\nu$ comes from the Heidelberg–Moscow (HM) experiment [40] on $^{76}$Ge even if similar results have been obtained also by the IGEX experiment [41]. In both cases a large mass (several kg) of isotopically enriched (86 %) Germanium diodes, is installed deep underground below heavy shields against gamma and neutron environmental radiation. Extremely low background levels are then achieved thanks to a careful selection of the setup materials and further improved by the use of pulse shape discrimination (PSD) techniques.

Both experiments quote similar background levels in the $\beta\beta0\nu$ region of $\sim$0.2 (c/keV/Kg/y) and $\sim$ 0.06 (c/keV/Kg/y) before and after PSD. Taking into account the uncertainties in the NME calculations, such experiments indicate an upper limit of 0.3–1 eV for $\langle m_\nu \rangle$.

As will be discussed later, new ideas to improve such a successful technique characterize many of the proposed future projects. However, given the NME calculation problem, more emitters should be investigated (e.g. $^{76}$Ge, $^{136}$Xe, $^{116}$Cd).

In January 2002, few members of the HM collaboration claimed evidence for $^{76}$Ge $\beta\beta0\nu$ [42] with $T^{0\nu}_{1/2}$ = 0.8–18.3 $\times 10^{25}$ y (best value $T^{0\nu}_{1/2} = 1.5 \times 10^{25}$ y) corresponding to a $\langle m_\nu \rangle$ range of 0.11–0.56 eV (best value 0.39 eV). This claim is based on the identification of tiny peaks close to the $\beta\beta0\nu$ region of $^{76}$Ge, one of them at the energy of the expected Q–value of the DBD. This announcement raised immediate scepticism [43]. Several re–analyzes of the data were published by the claim's authors [44–47], while other authors [48–50] still criticize it. It is therefore important to experimentally check this claim, both on $^{76}$Ge and other nuclides.

**Cuoricino**

Another technique, suggested [51] and developed [52] by the Milano group, is based on the use of bolometers. Besides providing very good energy resolutions they can in fact practically eliminate any constraint in the choice of the candidate nuclide. They are in fact constrained only by the requirement of finding a compound allowing the growth of a diamagnetic and dielectric crystal. Extremely massive [53] detectors can then be built, by assembling large crystal arrays.

Thermal detectors have been pioneered by the Milano group for $^{130}$Te $\beta\beta0\nu$ research and are the main characters of this Ph.D. work and will be described in detail later on. The present 41 Kg $TeO_2$ detector (named Cuoricino) is characterized by a good energy resolution (7–8 keV on the average at the $\beta\beta0\nu$ transition energy at 2528 keV) and a background level of $\sim$ 0.18 (c/keV/kg/y). The quoted limit of $2.2 \times 10^{24}$ y on the $^{130}$Te $\beta\beta0\nu$ half–life, corresponding to a limit of 0.2–0.9 eV on $\langle m_\nu \rangle$, represents the best limit after those reached by Ge diodes experiments.

**NEMO3**

Half-way with next generation experiments, NEMO3 [54] is a passive source detector located in the Frejus underground laboratory at a depth of $\sim 4800$ m.w.e. It consists of a tracking (wire chambers filled with an ethyl–alcohol mixture, operated in the Geiger mode) and a calorimetric system (1940 plastic scintillators) operated in a 30 gauss magnetic field. A well designed source system allows the simultaneous analysis of up to 10 kg of different $\beta\beta0\nu$ active isotopes. Despite a relatively modest energy resolution (11% FWHM at 3 MeV), implying a non negligible background contribution from $\beta\beta2\nu$, they achieved very good results on the study of the the latter $2\nu$ decay spectra of several $\beta\beta$ emitters ($^{82}$Se, $^{96}$Zr, $^{116}$Cd, $^{150}$Nd). The best result on $\beta\beta0\nu$ is related to $^{100}$Mo with a limit on the half–life of $4.6 \times 10^{23}$ y [55].

### 2.3.4 The future: next generation experiments

We have seen that the field of $\beta\beta0\nu$ searches is very active. The goal of the future experiments is to reach sensitivities capable of probing the inverted mass hierarchy, i.e. sensitivities on the decay time of the order of $\sim 10^{26} - 10^{27}$ y. There are several possibilities to achieve this goal and the way to do that is contained in the parameters of eq. (2.9) and (2.7). So far, the best results have been obtained by exploiting the calorimetric approach (active source detectors) which characterizes therefore most of the future proposed projects. Several experiments have been proposed after the recent indications and results. A complete report is beyond our scope and can be found in the presentations at the recent Neutrino 2006 conference [29]. We add few notes only on three of the most promising experiments with homogeneous detectors.

**GERDA**

GERDA [56, 57] (GERmanium Detector Array) is the only completely approved and funded experiment. It will be carried on at the INFN Gran Sasso National Laboratories. It is based on the technique already suggested by the HM collaboration: naked Ge diodes will be suspended in the centre of a very large liquid nitrogen container, which will act as a very effective shield. The experiment will consists of two phases: in the first one the detectors of the HM and IGEX collaborations will be collected and "naked", removing all the components that are not needed for operating them in $LN_2$. The total mass will be $\sim$17 kg of 86% enriched $^{76}$Ge. The collaboration will probe the HM claim within the first 1-2 years. They plan to reach zero background in the $\beta\beta0\nu$ region. The second phase will consist of the addition of new enriched detectors for a total mass of 60 kg (0.7 Kmol). For the second phase they will use background discrimination techniques.

**CUORE**

CUORE [58] (Cryogenic Underground Observatory for Rare Events), the extension of Cuoricino, will be described in detail in chapter 3. Among all the proposed experiments it is the only one that needs a background suppression of only a factor 10 with respect to the pilot Cuoricino experiment. A factor of two was already achieved in 2004. The expected sensitivity will be $7 \times 10^{26}$ y. The experiment has been approved and it is scheduled to start in 2010.

**Majorana**

MAJORANA [59], which involves many of the IGEX collaborators, will consist of an array of 210 isotopically enriched Ge diodes for a total mass of 0.5 tons. As opposed to the GERDA design, the use of a very low activity conventional cryostat (extremely radiopure electroformed Cu) able to host simultaneously a large number of diodes is proposed. The driving principle behind the project is a strong reduction of the background by the application of very effective PSD and the development of special segmented detectors. Despite the very promising R&D developed in the last years, the project is not yet funded.

# · Chapter 3 ·

# Cuoricino and CUORE experiments

## 3.1 Introduction

Many of the detector improvements on design, concept and operating behavior that will be presented in the next chapters are generally valid for most bolometers. We will infact discuss about the enhancement of the sensors (focusing on our NTD thermistors), the optimization of the detector couplings and, last but not least, about the possibility of providing some sort of spatial resolution. Given the experimental approach and the need of testing our ideas and simulations, we had to work on specific kind of detectors. Moreover, we believe that real experience and use of something is the best way to understand its limits and also its values. It proved very fruitful indeed the experience we gained in our research environment.

This is the reason why we are introducing in this chapter the Cuoricino and CUORE experiments. They are the context for the research work presented in this dissertation.

Moreover, part of this Ph.D. work has been devoted to contribute to the successful running of the Cuoricino detector itself by means of periodic shifts at the Gran Sasso Laboratory where the experiment is located.

As anticipated in the previous chapter, Cuoricino is a bolometric experiment looking for neutrinoless double beta decay of $^{130}$Te. It is in fact an array of 62 bolometers with $TeO_2$ absorbers. In the first section of this chapter we will see the details of this bolometers and we will also use the thermal model introduced in section 1.3 to simulate them. Then we describe briefly the read-out process and the related data acquisition and analysis.

Cuoricino is an outstanding physics experiment and it deserves definitely an overview (section 3.4). However, Cuoricino is also a prototype and test bench for a next–generation one–ton–scale experiment that aims at reaching a sensitivity of few tens meV on the Majorana neutrino mass (eq. (2.8)). This experiment is named CUORE. Cuoricino proved to be very useful from many points of view and we will try to show them in 3.7.

Even if no technological problem is foreseen, the road towards CUORE is not completely straightforward. The challenges we have to face are summarized in §3.9. Those challenges drove our work and defined our goals when working on the single bolometer. In this way our R&D work has been far from abstract optimization and thus more interesting!

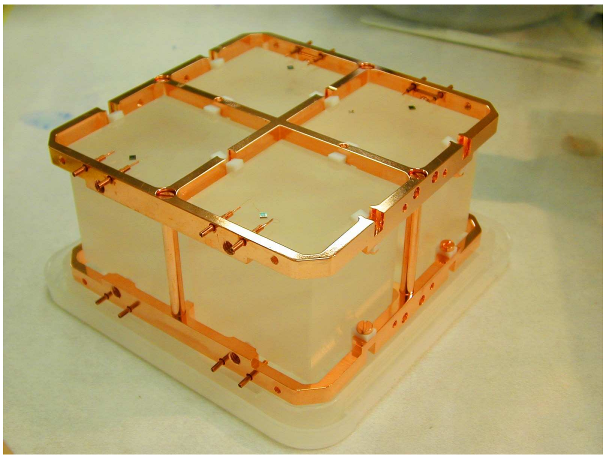

**Figure 3.1** - Picture of a Cuoricino module of four $5 \times 5 \times 5$ cm$^3$ bolometers.

## 3.2 Cuoricino bolometers

In the previous chapters we provided many informations about bolometers and now it is time to sum them up and get them real. Infact, until now, we mainly spoke about general bolometers. From now on, we will focus on that particular kind of bolometers that constitute the Cuoricino single module detector. In this section we will describe it. A picture of a module of four $5\times5\times5$ cm$^3$ Cuoricino bolometers is in fig 3.1.

### 3.2.1 The absorber

The design of a bolometer implies necessarily a trade–off between the thermal and mechanical properties of the absorber material and its content in $\beta\beta0\nu$ candidates nuclei. In section 1.2.2, we already described some of the general requirements of the bolometer absorber. Those requirements are generally well satisfied by dielectric and diamagnetic materials with high Debye temperatures.

The decision should also take into account other motivations that come from the $\beta\beta0\nu$ search to be performed:

- isotopic abundance or enrichment possibilities (at reasonable cost) of the candidate nuclide;

- Q-value of the $\beta\beta0\nu$ transition - the phase space term $G^{0\nu}$ that appear in eq. (2.7) is infact proportional to $Q^5$ and therefore higher Q–values are preferred for DBD search;

- radiopurity of the absorber material;

- nuclear matrix elements knowledge and values;

- position of the Q-value in the energy spectrum - it is obviously better if no other decay fall too close to the $\beta\beta0\nu$ energy.

Mechanically speaking, the absorber materials must be available in structure of few tens of $cm^3$ and must be resistant to thermal cycles.

The choice of the Milano group, at the dawn of bolometric $\beta\beta0\nu$ search, fell on tellurium dioxide ($TeO_2$ ). This material contains $^{130}$Te which is the $\beta\beta0\nu$ candidate with the highest isotopic abundance (about 35% - see table 2.1).

Moreover, its Q–value falls in an empty region of the energy spectrum, almost outside the natural radioactivity region, between the peak and the Compton edge of the $^{208}$Tl decay. $TeO_2$ is also a commercial material easily available at a reasonable price and radiopurity.

$TeO_2$ crystals can be grown in different sizes. Cuoricino uses crystal of $3 \times 3 \times 6$ $cm^3$ and $5 \times 5 \times 5$ $cm^3$ produced by SICCAS, a Chinese company. Details of the crystallization procedure can be found elsewhere [60].

Concerning the physical properties of $TeO_2$ , the Debye temperature $\Theta_D$ is the most important. Its value is reported in literature [61] to be 272 K but these measurements were performed at temperatures not lower than 0.6 K. Better measurements [62] were performed in the range 60-280 mK. The heat capacities of the auxiliary components (thermometers, heaters, holders,...) required for the measurements were also taken into account. The new value is $\Theta_D = 232 \pm 7$ K and is in agreement with the one obtained with other techniques.

From $\Theta_D$ and (1.2) we can derive the expression for the heat capacity per unit volume of $TeO_2$ crystals:

$$C_{\mathrm{TeO}_2} = 1.8 \times 10^{-5} \cdot T^3 \quad \left[\frac{\mathrm{Joule}}{\mathrm{K} \cdot \mathrm{cm}^3}\right] \tag{3.1}$$

Here the $TeO_2$ density is 6 g/$cm^3$.

### 3.2.2 The thermal sensors

Neutron transmutation doped (NTD) Germanium thermistors are employed as thermal sensors in Cuoricino bolometers and are produced at the Lawrence Berkeley National Laboratory (LBNL), California, USA.

**Thermistors doping and production**

The thermistors are doped close to the metal–insulator transition (of the order of $10^{15} - 10^{16}$ atoms/$cm^3$ for Ge). In this condition, a peculiar conduction regime holds which is named *hopping conduction*(§1.2.3). The doping is achieved by neutron transmutation. It consists in the production of doping atoms inside the semiconductor by means of nuclear transmutations from the irradiation of the Ge crystal with a beam of thermal neutrons from a nuclear reactor. The NTD process is usually the best choice to achieve uniform doping in the crystal.

Thermistors are cut from Ge wafers of 5 cm dia and 3 cm depth. The faces of the wafers are gold plated before sawing. The distance between the contacts is thus fixed while the thermistor section can be adjusted depending on the desired heat capacity and resistance. Typical dimensions of Cuoricino thermistors are $1.5 \times 0.4 \times 3$ $mm^3$ o $3 \times 1 \times 3$ $mm^3$. The electrical connections are obtained by ball–bonding 50 $\mu$m gold wires to the gold pads.

The resistivity of such semiconductors can be expressed in terms of the temperature $T$ and of a parameter $\gamma$ which depends on the conduction type, as in eq. (1.8):

$$\rho(T) = \rho_0 \exp\left(\frac{T_0}{T}\right)^{\gamma}$$

where $\rho_0$ e $T_0$ are related to the doping level [1].

The thermistor resistance is determined by the resistivity $\rho$ and the geometry:

$$R(T) = \rho(T)\frac{l}{s} = R_0 \exp\left(\frac{T_0}{T}\right)^{\gamma} \tag{3.2}$$

where $l$ and $s$ are the contacts distance and the section of the thermistor. In the following, we will always assume a *variable range hopping* conduction regime with high compensation level that implies $\gamma = 1/2$.

**Hot Electron Model**

A question naturally arises about the definition of the temperature that appear in the previous (3.2). For example, it is known that for metals, the temperature is defined by the conduction electrons. Similarly, for semiconductors, the *Hot Electron Model* (HEM) is introduced. This model assumes that at low temperature, thermal coupling between the electrons and the lattice is weaker than the couplings among the electrons. In this way, when Joule power is injected into the electrons, their temperature raises higher than that of the lattice. Thermally speaking, the thermistor must then be described as composed by two separate systems: the electrons and the lattice (or phonons). In particular, the resistance of (3.2) depends on the electrons temperature.

The decoupling $G_{\text{e-p}}$ introduced by the HEM reduces the performance of the bolometer because a fraction of the phonons from the incident particle might flow to the heat sink before reaching the electrons in case of too low $G_{\text{e-p}}$. Moreover, the electro–thermal feedback (see below) is more severe when the decoupling is too high. Other details will be given in 5.2.

**Thermistor operation**

Thermistors are operated as thermal sensors by injecting a weak current flow $I$ by means of a simple biasing circuit shown in in fig. 3.2. A load resistor $R_L \gg R$ is placed in series with the thermistor $R$ and biased with a constant voltage $V_B$. In this way, we can measure the voltage drop $V$ across the thermistor. The characteristic $(I, V)$ load curves for the thermistors can be also obtained as in fig. 3.3. However, the current flowing into the thermistor produces a Joule dissipation which increases its temperature. Heating the thermistor reduces its resistance (as in eq. (3.2)) with the final effect of a strong nonlinearity of the load curve. This behavior is called *electro–thermal feedback*.

The static conditions of the thermistor are determined by the intersection, in the $(V, I)$ plane, between the line $V = V_B - IR_L$ and the load curve $I - I(V)$, as

[1] Interesting consideration about the comparison of the measurements and the theory of the NTDs can be found in [63]. From this reading it is also clear that the behavior of such devices is not as simple as it could seem.

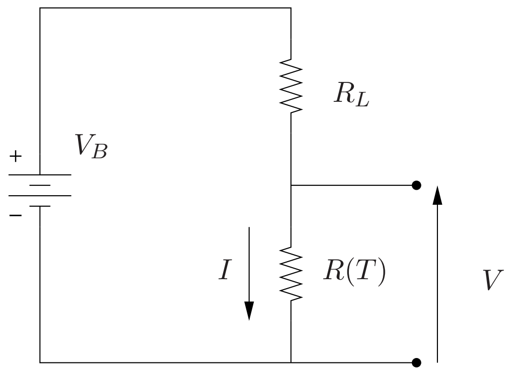


**Figure 3.2** - Basic scheme of a typical biasing circuit of thermistors.

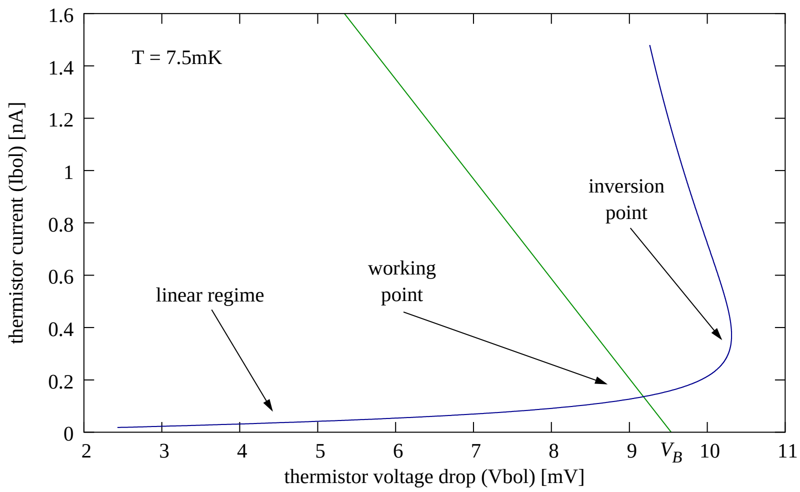


**Figure 3.3** - Simulated load curve $(V, I)$ for a Cuoricino NTD Ge thermistor.

in fig. 3.3. The intersection is usually called *working point*. The *optimal working point* is consequently defined as the point where the best detector performance is achieved in terms of signal amplitude or, better, as signal–to–noise ratio.

The voltage change $\Delta V$ across the thermistor due to a temperature rise $\Delta T$ is given by

$$|\Delta V| = V \cdot A \cdot \frac{|\Delta T|}{T} \tag{3.3}$$

where $A$ is the sensitivity defined in (1.6). It is clear that the signal amplitude grows with the bolometer voltage $V$ which unfortunately cannot be raised above the inversion value $V_i$. Moreover, usually the optimal working point is lower than $V_i$ because the heating produces a reduction of the sensitivity. For each detector is therefore necessary to measure experimentally the optimal working point as sketched in fig. 3.4.

The $R_0$ and $T_0$ parameters of (3.2) are characteristic of each thermistor and are related to the doping concentration and thus to the dose absorbed during the NTD process. Cuoricino thermistors have $T_0 \sim 3$ K and $R_0$ of few $\Omega$s. We will come back to this topic later in §5.2. Typical values of the resistance $R$ at

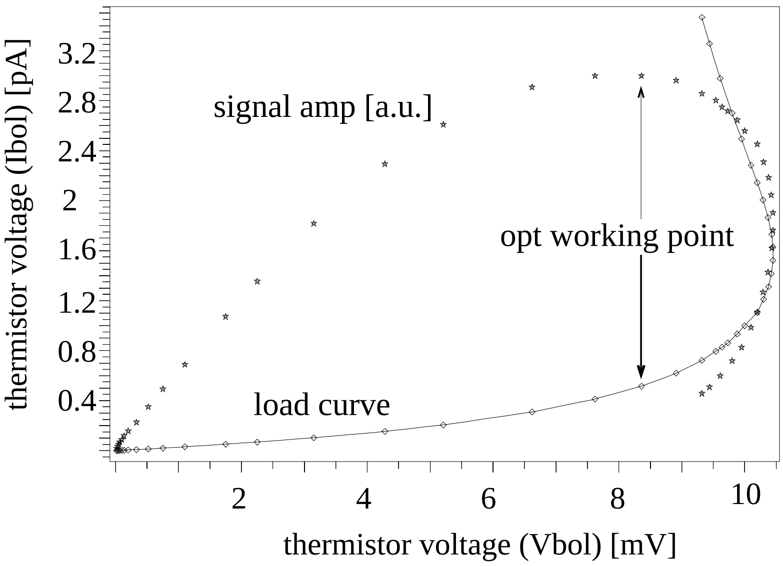


**Figure 3.4** - Example of optimal working point search for a typical Cuoricino bolometer. The signal amplitudes corresponds to the same monochromatic energy release at different working points.

the Cuoricino bolometers working temperatures range from 50 to 200 MΩ.

**Parameter values**

The electron–phonon conductance introduced by the *Hot Electron Model* has been determined with ad-hoc measurements [64]. Particular care was used to determine its relationship with temperature and sensor mechanical properties. It was observed that its value scales with the volume. The phenomenological relation is:

$$G_{\mathrm{e\text{–}f}} = 7.8 \times 10^{-2} \cdot T^{4.37} \quad \left[\frac{\mathrm{W}}{\mathrm{K} \cdot \mathrm{mm}^3}\right] \tag{3.4}$$

As far as the heat capacity of the electrons of the thermistor, we assume:

$$C_{el} = 1.1 \times 10^{-9} \cdot T \quad \left[\frac{\mathrm{Joule}}{\mathrm{K} \cdot \mathrm{mm}^3}\right] \tag{3.5}$$

in order to justify the observed experimental rise times of the signals [65].

The lattice heat capacity of the thermistor is instead fully ascribed to the Debye term of the Ge crystal ($\Theta_D = 362$ K) and its contribution is minimal:

$$C_{ret} = 3.004 \times 10^{-9} \cdot T^3 \quad \left[\frac{\mathrm{Joule}}{\mathrm{K} \cdot \mathrm{mm}^3}\right] \tag{3.6}$$

### 3.2.3 The other detector components

**Copper frame and PTFE connections**

Cuoricino bolometers are arranged into a $2 \times 2$ or $3 \times 3$ structure by means of a copper frame. The copper acts as a heat sink for the bolometers because it is in good thermal contact with the coldest part of the dilution refrigerator.

Small pieces of Teflon (PTFE) are employed to hold the crystal into the frame. This material was chosen for its good mechanical, thermal and radio–purity properties. We will come back on this subject later on in §6.2.

PTFE thermal conductances has been measured by the Milan group to as:

$$G_{\mathrm{PTFE}} = 4 \times 10^{-5} \cdot T^{2} \left[\frac{\mathrm{W}}{\mathrm{K}}\right] \tag{3.7}$$

but this value must be considered only as an estimation because it was obtained with an holder structure which is not exactly the same presently used in Cuoricino. However, we are quite confident that the value of this conductances scales with the contact area between the Teflon and the crystal.

The PTFE pieces are so small that their heat capacity can be neglected.

**Electrical contacts**

The electrical contacts of the thermistors with the read–out wires are made with gold wires of 50 $\mu$m diameter. The wire is attached to the gold pads of the thermistors by means of ball bonding.

These wires act also as a non–negligible thermal conductance toward the heat sink. These conductances appear to scale mainly with the area of the thermistor gold pads. Dedicated measurements [64] gave:

$$G_{\mathrm{wires}} = 1.6 \times 10^{-5} \cdot T^{2.4} \left[\frac{\mathrm{W}}{\mathrm{K} \cdot \mathrm{mm}^{2}}\right] \tag{3.8}$$

**Thermistor–absorber couplings**

A critical role in the bolometers dynamics is played by the thermal (and mechanical) coupling between the absorber and the thermistors. This coupling is in fact responsible for the rise time and amplitude of the signals read by the thermistor itself.

Cuoricino thermistors were glued directly on the absorber surface by means of few spots of Araldit®, a two–part epoxy glue. The spots are deposited on the $TeO_2$ surface with an array of pins and a proper micromanipulator to achieve high density and reproducible size (about 0.5 mm diameter and 50 $\mu$m thick). We decided to use glue spots instead of glue films because the first are able to balance the differential thermal contraction between Ge and $TeO_2$ .

Measurements performed by the Milano group [64] provided the following phenomenological behavior for the conductance of the glue spots:

$$G_{\mathrm{glue}} = 0.26 \times 10^{-3} \cdot T^{3} \left[\frac{\mathrm{W}}{\mathrm{K} \cdot \mathrm{spot}}\right] \tag{3.9}$$

## 3.3 Cuoricino electronics and data acquisition

The electronic system that we are going to describe is the result of the development pursued during the last 20 years by the Milano group to operate their $TeO_2$ bolometers with NTD Ge thermistors. We will focus here on the details and specification of the Cuoricino system. The main scheme is more or less the

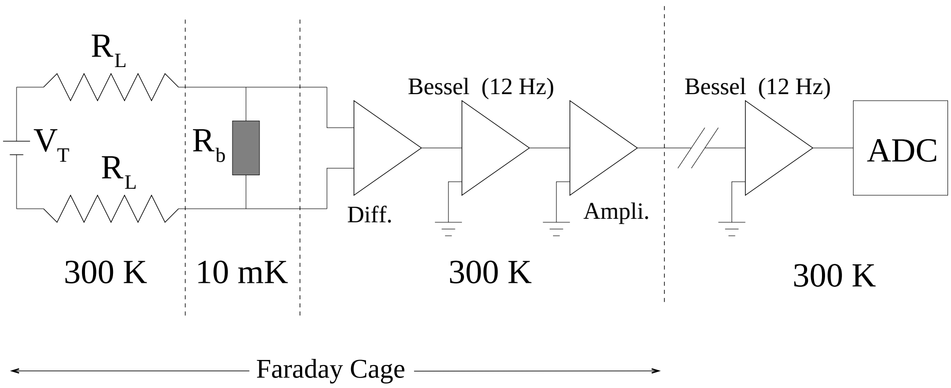


**Figure 3.5** - Scheme of the electrical read–out set–up.

same also for all the other $TeO_2$ bolometers that were used for the experimental tests reported in the next chapters.

The electrical read–out configuration of a bolometric system is shown in fig. 3.5 and can be divided into three main parts:

**Biasing system:** the thermistor is symmetrically biased by means of 2 load resistors $R_L$. In this way a differential signal is read, thus avoiding common mode noise. The value of $R_L$ must be greater than the thermistor impedance at the working temperature in order to have constant current bias and high signals. At T $\sim$ 10 mK the thermistors behave like a resistance of the order of 1—100 M$\Omega$; the load resistors are then chosen with values of the order of G$\Omega$. The Johnson noise for these high resistance values is no longer negligible.

**First differential stage:** it consists of a differential preamplifier with gain $G = 218$ (which contributes to the reduction of the common mode noise), an antialiasing Bessel filter (that cuts frequencies above 12 Hz) and a programmable gain stage. This first stage can operate at room temperature or can be cooled down to $\sim$ 120 K. In the latter case, series and parallel preamplifier noise is reduced by the fact that this noise decreases with temperature. Cold electronics can also help to reduce microphonic noise which is quite disturbing when observing low energy signals (as those needed for Dark Matter searches).

**Second stage:** an additional amplifier stage with adjustable gain is set before the signal is transmitted to the ADC.

After the second stage the signal is sent simultaneously to the Analog to Digital Converter (ADC) and to the trigger that commands the ADC. If the pulse amplitude is higher than the trigger threshold (that is independently set for each detector) the signal is digitalized and transmitted to a PC–VXI. This computer stores the data and performs pre–analysis routines that are useful to real–time check the measurement status.

The ADC parameters can be adjusted on pulse characteristic, but usually a voltage range of 0 – 10 V and 16 bits are used. A resolution in the amplitude

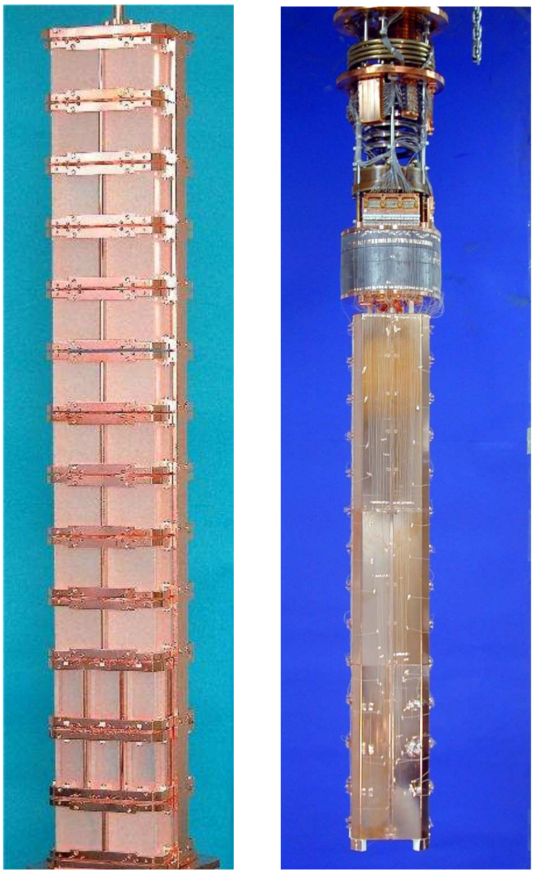

**Figure 3.6** - Pictures of the Cuoricino tower after bolometers assembly (left) and before insertion into the cryostat (right).

sampling of 0.15 mV is achieved. Signals are sampled every 8 s for a total of 512 samplings.

## 3.4 Cuoricino experiment

### 3.4.1 The Cuoricino detector

In the previous sections, we have seen the major character of this work, the $TeO_2$ bolometer that is the base element for the Cuoricino detector. In the second half of 2002, 62 of these bolometers were put together and arranged in 11 modules of 4 detectors each (already shown in fig. 3.1) and 2 modules of 9 detectors each. In the latter modules, bolometers size was $3 \times 3 \times 6$ cm$^3$ (330 g) while all the others were $5 \times 5 \times 5$ cm$^3$ (790 g). The final tower is shown in figure 3.6. All crystals are made with natural tellurite, apart two $3 \times 3 \times 6$ cm$^3$ crystals which are enriched in $^{128}$Te and two others enriched in $^{130}$Te with isotopic abundance of 82.3% and 75%, respectively. The total mass of Cuoricino is 40.7 kg of $TeO_2$ which corresponds to about $5 \times 10^{25}$ nuclides of $^{130}$Te (the candidate $\beta\beta0\nu$ nuclide). Cuoricino is the largest ever operated cryogenic detector.

| Run # | Start | Stop | Time [d] | Live time [%] | Statistic kg($^{130}$Te)·year |
|---|---|---|---|---|---|
| 1 | Apr 22, 2003 | Oct 27,2003 | 185 d | 29.8% | 0.94 |
| 2 | May 7, 2004 | May 10, 2006 | 730 d | 38.5% | 6.25 |

**Table 3.1** - Summary of the Cuoricino collected statistics up to May 2006. Statistic values are given only for $5 \times 5 \times 5$ cm$^3$ detectors.

All the assembly was carried out in clean room and nitrogen atmosphere. Cuoricino was installed in a dilution refrigerator in the Hall A at the GranSasso underground laboratory which provides 3500 m.w.e. shielding against cosmic rays.

As previously described, all crystals were grown with pre–tested low radioactivity material by SICCAS (China) and shipped to Italy by sea to minimize the activation due to cosmic rays. They were lapped with specially selected low contamination abrasives to reduce the radioactive contamination on the surface. All the copper and PTFE parts facing the detectors were separately treated with acids in order to reduce the surface contamination. All the detector mounting operations were performed in an underground clean room in a Nitrogen atmosphere to avoid Radon contamination. Archeological roman lead shields are placed all around the detector in order to reduce radioactivity coming from the cryostat. The tower is mechanically decoupled from the cryostat through a steel spring in order to avoid vibrations from the overall facility to reach the detectors. The dilution refrigerator is shielded against environmental radioactivity by two layers of lead of 10 cm minimum thickness each. The outer layer is of commercial low radioactivity lead, while the internal one is made with special lead with a $^{210}$Pb contamination of 16 $\pm$ 4 Bq/kg. The external lead shields are surrounded by an air-tight box flushed with fresh nitrogen to avoid Rn contamination to reach the detector. A borated polyethylene neutron shield (10 cm) is also present. All the structure is housed inside a Faraday cage in order to suppress electromagnetic interferences.

### 3.4.2 The Cuoricino operating setup

Cuoricino was first cooled in February 2003, but some read–out wires broke inside the cryostat, reducing the total mass under study to 26.5 kg. Before warming up to solve the problem some data were collected, up to 3.75 kg·y statistics and the first preliminary results were released [66]. At the end of October 2003 Cuoricino was stopped to undergo substantial operations of maintenance and to recover the lost read–out channels. The stop was longer than expected due to some restrictions in the Gran Sasso Laboratory required by the Italian authorities for safety reasons. The second run started in March 2004, with all the crystals working, except for 2 of them. A summary is presented in tab. 3.1.

Cuoricino is operated at a temperature of $\sim$ 8 mK with a spread of $\sim$ 1 mK. A routine energy calibration is performed before and after each subset of runs, which lasts about two weeks, by exposing the array to two thoriated tungsten wires inserted in immediate contact with the refrigerator. All runs where the average difference between the initial and final calibration is larger than the experimental error in the evaluation of the peak position were discarded.

Data are processed off–line as discussed in §3.5. Portions of measurement where the instabilities correction is not satisfactory are rejected. In the same way, portions of measurements where noise is too high (either when the energy resolution of the detector shows a sizable worsening and/or when a large fraction of the triggered signals are noise signals) are also rejected. The overall impact of these cuts on the measurements live time is however negligible.

### 3.4.3 Detector behavior

Figure 3.7 reports some examples of pulses from Cuoricino bolometers. The intrinsic irreproducibility of each detector is evident from the great variability of signals shapes, in particular the decay times. Several pulses infact show clearly a second longer decay constant. The origin of this behavior is still under investigation.

Despite these unusual pulses, most of the detectors do behave normally and the final sensitivity of the detector looks almost not affected by these unexplained behaviors.

Other interesting information and consideration on the Cuoricino detectors response can be found in [67] where an analysis of the characteristics of Cuoricino signals is performed.

### 3.4.4 Energy resolution

Cuoricino bolometers are performing very well. During the second run, the average pulse height obtained with the working detectors is of $167 \pm 99$ $\mu$V/MeV·kg for the $5 \times 5 \times 5$ cm$^3$ crystals and $147 \pm 60$ $\mu$V/MeV·kg for the $3 \times 3 \times 6$ cm$^3$ crystals[2]. The average resolution FWHM is $7.5 \pm 2.9$ keV for the bigger size and of $9.6 \pm 3.5$ keV for the small size crystals. The average resolution FWHM in the $\beta\beta0\nu$ region was evaluated on the 2615 keV gamma line of $^{208}$Tl, measured during calibration with a $^{232}$Th source.

A Cuoricino calibration spectrum is given in fig. 3.8.

### 3.4.5 Background

In fig. 3.9 the background spectra for the $5\times5\times5$ cm$^3$ and $3\times3\times6$ cm$^3$ crystals are shown. The gamma lines due to $^{60}$Co, $^{40}$K and of the $^{238}$U and $^{232}$Th chains are clearly visible. These lines, due to the low contamination of the experimental apparatus and setup, are not visible in the spectrum of single detectors since the statistic is too low. They appear only after summing the different detectors, and are a good check of the calibration and stability of the detectors during the background measurement. Other $\gamma$ lines from Te and Cu activation can be recognized. These are produced bu cosmic ray neutrons interaction while the

[2]The amplitude of the pulses usually scales with the detector size due to the larger heat capacity. In this specific case, the result is due to an optimization of the thermistor which are bigger and better coupled on $5 \times 5 \times 5$ cm$^3$ detectors.

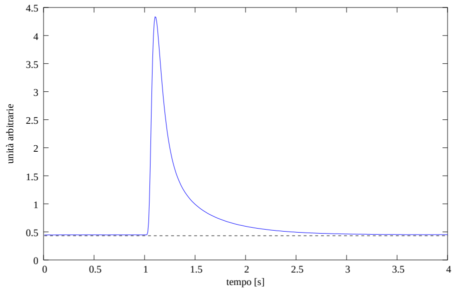


(a) classic fast pulse

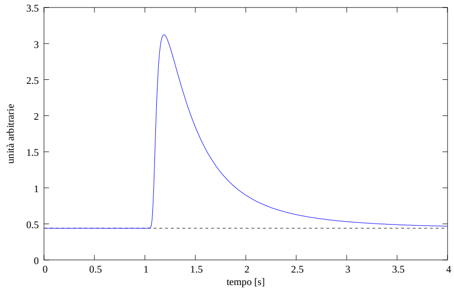


(b) classic slow pulse

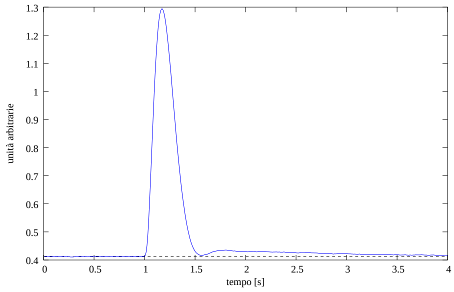


(c) pulse with oscillation

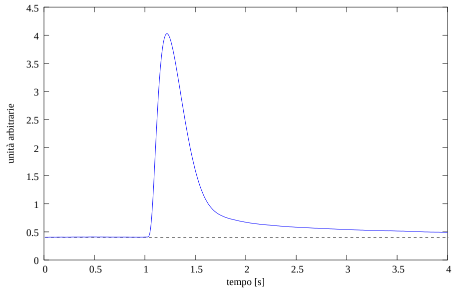


(d) pulse with long rise time and tail

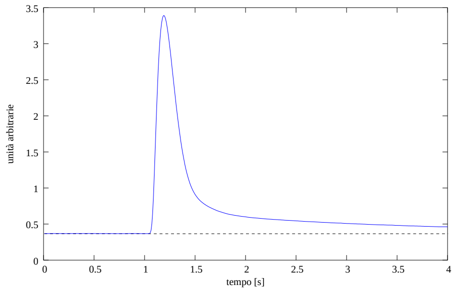


(e) pulse with tail

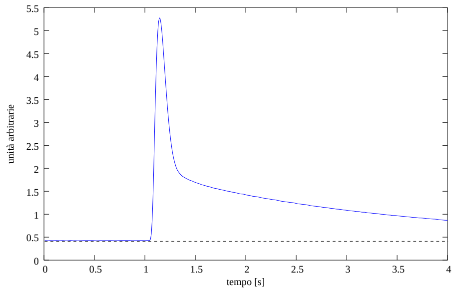


(f) pulse with tail

**Figure 3.7** - Examples of signals from different $5 \times 5 \times 5$ cm$^3$ Cuoricino bolometers.

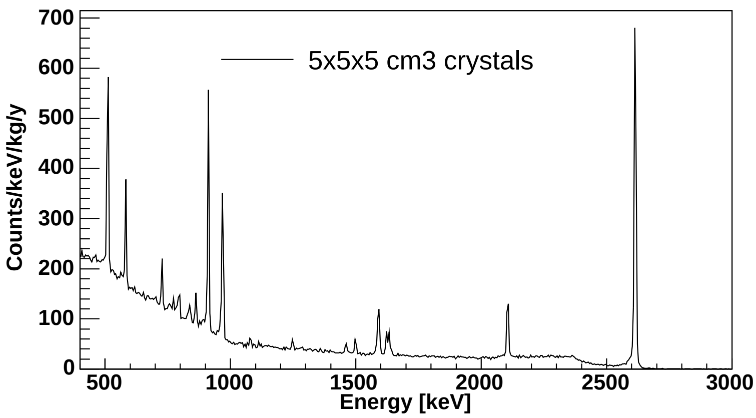


**Figure 3.8** - Calibration spectrum of the $5 \times 5 \times 5$ cm$^3$ bolometers of Cuoricino.

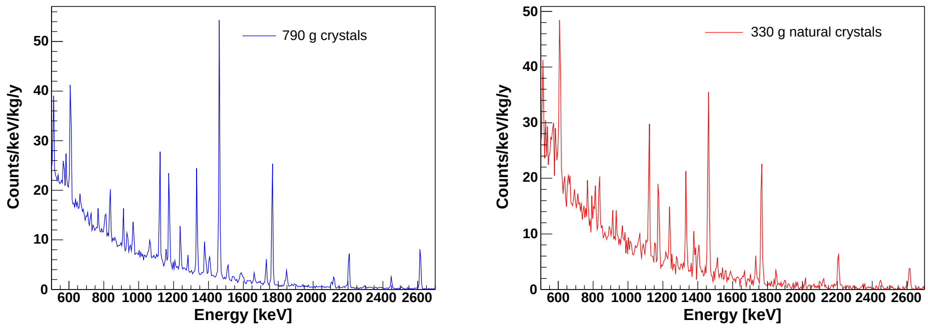


**Figure 3.9** - Anticoincidence background spectra of the $5 \times 5 \times 5$ cm$^3$ (left) and $3 \times 3 \times 6$ cm$^3$ (right) bolometers of Cuoricino.

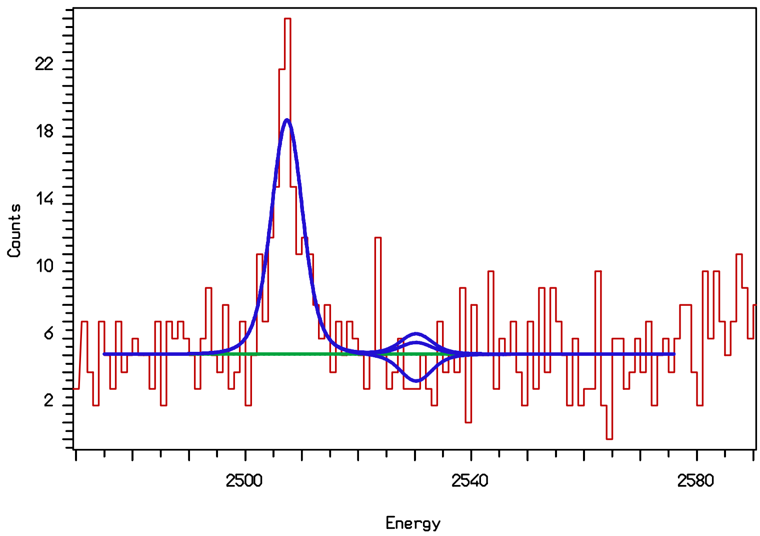


**Figure 3.10** - Detail of the Cuoricino anticoincidence spectrum in the region of interest for $\beta\beta0\nu$ (only $5 \times 5 \times 5$ cm$^3$ bolometers).

materials were aboveground. The FWHM resolution of $5 \times 5 \times 5$ cm$^3$ detectors at low energy, as evaluated on the 122 keV gamma line of $^{57}$Co, is 2.8 keV. The $^{208}$Tl $\gamma$ line at 2615 keV is used to evaluate the energy resolution in the region of double beta decay; the FWHM is 7 keV.

### 3.4.6 $\beta\beta0\nu$ half life and Majorana neutrino mass

The results presented here correspond to an effective exposure of 8.38 kg of $^{130}$Te/year. The sum of the spectra of the all crystals in the region of the expected $\beta\beta0\nu$ is shown in fig. 3.10. A small peak at 2505 keV due to the sum of the two lines of $^{60}$Co (1332 + 1173 keV) is present. This peak is only 3 FWHM away from the expected $\beta\beta0\nu$ and therefore cannot be excluded from the fit region. The background at the energy of $\beta\beta0\nu$ (i.e. 2475–2580 keV) is of

$0.18 \pm 0.02$ counts/kg/keV/y. This result is obtained assuming a flat background and adding the tail of the 2505 keV peak. We use as response function a sum of n gaussian each with the characteristic FWHM resolution at 2615 keV of the nth detector. No evidence of a peak is found at the energy expected for $\beta\beta0\nu$ of $^{130}$Te at 2530.3 keV.

By applying a maximum likelihood procedure [68, 69] we obtain a 90% C.L. lower limit of $2.4 \times 10^{24}$ years on the half-lifetime for $\beta\beta0\nu$ of this nucleus. Other approaches lead to similar result. Presently, the best fit yields a negative effect for the $\beta\beta0\nu$ peak. There is 5% variation of the limit when changing the energy region, the background shape (linear or flat) and when including or excluding the 2615 keV peak in the fit.

The upper bounds on the effective neutrino mass that can be extracted from our result depend strongly on the values adopted for the nuclear matrix elements, as reported in §2.2.2. Taking into account the above mentioned uncertainties, our lower limit leads to a constraint on the effective neutrino mass ranging from 0.18 to 0.94 eV which partially covers the mass span of 0.1 to 0.9 eV indicated by H.V. Klapdor-Kleingrothaus and others [70].

Since much literature pro and con on this issue appeared during the last years [44–50], an experimental confirmation or confutation of the claim is strongly demanded, and Cuoricino (together with the external source experiment NEMO3 [54, 55]) is at the moment the only running experiment that could do the job. In fact, a minimum $2\sigma$ level signal should be seen in 3 y, if the half-life for $^{76}$Ge is the claimed one, even if the less favorable NME is considered. On the other hand, due to the NME uncertainties, a null experiment on $^{130}$Te would not invalidate the claimed evidence. However, the measurement of the $\beta\beta0\nu$ in different nuclei is invaluable because it could reduce the NME uncertainties.

Cuoricino will run until 2010 when CUORE (§3.8) is foreseen to start. Assuming 60% of live time efficiency, in May 2010 Cuoricino would have added 2.4 years of statistics, reaching therefore 28 Kg ($^{130}$Te) resulting in a sensitivity of about $6 \times 10^{24}$ year on $\beta\beta0\nu$ half–life.

## 3.5 Cuoricino data analysis

Cuoricino data analysis is mainly performed off–line with dedicated software applications. The methods and tools we will describe here will be used extensively in the rest of this dissertation to analyze the reported data.

The main goal of the off–line analysis is the extraction of the relevant physics informations from the large amount of raw data recorded by the DAQ system. This analysis consists of two levels. The first level concerns the raw detector pulse analysis (e.g. amplitude evaluation, noise rejection, gain instability and linearity correction) aiming to the production of reliable ntuples and energy spectra. The second level analysis consist in a multi–dimensional analysis focused on retrieving physics results (namely $\beta\beta0\nu$ half life) from data. An insight on the various background sources is crucial to obtain meaningfull results.

Here we will focus only on first level analysis. Some details on second level analysis will be provided along with the Cuoricino results in §3.4.6.

As described in a previous section, for each triggered pulse an entire waveform is sampled and recorded. The acquired time window (few sec) must contain the entire pulse development in order to allow an accurate description of its waveform. The existence of a pre–trigger interval guarantees that a small fraction of samples can be used to measure the DC level (or *baseline*) of the detector (which is directly connected with the detector temperature).

**Goals**

The following are the important goals for the first level analysis (also called *pulse analysis*):

· maximization of the signal to noise ratio for the best estimate of the pulse amplitude. This is accomplished by means of the optimum filter (OF) technique [71];

· correction of the effects of system instabilities that can change the response function of the detectors (gain stabilization);

· rejection of the spurious triggered pulses by means of pulse shape analysis;

· identification and rejection of radioactive background pulses by means of coincidence analysis.

**The pulses parameters nutples**

In processing the data off-line, the following parameters are evaluated and recorded to disk for each digitized pulse (ntuple):

1. the channel number i.e., the number of ADC channels that exceededs the trigger threshold;

2. the absolute time at which the pulse occurred with a precision of 0.1 msec;

3. the OF amplitude i.e. the amplitude of the optimally filtered signals both in the time and frequency domain;

4. the baseline (evaluated on pre–trigger samples) and its rms noise;

5. the signal rise (10–90%) and decay times (90–30%) ;

6. the pulse shape parameters, obtained by comparing the acquired pulse with the expected response function of the bolometer after OF or adaptive filters;

7. the pile-up fraction and delay. The Wiener filter algorithm [17] is implemented in order to recognize and successively reject double events. When two signals are found to occur in the same acquisition temporal window their amplitudes and their temporal distance are evaluated. These two parameters are very important in order to study the coincidence events due to radioactive cascades.

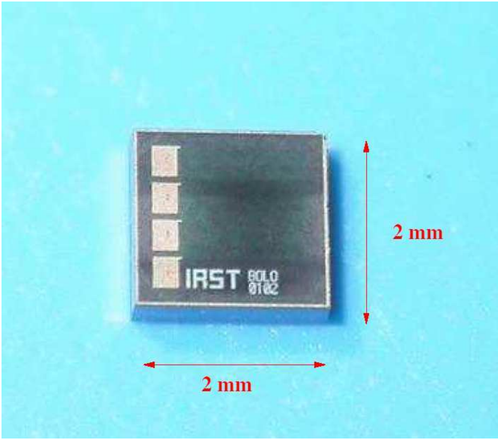


**Figure 3.11** - Si heater produced by the ITC-IRST company [72] and used for signal stabilization (see text).

### Instability correction

The next step is to corrected the OF amplitudes in order to reduce or cancel the effects of system instabilities responsible for the variation of the ratio between the deposited energy E and the amplitude V of the corresponding electrical pulse. These variations induce a worsening of the detector energy resolutions. There are three parameters that can modify the ratio $\Delta V/E$: the electronic gain $G$, the bias voltage $V_{\rm tot}$ and the temperature $T_b$ of the bolometer.

The electronic system is designed to guarantee a stability of $G$ and $V_{\rm tot}$ within 0.1% . It is however, much more difficult to stabilize at this level the detector temperature on long time scales. At a temperature of 10 mK this would require maintaining the temperature of all the crystals to an accuracy of 2 $\mu$K for a period of several days. Usually thermal instabilities are correlated with intrinsic instabilities of the cryogenic setup, mainly due to variations of LHe bath levels that determine small changes in the flow rate of the $^3$He/$^4$He mixture in the refrigerator.

To overcome this problem a Si resistor (fig. 3.11) is glued to each crystal and used as a heater to produce a reference pulse in the detector. It is connected to a high precision programmable pulser that produces a fast voltage pulse every few minutes dissipating the same amount of energy into the crystal each time. These voltage pulses mimic pulses produced in the crystal by particle interactions and are used to measure the value of the ratio $\Delta V/E$. The baseline of the reference pulse provides the contemporary measurement of the value of the temperature $T$. A fit is then used to obtain the values of $\Delta V/E$ as a function of temperature and used to correct the OF amplitudes. The effectiveness of this technique has been proved in the MiDBD experiment [73].

### Noise rejection

Pulse shape analysis is very useful in rejecting spurious signals produced by microphonics noise and electric disturbances. Using more than one pulse shape parameter results in better reliability of the rejection technique.

**Linearization**

The final step in data processing is the conversion of the OF amplitudes into energy values. During the discussion of the bolometer model (§1.3) we underline that the relationship between $\Delta V$ and $E$ is only approximately linear do to the presence of several parameters with different temperature behaviors and therefore it must be measured experimentally. This task is accomplished by periodical calibration with radioactive sources (usually $^{238}$U, $^{232}$Th and $^{56}$Co) where sets of ($\Delta V$,$E$) are measured for several $\gamma$ lines. A fit of this data, together with the knowledge of the temperature dependence of the thermistors resistance and crystal heat capacity, provide the calibration function $E(\Delta V)$. Natural radioactivity decays in background measurements are also used to help extrapolating the calibration function to the energy region of $\alpha$ particles.

**Coincidence analysis**

The analysis of the multiplicity of the events is a very powerfull tool. It allows to reject events that left energy in more than one detector and to study the background sources.

Events depositing their energy in more than one detector can be usually ascribed to high energy gamma rays from environmental radioactivity or from contaminations within the structure of the array. Also high and intermediate energy neutrons have a significant probability of depositing energy in more than one detector. Another source of multiple events can be the surface contamination of the crystals and of the materials directly facing the detectors. We will come later to this important subject.

In the final stage of off–line analysis these coincidence events can be identified by analyzing the various pulse parameters. Signals occurring almost at the same time in two or more nearby detectors are marked as coincident. By analyzing the energy released in the detectors and the number and position of the hit crystals is sometimes possible to find out the source that originated such event. The efficiency of this technique is obviously enhanced for tightly packed structures where bolometer proximity is assured.

**Database**

Up to now, Cuoricino RunII has performed more than 600 measurement (one measurement lasts usually one day for safety purposes) which are collected in several sets (a set is defined as a collection of measurements between two calibrations). For every measurements, several parameters need to be stored to help analysis process like:

- general measurements details (date, duration, type, comments, shifters names, . . . );
- map of the bolometers position in the tower;
- electronics and daq configuration and parameters for each channel (Bessel, front–end, bias, trigger, . . . );
- bolometers working points ;

· configuration of the pulser that controls the heaters.

After a few months, it became clear that we need to store all this informations in a way that allow them to be stored, ordered, shared, retrieved, searched and used easily. The obvious solution was to setup an `SQL` database and a web interface. The database is still under developing and we are now integrating it with the analysis process to include also the information on cuts, stabilization, measurements quality, analysis setups and so on.

## 3.6 Bolometers simulations on Cuoricino data

In the §1.3, we introduced a thermal model to describe bolometers behavior in both static and dynamic conditions. The goal of this section is to apply that model to Cuoricino bolometers and compare the results of the simulations with the Cuoricino data.

### 3.6.1 Thermal model for Cuoricino bolometers

The thermal model was deduced for a quite general bolometer with semiconductor thermistors and no details of the read–out circuit were introduced. The biasing circuit of 3.2 can be added easily to the equations. The expression for the Joule power on the thermistor can be written explicitly:

$$P_e = \frac{V^2(t)}{R(T_e(t))} \tag{3.10}$$

In a previous work [18], we also introduced in the simulation the effect due to parasitic electrical capacitances that might appear in the system. We are presently working to introduce the effect of the Bessel filter on the simulation output.

From the measurements of the Cuoricino elements and couplings reported in 3.2, we could deduce reasonable values for the parameters needed by the simulations software. However, some parameters (i.e. the parasitic powers and capacitances) could not be easily measured and their value must be guessed from physics considerations or from comparison with ad hoc measurements (which are unfortunately still missing). The situation is complicated by the fact that there is some degeneracy in the parameters.

In the same work previously cited, the simulations were extensively used for understanding bolometers behavior and for the optimization of some detector parameters like, for example, the number of glue spots used to attach the thermistor on the absorber.

### 3.6.2 Comparison between data and simulation

Simulations told us that some detectors parameters are more critical than others and that some may affect mostly the static behavior while others changes mostly the dynamics of the pulse. For example, small variations of the electron–phonon conductance $G_{\mathrm{e\text{–}p}}$ changes dramatically the load curve while the conductances

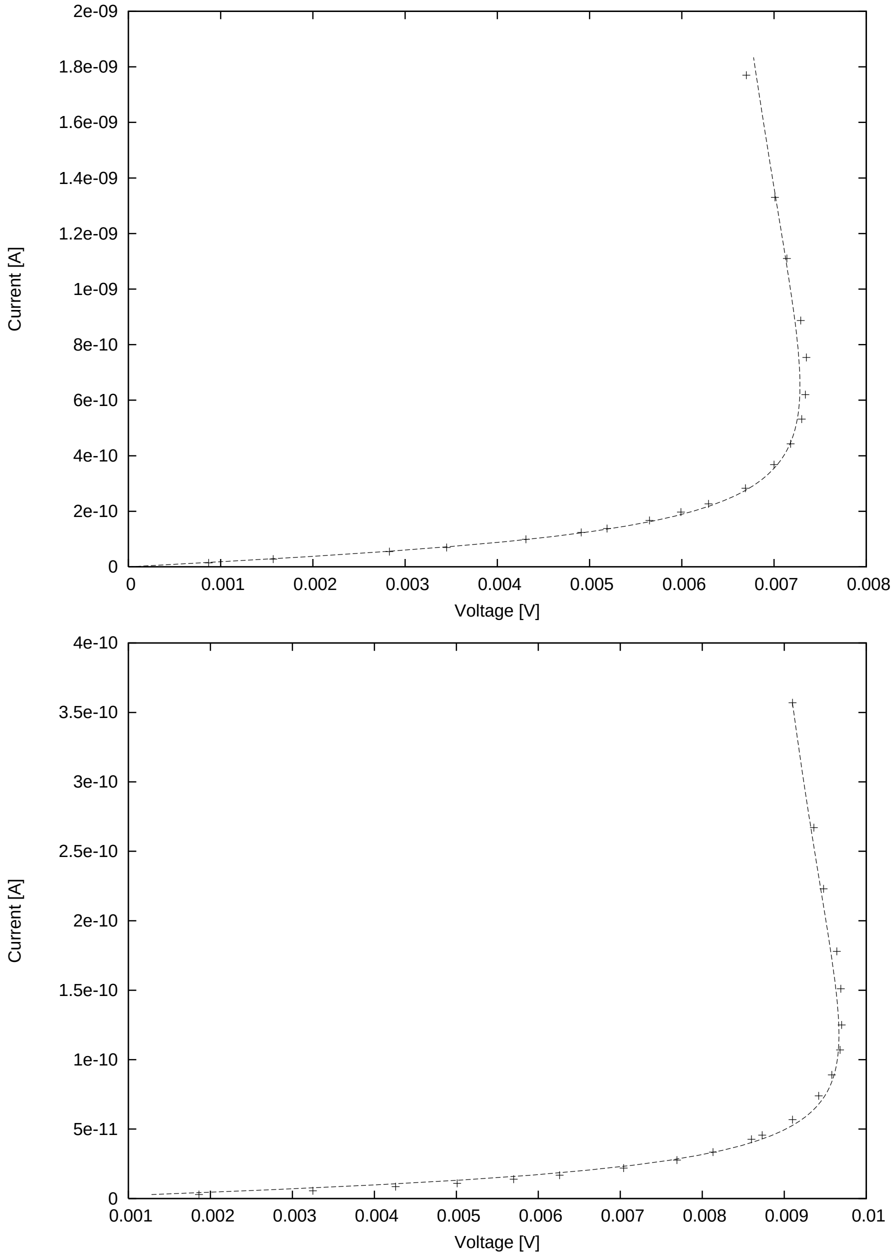


**Figure 3.12** - Comparison of an experimental $(V, I)$ curve (points) with a simulated one (full line) for a $5 \times 5 \times 5$ cm$^3$ (left) and $3 \times 3 \times 6$ cm$^3$ $TeO_2$ Cuoricino detectors.

between the absorber and the thermistor is not much relevant for the static behavior. The high number of parameters and their degeneracy make very difficult to perform meaningful quantitative comparisons with real data.

Nevertheless, we were able to reproduce the Cuoricino bolometers, as it is shown in figure 3.12 where two experimental load curves of Cuoricino bolometers are fitted with simulated curves. The starting point for the fit program is the set of thermal conductances evaluated from the values reported in §3.2. The heat sink temperature and the parasitic powers are free fit parameters. The co-

| Parameter | 3x3x6 cm$^3$ absorber | 5x5x5 cm$^3$ absorber | ratio (normalized when required) |
|---|---|---|---|
| $T_{base}$ [mK] | 8.459 | 8.35 | 1.013 |
| $G_T$ [W/K] | 3.939 x $10^{-5}$ | 6.28 x $10^{-6}$ | 6.272 |
| $G_{glue}$ [W/K] | 3 x $10^{-3}$ | 4.97 x $10^{-3}$ | 0.905 |
| $G_{el-ph}$ [W/K] | 0.1690 | 0.8003 | 1.056 |
| $G_w$ [W/K] | 9.714 x $10^{-5}$ | 1.508 x $10^{-4}$ | 3.221 |
| $P_{el}$ [W] | 8.9 x $10^{-14}$ | 2.7 x $10^{-12}$ | 0.033 |
| $P_{abs}$ [W] | 9.1 x $10^{-12}$ | 1.5 x $10^{-12}$ | 6.067 |

**Table 3.2** - Parameters obtained in the static behavior simulation of the 3x3x3 and 5x5x5 cm$^3$ crystal detectors.

efficients appearing in the temperature power law for the thermal conductances were also free to vary, but they did not change substantially with respect to the initial point. In addition, the ratio between $G_{el-ph}$ for the 3x3x6 detector and that for the 5x5x5 one is about 1/5. This was expected given the different sensor size used in the two cases (3x1.5x0.4 mm$^3$ in the first case and 3x3x1 mm$^3$ in the second one). Correctly, the bath temperature is almost the same in both cases. There are differences between glue spots and PTFE conductances, but they seem to lie within the range given by the intrinsic irreproducibility of the mounting procedure. The exponents of the potential due to conductance laws have been fixed since they derive from physical laws that are intrinsic properties of materials. Tab. 3.6.2 reports the value obtained by using the fit program from which the comparison of fig. 3.12 is derived.

An attempt was then made to reproduce the dynamic behavior of the detectors fitting the experimental pulses. We used the analytic approximation for faster calculations. Dynamic pulses are more difficult to reproduce but a good qualitative agreement was observed [74]. Unfortunately the use of fitting routines shows that pulses are not well reproduced, concerning both amplitudes and shape. An example is given in fig. 3.13. The fit is performed on the load curve and then on the pulse to try to fit all free paramters. Simultaneous fit of the static and dynamic behaviors has been taken into consideration as a future improvement.

The weakest point of the dynamic model is the description of the process that permits the conversion of the particle energy into phonons. An important role might be playes by the athermal (out–of–equilibrium) phonons which propagates ballistically in the crystal lattice. These phonons can be transmitted through the sensor–absorber interface and be thermalized by interacting with the conduction electrons of the thermistor. This possibility has been taken into account [18, 75] with encouraging results.

It is useful to remark that the numerical method used for dynamic behavior allows to simulate some pulse features that cannot be obtained with the analyt-

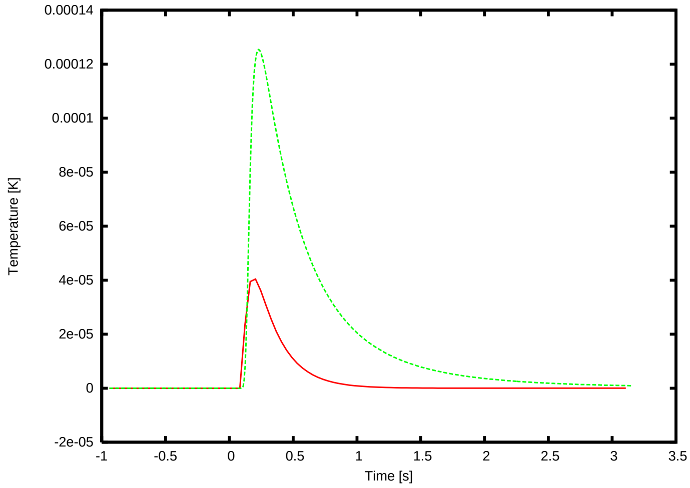


**Figure 3.13** - Comparison between the simulated and the experimental thermal pulse obtained in the Cuoricino experiment.

ical approximated solution. For example, slow-rise time and oscillations in the pulse tail, which were observed in some Cuoricino pulses, can be reproduced by taking into account the presence of parasitic capacitances in the read–out system.

## 3.7 Cuoricino as a prototype: what we learned

Even if Cuoricino is a standalone experiments which is giving outstanding results, it is also a first step towards the realization of bigger 1–ton–scale experiment named CUORE, an acronym for Cryogenic Underground Observatory for Rare Events. We will discuss this topic in the next sections but we want to point out here what kind of knowledge and experience Cuoricino (and its predecessors) brought us. The important results concern both the level and origin of the $\beta\beta0\nu$ background and the technical performance of the bolometric detectors (CUORE will be made of 19 towers similar to the Cuoricino one).

### 3.7.1 Background contributions in Cuoricino

Figures 3.14 and 3.15 show the background measured by $5 \times 5 \times 5$ cm$^3$ crystals in Cuoricino. The two histograms plotted in each figure are the amplitude spectrum of pulses collected operating the Cuoricino array in anticoincidence (therefore selecting events where just one crystal is hit within the time coincidence window of about 50 ms) and the spectrum obtained operating the array in coincidence (here the coincidence is obtained selecting events where two and only two crystals are simultaneously hit, spectra requiring higher multiplicity per event can also be plotted even if they show a by far lower counting rate). In both cases the energy spectra collected by each single (independent) detector of the array are summed together to produce the *sum energy spectra* plotted

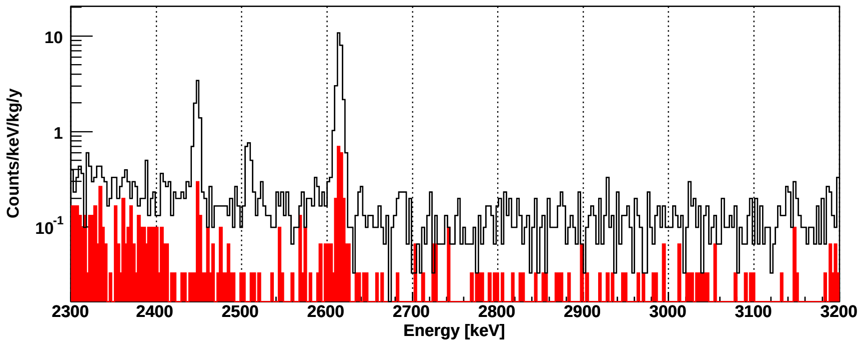


**Figure 3.14** - Cuoricino background in the $\beta\beta0\nu$ region. The black line refers to the anticoincidence events spectrum (only one detector hit) and the red filled histogram refers to coincidence events (two detectors contemporary hit). The 2448 keV $^{214}$Bi, the 2505 keV $^{60}$Co and the 2615 keV $^{208}$Tl line are clearly visible. The $\beta\beta0\nu$ decay should appear as a gaussian peak in the anticoincidence spectrum at 2530 keV (without any corresponding line in the coincidence spectrum). Above the 2615 keV line a flat continuous background, attributed to degraded alpha particles, is visible. The low contribution of coincidence event proves that only a small fraction of the continuum can be ascribed to crystal contaminations. This background extends clearly even below the $^{208}$Tl peak and partake to the counting rate measured in the $\beta\beta0\nu$ region.

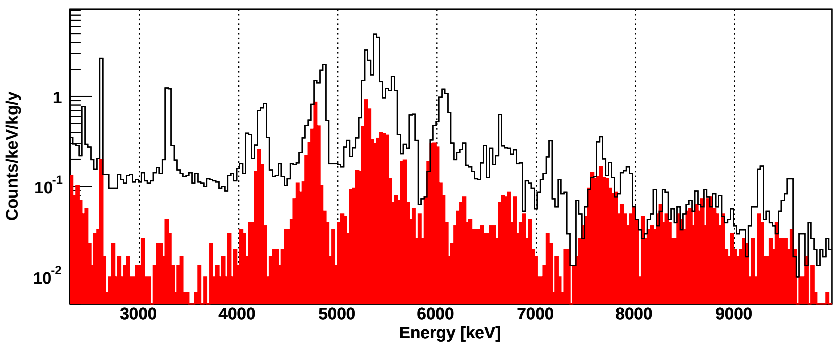


**Figure 3.15** - CUORICINO background above 2.3 MeV. The black line refers to the anticoincidence events spectrum (only one detector hit) and the red filled histogram refers to coincidence events (two detectors contemporary hit). Most of the peaks appearing in the region above 4 MeV are ascribed to U and Th surface contamination of the crystals: in the anticoincidence spectrum the peaks have their high energy side centered at the transition energy of the decay ($\alpha$+recoil completely contained in the crystal) and have a long, low energy tail (either $\alpha$ or recoil exit from the crystal depositing part of its energy outside). A similar pattern is observed in the coincidence events spectrum, in this case to give rise to a coincidence two crystals have to partake to the event. Therefore the maximum energy of the peak correspond to the $\alpha$ energy (i.e. the case in which the $\alpha$ is completely contained in one crystal and the recoil in the other one). The $\alpha$ peak centered at $\sim$ 3200 keV is ascribed to an internal contamination of the $TeO_2$ crystals in the long living isotope $^{190}$Pt: the shape of the peak is gaussian (no low energy tail) no peak appears in the coincidence spectrum, the energy of the peak is compatible with the transition energy of $^{190}$Pt.

| Source | $^{208}$Tl | $\beta\beta0\nu$ | 3–4 MeV |
|---|---|---|---|
| $^{238}$U and $^{232}$Th surf. contam. of $TeO_2$ | — | $10 \pm 5\%$ | $20 \pm 10\%$ |
| $^{238}$U and $^{232}$Th surf. contam. of Cu | $\sim 15\%$ | $50 \pm 20\%$ | $80 \pm 10\%$ |
| $^{232}$Th contam. of cryostat Cu shields | $\sim 85\%$ | $30 \pm 10\%$ | — |

**Table 3.3** - Estimate of the relative contributions of the different sources responsible for the background measured in Cuoricino

in the two figures. The $\beta\beta0\nu$ peak should appear as a gaussian line at about 2530 keV in the anticoincidence spectrum (the efficiency with which the two electrons are completely contained within one $5\times5\times5$ cm$^3$ crystal is 86%). The capability of operating the detectors in anticoincidence (that is made possible thanks to the independence of the detector read-out, trigger and acquisition) allows to reduce the background in the $\beta\beta0\nu$ region. Finally, from the differences between coincidence and anticoincidence spectra, important informations concerning the background origin and location are obtained as it will be clear in the following.

In a preliminary analysis of CUORICINO background, included in CUORE proposal [60], we tentatively quantified the different contributions to the $\beta\beta0\nu$ background as shown in table 3.3.

As shown in fig. 3.14 the background measured by CUORICINO on the left side of the 2615 keV $^{208}$Tl line and on its right side differs by about 30%, being almost constant on both sides. The $^{208}$Tl line is the highest natural $\gamma$ line due to environmental contamination and appears as the only possible $\gamma$ contribution (through Compton events) to the $\beta\beta0\nu$ background. The other two peaks appearing in fig. 3.14 are the 2448 keV, due to $^{214}$Bi, and the 2505 keV sum line due to the interaction, in the same crystal, of the two $\gamma$s emmitted by $^{60}$Co following its beta decay. Both peaks have an energy definetely too low to give any contribution to the $\beta\beta0\nu$ background. The $^{208}$Tl line originates from contaminations relatively far from detector, as proved by the reduced intensity of the low energy gamma lines coming from the $^{232}$Th chain. The contamination is more likely in the refrigerator itself, a possible guess for its exact position is some thermal shield or the superinsulation itself (the source is apparently seen in the same way by all the crystals of the tower). From this guess on the source position, it was possible to extrapolate - on the basis of a MonteCarlo simulation - the contribution gave from $^{208}$Tl to the $\beta\beta0\nu$ background.

The background measured on the right side of the $^{208}$Tl line is ascribed mainly to degraded alphas coming from U and Th radioactive chains (not necessarily in secular equilibrium) and due to surface contamination of the crystals or of the inert material facing them. This continuum clearly extends below the $^{208}$Tl line thus participating to the to the $\beta\beta0\nu$ background counting rate. While the heavy shielding forseen for CUORE will guarantee a deep reduction of the $\gamma$ background (and therefore of the $^{208}$Tl contribution), for $\alpha$ background (that comes only from the very inner part of the detector, i.e. the crystal themselves and the material directly facing the crystals) only a severe control of bulk and surface contaminations can guarantee the fulfillment of the sensitivity requirements for CUORE. To do that a correct identification and localization of the

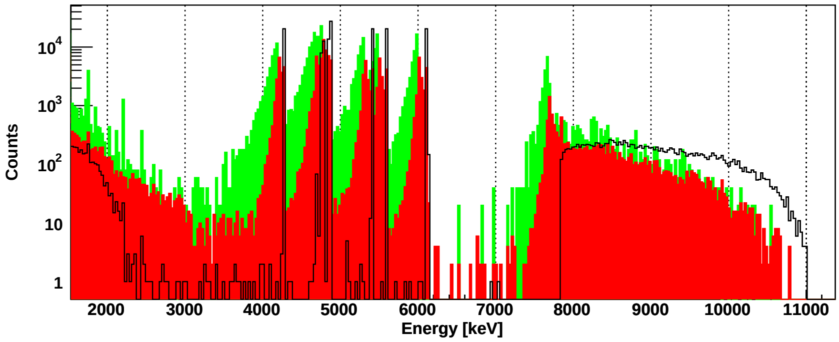


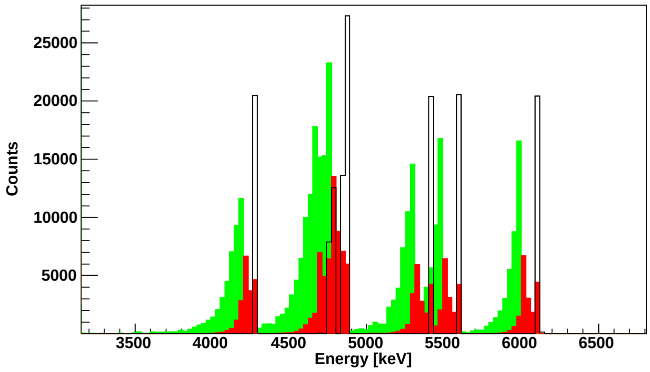


**Figure 3.16** - MonteCarlo simulation of the anticoincidence spectra produced in Cuoricino by a $^{238}$U contamination in crystal bulk (black line), crystal surface (red filled histogram) and copper mounting surface (green filled histogram). Surface contaminations has been simulated with an exponential density profile and a thickness of 0.1 $\mu$m. Bottom: A detail of the top histograms showing the different shapes of peaks.

sources of the continuous $\alpha$ background is mandatory.

Alpha peaks can be identified very clearly in bolometer spectra. The peak position and shape give strong indication on the location of the contamination: sharp gaussian peaks indicate contamination of either the crystal bulk, if the energy corresponds to the transition energy of the decay (i.e. $\alpha$+recoil), or of an extremely thin surface layer (could it be on the crystals surface or on the inert material surface facing the crystal) if the energy corresponds to the alpha energy. On the contrary asymmetric, “long-tailed” peaks are produced by thick contamination of surfaces. Finally a bulk contamination of an inert material facing the detector should produce just a continuum without any peak (but several, visible $\gamma$ peaks). Examples of the characteristic features resulting from the different location of the contamination are shown in fig. 3.16.

Side information, useful in this study, come from the analysis of coincident events in the array and from the study of gamma peaks. Indeed when the background is dominated by $\alpha$ particles a coincidence between two crystals is produced only if the $\alpha$ emitter is on the surface of one crystal and the $\alpha$ or the recoiling nucleus exit from one crystal and enters into one other, producing a characteristic pattern clearly visible in fig. 3.16 (bottom).

Unfortunately, while $\alpha$ peaks are clearly evident and their origin rather easily understood the continuous background underlying the peaks and extending towards the $\beta\beta0\nu$ region cannot be easily correlated to the one or the other peak (i.e. to the one or the other contamination). Hypotheses can be done on the basis of MonteCarlo simulations that however require as input a contamination intensity and a density profile, both unknown.

In Cuoricino (fig. 3.15) most of the peaks appearing in the region above 4 MeV are ascribed to U and Th surface contamination of the crystals. Indeed these peaks are visible in both coincidence and anticoincidence spectra, moreover they have a large low energy tail that once more is (as discussed) a prove that the contamination is at the crystal surface.

Four peaks do not belong to this category:

· the $\alpha$ peak centered at $\sim$ 3200 keV. It is ascribed to an internal contamination of the $TeO_2$ crystals in the long living isotope $^{190}$Pt: indeed the shape of the peak is gaussian (no low energy tail) and no peak appears in the coincidence spectrum, the energy of the peak is compatible with the transition energy of $^{190}$Pt. The contamination is probably due to inclusions of fragments of the Pt crucible used in $TeO_2$ crystal growth;

· the $\alpha$ peak centered at $\sim$ 4080 keV. It grows on the low energy tail of a surface contamination peak but, as will be discussed in next section, it is attributed to a bulk contamination in Th;

· the $\alpha$ peak centered at $\sim$ 5300 keV. It is centered at the $\alpha$ (and not $\alpha$+recoil) emitted by $^{210}$Po. The peak is stable in time and is therefore attributed to a $^{210}$Pb contamination ($^{210}$Pb has a half-life of 22 years while that of $^{210}$Po is 138 days). The position of the peak indicates that the contamination has to be on a very thin layer (much thinner than the U crystal surface contamination described above) either on the crystal surface or on the mounting surface. From the coincidence spectra and scatter plots it is then possible to conclude that at least part (probably not all) of the peak has to be due to a contamination of the crystal surface. If this is the case also part of the 5.4 MeV peak has to be attributed to a such contamination;

· the $\alpha$ peak centered at $\sim$ 5400 keV. It has an intensity clearly decreasing with time in agreement with $^{210}$Po half-life. The $^{210}$Po contamination, usually observed in recently grown $TeO_2$ crystals, is ascribed to a bulk contamination (no coincidences are observed). Part of the peak is however attributed to the U and $^{210}$Pb surface contamination discussed above. When Cuoricino was started the 5.4 MeV peak was by far dominated by the bulk contamination $^{210}$Po peak (with an intensity as high as 0.2 c/h/crystal), now the peak has a much reduced intensity ($\sim$ 0.03 c/h/crystal) where the surface contamination seems to dominate.

Finally the small amount of coincidences in the 3–4 MeV range as well as the extrapolation (based on MonteCarlo simulations) of the counts attributable to crystal surface contaminations, indicate that a large fraction of the flat continuum between 3 and 4 MeV has its source outside the crystals. Degraded $\alpha$s could come either from surface or bulk contamination of the mounting components, however the reduced rate of low energy (hundred keV) gamma peaks allows to exclude that this continuum could be due to U and Th bulk contaminations of the copper mounting structure.

Excluding important contributions from the bulk contamination of the small parts of the detector (thermistors, heaters, bonding wires, PTFE parts ...) on the basis of the radioactive measurements made before the construction of Cuoricino and excluding neutrons on the basis of both MonteCarlo simulations and experimental results we have concluded that most of the background measured by Cuoricino should come from crystal and copper surfaces. The surface background contribution extrapolated in tab. 3.3 was obtained on the basis of this model.

### 3.7.2 Proved technology and technical feasibility

Technically speaking, CUORE will be an almost pure multiplication of the Cuoricino tower. From this point of view, it has been an important test–bench for what concern the design, preparation, assembly and operation of a big cryogenic detector.

## 3.8 The next generation: CUORE

### 3.8.1 Scientific motivations

As discussed in chapter 2, a number of recent theoretical interpretations of atmospheric, solar and accelerator neutrino experiments imply that the effective Majorana mass of the electron neutrino could be in the range from 0.01 eV to the present bounds.

We also pointed out that the next generation of experiments for $\beta\beta0\nu$ search should be able to explore the inverted hierarchy mass region (see §2.3.4). From Fig. 2.6 this corresponds to a sensitivity in $\langle m_\nu \rangle$ better than 50 meV. In the case of $^{130}$Te this came out to correspond to a sensitivity for $T^{0\nu}_{1/2}$ better than a few $10^{26}$ y.

The consistent improvements in cryogenic spectroscopy achieved by the MiDBD and Cuoricino experiments, presented in the previous sections, show that we have today available a technology to achieve such a fundamental physics goal. This is the starting point from which the *Cryogenic Observatory for Rare Events* (CUORE) was developed.

In this section we will present an overview of the CUORE experiment with only some details about the main detector, the setup and the collaboration (for details see [60]). Finally, the experimental laboratory and setup are described.

### 3.8.2 The detector

Like Cuoricino, CUORE will be based on an elementary module of 4 $TeO_2$ crystals. In the final design of the detector, groups of 13 modules are stacked together to form a tower. The CUORE array will consist of 19 of these towers in a

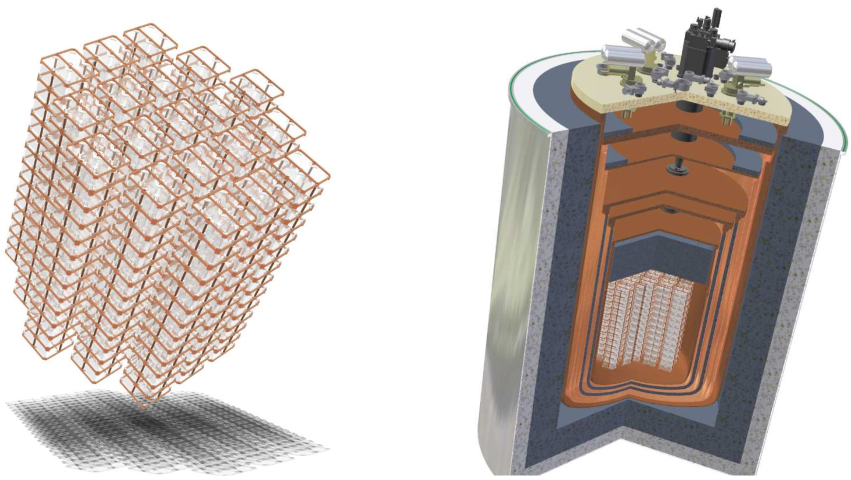

**Figure 3.17** - Design of the CUORE detector (left) and of the whole system with dewar, shields and cryostat (right)

| Time [y] | FWHM [keV] | bkg [c/kev/kg/y] | $F^{0\nu}$ $10^{26}$[y] | $\langle m_{\beta\beta}\rangle$ [meV] |
|---|---|---|---|---|
| 5 | 5 | 0.01 | 2.1 | 19-100 |
| 5 | 5 | 0.001 | 6.5 | 115-57 |

**Table 3.4** - Projected CUORE sensitivity.

cylindrical structure, with a total active mass of 741 kg, corresponding to 200 kg of $^{130}$Te. A prototype design of the final structure is shown in fig. 3.17(left). Each tower will be very similar to the tower tested in Cuoricino, both from the mechanical and from the thermal point of view, and substantially independent from the nearby towers. The close packing and the high granularity will help in background identification and rejection.

The array will be operated underground at a temperature of 10-15 mK. The experiment has been already approved by the Scientific Committee of Gran Sasso Lab and the special dilution refrigerator that is intended to house the detector has been funded. A preliminary design is shown in fig. 3.17. At the time of writing, CUORE, togheter with GERDA [57], are the only next-generation $\beta\beta0\nu$ experiments for which a location does exist. Infact, CUORE will be placed in the Hall A of the GranSasso Laboratory (Italy). The design and construction of the building that will host CUORE has already started as shown in fig. 3.18.

#### 3.8.2.1 Expected sensitivity

The CUORE sensitivity foreseen is given in tab. 3.4 where we used (2.9).

### 3.8.3 CUORE work packages (WPs)

As a synthetic way to describe the fervent activity that is currently growing around the CUORE experiment, we will list here all the present working groups

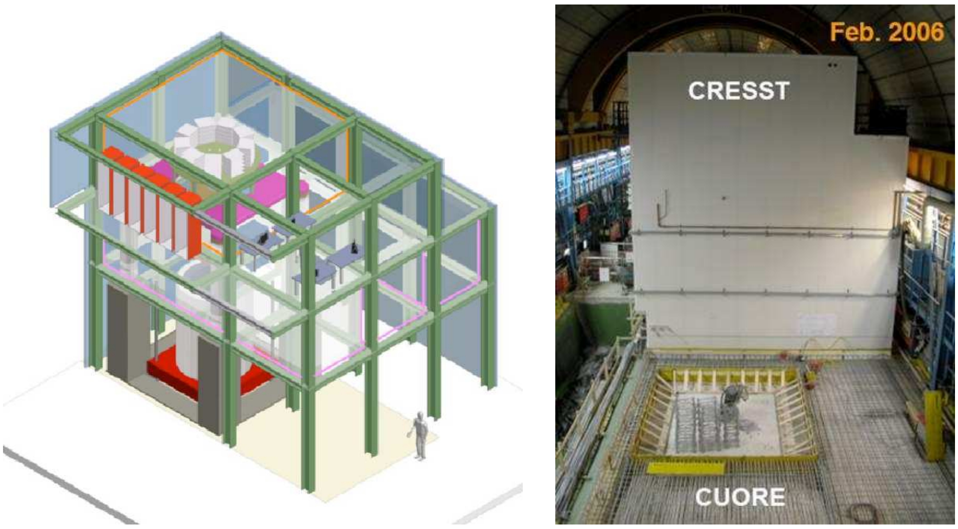


**Figure 3.18** - CAD design of the CUORE hut (left) and picture of the hut basement construction in Hall A (right)

(WPs) of the CUORE project and their main activities.

**Single Module Development**

This is the work packages to which the activity of this dissertation is mostly linked. This WP has to take care of optimizing and developing the single CUORE bolometer. In particular, the work is focused on

· preparation of the NTD Ge thermistors (see also §5.2);

· characterization of the thermistors and of the heaters;

· optimization of all the detectors couplings from both thermal and mechanical point of view (see also §6);

· modelization of the static and dynamic behavior of the detectors (we already spoke about this point in §1.3 and 3.6);

· study of alternative solutions (see chapter 7).

**CUORE Assembly**

The aim of this WP is focused on the structure of the complete CUORE detector. Specifically

· batching procedures for mounting, cleaning, gluing, . . . ;

· standardization and engineering of the assembly process;

· improve reproducibility;

· new module design with less copper and/or different materials;

· study of detector vibration modes induced by the cryostat or by other external source and consequently actions to reduce it.

**Electronics**

The electronics for CUORICINO has been designed in view of CUORE and it is showing more than adequate results. In principle it needs little optimization, R&D and realization on a large scale.

**Data Analysis**

The goals of this WP are to develop the 1st and 2nd level analysis software starting from the existing Cuoricino algorithms. Alternative approaches (e.g. Neural Networks) will be investigated. Independent analysis techniques will be pursued as well.

It also has to take care of data storage, management and distribution machine maintenance.

At present, a common data analysis and DAQ framework is under active development.

**Radioactivity**

A lot of efforts are focused on the radioactivity issues like:

- selection, storage and radioactivity study of the required materials, eventually with the development of special techniques for surface and bulk contamination measurements;
- cleaning procedures and treatments to reduce and/or avoid radioactive contaminations;
- reducing the environmental radioactivity in experimental areas;
- design and realization of passive and active shields for the detector;
- MonteCarlo study of the radioactive background of CUORE from Cuoricino data and specific measurements.

Our contribution to these activities has been in the realization of a database and its web interface for storing and easily retrieve all the details of the radioactivity measurements performed by the CUORE collaboration [76].

**Data Acquisition**

The following items are to be addressed by this WP:

- hardware and software for data acquisition (selection and realization);
- choice and development of the triggers;
- complete automatic system (hardware and software) to search for the optimum working point of each bolometer of the CUORE array;
- specific software for detector characterization and noise analysis;
- remote acquisition monitor;
- remote monitor and control of the cryogenic systems.

**Cryogenics**

The main task of this WP is the realization of the cryostat, from the project to the construction and final commissioning, taking into consideration all the requirements from radioactivity in the material choice. Side work involve:

· mechanical vibrations and EMI study, shielding and reduction with active/passive systems;

· cryostat wiring;

· thermal stabilization;

· calibration sources placement.

Part of the work of this dissertation is related to this subjects and will be addressed in the next chapter.

**Lab Facilities and Location**

The work to build the CUORE hut in the LNGS Hall A started in 2006 and are currently going on under the supervision of this WP. It has to take care of:

· logistics and laboratory engineering (air, water, ventilation, gases, . . . );

· main power supply and problems connected (UPS, ground loops, interferences, . . . );

· safety.

**Crystals Preparation**

An important role is played by this WP that has the responsibility of selecting the $TeO_2$ powder and follow the crystal growth process by assuring the required levels of radiopurity and quality (size, surface treatments, . . . ) of the CUORE crystals.

**Integration**

The project integration consists of a number of activities aiming to assure that:

· the design work of the various groups is carried out harmoniously by keeping an effective control of the interfaces;

· all the systems, parts and assemblies fit together with reasonable clearances and manufacturing tolerances;

· all the parts can be properly assembled with minimal risk for the detector and personnel;

· the access and maintenance requirements have been properly taken into account.

## 3.9 Challenges for CUORE

As all the great human attempts of all the times, the CUORE experiment poses some challenging issues that must be faced and solved if we want to succeed in our effort.

We have identified, schematically, three main aspects: the reduction of the background, the standardization of all the procedures for detector mounting and setup and finally, the challenge of cooling down and keep cold for long time such a big detector. The latter is mainly a technological problem which has never been addressed because no one has never tried to cool such a huge mass ($\sim$ 1 ton) in the mK region. Concerning the second point, we must underline that up to now we used to manually prepare our detectors. For CUORE this is clearly impossible and standard and automatic solutions must be found in all fields (from material preparation to assembly, from operation to analysis). Finally, the challenge that concerns us most is the reduction of the background which is really the critical key for a successful experiment. We will thus start from this topic.

### 3.9.1 Background reduction

The aim of CUORE is to investigate the inverted hierarchy region of neutrino masses. To achieve this result, the background in the $\beta\beta0\nu$ region must be at least lower than 0.01 c/keV/kg/y, as in tab 3.4.

**CUORE shielding and anticoincidences**

We have already described the Cuoricino background in depth. Compared to Cuoricino, the heavy shielding surrounding the CUORE detector will substantially reduce the event rate due to environmental radiation of various origin (neutrons and photons), environmental radioactivity (natural decay chains U/Th, $^{210}$Pb, $^{40}$K,...), as well as muons interactions in the surroundings rock or in the shielding itself.

Furthermore, while in Cuoricino the fraction of coincidence events is relatively small (see fig. 3.19), in CUORE the large mass and the high granularity of the array will allow to achieve a relevant reduction of the counting rate by appling an anticoincidence cut.

**The RAD detector**

An R&D project focused on the reduction of the background was started by the CUORE collaboration in 2004. The first product of this work was the realization of a dedicated detector name RAD (Radioactivity Array Detector). It consists in a 2-plane array of four $5 \times 5 \times 5$ cm$^3$ $TeO_2$ crystals, almost similar to Cuoricino ones, and operated in the Hall C cryostat at LNGS. An ad hoc procedure for crystal and copper cleaning was settled and only ultrapure materials were used at all steps. Pictures of RAD1 and RAD3 detectors are in fig. 3.20.

Since the background in the $\beta\beta0\nu$ region cannot be measured directly because of the unavoidable Tl contribution coming from $^{232}$Th contamination, we

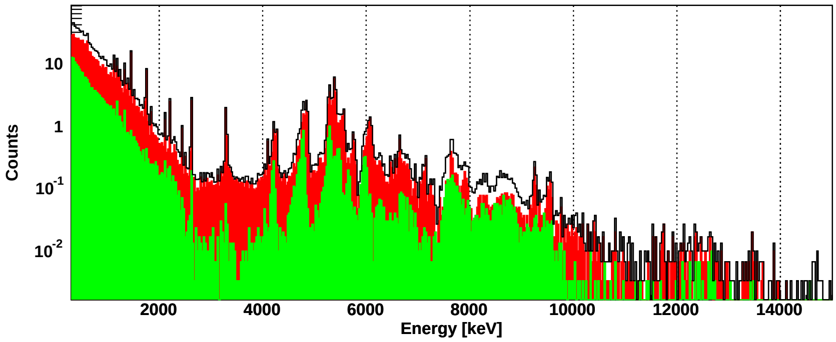


**Figure 3.19** - Cuoricino background. The black line refers to the total spectrum (all the events are counted), the red filled histogram refers to anticoincidence events (one detector contemporary hit) and the green filled histogram refers to coincidence events (two detectors hit per event).

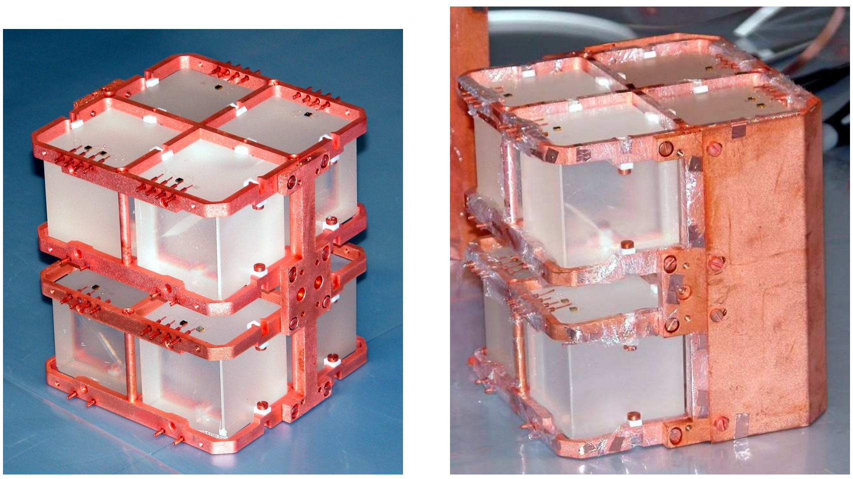

**Figure 3.20** - The RAD detector: RAD1 (left) and RAD3 (right).

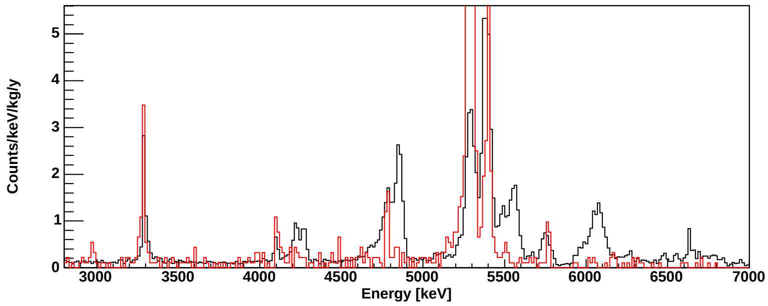


**Figure 3.21** - CUORICINO background (black) compared with RAD1 (red): the disappearance of crystal surface contamination peaks (visible in CUORICINO spectra as large asymmetric peaks) is evident. The only peak that remain in RAD1 are the doublet of $^{210}$Po and the gaussian sharp peaks ascribed to a bulk contamination of the crystals in long living Th isotopes (to a level of about $10^{-13}$ g/g).

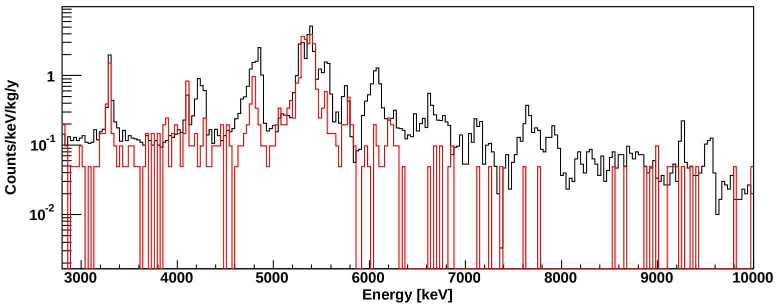


**Figure 3.22** - CUORICINO background (black) compared with RAD3+RAD4 (red): the 5.3 MeV peak due to $^{210}$Po has here a much reduced intensity with respect to that of RAD1, now compatible with CUORICINO. The continuum background between 3 and 4 MeV appears reduced with respect to CUORICINO (the reduction factor is $(38 \pm 7)$%).

will use the 3–4 MeV region to check the background achievements.

Four RAD runs were performed up to now with encouraging results. In particular, RAD1 was quite successful from the point of view of crystal cleaning as shown in fig. 3.21. The crystal surface contamination is reduced by a factor 4.

RAD2 was used to rule out (at least partially) the contribution coming from the so-called "small parts" of the detector: PTFE pieces, Si heaters and gold wires.

The most interesting results were obtained from RAD3 and RAD4 where the only change with respect to RAD1 was the almost complete coverage of the copper of the holder with multiple films of a radio-clean polyethylene. Before RAD4, we introduced a neutron shield outside the cryostat. RAD3 and RAD4 are statistically compatible. The major result is that the 3–4 MeV counting rate is reduced by a factor $2.0 \pm 0.4$ as shown in fig. 3.22.

### The CAW detector

A new 3-planes detector named CAW was also prepared and tested. It is designed to be as close as possible to the final CUORE structure as will be described in the next paragraph. Concerning the background, this new mounting structure reduces the amount of inert material (i.e. Copper) in between the detectors. Assuming that a large fraction of the background is due to surface contamination of the mounting structure the reduction by about a factor 2 of the copper surface interposed between the detectors is particularly relevant.

After a first technical run, at the beginning of 2006 the CAW array was used for a background test. The array was prepared in the same way as the final RAD to check the technique reproducibility on a different structure. The measurements ended in September 2006 and data analysis is in progress.

**Surface sensitive bolometers**

A new and promising technique for background reduction was developed during this PhD work and consist in new bolometer technology that make them able to discriminate events origin. The test performed and the results achieved are reported in chapter 7.

### 3.9.2 Detector assembly, standardization and engineering

As already said, the CAW detector is a 3 plane array having a structure only slightly different from that of Cuoricino. This new design is the result of an intense program of optimization of the CUORE detector structure started in 2004, involving all aspects of the single module structure and of its assembly procedure in the final CUORE towers. The new structure should guarantee a high degree of reproducibility in its mechanical features as well as a simple assembly procedure. The CAW detector is a prototype constructed and successfully tested in 2005 from the technical point of view (i.e. detector performances).

Unlike Cuoricino, CUORE will require a new approach to detector preparation and assembly as it will not be possible to use an “handcraft” approach. A probably incomplete list of points that need to be addressed (mainly by the CAW working group) includes:

· increase reproducibility of detector couplings;

· define standards for material selection and quality (in addition to radioactivity requirements);

· keep vibrations under control;

· study serialization of the assembly;

· ...

In this PhD work we have addressed some of the problems outlined above. In particular, improvements in the thermistors and in the detector couplings were suggested, as reported in chapters 5 and 6.

### 3.9.3 Cryogenic issues

At the moment, Cuoricino is the largest operated bolometric detector.

As will be clear in the next chapter, experiments at such low temperatures are quite 'tricky'. From the Cuoricino experience, we are confident that a cryogenic apparatus like CUORE could be done but it will require significant efforts and skills.

We will not enter here into the technical details of the realization of a cryostat able to cool–down the CUORE detector (and shields) and to keep it stable at few mK for long times. We only state that the cryostat needs to be custom made and we opted for a new kind of cryostat (pulse tube assisted). In the last three years, we operated a small prototype of this cryostat at the Low Temperature Laboratory of the Insubria University in Como and we will discuss it in the next chapter.

# · Chapter 4 ·

# Experimental setup

We already discussed many of the properties and characteristics of bolometers, that place them among the most interesting and promising detectors for nuclear and particle physics. In the next chapters we will see these devices at work in different situations. Here we will go deeper in the experimental description of their operation. In particular, we will focus on the specific environment and instrumentation that we used to carry on the R&D work described.

## 4.1 Requirements for bolometer operation

The bolometers' working principle is incredibly simple - converting energy into a temperature rise and measuring it - but when it comes to real operation, the situation is quite far from being simple! In particular, low temperatures, low noise and low counting rate are important requirements for successful operation.

### 4.1.1 Very Low Temperatures

Bolometers are very nice and simple detectors, but they can also be very tricky. The main reason is that they need to work at very low temperatures. We mentioned this fact previously, but it is worth reminding it now. Bolometers behavior is mainly ruled by two equations:

$$\Delta T = \frac{E}{C} \quad \text{and} \quad \tau = \frac{C}{G} \tag{4.1}$$

that provide, as a first approximation, the temperature rise of an absorber of heat capacity $C$ for a given energy release $E$ and the decay time $\tau$ of the temperature signal. Obviously, we like to have $\Delta T$ as big as possible while reducing $\tau$, and both can be obtained by lowering $C$ - which means, after proper material choice, to reduce the working temperature (cfr. §1.2.2).

Temperatures of few mK can only be reached by means of a technology proposed by H. London in 1951, which made use of the properties of $^3$He-$^4$He mixtures and goes by the name of *dilution refrigeration*. More details on this technique will be given in section 4.2.

Many difficulties could arise from working at such low temperatures:

- cooling time: the cool down process is usually slow, ranging from few days to weeks or even months, depending on the mass to be cooled and on the conductances of the system; unsuitable materials will never cool!

· high vacuum environment is required;

· temperature stabilization might be difficult to achieve, especially for long periods;

· low power read-out must be used because it is easy to warm up the cooled system;

· material selection: avoid magnetic materials, take care of differential thermal contraction among materials, ...

### 4.1.2 The noise issues

Bolometers based on semiconductor thermistors suffered from different sources of noise which can be divided into intrinsic and extrinsic noise.

We already faced **intrinsic noise** (namely Johnson and thermodynamic noise) in §1.2.4. It determines the energy resolution limit of the detector. On the other side, the **extrinsic noise** sources are the totality of noise sources not generated inside the detector, such as cryogenic apparatus, electronics and read-out set-ups. These sources usually dominate the intrinsic noise, so that they determine the real limits of the energy resolution. There are also other sources of noise that can be included in this category, such as electric microphonic noise, electromagnetic interferences, and mechanical microphonic noise. Specific solutions like damping systems, mechanical and electronics filters, thermal stabilizations and so on, need to be implemented on the experimental setup to reduce these noise sources.

### 4.1.3 Reduced counting rate

Bolometers are intrinsically slow and cannot account for high event rates. Thermal relaxation time can be very long, depending on the size. For a typical Cuoricino bolometer, it is of the order of hundreds of milliseconds. Luckily, bolometers are mainly used for the physics of very rare events, which already requires very low background. However, pile-up can be a problem especially during calibration measurements or in aboveground experiment where the cosmic rays flux can easily blind big-size detectors.

This explains why in the Cryogenic Detectors Laboratory of the Insubria University (§4.3) we operated only small-size prototypes (not bigger than 2x2x2 $cm^3$), while full-scale Cuoricino-like tests are performed only in the Gran Sasso Underground Laboratory (§4.4).

## 4.2 Getting cold with $^3$He–$^4$He dilution refrigerators

Temperatures below 1K can be easily achieved nowadays by means of dilution refrigerators (DRs). Their principle of operation was originally proposed by H. London in 1951, but the first working systems were not built until more than ten years later. Since that time, the performance of these systems has

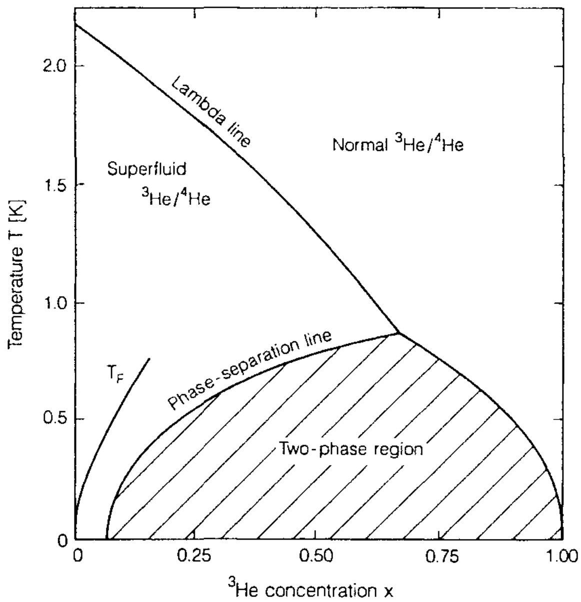


**Figure 4.1** - Phase diagram of liquid $^3$He-$^4$He mixtures at saturated vapor pressure. Taken from [78]

greatly improved and the physical processes involved have become much better understood.

Here we will give a brief introduction to the DR working principle and a description of their operation. More complete informations and details can be easily found elsewhere [77, 78].

### Basic principle

When a mixture of the two stable isotopes of helium is cooled below the critical temperature, it separates into two phases (see figure 4.1). The lighter *concentrated phase* is rich in $^3$He and the heavier *diluted phase* is rich in $^4$He. The concentration of $^3$He in each phase depends upon temperature. Since the enthalpy of the $^3$He in the two phases is different, it is possible to obtain cooling by "evaporating" the $^3$He from the concentrated to the diluted phase. The reason for this effect is hidden in the quantum mechanical behavior of the two He isotopes (remember that $^3$He is a fermion while $^4$He is a boson). However, to understand the underlying idea, it is helpful to think of the concentrated phase of the mixture as liquid $^3$He and the diluted phase as $^3$He gas. The $^4$He which makes up the majority of the diluted phase is superfluid, with little heat capacity and no impedance to the flow of $^3$He "gas". This "gas" is formed at the phase boundary. The "evaporation" process described above continues to work even at the lowest temperatures, because the equilibrium concentration of $^3$He in the diluted phase is still finite ($> 6.6\%$) even at the lowest temperatures. The cooling power of the diluition process can be calculated as:

$$\dot{Q} = 84\dot{n}T^2 \tag{4.2}$$

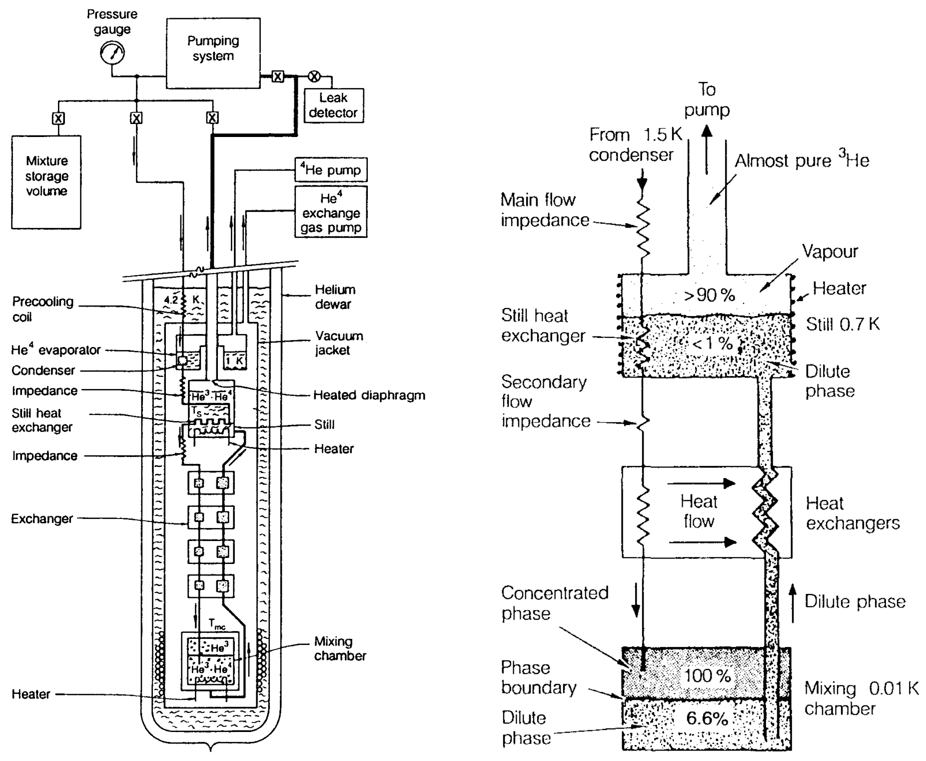


**Figure 4.2** - Schema of a typical dilution refrigerator with 1K pot condensation (left) and details on the parts involved in the dilution process (right). From [78]

where $\dot{n}$ is the molar flow rate of $^3$He.

## Design and operation

A schematic diagram of a DR is given in fig. 4.2. There are three main parts: the still, the mixing chamber and, between them, the heat exchangers. In a continuously operating system, the $^3$He must be extracted from the diluted phase and returned into the concentrated phase. The system is thus kept in a dynamic equilibrium. The $^3$He is pumped away from the liquid surface in the still, which is typically maintained at a temperature of about 700 mK. At this temperature the vapor pressure of $^3$He is about 1000 times higher than that of $^4$He, so $^3$He evaporates preferentially. A small amount of heat in form of electrical power is usually supplied to the still to promote a sufficient circulation (and cooling power).

As a consequence of the still pumping, the concentration of the $^3$He in the diluted phase in the still becomes lower than in the mixing chamber and the osmotic pressure difference drives a flow of $^3$He to the still. The $^3$He leaving the mixing chamber is used to cool the returning flow of concentrated $^3$He in a series of heat exchangers. In the region where the temperature is above 20–50 mK, a conventional counterflow heat exchanger can be used effectively. At lower temperatures the Kapitza resistance between the liquid and the solid walls requires the contact area to be increased as far as possible. This is often achieved by using sintered silver heat exchangers (also called “step” exchangers).

A full leak-tight pumping system at root temperature is used to remove the $^3$He from the still and compress it to a pressure of few hundred millibars. The gas is then passed through filters and cold traps to remove impurities and finally returned to the cryostat, where it is pre-cooled in the main helium bath and condensed on the 1K pot (a bath of pumped $^4$He). A flow impedance is used to maintain a high pressure in the 1K pot region to help the gas condensation.

The experimental samples are to be placed in good thermal contact with the mixing chamber and the diluted phase. All connections to the room temperature devices must be thermally anchored at various stages on the refrigerator to reduce the heat load on the mixing chamber to obtain the lowest possible base temperature.

A list of acronyms commonly used in cryogenic physics is given below and will be used through the rest of the chapter.

| | |
|---|---|
| IVC | inner vacuum chamber |
| OVC | outer vacuum chamber |
| MC | mixing chamber |
| GHS | gas handling system |
| JT | Joule–Thomson |

## 4.3 Low Temperatures Detectors Laboratory @ Insubria University

The Low Temperatures Detectors Laboratory at the Insubria University is located in Como, Italy, and is directed by prof. Andrea Giuliani. He realized this laboratory with the main aim of providing a complete environment for bolometers R&D. It is equipped with a radio-chemical room, a class 1000 clean-room and all the facilities for low temperatures experiments. The work-horses of the lab are two dilution refrigerators able to go as low as 10–20 mK. Those two machines will be described in the rest of this section. A pumped Helium cryostat able to reach 1.2 K is also available. It is used for thermistors and heater characterization.

Deep intersection and collaboration are effective with the Baradello Underground Laboratory, where a HP-Ge detector is installed for low background radioactivity measurements.

Electronic systems similar to that used for Cuoricino are present. There are in fact a set of modules for biasing and pre-amplifying and filtering the signals from bolometers. A great feature of these modules is that they are easily customizable in most configurations: this is very handy when dealing with R&D prototypes detectors.

The same consideration holds for the acquisition hardware, which is rather old (CAMAC boards), but the custom acquisition software written by L. Foggetta [79] is able to unleash its hidden potential and exploit its features.

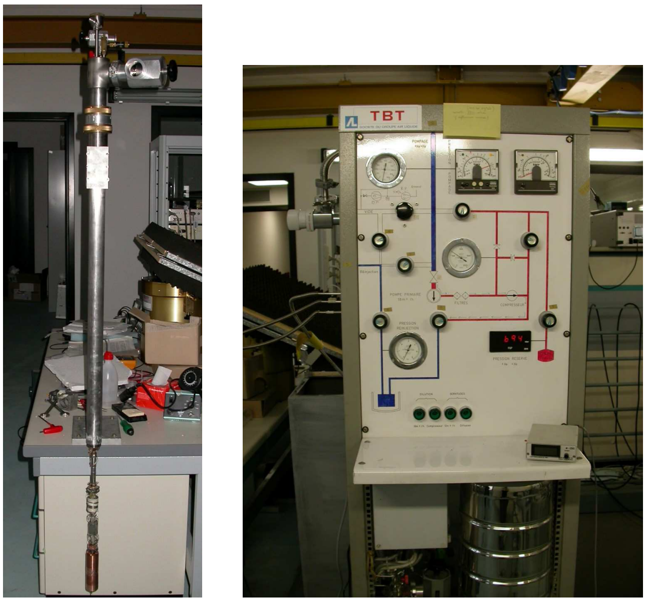


**Figure 4.3** - Picture of the TBT refrigerator (left) and its gas handling system (right).

### 4.3.1 TBT cryostat

#### 4.3.1.1 Description

The "TBT" cryostat (named after the French company "Tres Bas Temperatures" that produced it) is a small low power dilution refrigerator. The dimensions of the dilution unit can be appreciated from fig. 4.3. The reduced size of this refrigerator makes it very easy to handle, and the cool–down is usually very fast (two days). The only problem is the stainless steel IVC sealing. The bottom part of the IVC is in fact screwed on the top. After several attempts, we found a special material [80] which can be wrapped around the point of connection of the two IVC parts to guarantee leak tightness even at LHe temperature.

The working principle for this cryostat is pretty much the same of that outlined in §4.2. Only the 1K pot is absent in this system. A **Joule–Thomson expansion stage** is instead used to condense the mixture. We remind that the JT effect is a process in which the temperature of a real gas is either decreased or increased by letting the gas expand freely at constant enthalpy (no heat transferred to or from the gas and no external work extracted). For a given pressure range (depending on the gas), a real gas has a JT inversion temperature, above which expansion at constant enthalpy causes the temperature to rise, and below which it causes cooling. For He at 1 atm, the inversion point is about 51K. To achieve effective JT condensation, a compressor is present on the circulation route to increase the mixture pressure on the inlet line. The GHS (fig. 4.3) hosts also a 18 $m^3/h$ rotary pump, an auxiliary rotary pump (12 $m^3/h$) and a diffusive pump for high vacuum.

In the TBT cryostat there are also no thermal shields after the 4K IVC shield. For this reason it is always safer to provide an adequate shielding of the detectors at the mixing chamber temperature.

**Figure 4.4** - Picture of the final setup of the TBT cryostat. Here the cryostat is inserted in the blue LHe dewar. The Faraday cage is open. On its left the sand box is visible with the mixture tubes entering from the top. At the far left is part of the gas handling system.

Inside this cryostat we are able to reach a temperature of 13 mK with a cooling power of 20$\mu$W at 100 mK. The experimental space available under the mixing chamber is unfortunately very limited: it is about 25 cm with a diameter of 5 cm. Special bolometers' holders were prepared to fit in this space. The cryostat is equipped with a 9 channel wiring, which is now being replaced with a newer one.

A Faraday cage with acoustic absorption panels surrounds the LHe dewar where the refrigerator is inserted. Moreover, to reduce the microphonic noise from the pumping system, the cryostat pumping lines were inserted in a sand box to damp vibrations. The final setup is shown in fig. 4.4.

#### 4.3.1.2 Holder structure

We designed special holders for hosting prototype bolometers in the TBT cryostat. We tried to create a structure which fulfills these requirements:

· minimal burden;

· reproduce as close as possible the Cuoricino holder, at least for what concerns materials and absorber–to–bath conductance;

· allow hosting prototypes with different size and shape.

We come out with a design that happens to be quite good and with satisfactory features. Figure 4.5 reproduces the mechanical design along with the

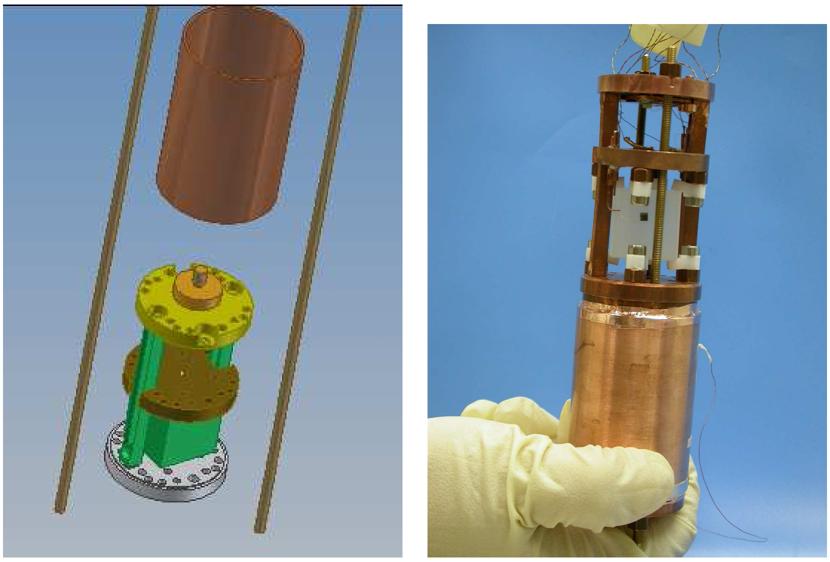

**Figure 4.5** - Mechanical design of the TBT holder (left) and a real two plane frame with detectors inside (right).

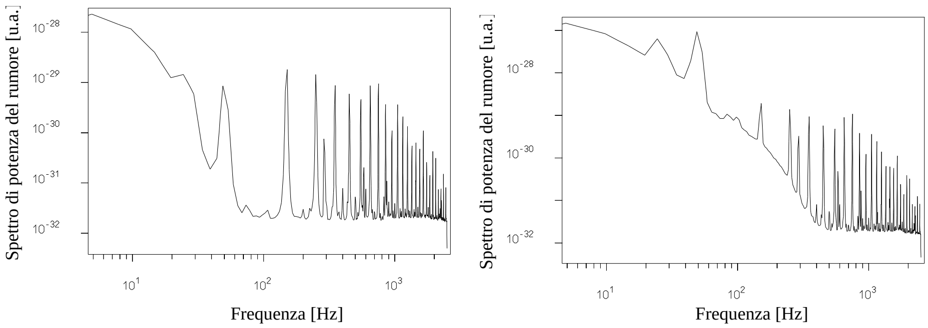


**Figure 4.6** - Noise spectra for two different detectors from the measurement number 5 in the TBT cryostat. Bessel filter is 12 Hz (left) and 120 Hz (right). The presence of interference from the 50 Hz CA of the electrical cabling is evident.

real structure. With some tricks, we are able to stack three holders of this kind, one below the other, under the TBT cryostat mixing chamber.

#### 4.3.1.3 Noise and vibrations

The TBT environment is not optimized for low noise measurements. Some work has been done to reduce microphonic and EMI noise to an acceptable level, compatible with our R&D goals and measurements apparatus. Large-size bolometers measurements that require high energy resolution must be carried on in dedicated environments in underground locations.

As an example, we reported in figure 4.6 two noise spectra from two detectors. It is clear that the principal noise source is the EM interference at 50 Hz (and odd multiples). Unfortunately the sampling frequency does not allow to investigate properly the low frequency region (which is usually affected by mechanical vibration and thermal instabilities).

## 4.3.2 AL cryostat: a liquid-free cryostat

### 4.3.2.1 Description, operation and features

In September 2003 a new cryostat arrived at the Como laboratory directly from the Air Liquide [81] laboratories (hence the name “AL”) of Grenoble, FR. The design of the cryostat is sketched in figure 4.7. Pictures of the system are in figure 4.8.

**Design**
Even from the very first glance, this cryostat appears to be a bit different form the TBT one, and not only for its size! In fact it is quite different from usual cryostats, because it has been designed to work without the LHe bath. The condensation of the mixture is in fact achieved by means of a cryocooler (namely a Pulse Tube) and a JT expansion. This design is very innovative, and first attempts to realize such systems are very recent [82, 83]. In the next section we will describe the principle of Pulse Tube (PT) cooling. Right now, it is sufficient to know that this machine is equipped with two stages that can reach about 65 K and 4 K respectively, by means of a closed cycle regenerative process.

**Description of operation**
Let’s follow the mixture in its flow from the tank down to the mixing chamber and back into the tank. A look at the GHS (figure 4.9) might help following the route. The mixture is circulated through a turbo–molecular pump, a rotative pump and a compressor. A common $LN_2$ trap is present on the inlet line followed by an inert gas purifier from Aeronex [84] (model CE-500K-I-4R). This gas purifier turned out to be very practical, providing advantages similar to those of a LHe trap, but without its hassles.

Citing the operating manual,

> AERONEX’s GateKeeper® Gas Purifier removes gaseous contaminants to sub-ppb levels. The electropolished, 316L stainless steel housing has inlet and outlet filtration to retain the media and capture particles. Filtered units will remove 99.9999999% of particles 0.003 micron or larger.
>
> The body contains an inorganic media composed of a specialty zeolyte, metallic catalyst, or a combination of the two types. Unlike other older technologies, the GateKeeper® patented media does not contain hydrocarbons that outgas. Additionally, the media can be regenerated, thereby eliminating hazardous waste disposal issues and providing the lowest cost of ownership available.
>
> The GateKeeper® purifier operates at room temperature, so no power or heat is required. This makes the GateKeeper® purifier safe and simple to use, without the facility requirements associated with heated technologies.

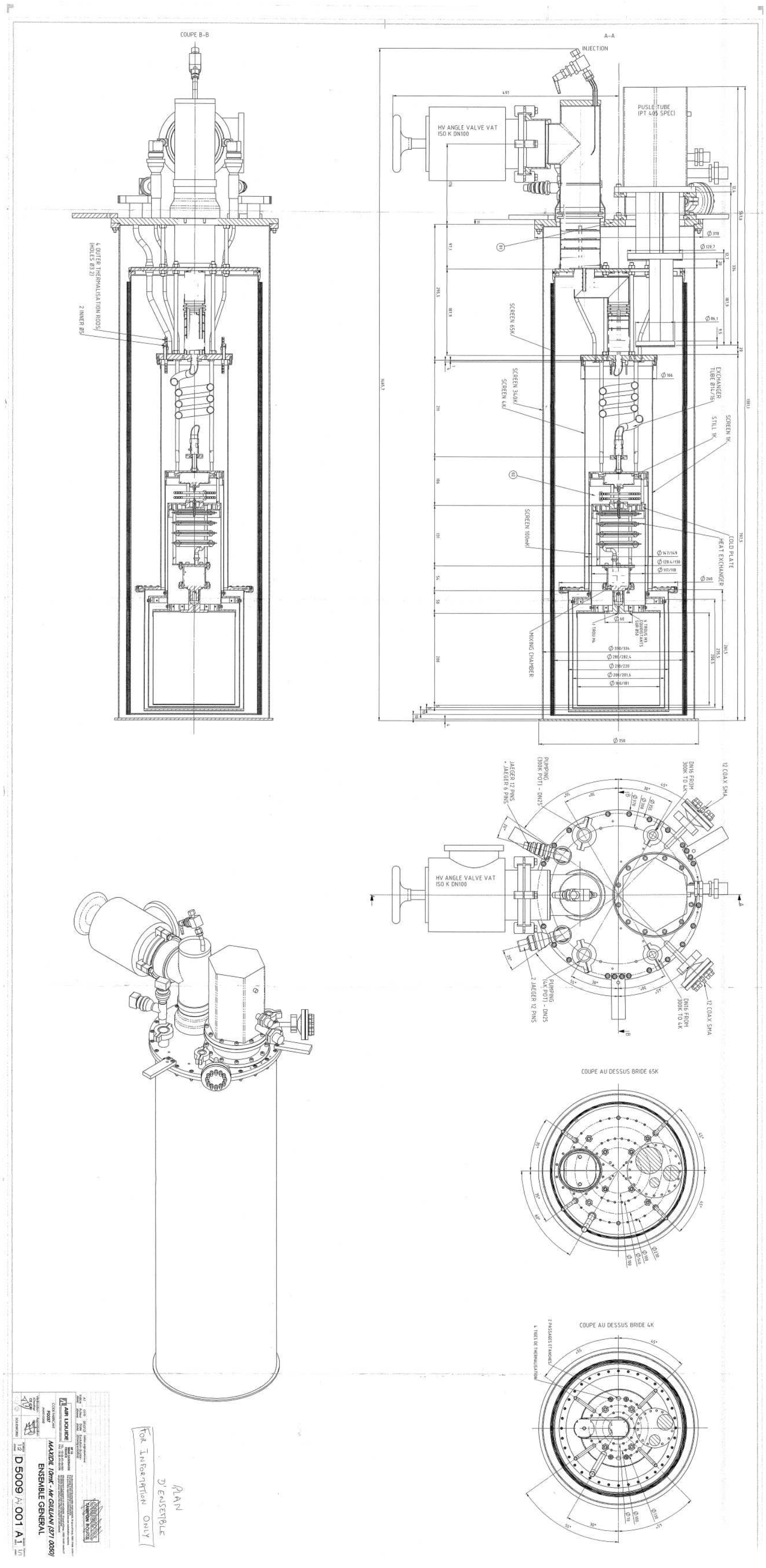

**Figure 4.7** - Mechanical design of the AL cryostat. Courtesy of Air Liquide [81].

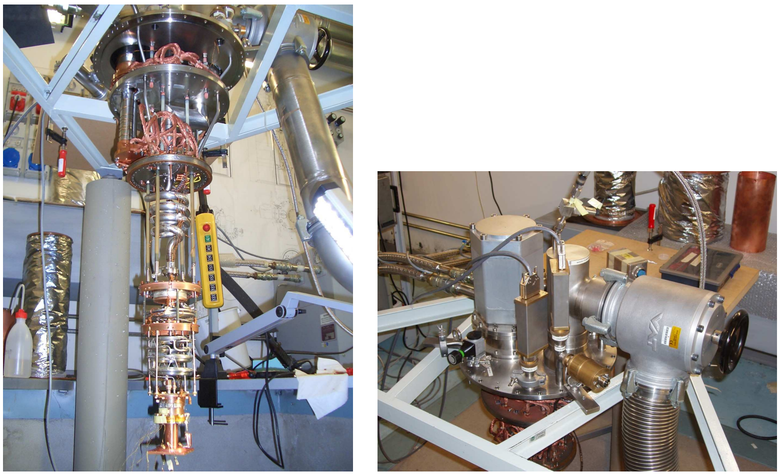

**Figure 4.8** - Pictures of the cryostat final arrangement in the BRAIN lab. The bottom view (left) shows all the parts of the DU. From the top (right) the Pulse Tube motor head is clearly visible on the left side.

**Figure 4.9** - Gas Handling System for the AL cryostat. The big tank on top of the GHS is the mixture dump.

> The purification process is based on a chemical process known as catalysis. Some typical reactions that can occur to remove impurities include chemisorption, oxidative addition, simple oxidation and simple apsorption. Initial activation at the factory removes all impurities within the purification media providing a clean, unsaturated media ready for use. The media gradually saturates by binding contaminants. The saturation zone moves through the purifier. When the zone nears the outlet, the purifier performance slowly degrades. This leads to incomplete gas purification. Once contamination levels reach an unacceptable level, the purifier requires regeneration.

The mixture then gets into the DU from the inlet line and thermalizes to the 65K and 4K flanges. These two flanges are cooled directly by the two PT stages. To reduce vibration from the PT cold heads, the flanges are connected to the PT exchangers by means of copper braids as shown in figure 4.10(a). The injection line is wrapped many times around the 4K flange to ensure good thermalization. A Joule–Thomson expansion is used to condense the mixture given the lack of a 1K pot. A secondary impedance is installed after the still to ensure an adequate pressure (fig. 4.10(b)) and avoid immediate evaporation. After the continuous and step heat exchangers we finally reach the mixing chamber (see fig. 4.10). Obviously, since no LHe is used, there is no LHe bath between the IVC and the OVC.

Nominal base temperature for this system approaches 10 mK, but we were able to reach this value only once and without calibrated thermometers. As we will discuss later, the system is quite sensitive to vibrations and suffers also from some electrical problems (ground loops, EMI pickup, . . . ). These facts affect the final base temperature that can be achieved on the detectors, usually around 15-20 mK, depending on the setup.

A quite large space is available below the MC (20 cm height $\times$ 18 cm diameter). The usable diameter is unfortunately reduced to about 11 cm due to a misshape of the innermost shield.

The cryostat is equipped with a set of thermometers, and two Jaeger connectors with 12 pins each are available for detectors. The wiring was made by AirLiquide and thermalized at different stages by means of proper thermalizations and by winding them around copper cylinder and cemented with varnish. A new wiring was studied and is ready to be mounted.

**Differences between PT supported and LHe bath cryostats**

We conclude this section by summarizing the main differences between a common LHe bath cryostat and a PT cryocooler supported cryostat:

**time:** the possibility of using LHe to cool the cryostat down to 4K and, more importantly, to thermalize the mixture by means of the 1K pot, plays an important role in the time schedule of a cryogenic experiment. In fact, due to the limited cooling power of the PT, both process are longer in a PT assisted refrigerator, especially if you do not care about wasting cryogenic liquids. However, PT technology is growing fast and the performance of

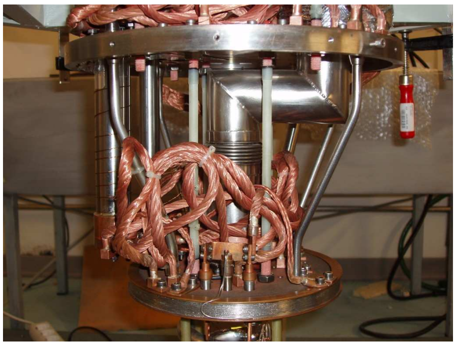

(a) Thermalization of the 65K and 4K flanges by means of copper braids. The PT cold heads are on the left side.

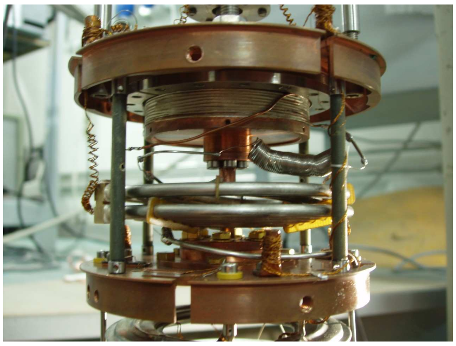

(b) Bottom view of the still with the inlet line thermalized around it. The second flow impedance is the long curled capillary visible on the right. Below the still are the continuous heat exchangers and the 100mK shield flange.

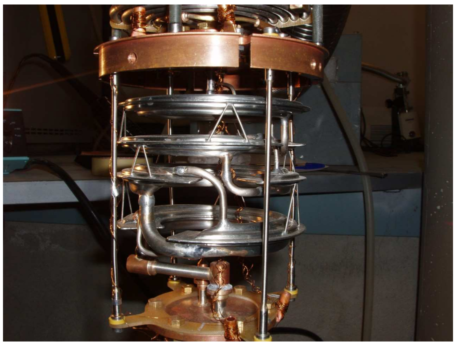

(c) Step exchangers.

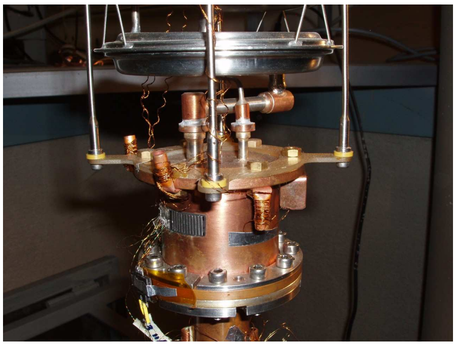

(d) Mixing chamber.

**Figure 4.10** - Parts of the AL cryostat dilution unit.

this device is already very good. In our case, the PT took about 21 hours to bring the cryostat from room temperature down to a situation where injection of the mixture can be sustained.

An interesting option that can be taken into consideration in those cases where time matters and/or where very huge masses need to be cooled (as in the CUORE detector) is to provide the cryostat with a fast precooling system by means of cryogenic liquids.

**money:** liquid Helium is nowadays very expensive and is sometimes wasted because of improper transfer, handling, or delays. On the other hand a PT needs only electricity and is always available and ready: it is just a matter of turning it on. PTs themselves are less expensive than other cryocoolers due to their simplicity, and require almost no maintenance.

**stability:** the rate of evaporation of LHe from a dewar is usually about 2% per day. When a cryostat is inserted into the main bath and mixture is circulating, the evaporation rate can be quite high. This means that the level of LHe in the main bath changes and consequently changes the temperature gradient of the whole cryostat. On the contrary, once a stable condition is achieved, a PT can keep the situation stable for a theoretically unlimited time.

**live time:** evaporation of LHe also implies that the main bath must be refilled regularly to avoid cryostat warm up. During refilling procedures, detectors cannot be operated because of the vibrations induced on them. After refilling, more time is needed to allow detectors to return to a quiet situation. To give an idea, refilling of the Cuoricino main bath takes about a couple of hours. With PT you do not have to care about such problems. In principle detectors can run continuously.

**vibrations:** this item will be discussed later, but we will underline here that, from a pure cryogenic point of view, in a normal cryostat, the 1K pot could be a source of noise from the LHe boiling. With a PT, the problem comes instead from vibration due to the oscillation of the working gas in the cold–stage. However, due to the lack of moving parts at low temperature, PTs are generally quieter than other cryocoolers. See §4.3.2.4 for more details.

#### 4.3.2.2 Introduction to Pulse Tube cooling

It is really a pity that we could not linger too much on the techniques developed during the last centuries to achieve low temperatures. A large part of the literature on the subject is however available [77]. Here we just want to resume some key information related to the production of temperatures down to 1 K, and finally come to a short review of the Pulse Tubes concept. Interesting reviews of this topic are [85–87] and proceedings from recent Cryogenic Engineering Conferences.

We already spent a few words on the Joule–Thomson cooling process. A vital part of its successfulness is the presence of a countercurrent heat exchanger. This ensures that the gas entering the final expansion stage has been cooled sufficiently, so that the JT coefficient is positive.

Heat exchangers are a key part also in all cryocoolers, where the cooling process (generally an isothermal compression and an adiabatic decompression) is repeated cyclically. Modern cryocoolers, like those based on the Stirling or the Gifford–McMahon cycles, use a discontinuous flow process. Regenerative heat exchangers were developed to act as a “cold storage” system for this kind of cryocoolers. The heat is stored here so that the heat output from one step of the cooling cycle may be recovered at some later step.

Pulse Tube refrigerators belong to the same family of Stirling and G–M cryocoolers, as their operation depends on a regenerative cycle. However, as we will see later, PT differs in the mechanism and nature of the cooling process.

**Historical perspective**

A brief history of PTs development could be illuminating on their behavior. They were first described by Gifford and Longsworth in 1959. In the next few years they observed that a pressure wave that propagates into a metallic tube closed at one end warms up, due to the interaction between the tube’s wall and

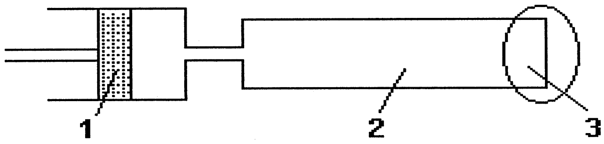


**Figure 4.11** - Pulse Tube closed end heating process. (1) compressor; (2) pulse tube; (3) warm area. From [86]

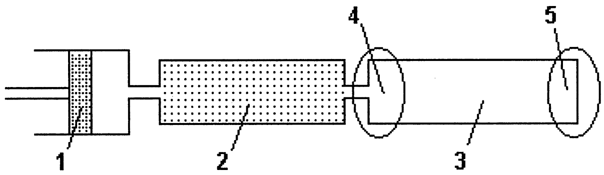


**Figure 4.12** - Basic Pulse Tube Refrigerator. (1) compressor; (2) thermal refrigerator; (3) pulse tube; (4) cold part; (5) warm area. From [86]

the gas itself (fig. 4.11). Later on, they added a thermal regenerator between the pressure wave generator and the pulse tube as in fig. 4.12. They observed that the closed end of the tube gets as warm as before, but also that a strong cooling happens at the other end. This device is usually named *Basic Pulse Tube Refrigerator* (BPTR). The efficiency of such system is strongly related to the phase shift between the pressure waves produced at one end and reflected at the other. BPTR design has some analogy with a twin piston Stirling cryogenerator, where one solid piston is replaced by a compressible gas piston. BTPR typically operates at a pulse rate of few Hertz.

A major advancement was proposed by Mikulin and colleagues in 1983. They added a buffer volume to the warm end of the pulse tube connected through an orifice as in fig. 4.13. For this reason this design is commonly known as *Orifice Pulse Tube Refrigerator* (OPTR). The orifice impedance and the buffer size can be used to optimize the wave shift.

Other constructional solutions were developed later and will not be discussed here for the sake of clarity. We underline that this field is still subject of intense activity and development.

### Working theory

Let us now focus on the theoretical analysis of the PT working cycle. Thermodynamic cycles (like the already mentioned Stirling and G–M) are usually described, as a first approximation, from the hypothesis that the whole working gas follows the same series of processes. Unfortunately, this seems not to

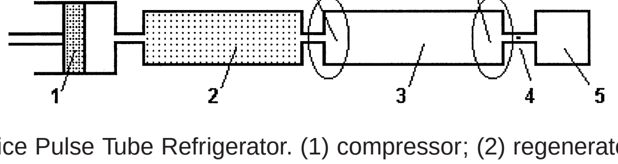


**Figure 4.13** - Orifice Pulse Tube Refrigerator. (1) compressor; (2) regenerator; (3) pulse tube; (4) orifice; (5) buffer reservoir; (6) cold part; (7) warm part. From [86]

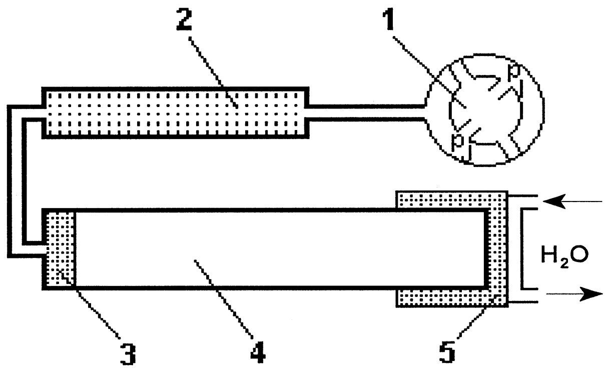


**Figure 4.14** - Scheme of a BTPR with rotating valve from [86]. (1) rotating valve; (2) regenerator; (3) low temperature heat exchanger; (4) pulse tube; (5) high temperature heat exchanger with water cooling

hold for pulse tube cycles, where, on the contrary, each portion of the gas undergoes a different process depending on its position. The refrigeration effect obtained in the Pulse Tube refrigerator is thus quite complex to be understood and described.

For BPTR it is widely accepted that the leading mechanism of refrigeration is *surface heat pumping* performed by the outer annular column of gas by means of stepped transfer of heat through the tube wall. This simple explanation is not adequate to explain the operation of OPTR, for which the pulse rate is too fast (about 50 - 60 Hz) to allow for an effective surface pumping. Some suggested that in this case the heat pumping occurs primarily within the pulsating gas column by means of a *non–symmetric thermodynamic gas process.*

**The PT at Como Lab**

Our AL cryostat hosts a Cryomech, Inc. [88] PT405 cryocooler (see figure 4.15). Figure 4.15 shows the PT itself and its final arrangement in the BRAIN laboratory at Como. It is a two stages PT. The first stage has a cooling power of 25W@65K, while the second can sustain 0.5W@4.2K. Minimum temperature is 2.8K (with no heat load). We presume that the scheme of the PT is similar to that shown in figure 4.14, where a rotating valve is attached to a compressor that provides pressurized helium through flexible metal hoses. Water cooling needs to be supplied to the compressor. The cooling power curve of this device is shown in figure 4.16.

The great advantage of these devices is the absence of moving parts at low temperature, along with their constructional simplicity, reasonable cost, and good reliability. These features make them very attractive in many low temperature physics fields.

#### 4.3.2.3 Cooling power measurements of the fridge

We performed a set of cooling power measurements on the AL cryostat. The results are plotted in fig. 4.17:

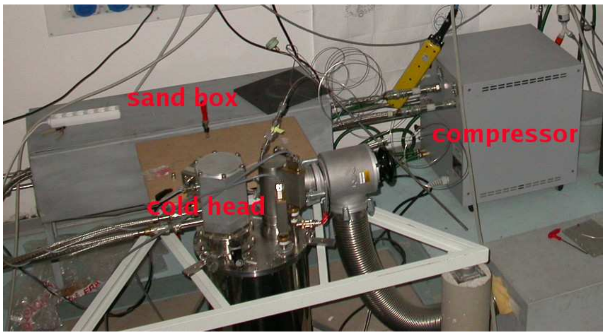


**Figure 4.15** - Picture of the PT405 Pulse Tube hosted in our AL cryostat (left - courtesy of Cryomech, Inc. [88]) and the arrangement in our lab (right) with the compressor, the pipes (damped in a sand box) and the PT on the top of the cryostat.

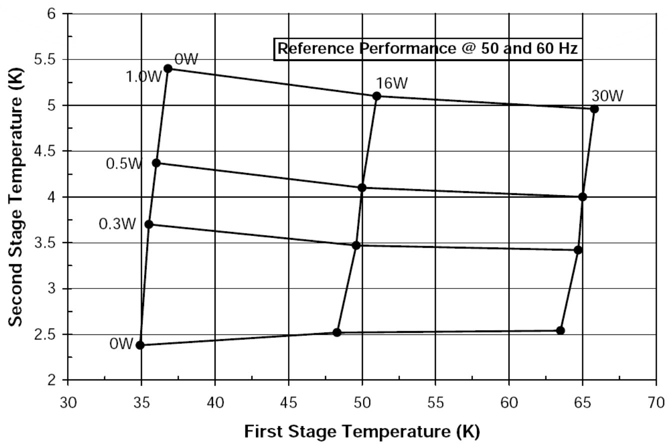


**Figure 4.16** - Capacity curves for the Cryomech PT405 pulse tube. Picture is courtesy of Cryomech, Inc. [88]

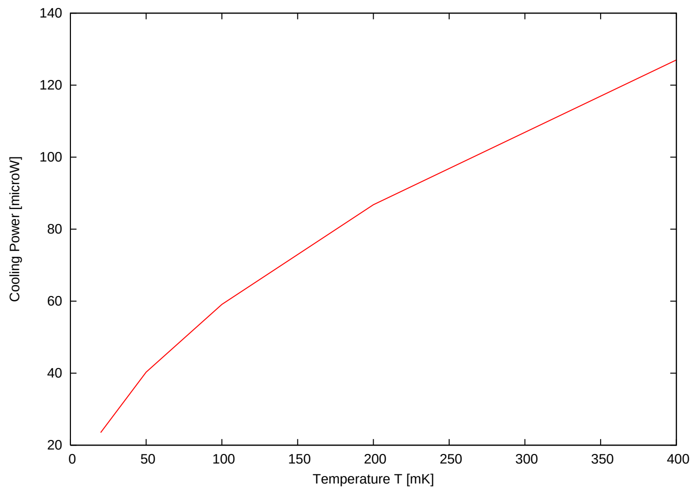


**Figure 4.17** - Cooling power as a function of the temperature for the AL cryostat at BRAIN lab. Data are for a still power of 3 mW.

| Power [$\mu$W] | 20 | 50 | 100 | 200 | 400 |
|---|---|---|---|---|---|
| Temp [mK] | 23.5 | 40.3 | 59.1 | 86.8 | 127 |

These data were collected with 3 mW of power on the still.

#### 4.3.2.4 Vibration measurements

We already pointed out that a PT driven refrigerator is somewhat new to us. Once we get skilled with its operation and its reliability, we then face the problem of the vibration induced on our detectors. Recently, several authors [89] investigated the noise performances of PT aided cryostats. Interest in this field comes for example from the possible use of these systems for gravitational wave detectors cooling, if their vibration level is reduced to a negligible level (i.e. below seismic noise). Also PT producers become aware of the problem. For example, Cryomech recently released a remote option for their PTs that allows to move the cold head far away from the cold stages. Development of systems with active compensation of PT vibrations are also under study [90].

Since we are going to design a cryostat for CUORE that will make use of PTs, we are worried by the possible presence of microphonic noise induced by the PT system. We thus performed some noise measurements to try to estimate the effect of vibration on our bolometers. This is a preliminary work and is not meant to be conclusive, but to start an investigation that should be carried on carefully to avoid unpleasant unexpected microphonic noise in CUORE detectors.

**Setup**

The cold head of the PT hosted in our AL cryostat is placed directly on top of the 300K flange. The two cold stages are connected to the 70K and 4K flanges by means of copper braids 4.10(a). This should reduce direct transmission of vibrations.

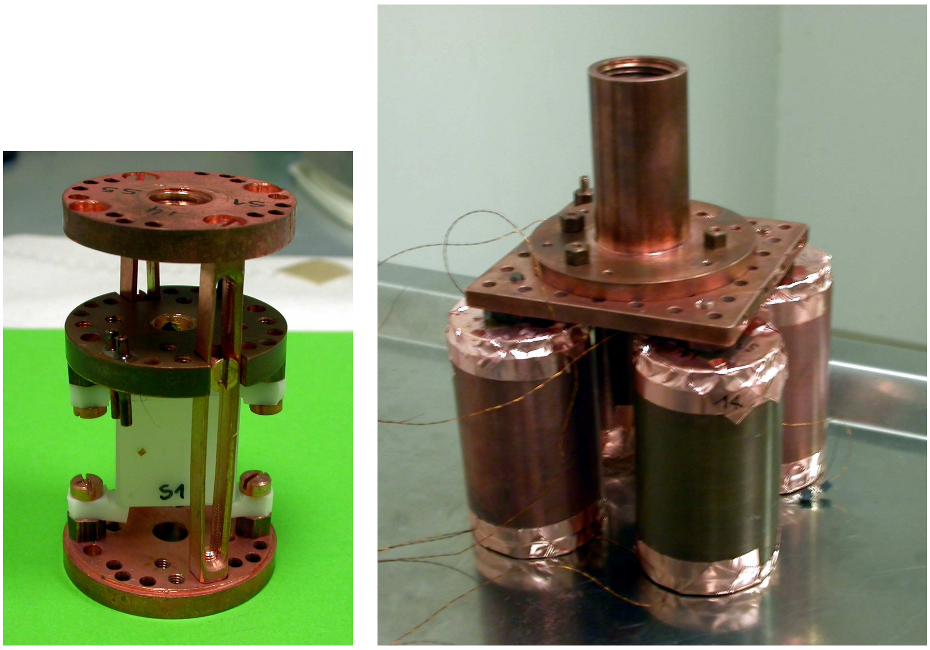


**Figure 4.18** - (left) One of the detectors mounted on the cryostat and used for the vibration measurements. (right) The four detectors structure ready to be installed on the cryostat cold finger.

Our goal is to try to evaluate the microphonic noise induced on the bolometers.

The possible source of microphonic noise are:

· PT cold head and cold stages vibrations

· PT compressor and tubes vibrations

· acoustical noise (i.e. sound waves propagating through floor and atmosphere) from PT compressor and mixture circulation pumps

· vibrations of the tubes connected to the mixture circulation pumps

We plan to switch off each source in order to try to identify their contribution to the global noise level. Obviously, not all contributions can be separated easily.

We mounted four bolometers on the bottom of the cold finger of the cryostat as shown in figure 4.18. Each bolometer is hosted in a TBT holder (§4.3.1.2). The detectors are special bolometers which will be described in chapter 7, but for the purpose of these measurements we can safely regard them as normal bolometers. The main absorbers are $2 \times 2 \times 0.5$ cm$^3$ $TeO_2$ crystals and a #34 NTD thermistor ($R_0$ = 6.24Ω, $T_0$ = 3.11 K) was placed on each crystal. Unfortunately, during the cool down, we lost the connection of one wire, so the measurements were performed on the other three detectors.

The cryostat was cooled down in September 2006 and reached a base temperature of about 11 mK.

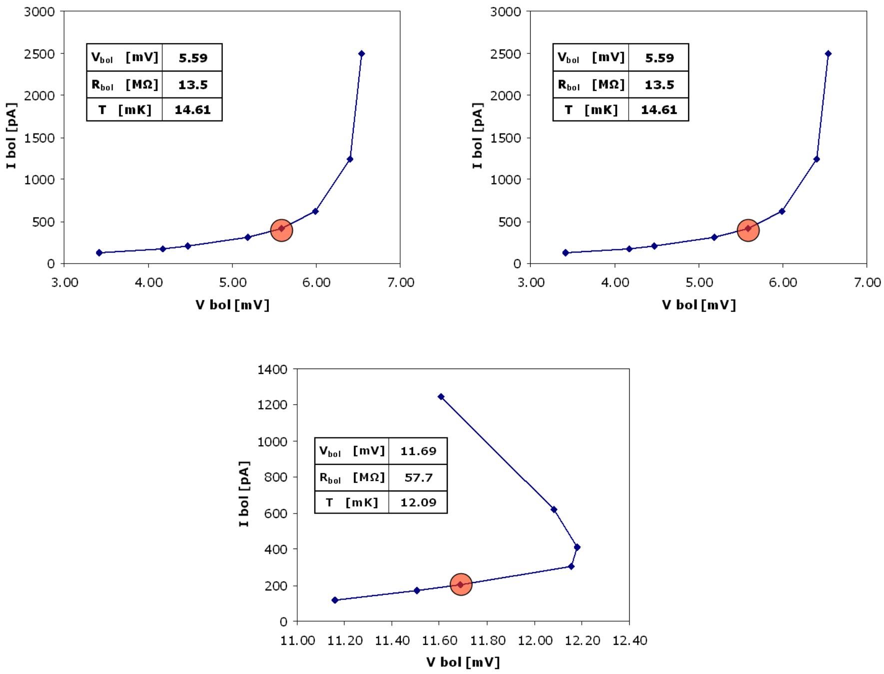


**Figure 4.19** - Load curves of the detectors used for the vibration measurements. The red circles highlight the working point, whose parameters are given in the corresponding table.

### Measurements

Before starting the measurements we set up the detector working points, which are reported in figures 4.19 along with the load curves.

In order to get information about the noise of our setup, the acquisition of the baselines of each channel should provide important results. These results will be more interesting if we are able to lower the sampling frequency (and thus the Nyquist frequency) as much as possible. There is however one limitation imposed by the high rate of events above threshold on each detector ($\sim$ 5–6 Hz), and it is mainly due to cosmic rays. A typical pulse from this mid–size bolometer last for about 100 ms. Basing on these considerations, and taking into account the Poisson statistic and the fact that we would like short measurements, we decided to set the sampling rate at $f_c = 5$ kHz.

Two sets of measurements were performed, the first with the Bessel filter of the electronics set to 12 Hz and the second to 120 Hz. Each set is composed by a sequence of three measurements performed in different conditions to allow comparison:

1. system running normally
2. compressor of the GHS switched off
3. compressor of the GHS and PT switched off

### Results

The two data sets were taken on two consecutive days, to allow the cryostat

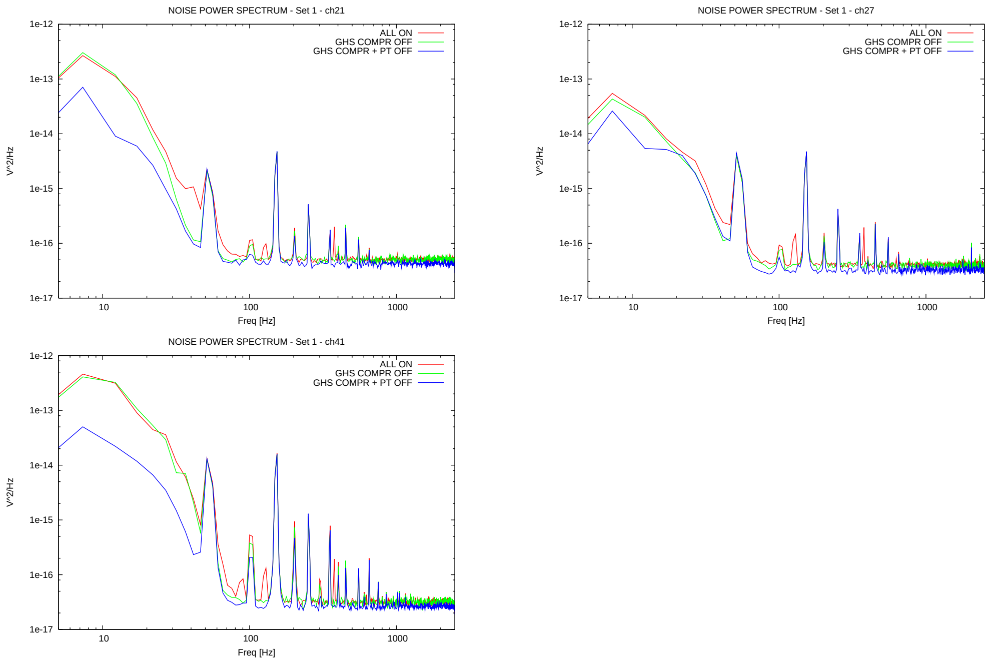


**Figure 4.20** - Power spectra for data of measurements set 1.

to come back to its normal operation after the PT was restarted, following the third measurement of the set.

Each measurement lasted about 5 minutes and for each channel we acquired 250 baselines. The off–line analysis was used to reject possible pulses that could have been wrongly acquired. A trivial max–min restriction did the job.

From the baselines, the analysis software produces the noise power spectra which are reported in fig4.20 and 4.21. The noise integrals in the frequency range between 5 and 95 Hz are reported in 4.1. We choose this range to have a reasonable number of values to integrate and to keep out the noise at 100 Hz. Since we are interested in comparative results, the noise peak at 50 Hz does not affect the result because, for each channel, it is always the same for each measurement in the same dataset.

From these data we can extract a good deal of useful information:

- as we already pointed out for the TBT cryostat, also the AL setup suffers from strong electromagnetic interference (50Hz and multiples). The fact that this noise is not attenuated by the Bessel filter is a good indication that it was probably picked up after the electronics, most likely on the BNC cables that reach the DAQ boards. A better setup is being studied to get rid of this effect;
- one of the three channels, namely ch41, is more sensible to vibration, as it is clear from the data. Even if this is not a desired feature, it was useful because it amplified somehow the effect of vibrations and allowed to recognize critical frequencies;
- from the measurements with 12 Hz Bessel, we see the presence of two

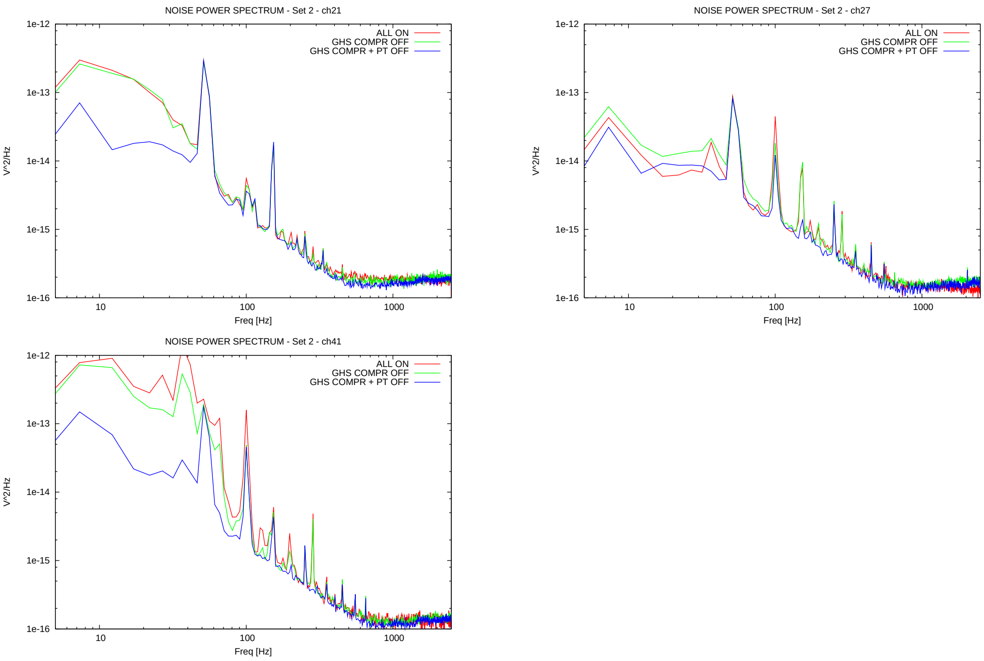


**Figure 4.21** - Power spectra for data of measurements set 2.

| SET 1 | | | Bessel: 12 Hz |
|---|---|---|---|
| ch | all on<br>meas 99 | compressor off<br>meas 100 | compressor + PT off<br>meas 101 |
| 21 | 1.48 | 1.52 | 0.68 |
| 27 | 0.70 | 0.64 | 0.49 |
| 41 | 2.19 | 2.16 | 0.75 |

| SET 2 | | | Bessel: 120 Hz |
|---|---|---|---|
| ch | all on<br>meas 102 | compressor off<br>meas 103 | compressor + PT off<br>meas 104 |
| 21 | 2.56 | 2.51 | 1.70 |
| 27 | 1.11 | 1.23 | 1.03 |
| 41 | 5.41 | 4.06 | 1.75 |

**Table 4.1** - Noise integrals of the power spectra for the two measurements datasets. Values are given as $\mu$Volt.

peaks, clearly due to the vibration of the compressor in the GHS at about 125Hz and 375Hz. All the machines (PT, GHS with pumps, cryostat) are close one to the other in the same room, and we have not taken yet any measure to reduce the acoustic noise - but we will do so soon. Currently, we are also testing the possibility of running the cryostat continuously with the compressor switched off;

· concerning the low frequency region, we see that an important contribution comes from the PT. This is not new and unfortunately, with our resolution at low frequency, we are unable to resolve any peaks; more precise measurements at low frequency could be performed only if the cosmic rays flux on detectors could be reduced (e.g. in underground tests) and therefore allow for longer baseline samples;

· even if some setup improvements will be welcome, we must emphasize that this noise does not prevent us from performing quality measurements, because our detectors' typical pulses are fast enough. On the other hand, the effect of this low frequency noise on big–size CUORE–like bolometers (with typical pulses of few seconds) needs to be carefully investigated.

## 4.4 CUORE R&D area @ HallC - LNGS

The R&D area of the Milano group at LNGS is equipped with an old but powerful Oxford Instruments dilution refrigerator, very much similar to the one placed in HallA that hosts Cuoricino. Given this similarity and the fact that we have not given yet any details on the Cuoricino cryostat, we will describe them both here. A picture of the bottom part of the HallC cryostat is shown in fig. 4.22.

In principle, they had a base temperature of 5.5 mK and a cooling power of 1000 $\mu$W (HallA) and 200 $\mu$W (HallC) at 100mK. Though they have been modified many times from their initial configuration, those parameters are likely to be still the same.

**Radioactivity**

The experimental set–up is drafted in fig. 4.23. Due to the low background constraints, the refrigerator was built with a contamination level lower than 100 mBq/kg for those materials whose total mass is less than 1 kg. For all the other materials the radioactive level had to be less than 10 mBq/Kg. Less stringent constrains were set on HallC cryostat.

Furthermore, to reduce the background due to the inner rocks of the laboratory, the HallC refrigerator is shielded with about 5 cm of copper and 10 cm of lead. The lead is placed inside the cryostat and is composed by a special "Roman" lead, whose radioactivity content is lower than 16$\pm$4 Bq/kg in $^{210}$Pb. A similar configuration is implemented in the Cuoricino setup.

**Liquefier**

As it is shown in fig. 4.23, the refrigerators are coupled with a helium liquefier,

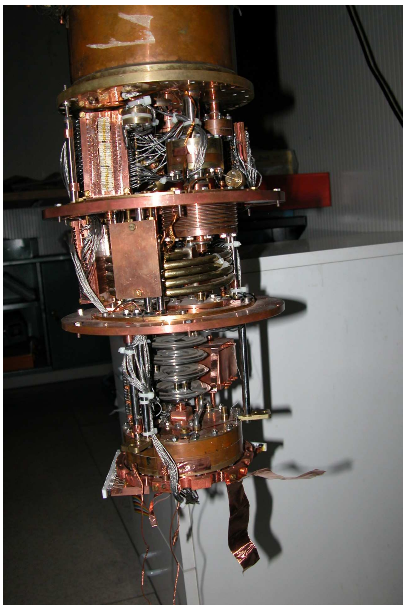

**Figure 4.22** - Picture of the bottom part (from the still to the MC) of the cryostat in HallC used for CUORE R&D activities.

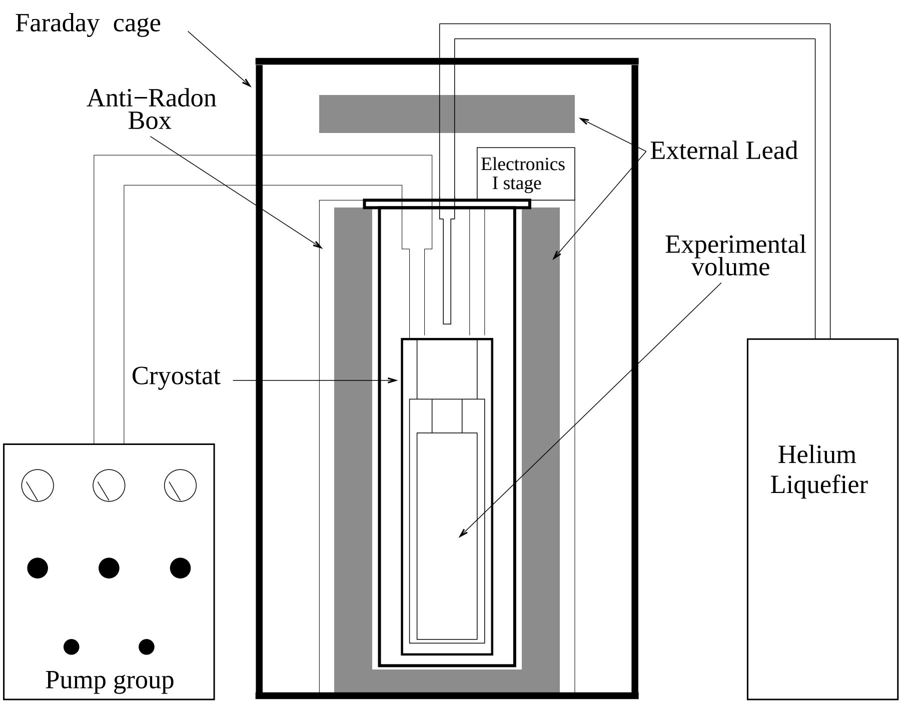


**Figure 4.23** - Scheme of the cryogenic set-up in LNGS HallC.

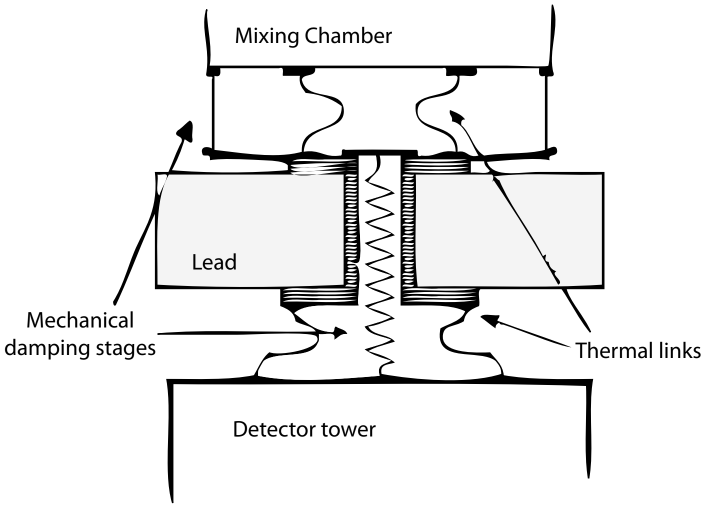


**Figure 4.24** - Scheme of the damping and thermalization system of the detector in the HallC cryostat.

which is useful to keep the liquid helium level inside the main bath at a constant level. This is important to reduce the variation of detector temperature that is correlated with the levels of the cryogenic liquids. It also helps reducing the maintenance costs and increasing the detector life time. In fact, when operating without the He liquefier, the HallC cryostat needs to be refilled with LHe every day (every 2 days for the Cuoricino cryostat). The refilling procedure is definitely a tedious waste of time and, more importantly, it requires to insert a tube into the main bath, plus other operations that are quite disturbing for the detectors. They warm up a bit (mainly because of vibrations) and become noisy, and it takes some time for the system to come back to a fair and steady situation. That means (if we are lucky) about a couple of hours per day without the possibility of acquiring data. On the other hand, the liquefier itself could be a source of noise and vibrations for the detectors, not to speak of the bother of keeping it running because it is a quite delicate machine.

**Vibration damping**

All the pipes and tubes for the mixture and the pumping are immersed into a big sand box to dump the vibrations produced by the pumps.

Inside the cryostat, a special damping system reduces the noise contribution of incoming vibrations. The cryostat itself acts as a pendulum with its characteristic frequencies involved. These vibrations are the source of friction between absorbers and supports, which could determine sudden heat release or unwanted temperature instabilities. Bolometers are particularly critical to low frequency noise. A damping system which decouples the detectors from the cryogenic setup is therefore extremely important.

The damping system in the HallC cryostat is a double stage harmonic oscillator (see fig 4.24) The first stage consists of 14 kg lead disk pending from the mixing chamber by means of three stainless steel wires. These wires are connected to the lead trough three harmonic stainless steel strips that can slightly bend. The resulting longitudinal intrinsic oscillation of this stage is at the frequency of $\sim 7$ Hz. The lead on the first stage acts as a good radioactive shield, because it is made out of ancient Roman lead with negligible content in $^{210}$Pb. The second damping stage is realized by hanging the detector box to the lead structure trough a stainless steel spring and a copper bar. The intrinsic frequency here is $\sim 3$ Hz. The thermal link between the detectors and the cryostat is ensured by two thin strips of pure copper that connect the mixing chamber to the first stage and the first stage to the second.

The experimental volume below the mixing chamber of the HallC cryostat is big enough to host a tower of three CUORE–like frames (each one has four 5x5x5 cm$^3$ crystals). More space for smaller prototypes is available on the top of the mixing chamber, and attached to a cold finger coming from the first damping stage.

**Electronics**

Usually, the signals from the detectors are carried out with 60 $\mu$m dia twisted pairs of Constantan wires up to the MC. 100 $\mu$m dia NbTi wires were instead used from the MC to room temperature. In the latter case the twisted pairs are also shielded by a CuNi wire netting.

Two different front-end systems are available: cold and room temperature electronics. A cold buffer stage is thermally anchored to a 4.2 K plate inside the cryostat. A room temperature 12-channel front-end can be adopted elsewhere [91]. The cold buffer stage consists of 12 independent differential channels, composed of 12 pairs of silicon JFET transistors in source follower configuration, and 12 pairs of load resistors (27+27 G$\Omega$) for thermistor biasing [92]. The operating temperature of about 110 K for this stage is achieved by thermally decoupling the two printed circuit boards, each of them housing 6 channels, from the box in which they are enclosed by means of nylon wires. The thermal impedance thus achieved guarantees the correct temperature to the FETs when they are working, and therefore dissipating power. In order to avoid any possible irradiation from the circuit boards, the box is gold plated and is as hermetic as possible to IR rays.

The room temperature front–end and the second stage of amplification are located on the top of the cryostat. A big Faraday cage, containing the cryostat, the electronics on top of it, the radioactive shields made of Cu (5 cm minimum thickness) and Pb (10 cm minimum thickness) and the anti-radon Plexiglas box, is used to avoid EM interferences to the detector read-out.

After the second stage, and close to the acquisition system, there is an antialiasing filter (a 6 pole roll-off active Bessel filter) and a programmable analog triggering and shaping circuit [93]. A small Faraday cage encloses this last stage of amplification. The signals are acquired for off–line analysis by a 16 bit ADC embedded in a VXI acquisition system.

# · Chapter 5 ·

# Thermal sensor optimization

## 5.1 Introduction

We have already discussed the role and the importance of the thermal sensor in the design of a bolometer.

During this Ph.D. work, we faced the problem of the optimization of the sensors for CUORE from different points of view. Three approaches were pursued.

First, starting from the well–known and well–performing thermistors of Cuoricino, we asked ourselves if it would be possible to act on any of their parameters and improve them. Historical and theoretical considerations led us to focus our attention on the $T_0$ parameter, which primarily characterized the response of the thermistors. This topic will be discussed in the next section, along with the performed experimental measurements.

Compared to Cuoricino, CUORE will definitely require some sort of engineering in all the assembly procedures. One of these steps deals with the wiring and mounting of the thermistors. Even if it looks like a non-physics-related problem, the solution that we will propose here involves a shape modification of the thermistor, which could in principle change its behavior and performances. For this reason we tried to simulate the new thermistors thermal behavior and §5.3 will cover this work.

Finally, we attempt a more ambitious and general approach. In principle, any kind of physical quantity that changes with temperature is suitable to work as a phonon sensor. For this reason, we studied the possibility to develop capacitive sensors for bolometers, based on the temperature variation of the dielectric constant $\varepsilon_r$. Moreover, thermistors readout dissipates power on the detector because of the thermistor biasing; it also introduces a Johnson noise term. Thus the use of capacitive sensors could allow us to achieve a better signal-to-noise ratio. In §5.4 we report the work done on this subject, even if the results are not satisfying.

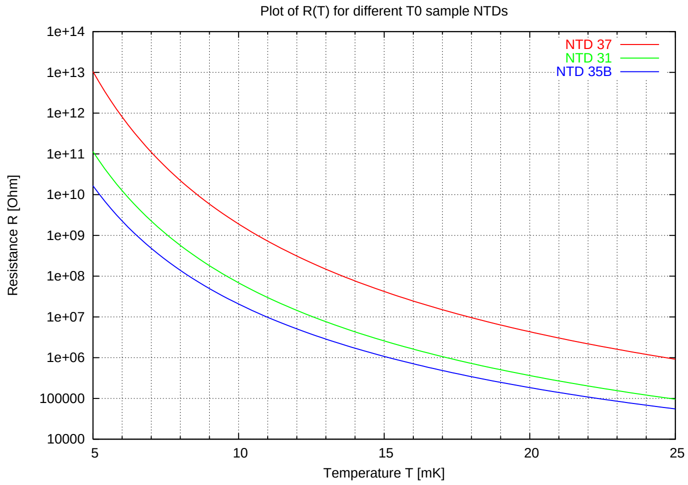


**Figure 5.1** - Plot of $R(T) = R_0 \exp{(T_0/T)}^{1/2}$ for the different values of $R_0$ and $T_0$ of the NTDs used in the $T_0$ run. See table 5.1 for $T_0$ values.

## 5.2 Investigation on $T_0$

### 5.2.1 Introduction, motivation and goals

We already know from the previous chapters that in the Cuoricino detectors the thermal pulses generated by an event in the main $TeO_2$ absorber are read by an NTD thermistor. Operated in the variable range hopping regime with coulomb gap, their resistivity scales with temperature according to the exponential law (cfr. eq. (1.8)):

$$\rho(T) = \rho_0 \exp\left(\frac{T_0}{T}\right)^{1/2} \tag{5.1}$$

where $\rho_0$ and $T_0$ depend on the dopant level.

The thermistors we use for our bolometers come from different *series*, which are labelled with a number. Thermistors of the same series share the same parameters. In the following we will often use the term *NTD* alone to indicate NTD thermistors.

In Cuoricino, the thermistors used are all of the same kind (at least for the $5 \times 5 \times 5$ cm$^3$ detectors). They have been selected from the #31 series and their properties are:

$$\rho_0 = 1.17 \quad [\Omega \cdot \mathrm{mm}] \qquad T_0 = 3.20 \quad [\mathrm{K}] \tag{5.2}$$

Given the expression (5.1) above, what is most important is the $T_0$ value. In fact, as shown in fig. 5.1, the thermistor working resistance at a given temperature can be very different (orders of magnitude) even for a small change of $T_0$.

No optimization has ever been done on the values in (5.2). They were selected only because the resistance values at the bolometers working temperatures were compatible with the electronic setup. Nevertheless, we documented in §3.4 that Cuoricino detectors are performing very well and behavior of NTD#31 thermistors is quite well known. Nevertheless, it must be noted that, in principle, the use of thermistors with different $T_0$ could lead to even better performances.

In fact, compared to NTD #31, a thermistor with a *lower* $T_0$ has a lower resistance (if operated at the same temperature), which will probably mean a lower spurious noise, but also smaller pulses. Moreover, because of the correlation between $T_0$ (i.e. the dopant level) and the electron–phonon coupling [94], a lower $T_0$ could also lead to a less severe electron-phonon decoupling. Thermistors with *higher* $T_0$ could be useful as well. For example, they could be operated at higher temperature. Working at $\sim 15$ mK (instead of the current $\sim 9$ mK of Cuoricino) is much better because signals are faster, stabilization is easier, and in addition the performances of the refrigerator are less critical. On the other hand, the crystals heat capacity increases with temperature, thus reducing the pulse amplitude.

From this short introduction, it is clear that there is a lot of parameters that act in different directions and that the value of $T_0$ can be optimized for better performances.

Thus, the goal of the study presented in this chapter is to find a reasonable answer to these questions:

- Is the $T_0$ value critical?
- Is there an optimum $T_0$ value?
- Is the $T_0$ truly correlated with the electron–phonon decoupling? How does this correlation affect the detector performances?
- Is the $T_0$ linked to other detector parameters?

The question related to the constraint on the NTDs $T_0$ value is important not only from a "theoretical" point of view (e.g. optimization of the detectors), but also from the point of view of the preparation of the thermistors for CUORE. The thermistors realization is a quite long process, which requires the Germanium batches to be exposed to a neutron flux from a nuclear reactor. By means of (n,$\gamma$) reaction, the $^{70}$Ge and $^{70}$Ge isotopes produce Ge unstable isotopes, which will decay by $\beta$ emission or electron capture producing dopant agents. The dopant level will thus depend on the neutron flux. The neutron flux on target is not known with the required precision, and thus two irradiations are needed to achieve the desired dose. In the first step, Ge will be irradiated with $\sim$80% of the expected dose. A sample is then measured to evaluate the $T_0$ value and to calibrate the exposure time for the second irradiation. This second irradiation could be avoided only if the constraints on the $T_0$ are less strict, i.e. if there is a quite wide range of values for which detectors performances are acceptable. Since the longest part of the thermistor preparation is the cooldown (decay) time after irradiation, which is about 1 year, it is important to timely define the configuration of the thermistors in order to avoid any delay on the CUORE schedule.

| Type | Geometry mm$^3$ | $R_0$ [Ω] | $T_0$ [K] | $T_0$ diff from #31 | R @8mK [Ω] | R @15mK [Ω] |
|---|---|---|---|---|---|---|
| 37_K | $3 \times 3 \times 1.5$ | 1.20 | 4.32 | +36% | $1.48 \times 10^{10}$ | $2.81 \times 10^7$ |
| 31_L | $3 \times 3 \times 1$ | 1.17 | 3.20 | - - | $5.68 \times 10^8$ | $2.58 \times 10^6$ |
| 35B_L | $3 \times 3 \times 1$ | 2.06 | 2.60 | -19% | $1.39 \times 10^8$ | $1.07 \times 10^6$ |

**Table 5.1** - Properties of the NTDs selected for the run. The values for $T_0$ are expressed with the Milano thermometry.

### 5.2.2 Measurement Design

An experiment to answer the questions of the previous section was prepared at the end of 2004 in the Hall C cryostat.

Between all the available thermistors, three different types of NTDs were selected in order to have three different $T_0$ values (see tables 5.1 for their properties). Obviously, one of the three thermistors belongs to the well known #31 series to allow comparison.

Since we know that many variables and parameters play different (and sometimes not well understood) roles in the behavior of the detectors, we decided to cool down 4 detectors in a Cuoricino–like structure (1 plane of $5 \times 5 \times 5$ cm$^3$ $TeO_2$ crystals). In this way each crystal hosts 3 thermistors (one for each series): comparisons can be made among thermistors on the same crystal and across different crystals, to gain as much information as possible.

It is important to note that, unfortunately, the #37 thermistors have a slightly lager size, since no thermistors with the 'L' geometry were available for that series. This difference can be nonetheless taken into account, for example by comparing the resistivity instead than the resistance. Moreover, it's worth reminding that the relationship between the electron-phonon decoupling in the thermistors has been always assumed phenomenologically as:

$$G_{\text{e–ph}} = g_0 \cdot T^{4.37} \quad \left[\frac{\text{W}}{\text{K} \cdot \text{mm}^3}\right] \tag{5.3}$$

where the value is expressed in units of thermistor volume. Moreover, the value of the temperature exponent could in principle be a function of the thermistor doping. The value used here was obtained for the #31 thermistors. In our discussion we also have to remind that, as already said, $G_{\text{e–ph}}$ decreases when $T_0$ increases. These considerations must be taken into account when discussing the results of the measurements.

With the selected $T_0$ values, we could compare the behavior of the bolometers by operating them at different temperatures (e.g. 8, 10, 15 mK) and comparing different thermistors at the same temperature, or by looking at how their behavior changes at different temperatures. Load curves, optimum point search and pulse comparison must be performed at each temperature for each thermometer.

The possibility of using smaller crystals (and thus cooling them in an aboveground cryostat instead than in the Hall C one) has been taken into account,

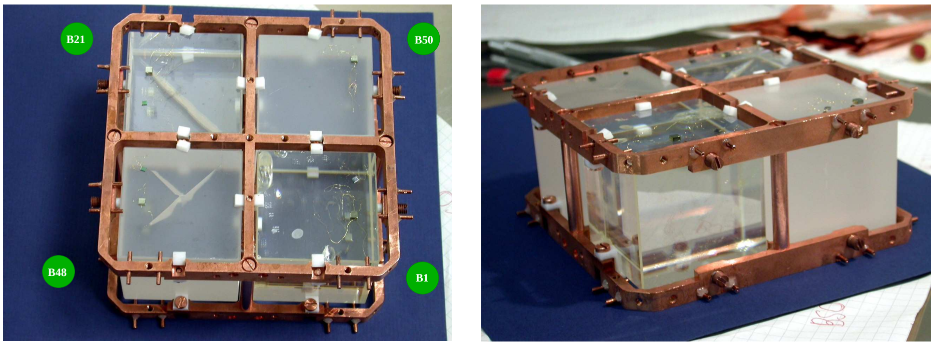


**Figure 5.2** - The final frame of 4 crystals

but rejected, because extrapolation from small scale prototypes could lead to unreliable results.

## 5.2.3 Run Preparation

### 5.2.3.1 Detectors Assembling

We prepared and assembled the detectors in Como in December 2004. No special treatment has been performed on crystals or copper or Teflon, except usual cleaning. The crystals are labelled B1, B21, B48 and B50.

The gluing process of the thermistors was followed with great attention, in order to control the thermal conductance of the glue itself. For this reason, the same gluing tools adopted for Cuoricino were used [75]. Those tools makes gluing a quite reproducible process (although not completely). Each thermistor is glued on the crystal with nine glue spots of Araldit. The B48 and B50 crystals came with their NTD #31 already attached, and they were not removed. On each crystal we also placed a heater (R $\sim$ 100 K) with a single glue spot. No information is available on crystal axis for B1. For the other crystals, we selected the hard face to host the NTD thermistors.

### 5.2.3.2 Detectors Mounting

Before bringing the detector to GranSasso, the crystals were placed into a copper frame in a $2 \times 2$ configuration, as in the planes of Cuoricino. Since all the crystals have different sizes (min: 50.2 mm - max: 51.1 mm), it was not easy to fit them into the holder. It was especially hard to find a configuration in which all the Teflon pieces work well on every crystal. The final setup is shown in fig. 5.2 from different sides. At the end the whole frame was surrounded with copper for full shielding.

### 5.2.3.3 Holder setup in the Cryostat

The last step of the mounting procedure consisted in the placement of the frame in the Hall C cryostat and the connection of the wires. The frame was connected to the bottom of the second decoupling stage hung to the mixing chamber. The thermal connection of the holder to the first stage was obtained using a copper wire and a copper sheet (see §4.4).

To accommodate all the wires (other detectors were also present) we decided to put two bolometers on the cold electronics and two on the warm one. To monitor and control the temperature of the holder, we placed a thermometer and a heater on the external copper shield of the frame. We also placed a heater on the mixing chamber, but unfortunately we didn't have a thermometer on the mixing chamber.

#### 5.2.3.4 Cryostat cool down

The procedure for cryostat cool down started in January 2005, but a leak in the IVC Indium sealing forced us to remove the cryostat, replace the sealing and repeat the cooldown. Other problems emerged during the run, but they are not reported here.

It is however important to note that, for unknown reasons[1], the cryostat did not reach the expected base temperature: instead, it kept at about 15mK, going down very slowly.

In this configuration we were unable to perform all the tests and measurements we had planned. However, taking into account the urgency of an answer on the $T_0$ for CUORE thermistors, and the fact that no other cryostat–time would be available for other tests, we decided to go on with the run and to try getting as much information as possible, even if at higher temperature. Moreover, the NTDs of the #37 series are supposed to have reasonable resistances at this temperature. In addition, this is a good simulation of the unwanted possibility of lack of base temperature of the CUORE cryostat.

During the cool down, we also lost the connection of the heater on the B1 crystal.

### 5.2.4 Measurements

Measurements were performed during the last week of January (at the beginning we planned at least two weeks of data collection, but this was not possible because of the delay introduced by the cryogenic problems).

Measurements are divided into static measurements (load curves of the thermistors) and dynamic measurements (pulses from heaters and calibration source).

#### 5.2.4.1 Static measurements

**Almost zero bias measurements**

We started measuring the resistance of the thermistors at very low bias, so that almost no power is injected. The plot obtained is shown in fig 5.3. Converting resistivity into temperatures (fig. 5.3), it is evident that we were

[1]During the run, we thought that the possible reason for the lack of base temperature was a very bad thermal conductance between the holder and the mixing chamber. It was discovered later that the real explanation could be the fact that a non negligible power is dissipated on the cryostat by one of the LHe level meters.

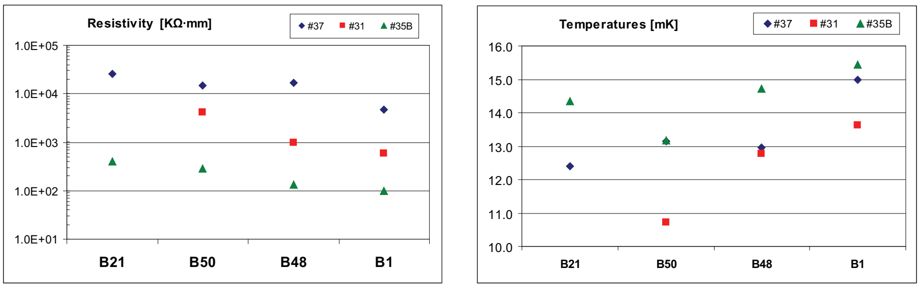


**Figure 5.3** - Values of the resistivity and of the temperature of the thermistors on each detector of the $T_0$ run. Values obtained when the power injected is almost null.

working at $\sim$ 15 mK. The temperatures spread is fully compatible with the uncertainty of bolometers operations. Not unlikely, small systematic errors on the values of $R_0$ or $T_0$ are also present.

### Load curves and static behavior

In figure 5.4(b), 5.4(a), 5.4(c) we reported the IV curve for crystals B48, B50 and B21 respectively. Several curves were taken in different days but, given the thermal uncertainty, they are all compatible. No static data are available for the B1 thermistors.

The first consideration on the load curves is that, because of the lack of base temperature, the tests on #35B chips are unreliable, since their resistance ($\sim$ 1 MΩ) is too low to make them stand a reasonable bias.

Unfortunately, the static I-V curves are not encouraging for #37 chips. In fact they handle much less power than #31 chips, therefore their I-V curve bends at much lower thermistor voltages. Typically, for the same current, #31 thermistors show a voltage bias 2–4 times higher than #37 thermistors in the region of the I-V curve interesting for bolometric operation.

Additional information can be obtained by looking at the change of the thermistors resistivity for different injected power (fig. 5.5). Converting the resistivity into temperatures values, we could get rid of the differences between the thermistors geometry and configuration as in fig. 5.6.

These plots show clearly that, for the same injected power, the temperature of the electron component of the thermistor increases with the $T_0$, as expected from the relationship between the electron-phonon decoupling and the $T_0$ value. As $T_0$ increases, it's thus difficult to bias the thermistors, since they get easily hot. The situation of the #37 could be even worse if you remember that they are larger than #31 and #35B. Therefore, given (5.3), the electron-phonon decoupling is moderated by the bigger volume.

This is a first hint of the possible problems that could arise when using thermistors with higher $T_0$. It is however important to note that in Como we operated successfully thermistors of series #36 at a even higher temperature of about 20 mK. Such thermistors are of small size and high $T_0$. However, their load curve looks more like the usual one obtained by operating thermistors of #31 series from Cuoricino. This behavior could be explained considering again equation (5.3), from which it is easy to see that at 20 mK the electron-phonon

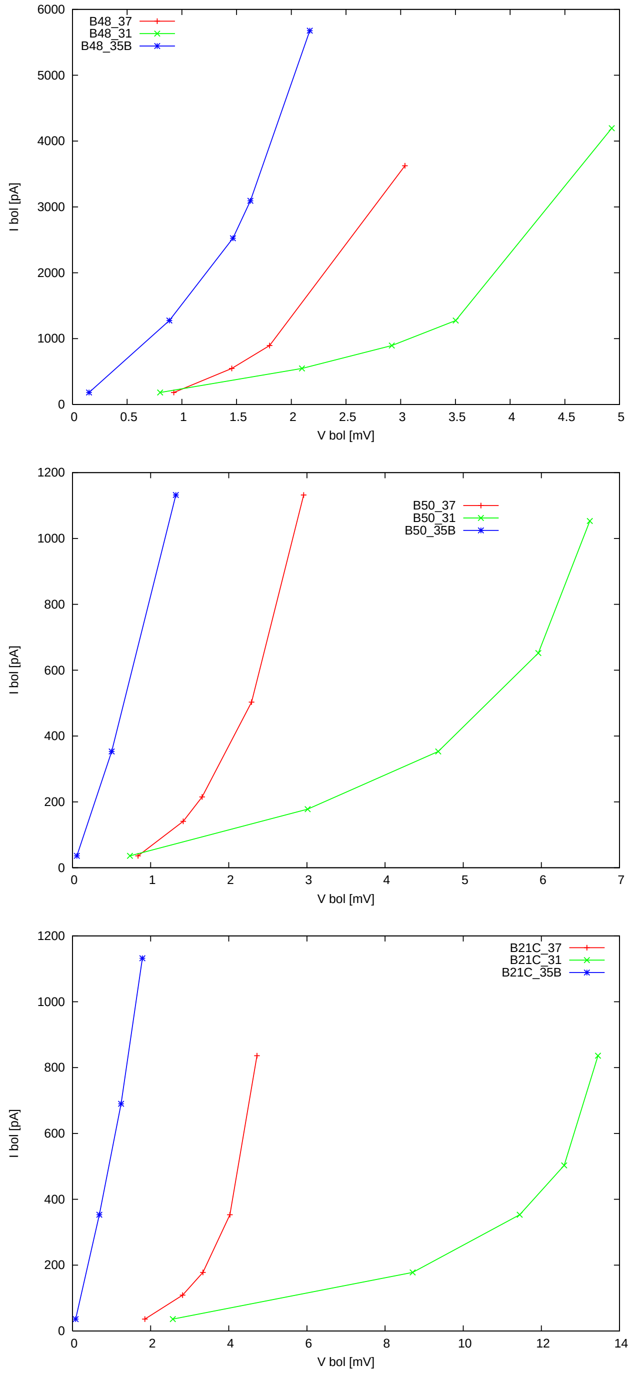


**Figure 5.4** - IV load curves for thermistors on the B48, B50 and B21 crystals.

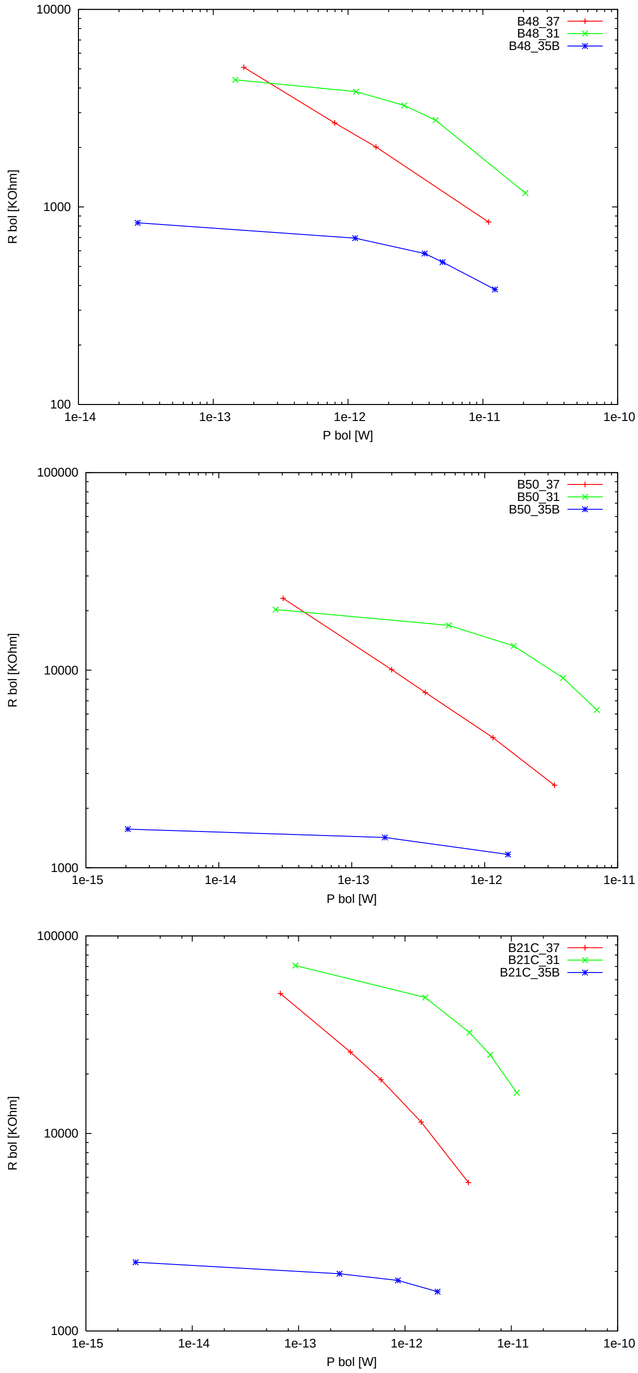


**Figure 5.5** - RP curves for thermistors on the B48, B50 and B21 crystals.

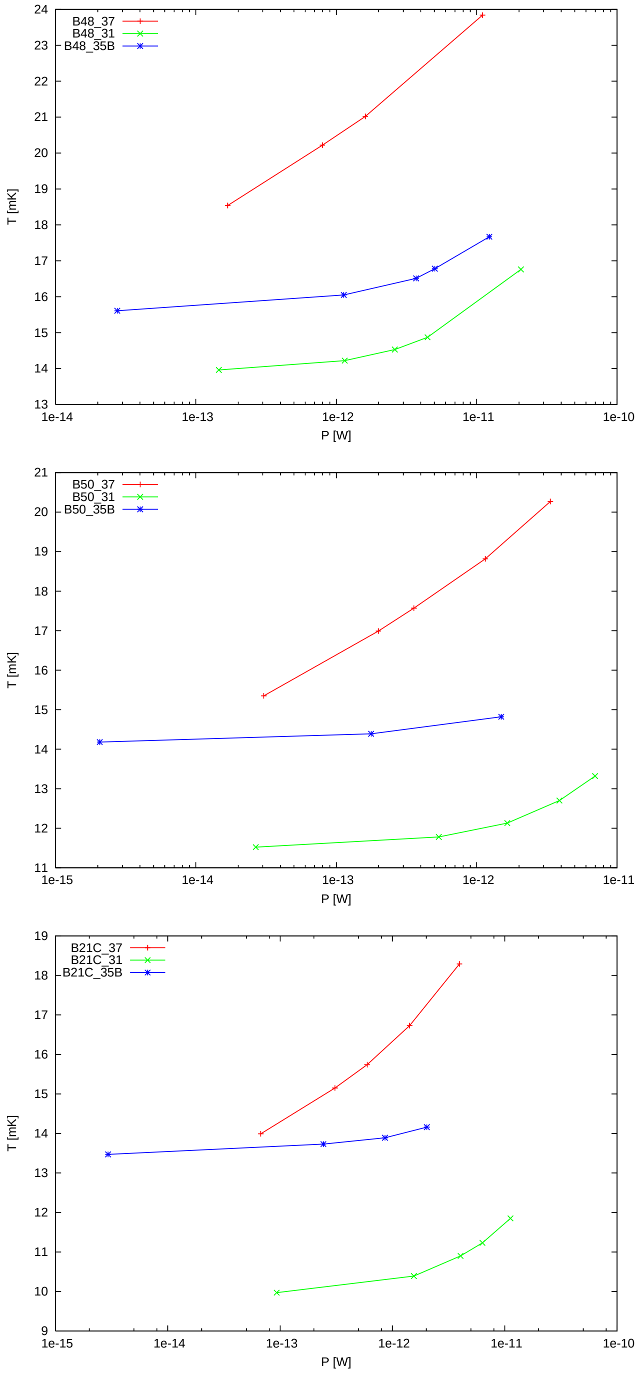


**Figure 5.6** - TP curves for thermistors on the B48, B50 and B21 crystals.

coupling is 3.5 times stronger than at 15 mK. We would like to stress the fact that in Como we use smaller crystals, and that extrapolations from these conditions are not always safe.

#### 5.2.4.2 Dynamic measurements

For almost each point on the load curve, the amplitude of heater pulse was acquired. The heaters values are: B48: 21.9 KΩ, B50: 66.3 KΩ, B21: 109.9 kΩ. The heater pulse was set to 3 Volts. The data are plotted in fig. 5.7.

It is clear that pulses on the #37 chips are way worse than those obtained with #31 ones. Moreover, they are smaller than the #35B pulses in two cases. This behavior can be better seen in fig. 5.8, where the coincident pulses acquired are plotted together. In this case we were able to acquire pulses also from the B1 crystal. Thermistors on crystal B48, B21 and B50 were biased reasonably close to their optimal point. Since no heater was available on crystal B1, the working point of its thermistors was set up only from consideration about the other crystals chips.

As already explained, as a consequence of the thermal instabilities of the holder (i.e. the slow temperature drift), we were not able to perform long measurements. A long measurement could have been useful to estimate the resolution of the detectors.

### 5.2.5 Conclusions

The results presented here can be very well explained by assuming a much lower electron–phonon conductance for #37 chips with respect to #31 chips. The consequence on the static and dynamic behavior of the bolometers is a reduction of the pulse amplitude. This is compatible with the specific measurements performed by E. Pasca and reported in his PhD thesis [94]. The agreement is qualitative: a full quantitative check should be performed in the future.

Given the fact that the production of the thermistors for CUORE needs to be started as soon as possible, our conclusion is that we need a rather precisely $T_0 \simeq 3.0$ K value, e.g. #31 or #34B thermistors. It must however be noted that we did not perform all the measurements to obtain a full answer on the $T_0$ behavior. In particular, we were unable to test chips with lower $T_0$, or to confirm the result on higher $T_0$ at the usual working temperature of bolometers.

Basing on the above considerations, it is clear that we will need two irradiations for NTDs production. Given this fact, it is actually possible to delay the final decision on the value of the $T_0$ for CUORE after the first irradiation. At that point, thermistors will be tested on bolometers and the final decision will be made. Meanwhile, investigation on $T_0$ data could be carried on to try gaining a deeper understanding of the bolometers' behavior and of the role of the $T_0$.

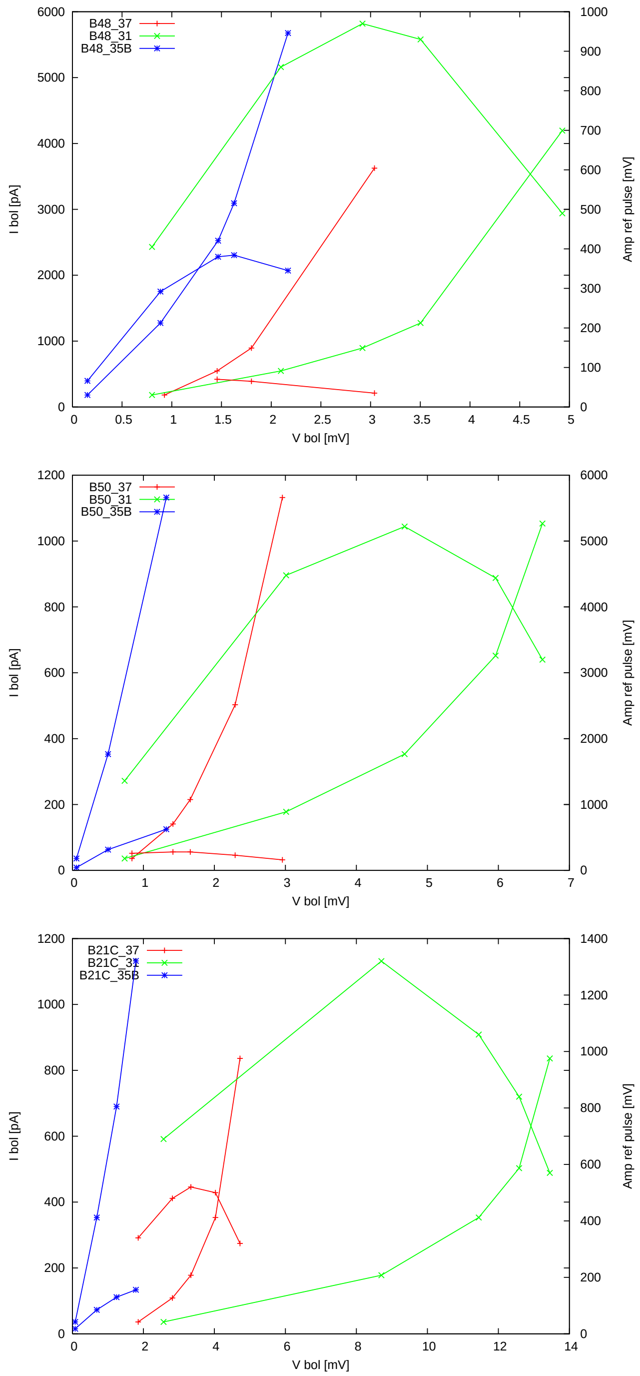


**Figure 5.7** - For each load curve (left Y scale) the pulse amplitude acquired with a reference heater pulse is plotted (right Y scale). Plots are for the B48, B50 and B21 crystals (top to bottom).

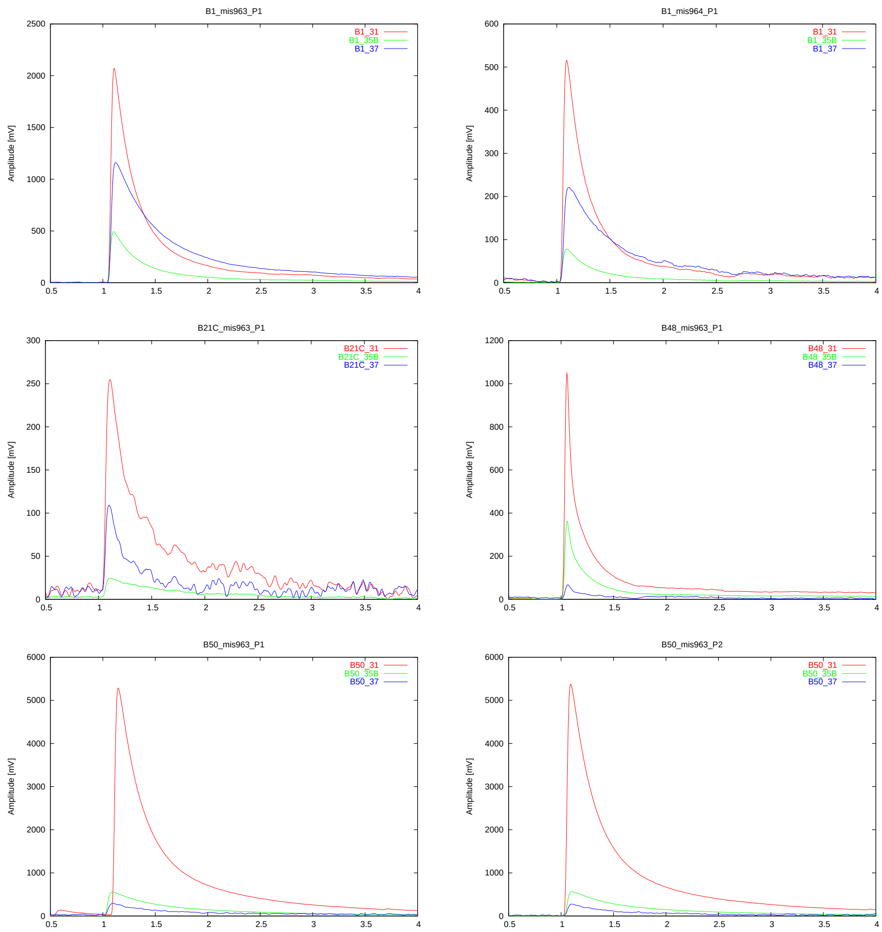


**Figure 5.8** - Comparison among acquired pulse for different detectors in the $T_0$ run

## 5.3 Reshaping thermistors

### 5.3.1 A possible solution to the thermistors wiring problem

In §3.8.3 we introduced the concept of "batching procedures" for building the CUORE detector. The size and the complexity of CUORE will definitely require an approach to the detector assembly focused on reproducibility, time and cost containment, standard well–defined procedures. We wrote there that one of the "weak" steps of the assembly process is the realization of the electrical connections between the thermistors and the wires.

In this section we will reshape the thermistors to allow for an easier procedure of thermistor wiring. Before going on, let us review the status of the art of the Cuoricino thermistors mounting and connection. It consists of few steps:

· Preparation and selection of the proper thermistor, which are available in different sizes, shapes (see later chapter 6) and parameters ($R_0$, $T_0$);

· Bonding: two gold wires (50 $\mu$m diameter) are ball–bonded on each gold pad of the thermistor; the other end of the wire is left free;

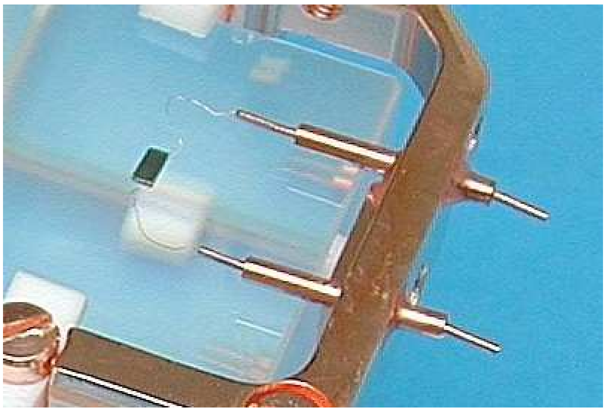

**Figure 5.9** - Picture of a thermistor glued on a $TeO_2$ crystal and connected to a couple of copper pins inserted in the frame. Gold wires of 50 $\mu$m dia are used. The pins are held in place by means of epoxy glue, which also ensures electrical isolation.

- Gluing: using ad–hoc tools [75] or properly prepared needle tips arrays, we placed a certain number of Araldit glue spots on the absorber crystal surface. We then placed the thermistor on the spots. Pieces of mylar are employed to assure 50 $\mu$m of spot highness.

- Placement: at this point the bolometers are usually ready to be inserted in their copper frame;

- Wiring: the gold wires are crimped inside a female copper pin, which is itself inserted into another bigger female copper pin; the latter is placed in the copper frame; the electrical isolation is obtained by means of Araldit® glue; see figure 5.9;

- Connection to cryostat wires: we usually prefer Costantan twisted pair of wires that are crimped on the other side of the female copper pins; these wires then reach the first thermalization stage on the mixing chamber (see figure 5.10).

This procedure is long and complicated. We list here only its major difficulties, which are all related to the handling of the 50$\mu$m gold wires:

- time consuming: many steps are required, and parallelization is not always possible;

- highly skilled manpower: handling a 50$\mu$m wire is a very difficult task; they are very fragile and they easily break; the bond itself is the most critical part, and should never be stressed, pulled or bend directly; from the operator's point of view, handling these wires turns out to be a complicated exercise of patience;

- errors and damages very difficult to fix: if one wire breaks apart, it is usually necessary to remove the thermistor and bond it again, or to glue a new thermistor (leaving the previous in place); it is almost impossible to bond thermistors already glued on a detector absorber.

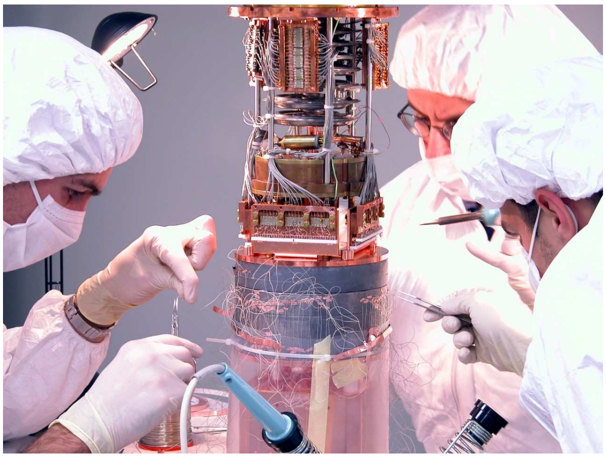

**Figure 5.10** - A moment of the final wiring of the Cuoricino detector already mounted below the cryostat. To reduce microphonic noise, the Constant wires are kept firm by small pieces of copper tape. The thermalizations at the MC and 100mK stages are also visible.

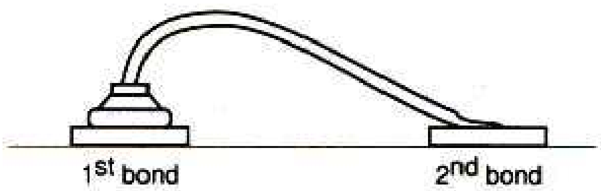


**Figure 5.11** - Scheme of the widely used ball (1st bond) and wedge bonding (2nd bond) technique.

CUORE will have about 1000 detectors. Each detector hosts a thermistor and a heater (heaters are electrically connected in the same way as thermistors). We believe that hand–made thermistors mounting is something definitely not worth doing. That is the reason why we came out with a different solution.

The new idea was born considering that the overall procedure would be greatly simplified if the thermistors could be bond after the gluing, and if the connection with the outside wires could be done with another bond instead of using pins. These ideas may become possible if we are able to bond the thermistors from the top (the gold pads are now on the two sides). The Au wires could be then connected directly to a proper pad on the Cu frame by means of a wedge–bond, as exemplified in fig. 5.11.

Unfortunately it is not possible to extend the Au pads on the top face of the thermistors, because of their production procedure. In fact, thermistors are cut with a tungsten saw from a single Ge wafer of 5 cm diameter and 3 mm thick. The wafer faces are gold–plated before cutting. The size of the thermistor may vary, but the contact distance is fixed at 3 mm. It is however possible to "notch" the thermistors by placing a series of shallow saw cuts in the flat surfaces of each NTD wafer, just before processing the contacts [95].

Thermistors of this type have been prepared by Jeff Beeman at Lawrence Berkeley National Laboratory. Pictures of some samples are reported in figure 5.12. Dimensions are reported in the scheme of 5.13

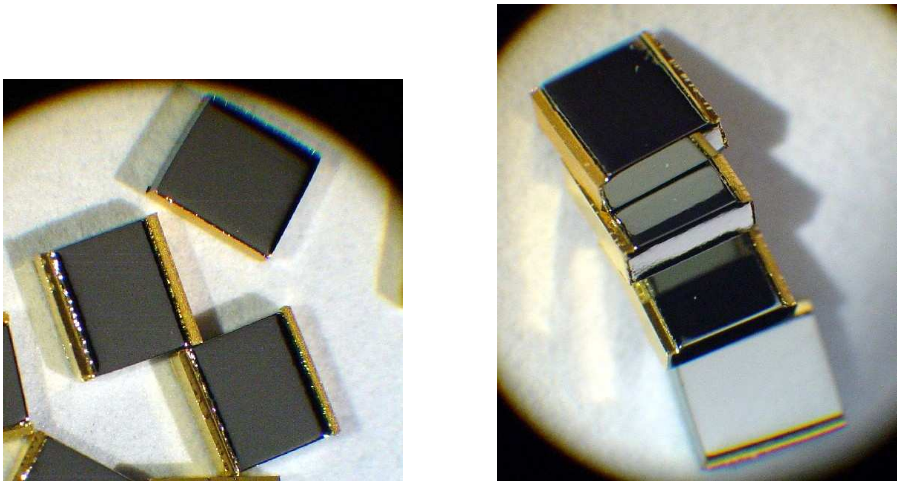

**Figure 5.12** - Pictures of few samples of the notched thermistors. Picture taken with a microscope.

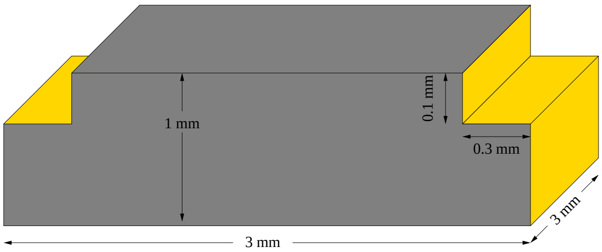


**Figure 5.13** - Not in scale drawing of a notched thermistor. This shape is obtained from the typical $3 \times 3 \times 1$ mm$^3$ thermistor by cutting the upper edges.

### 5.3.2 Shape effects on thermistors behavior

We compared the parameters of a typical Cuoricino NTD thermistor (type #31) with a new notched thermistor, assuming the same doping level (i.e. the same $T_0$). The results are given in table 5.2. As it is clear, the changes are negligible, but we are considering only the different volume and pad area of the new thermistors.

In fact, what is more important is that the different shape of this new device

| Parameter | | Cuoricino like | Notched | Ratio |
|---|---|---|---|---|
| Volume | [mm$^3$] | 9 | 8.94 | 0.99 |
| Pad Area | [mm$^2$ | 3 | 3.3 | 1.1 |
| $R_0$ | [$\Omega$] | 1.17 | 1.14 | 0.97 |
| $G_{\text{e-ph}}$ | [W/K] | 0.7 | 0.69 | 0.98 |
| $G_{\text{wires}}$ | [W/K] | $9.6 \times 10^{-5}$ | $1.06 \times 10^{-4}$ | 1.1 |
| $C_{\text{lattice}}$ | [J/K] | $2.7 \times 10^{-8}$ | $2.69 \times 10^{-8}$ | 0.996 |
| $C_{\text{elect}}$ | [J/K] | $9.9 \times 10^{-9}$ | $9.8 \times 10^{-9}$ | 0.99 |

**Table 5.2** - Comparison of thermistor parameters between usual Cuoricino like thermistors and new notched ones. The $T_0$ value is assumed to be the same in both cases.

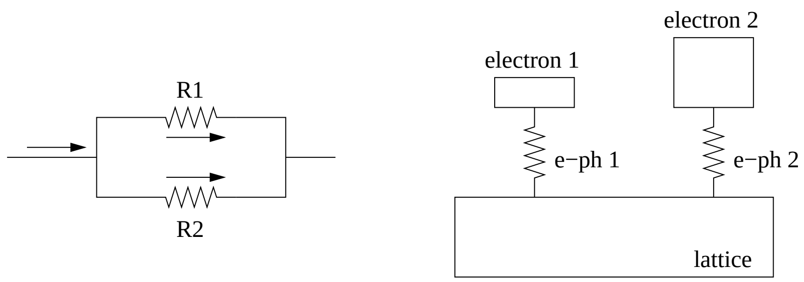


**Figure 5.14** - Electrical equivalent model for the notched thermistors (left) and thermal scheme (right) used for simulations

could also change its internal electric field when biased. Therefore this affects the current flow inside the thermistors, and thus the power density distribution. It is important to find out whether the behavior and performance of the thermistors remain unchanged in this new shape.

A better understanding of the problem emerges from an insight of the electro–thermal feedback effect, which we discussed in §3.2.2. An important role in this game is also played by the electron–phonon conductance introduced by the Hot Electron Model. In fact the electro–thermal feedback is responsible for the non–linearity of the load curve while the e–p conductance is linked to the maximum bias that can be reached before warming up the system. The two effects are clearly intercorrelated.

### 5.3.3 Modelization and simulation

Before the production and testing of this new thermistor, we investigated theoretically the possible effect of the new shape by means of a simple model.

As a first and raw approximation, we can electrically model our new thermistor as if was if made out of two parallel resistors, as in figure 5.14(left). As far as the thermal behavior is concerned, we remind the reader that thermistors are usually modeled with an electron capacity coupled to the lattice one via an electron–phonon conductances. This is done in agreement with the already mentioned Hot Electron Model. The electron–phonon decoupling is assumed to be a function of the thermistor's volume. We can thus think of our newly shaped thermistor as two smaller thermistors placed one over the other. The thermal model is depicted in fig. 5.14(right). The lattice is "shared" by two electrons components decoupled via two different electron–phonon conductances.

The simulation of the thermistor's behavior needs to mix together the electrical and the thermal model in order to compute properly the injected power and the temperatures of the different thermistor parts. At the beginning, we can assume that the lattice acts as a heat sink with infinite thermal capacity.

The simulation algorithm goes as follow:

1. inject a current $i$ in the resistors in parallel;

2. evaluate current and joule power in each resistor;

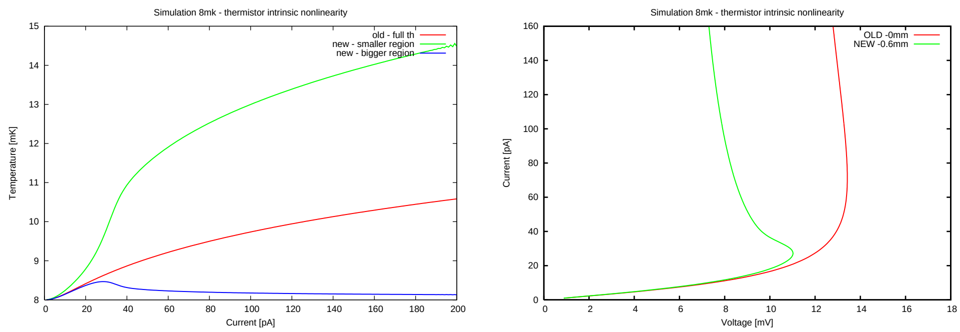


**Figure 5.15** - Simulation of the new notched thermistors behavior by means of temperatures of the two parts (lett) and by its IV curve (right).

3. calculate temperatures of both resistors; these temperatures are the electrons temperatures;
4. calculate the new values of the resistances;
5. calculate the voltage $v$ across the resistors parallel;
6. plot the $(i, v)$ point on the load curve;
7. iterate with a new current $i'$ until the whole load curve is covered.

We coded the algorithm described above into a simple C program. The parameters used are the dimensions of the thermistor's parts and the usual expressions (3.2) and (5.3) for the resistance and electron–phonon decoupling. The heat sink temperature is assumed to be 8 mK, $T_0 = 3.35$ and $\rho_0 = 1.17$ (typical of #31 thermistors).

The results of these simulations are shown in figure 5.15 and illustrate the intrinsic nonlinearity of the notched thermistors. In the left plot the thermal behavior of the system is investigated by looking at the temperatures of the two electron parts, as described in the model above. The current density in the two thermistors is determined by their resistivity. The more current flows in a part, the more it warms up. That means that the resistivity drops and the current fraction increases. The final effect is that the smaller part warms up a lot more than the larger part. The whole thermistor acts mainly as it was only made out of the smaller part. The plot on the right is the final (I,V) load curve of the new thermistor compared to the old one. The electro–thermal feedback is more enhanced for the notched thermistor, but still reasonable.

If we introduce a thermal conductance between the thermistor lattice and the heat sink, the situation becomes less critical, as shown in fig. 5.16. The load curves for the usual and the notched thermistors are similar.

### 5.3.4 Conclusions

- Notched thermistor are feasible with only little additional time for sawing. If they will be implemented in CUORE, the overall schedule of the experiment will thus not be affected;

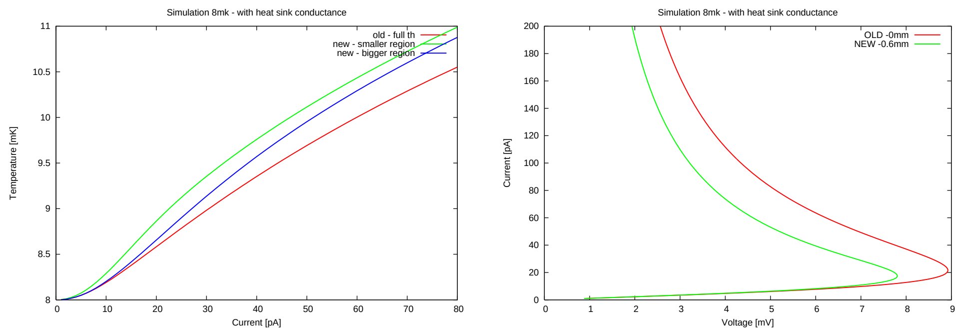


**Figure 5.16** - Simulation of the new notched thermistor's load curve compared to that of a usual thermistor, when a finite conductance is introduced between the thermistor lattice and the heat sink.

- it is possible to produce a much simpler, faster and reliable wiring; the male–female copper pins need to be replaced with proper pads, where a wedge bond could fit;
- the simulations showed that a small performance reduction is likely to be expected;
- given the possible presence of field effects and other not completely understood behaviors, experimental tests are strongly required and will be performed soon.

## 5.4 DERBY: DEvelopment of Reactive BolometrY

### 5.4.1 Considerations About Bolometer Noise and Energy Resolution

Here we want to stress again one of the most notable features of bolometer detectors: their energy resolution. We remind the reader that, with such devices, record energy resolutions have been achieved for X-rays and $\alpha$ particles (5eV @ 6keV and 7keV @ 2.5MeV respectively), while $\gamma$-rays were up to now detected with a resolution comparable to that obtained with the best Ge-diodes, but with much more efficient absorbing materials.

Ideally the energy resolution, in a first approximation, is limited only by the thermodynamic fluctuation of the thermal phonons exchanged with the heat sink through the sensor–to–bath thermal conductance and by the Johnson noise of the thermistor. Due to the electrothermal feedback, the thermistors could not be thought as pure resistors, at least when the thermal conductance to the bath is small (as in our case). However, we could easily estimate the value of the noise by neglecting the variation of the resistance during the pulse evolution. The resistance of a typical Cuoricino–like thermistor working at $\sim 12$

mK is $\sim 150\text{M}\Omega$ and thus the Johnson noise spectra could be evaluated[2] as

$$\sqrt{4kT \cdot R_{\text{therm}}} \simeq 10 \ \frac{\text{nV}}{\sqrt{\text{Hz}}} \tag{5.4}$$

Moreover, thermistors are dissipative devices, with an increase of temperature (a few mK/pW in Cuoricino–like bolometers) caused by the bias current.

During this PhD work, we investigated the possibility of using non dissipative sensors for bolometers readout. Capacitive sensors are good candidates and will be studied here. The use of this type of sensors aims at achieving a better signal–to–noise ratio thanks to:

- the elimination of the intrinsic Johnson noise;
- the increase of the signal amplitude, thanks to the reduction of the working temperature, due to elimination of the bias power.

In principle, capacitive bolometers could also give better resolution and threshold. These latter qualities could be advantageous for detectors used in dark matter searches.

### 5.4.2 Capacitive Sensor: material selection

The first step toward the realization of capacitive sensors is to find out materials with an adequate temperature dependence of the relative dielectric constant $\varepsilon_r$, even at the very low bolometer working temperatures. This property can be found among amorphous solids, in particular glasses. For these materials, there is a general agreement [97–99] that their behavior is due only to the quantum tunneling between two potential minima. This "two level model", in the case of a material like the pure amorphous $SiO_2$, leads to a characteristic temperature $T_0$ for which the dielectric constant $\varepsilon_r(T)$ shows a minimum. Around this minimum:

$$\varepsilon_r(T) = \begin{cases} \ln(T/T_0) & T > T_0 \\ \ln(T_0/T) & T < T_0 \end{cases} \tag{5.5}$$

Moreover, $T_0 \propto f^{\frac{1}{3}}$, where $f$ is the frequency of the field used to measure $\varepsilon_r$. For the same material, an almost linear dependence of the specific heat [100] on T is found at very low temperatures ($T \ll 1\text{K}$).

We must note that the behaviour in DC (static field) condition is still subject of debate as it could be possible that the previous expression could not be valid anymore and $\varepsilon_r$ could became constant. Moreover, very few measurements of glasses exist in the mK temperature region, either in AC or DC excitation.

It is worth reminding that the physical characteristics of the amorphous systems are extremely sensitive to the chemical composition: small concentrations of heavy metal oxides ($BaO$, $Pb_2O_5$, ...) or ionizing metals ($Na_2O$, $B_2O$, ...) usually present in commercial glasses, strongly influence the thermal behavior of the materials and, overall, of the dielectric constant [101, 102]. Unfortunately, there is not a fully developed theory able to explain the properties of

[2]Due to the electrothermal feedback, the Johnson noise is in fact smaller (see [96]

such vitreous multicomponent glasses. On the other hand, these glasses seem very promising for the realization of bolometers, due to their thermomechanical properties.

### 5.4.3 Capacitive Sensor: read–out

As a second step, let us focus on the read–out of capacitive sensors. In a conventional readout, the capacitor $C$ is biased by a DC voltage $V_b$ through a load resistor $R$: a voltage change $V_c$ represents the electrical signal.

Since in this case the excitation frequency is zero ($T_0 = 0$), $C(T)$ can be represented by:

$$C(T) = a \cdot \ln T + b \tag{5.6}$$

where $a$ fixes the sensitivity of the method and may be obtained from graphs reported in the literature for glasses. Observed sensitivities correspond to values of $K = 1/C \cdot (dC/dT)$ of about $5 \times 10^{-2} K^{-1}$ at the temperatures close to those of interest.

The maximum signal $\Delta V_c$ for a $\Delta T/T$ fractional temperature change is given by:

$$\Delta V_c = V_b \cdot A_c \cdot \frac{\Delta T}{T} \quad \text{with} \quad A_c = \frac{d \log C}{d \log T} = K_c \cdot T \tag{5.7}$$

to be compared with the corresponding expression for resistors:

$$\Delta V_R = V_b \cdot A_R \cdot \frac{\Delta T}{T} \quad \text{with} \quad A_R = \frac{d \log R}{d \log T} = K_R \cdot T \tag{5.8}$$

In the case of massive resistive bolometers, such as in the CUORE case, $A_R \approx 8$, $V_b \approx$ 5mV and $V_b \cdot A_R \approx$ 4x10$^{-2}$ V; in the capacitive case $K \approx 0.05$, and $A_c \approx$ 5x10$^{-4}$ at 10 mK. However $V_b$ could be in principle as high as 100 V if the dielectric strength of the material is sufficiently high. With $V_b$=20 V, a quite low value, a 50 $\mu$V/Mev signal is expected from a capacitive sensor in a Cuoricino–like bolometer, to be compared with 200 $\mu$V/Mev from a resistive sensor. This reduction in the signal may be, however, largely compensated by lower contributions to the noise.

Detailed calculations of the S/N ratio for a capacitive bolometer in a CUORE–like detector show that an energy resolution $\sim 5$ times better than the present one ( $\approx$ 1 keV rms) can be achieved.

### 5.4.4 First experimental measurements

As a beginning approach, we characterized several types of commercial Surface Mount Devices (SMD) in a dilution refrigerator. As an example, we report the results on two Ceramic Y5V SMD capacitors B1 and B2 whose properties, at room temperature, are: (B1) 25V DC, 0.1$\mu$F, 1.6×0.8×0.8 mm$^3$ and (B2) 50V DC, 47 nF, 1.6×0.8×0.8 mm$^3$. Measurements were carried out at 1 kHz by means of an Andeen-Hagerling capacitance bridge (AC excitation). In figure 5.17(a) we report the measurement of the capacitance of these two capacitors for different temperatures. The behavior is compatible with the expected one.

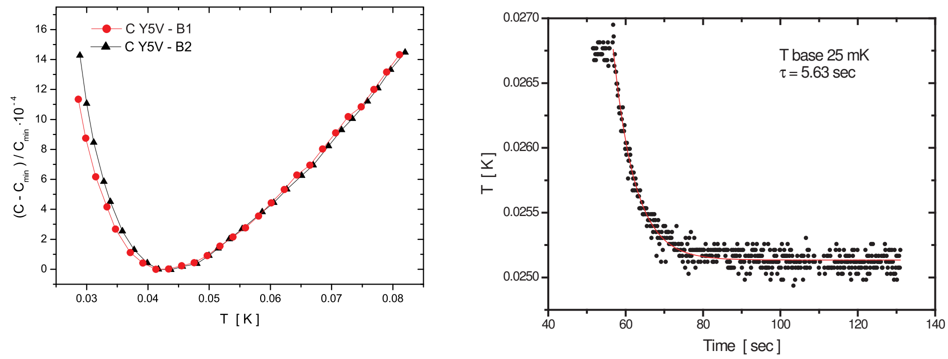


**Figure 5.17** - (left) Experimental measure of C(T) for capacitors B1 and B2. (right) Example of thermal discharge at 25 mK

We subsequently measured the relaxation time constant for capacitor B2, which was mounted on top of an NTD Ge thermistor used as a fast heater (with a time constant of about $2 \cdot 10^{-4}$ s at 25 mK). The capacitor acted as a thermometer. The thermal response time of the system was measured by injecting a constant Joule power through the NTD thermistor and by suddenly releasing this power. The relaxation time constant was $\sim 5$ s. Fig 5.17(b) show an example of thermal discharge. The reason of this slowness is probably due to the intrinsic response time of the capacitive sensor (e.g. the time required by the dielectric constant to change as a consequence of an instantaneous temperature variation).

Part of this behavior could also be attributed to the spurious material (contacts, substrate) inevitably present in commercial capacitors. To get rid of this problem, we designed, in collaboration with the ITC-irst [72], integrated capacitors developed with microelectronic technology. They have been designed to have a large capacity (in order to minimize the effects of any possible parasitic capacities) and with a very high dielectric strength ($\sim 10^8$ W/m) to allow the application of high static voltages. In figure 5.18 a model of such a capacitor is shown, along with a picture of the final device. The dielectric material used is an amorphous $SiO_2$ layer, deposited on a silicon substrate. Samples have been produced with different geometry (dielectric thickness and surface area) and with different $SiO_2$ doping level (none, 1% and 8% of B atoms). Dopants were introduced to test their effect on the temperature dependence of the dielectric constant.

These integrated capacitors have been characterized statically in probe station at room temperature. The range of capacitance was $1 - 50$ nF and scaled with the thickness and area as expected. Figure 5.19 shows the C(T) curve for one of these capacitors (with a geometry of $2 \times 2$ mm$^2$ and $0.1\mu$m thick) measured under AC excitation ($f = 1$ kHz). The behavior is in agreement with the theory of glasses and is similar to that measured on amorphous silica prepared with different techniques. No difference has been observed between pure and B-doped capacitors. The same figure reports also the capacitor loss, which we would like to avoid in order to have no dissipation. For this reason, the goal is

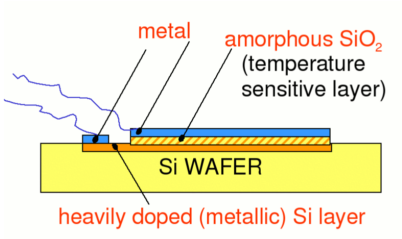


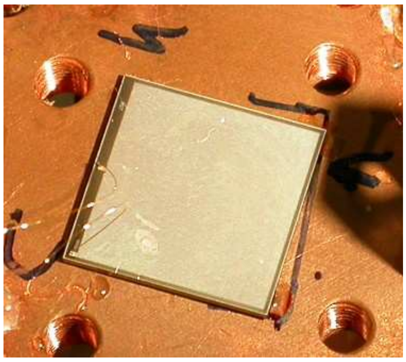

**Figure 5.18** - Scheme of the integrated capacitors developed by ITC-irst (left) and picture of a 2×2 mm$^2$ sample mounted on a copper support

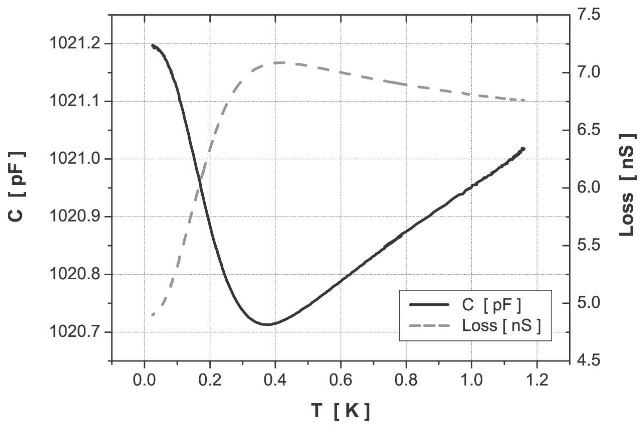


**Figure 5.19** - Capacitance and loss of an integrated $SiO_2$ capacitor as a function of temperature. The minimum of capacitance is at $T_0 = 0.378$ K, measured with $V_{\mathrm{rms}} = 0.25$ V at 1kHz.

to excite the sensor in DC condition.

### 5.4.5 Dynamical tests on ITC–IRST devices

We prepared a first set–up for dynamic tests in late 2004. We wanted to evaluate the sensitivity of these sensors to fast temperature variations. We coupled two capacitive sensors ($10 \times 10$ mm$^2$ surface) with a heat sink by means of 4 small spots of an epoxy glue. On the back side (i.e. on the Si crystal substrate) of each of these devices we glued a heater and a Ge NTD thermistor (see picture 5.20). In this way we are able to inject power/energy on the system through the heater, to monitor the temperature with the calibrated thermistor and hopefully to read–out capacity variations. We should then be able to relate temperature and capacitance of the device.

The same setup described above was used for dynamical tests both in Florence and in Como. Measurements in Florence were performed under AC excitation while in Como we tested DC couplings. In Florence the setup was cooled down at about 30 mK and measured with a capacitance bridge with a sampling rate of 17 Hz. With this poor time resolution, it is possible to observe fast

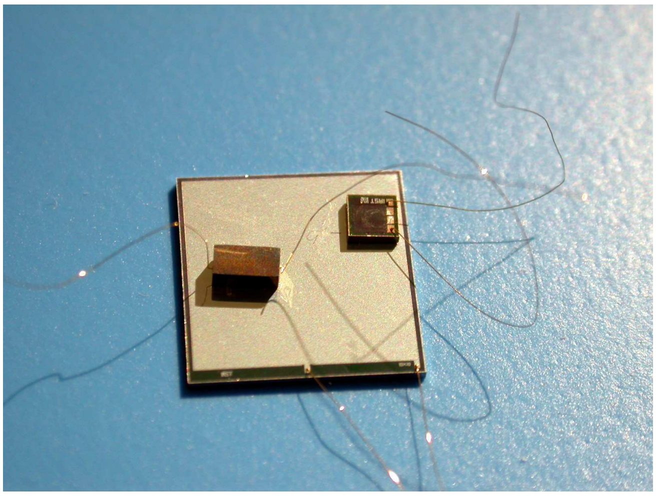

**Figure 5.20** - A sample of ITC–IRST capacitor with a Ge thermistor and a heater glued on it.

capacitive pulses, of the order of $\Delta C/\Delta T \sim 1$ pF/mK. These devices are able to stand a bias as large as 100 V and we did not dare to test greater bias. On the other hand, in Como, the system was cooled at about 13 mK. The static excitation (up to 25 V) was provided trough a couple of load resistors and the voltage drop across the capacitor was read by a low noise amplifier, similar to that used for thermistors. This test gave unfortunately negative results and we were not able to observe any signal from the capacitor. We must underline that a better electronic circuit for biasing and read–out is probably needed. Moreover, theoretical models of the behavior of DC coupled amorphous material at such low temperatures are still controversial.

Given the results of these tests, we prepared in June 2005 a new set–up which is pictured in fig. 5.21. We prepared two ITC-IRST capacitors (10×10 surface area and 4nF capacitance).

The first capacitor is glued directly on a copper plate. An NTD Ge thermistor is glued on the capacitor itself. One side of the capacitor was exposed to a radioactive $\alpha$ source (see §7.5.3) to embed $\alpha$ particles in the Si substrate. We believe that the phonons produced in the device by a particle could have a different spectrum from those released by a heater (as in the previous tests). In the following, we will refer to this setup as *detector A*.

The second capacitor is instead glued on a small $TeO_2$ absorber. A NTD Ge thermistor of the same kind of the previous one is glued onto another face of the absorber. We will call this bolometer *detector B*. We do not need any $\alpha$ source here, because the cosmic rays interactions produce many clear events.

Both detectors were kept in a copper frame, which was mounted and cooled down in Florence in a dilution refrigerator similar to that described in §4.3.1.

During the cooldown, we monitored the capacitors with the capacitance bridge ($f$ = 1 kHz). A plot of $C(T)$ is given in figure 5.22. Final detectors temperature was about 25-30 mK.

We measured both detectors in different configurations, both under DC and AC excitation. Let us start looking at the DC measurements of detector B. We

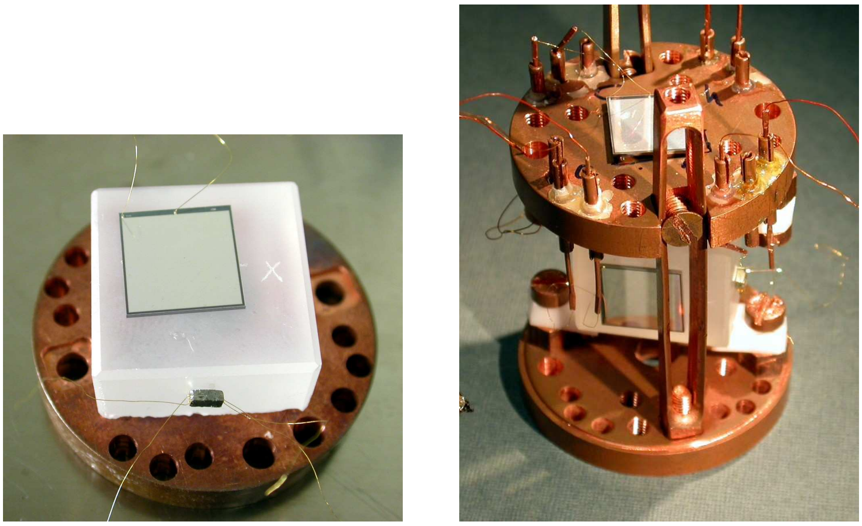

**Figure 5.21** - Pictures of the setup cooled down in the last DERBY measurement in Florence. (left) $TeO_2$ absorber with the capacitive sensor on the top and the thermistor on the side. (right) The same bolometer inside its copper frame and with the other standalone capacitor on the top plate.

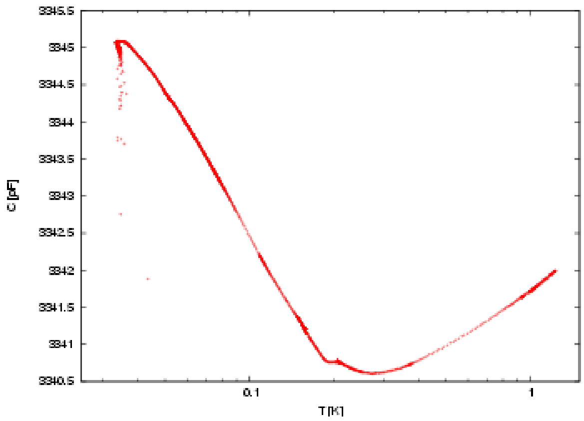


**Figure 5.22** - Experimental measurement of the capacitance of detector A during the cool–down. The minimum of the curve is at 280 mK.

performed 3 measurements with different bias on the capacitor. The thermistor is read with the usual Cuoricino–like electronics. Unfortunately, no coincidence signal is seen between the thermistor and the capacitor. When the bias across the capacitor is high ($\sim$ 10V), cross–talk signals appear on the capacitor channel. If we unbias the thermistor while keeping the capacitor biased, no signal is seen any more, thus confirming the hypothesis of a cross–talk. Nothing is observed on the capacitor when we switch to AC excitation. The same measurements were performed at higher temperature, but with negative results.

Concerning detector A, the situation during DC measurement is similar to that observed for detector B. The cross–talk here was even worse, and it was present even if the capacitor bias was null. On the other hand, AC measurement looked encouraging. We monitored the capacitor with the capacitance bridge

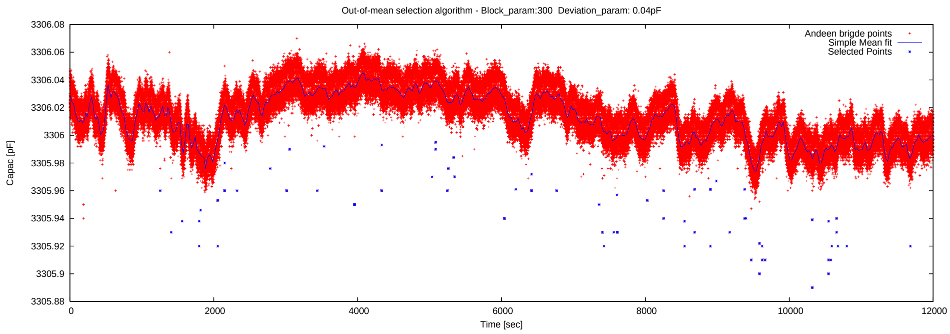


**Figure 5.23** - Time chart of measured capacity for detector A for a period of over 3 hours. Time sampling interval of the capacitance bridge used for this measurement is 70 ms. Blue dots are possible selected events (see text).

while looking for $\alpha$ particles on the thermistor channel. Figure 5.23 shows the analysis on the acquired data. One can notice a band of noise and many measurements which are well below this band (blue dots). Since we are in the $T \simeq 30$ mK $< T_0$ regime, these lower values of $C(T)$ could correspond to temperature raises. To see if they arise from radioactive events from the implanted $\alpha$ source, we can estimate the temperature increment $\Delta T_C$ corresponding to a typical decrease of $\Delta C \simeq 0.1$ pF below the noise band, and see if it is compatible with the value $\Delta T_R \simeq 2.7$ mK typically observed with the coupled thermistor. From figure 5.22 at 30 mK we see that $\Delta T_C \simeq 4.6$ mK and this is entirely compatible with $\Delta T_R$. Furthermore, we remark that the average interval between two radioactive emission rates was $\sim 47$ s, and that the capacitance deviations observed in figure 5.23 were concomitant with $\alpha$ signals in the thermistor within 2 s. This gives us a good evidence that radioactive events can be monitored with capacitive glass–based sensors. However, to be honest, from our measurements we cannot completely rule out the possibility of cross–talks.

### 5.4.6 Conclusions

In spite of the partially positive results achieved under AC excitation, we did not pursue this project further, as a consequence of the lack of capacitive signals under static DC condition. Moreover, there are theoretical indications that the dielectric constant falls into a saturated flat regime in static condition.

The AC measurements were not improved mainly because of the unavoidable loss that appears in this condition, and nullify one of the main motivations for this project. A possible development of this activity could follow from noticing that dissipation can in principle be avoided not only in static condition, but also when the frequency of the applied field is very high (ideally at infinity).

# · Chapter 6 ·

# Bolometer couplings optimization

## 6.1 Introduction and motivations

In every devices, high performances can be achieved only by the perfect tuning and optimization of all its elements. This is true for a racing car but also for a bolometer.

In the previous chapter, we dealt with different solutions that could be implemented to increase the performances and the usability of the bolometers by acting on the thermal sensor. In this chapter, we will carry on that investigation by trying to optimize the couplings among each element of our bolometers.

Part of the irreproducibility of our bolometers comes from the spread of the detectors parameters, especially the thermal couplings among the different parts of the detectors. Two of them are particularly critical for what regards the signal amplitude and shape: **the absorber to heat sink coupling** (its value is related to the thermal discharge of the detector) and **the sensor to absorber coupling**.

The reproducibility is not the only important aspects of bolometers couplings. As a first step, we should define what is the best value for that particular coupling. The goal is to get the highest signal-to-noise ratio. Usually a first investigation is carried on using the bolometers simulation software. Prototypes are then realized, tested and compared to Cuoricino detectors.

The coupling elements act as thermal connection but, at the same time, they can play a mechanical role that cannot be neglected. Moreover, when different materials are to be coupled, the problem of differential thermal contractions might arise.

The optimization is therefore not limited only to obtain and realize the best thermal conductivity or to improve detector performances. It should consider all the aspects of the problem and find the best trade-off between all the variables.

## 6.2 Absorber to heat sink coupling

### 6.2.1 Present status

In Cuoricino, the connection between the copper structure and the $TeO_2$ absorber crystals is done with small Teflon (PTFE) pieces.

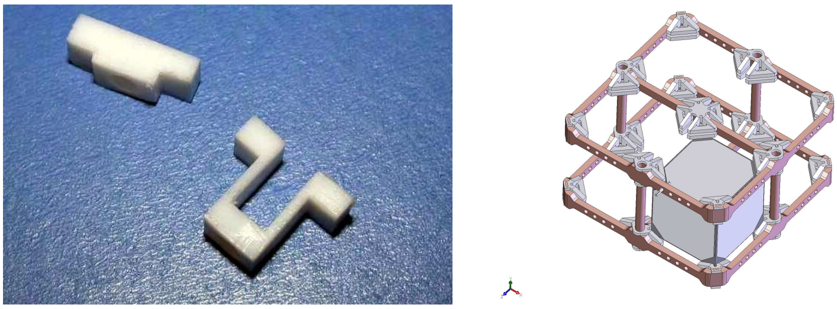

**Figure 6.1** - Pictures of Teflon pieces used in Cuoricino bolometers (left) and the new structure that will be used in CUORE (right). The new Teflon pieces are designed for better tolerance to stresses and thermal cycles and to reduce vibrations while simplifying the assembly procedure. The thermal coupling is the same as in Cuoricino because the contact area between the Teflon and the $TeO_2$ is almost unchanged.

Infact good bolometer performances are achieved only if this coupling satisfies several conditions:

- good mechanical coupling of the crystal that must stay firm in position and avoid vibrations that could warm it up;
- weak thermal link to the heat sink; initially the heat must generated by particles interactions must flow into the thermistors and only later it can flow away toward the heat sink; simultaneously this thermal link must not be too weak otherwise the signal decay time will be too long and it can be very difficult to cool down the detectors;
- ability to compensate different thermal contraction;
- high radiopurity.

During the last few years, the shape of the Teflon pieces was changed several times to simplify the mounting procedure, reduce the dimensions and the stresses induced on the crystal (see fig. 6.1).

### 6.2.2 Different concepts

While the CUORE baseline will have the Teflon pieces shown in fig.6.1(right), we pursued a more radical approach. Our goal is to find a new way of holding the crystal in a copper frame which is even simpler, eventually getting rid of Teflon itself.

From a thermal point of view, the conductance of the Teflon pieces is not very well defined because it depends on the effective contact area between the Teflon and Copper and between Teflon and $TeO_2$ . The contact area itself depends on the pressure which cannot presently be carefully controlled. Other reasons for removing the Teflon clamps are related to possible radioactive contamination of the Teflon itself and to the fact that it release energy in the absorber due to crack or stresses at low temperature.

Several ideas were tested but unfortunately none of them was deeply pursued (mainly due to lack of time) or provide outstanding results:

· direct contact of the $TeO_2$ crystal on copper; this solution could work only for big–size crystals were the gravity help keeping them in place;

· direct gluing of the crystal on the copper frame;

· glue Ge stand–offs as intermediate layer between the crystal and the copper to compensate the thermal contractions;

· special copper pedestal able to bend to compensate thermal contractions.

As a matter of fact, there are neither urgent motivation for removing Teflon pieces from the present setup, nor any clear indication that they degrade the bolometers performances. Therefore we concentrate our efforts on other topics.

## 6.3 Absorber to sensor coupling

### 6.3.1 Present status

As of today, Cuoricino NTD Ge thermistors are coupled to the $TeO_2$ absorbers with 9 glue spots of Araldit. In a previous work [18], we used the simulations described in 1.3 to find the optimal number of glue spots. As it could be easily understood, better results are achieved by increasing the number of spots, i.e. increasing the thermal coupling. As a matter of fact, the electron–phonon conductance in the thermistor play a limiting role that can not be avoided. Therefore, after a certain point, an increase in the number of spots will not lead to any advantages.

However, other aspects should be taken into account. First, the gluing procedure is not as easy as it could seem, especially if you consider the fact that 9 glue spots should be placed close together in a $3\times3$ mm$^3$ area. Then, differential thermal contractions between Ge and $TeO_2$ are also a critical problem. Finally, also the reproducibility of the coupling is an important parameter.

In the following, we will report the test performed on thermistors where the shape has been slightly changed to improve the coupling technique. We also report about the attempts of replacing the glue with vacuum grease.

### 6.3.2 Table–legs thermistors

The idea of interposing a small Ge stand–off between the thermistor and the $TeO_2$ crystal dates back to the R&D of Cuoricino. Unfortunately, thermistors attached with that method had quite poor performances, probably because the connection is made by three layers of materials. To overcome this problem, the idea of "table–legs" thermistor was developed. The thermistors were micro–machined in such a way that four $1 \times 1 \times 0.5$ mm$^3$ stand–off are present at each thermistor corner (hence the name "table–legs" - see fig. 6.2(left)). The performances of these new sensors were better but not as those achieved by gluing and for this reason they were discarded for Cuoricino.

Recently, we decided to try to test them again because of their really simple coupling procedure. Table–legs thermistors are infact attached with only a thin veil of Araldit below each leg.

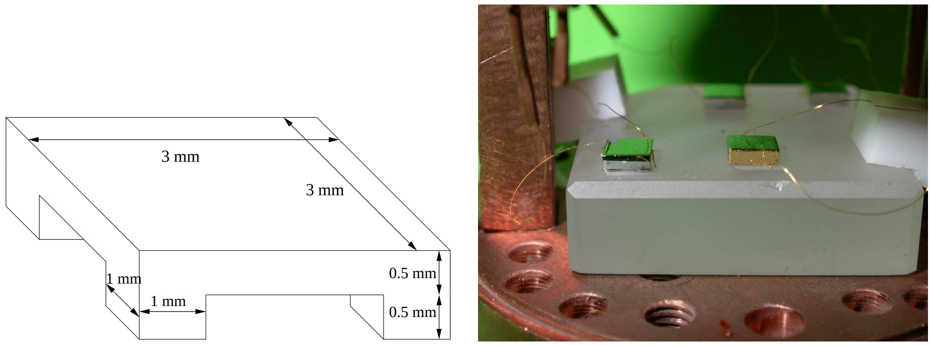


**Figure 6.2** - (left) Model of a table–leg thermistor. (right) $TeO_2$ bolometer with thermistors of different kind for comparison. The thermistor on the left is a “table–legs“ thermistor while the one on the right has a classical parallelepiped shape.

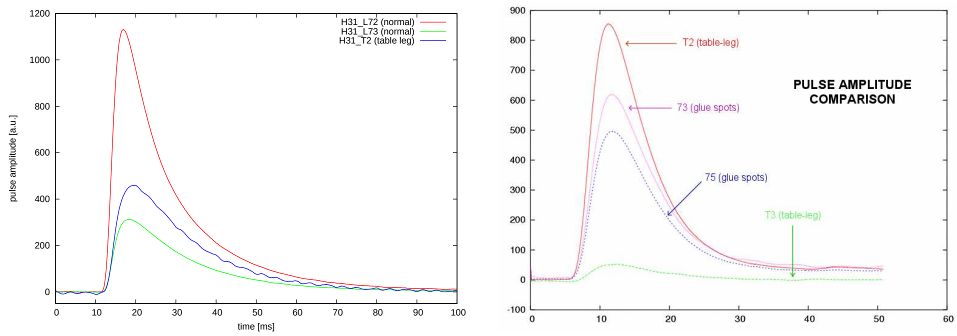


**Figure 6.3** - Pulse comparison of thermistors signal for the same event for run 3 (left) and run 7 (right).

As a starting point, we performed several tests at $LN_2$ temperature to check the effect of the thermal contractions either on the hard (perpendicular to $< 001 >$ axis) and soft (parallel to $< 001 >$ axis) faces of the crystal. We found that the stresses induced by the contraction on the legs are not well compensated and are often causes of breakage either of the $TeO_2$ crystal or of the leg itself, especially when the gluing is performed on the soft face.

After that, two bolometric run were performed.

In run 3, we cooled, in the TBT cryostat, a small $TeO_2$ absorber with 4 thermistors glued on it, two of each kind, normal and table–leg, as in fig. 6.2(right). Due to the stresses induced by the glue and the fact that the $TeO_2$ absorber was glued directly on the copper frame by means of Ge-stand–off, the crystal broke apart and thus coincident pulse comparison can be performed only on the 3 thermistors that shared the same absorber piece. Unfortunately, no definite answer can be extracted from this data. Infact, as it is shown in the pulse comparison of fig. 6.3 (left), the amplitudes of the three thermistors for the same signal are spread and do not scale with type. Moreover, the microphonic noise on both table–leg thermistors is more evident than in the others.

The working point for both sensor was set with this parameter: $V_{bol} = 2.1$ mV; $R_{bol} = 83.8$ M$\Omega$; $T_{bol} = 20.6$ K.

We performed a second run (run 7) in the hope of reaching a conclusive

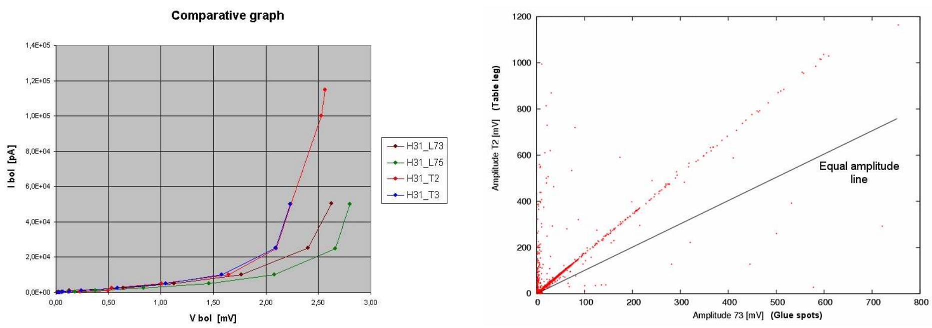


**Figure 6.4** - (left) Load curve for the two table–leg thermistors (T2 and T3) and the two normal Cuoricino–like thermistors (L73 and L75) obtained in run 7. (right) Scatter plot of amplitudes. For each event, the amplitudes of two different sensors are plotted.

statement on the subject. Again, we attached 4 thermistors on a $2 \times 2 \times 0.5$ cm$^3$ $TeO_2$ absorber. Two thermistors (T2 and T3) are of the table–leg type while the others are normal thermistors.

The table–leg type thermistors exhibit a very similar static behavior, as you can see from the comparative graph of all sensors' load curves in fig. 6.4. Notice how load curves of the two table-leg NTDs, T2 and T3, superimpose. We deduce from this experimental fact that this kind of sensor–to–absorber coupling looks very reproducible.

Things are quite different when the dynamic behavior is considered. A pulse amplitude comparison (see fig. 6.3 (right)) shows that we probably had a problem with the T3 table-leg thermistor. Anyway, the other one (T2) worked well and suggests that table-leg NTDs might have the potential to give good results, comparable to usual sensors, as shown also in the scatter plot of fig. 6.4(right). However, we cannot tell if the malfunctioning thermistor was just an unlucky case.

No clear indication can be deduced from the results of these two runs. The experiments showed however that the table–leg configuration stresses significantly both the $TeO_2$ crystals and the Ge itself and this can be the reason of the scattered results obtained with these sensors.

### 6.3.3 Pedestal thermistors

A similar approach to table–leg thermistors is provided by another thermistor shape. A number of NTD thermistors of the # 34 series were cut in such a way that a small pedestal appear on their base, as in fig. 6.5. The thermistors size is $3 \times 1 \times 0.6$ mm$^3$ and the pedestal is $1 \times 1 \times 0.6$ mm$^3$. The therm al and mechanical connection is again obtained with a thin veil of Araldit glue on the pedestal.

We used these thermistors in several experiments that will be reported later (see for example §7.6.8, §7.6.9 where these thermistors are used on slab–bolometers) and they always gave good results, in terms of pulse shape and amplitude and thermal contractions.

**Figure 6.5** - Picture of a thermistor with pedestal.

| **Measurement 51** | | | | Duration: ∼17 h |
|---|---|---|---|---|
| Thermistor | Bessel [Hz] | Vbol [mV] | Rbol [MΩ] | Tbol [mK] |
| H34b_W-R11 (glue) | 120 | 2.87 | 0.3 | 27.1 |
| H34b_W-7 (grease) | 120 | 2.64 | 0.3 | 27.5 |

**Table 6.1** - Bessel cut frequency and working points of detectors of measurements 51

### 6.3.4 Glue vs vacuum grease

Finally, we tested the possibility of substitute the Araldit epoxy glue with vacuum grease for attaching the thermistors to the $TeO_2$ absorber. The glue is not elastic enough at low temperatures and so we want to check if the vacuum grease is instead able to better compensate the thermal contractions.

**1st measurement**

A first test was performed in the TBT cryostat (see also later in §7.6.9) where a thin Si foil of $1.5 \times 1.5$ cm$^2$ area and 500 $\mu$m thick was used as absorber. Two pedestal thermistors of the series #34b were used as thermal sensors. The W-R11 thermistor was glued with a thin veil of Araldit while the other W7 thermistor was placed with a veil of Dow Corning® vacuum grease.

The parameters of the analyzed measurement are in tab. 6.1. The setup was quite "hot" due to bad thermal coupling of the absorber and so the thermistors resistances were lower than usual. The load curves are plotted in figure 6.6 and are very close to each other.

As the static behavior, also the dynamics of the two thermistors is similar. A scatter plot (fig. 6.7) of the amplitudes of the two thermistors show that the W-7 thermistor (grease) pulses are smaller by about 25%. A similar analysis can be performed on other pulses parameters (rise time and decay time) to check for shape modifications induced by the different coupling. We found that these parameters are the same within few %.

This first measurements tell us that no dramatical changes are expected from the use of vacuum grease to stick the thermistors. However, we learned also that mechanical problems could arise because the gold wires of the thermistors act

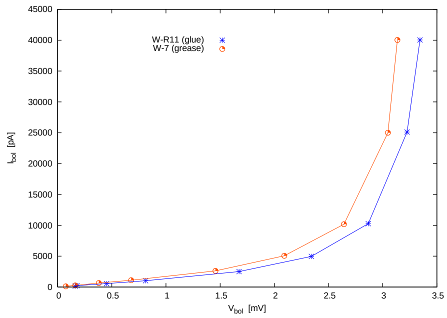


**Figure 6.6** - Load curves for the two thermistors attached to the Si absorber in different ways.

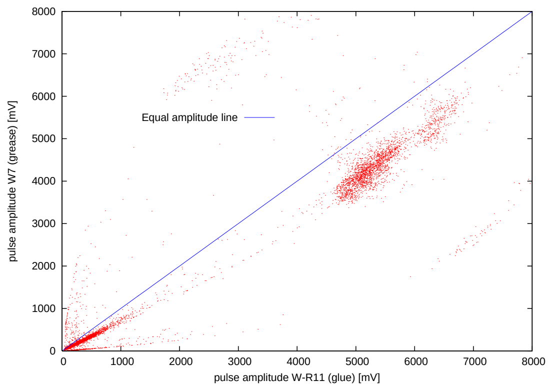


**Figure 6.7** - Scatter plot of the amplitudes of the two thermistors for the same event in measurement number 51.

sometimes in such a way to move the thermistor itself from its position. At room temperature, the vacuum grease is not sticky enough to keep the thermistors in place. This problem might be avoided by using 25 $\mu$m dia wires instead of the usual 50 $\mu$m ones.

### 2nd measurement

We performed a second measurement in the AL cryostat, this time using a bigger $2 \times 2 \times 0.5$ cm$^3$ $TeO_2$ crystal on which two pedestal thermistor were attached. Again, one was glued with a thin Araldit layer while the other was turned upside down and a thin vacuum grease layer was applied under its wider face (not under the pedestal). The detector is pictured in fig. 6.8.

This time the thermistors were cooler and their resistances one order of magnitude bigger (see tab. 6.2).

The measurement was performed as the first bolometric test of the AL cryostat. The collected data support the fact that the use of vacuum grease is not as good as gluing thermistors, as it can also be seen in fig. 6.9.

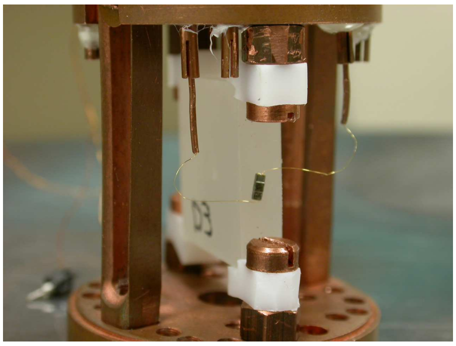


**Figure 6.8** - Picture of the detector mounted in the AL cryostat for thermistor coupling test. The reversed pedestal thermistor attached with vacuum grease is visible.

| **Measurement 56** | | | Duration: $\sim$ 17 h | |
|---|---|---|---|---|
| Thermistor | Bessel [Hz] | Vbol [mV] | Rbol [MΩ] | Tbol [mK] |
| H34b_W-5 (glue) | 12 | 3.83 | 3.0 | 18.11 |
| H34b_W-7 (grease) | 12 | 1.84 | 1.5 | 20.32 |

**Table 6.2** - Bessel cut frequency and working points of detectors of measurement number 56

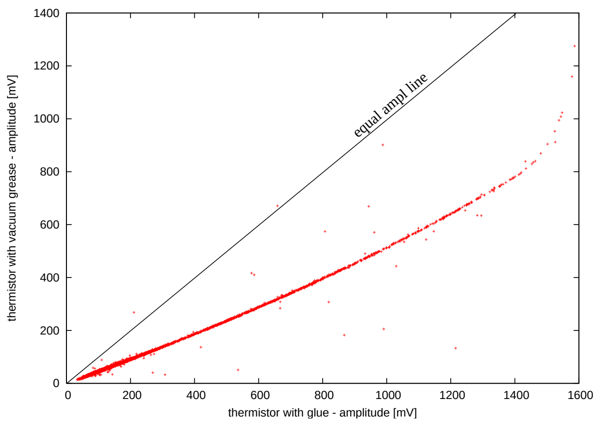


**Figure 6.9** - Scatter plot of the amplitudes of the two thermistors for the same event in measurement number 56.

# · Chapter 7 ·

# Surface Sensitive Bolometers for background rejection

This chapter will introduce a new technique developed during the last two years of this PhD work. It is a major step toward a new generation of bolometers with a partial ability to recognize event origin, thus overriding a common disadvantage of these devices.

## 7.1 Strategies for surface background reduction in CUORE

We have already discussed in §3.7.1 and §3.9.1 the different sources of the Cuoricino background and their implications on CUORE. In particular we pointed out that we are worried by the presence of surface contaminations. Indeed, degraded $\alpha$ and $\beta$ particles released from surfaces close to the detectors give rise to a continuum background, which extends down to the region of the expected $\beta\beta0\nu$ . We also showed that the background is the real obstacle to the CUORE sensitivity. CUORE aims at investigating the region of the inverted neutrino mass spectrum, and this goal could only be accomplished if its background level is of the order of at least 1/10 of the present Cuoricino values of about 0.18 c/keV/kg/y.

An intense and broad R&D program is ongoing, in order to achieve effective background reduction. Three different solutions are currently pursued simultaneously:

- Increasing the quality of the surface treatment. This means better cleaning procedures, as in the case of the RAD measurements described in 3.9.1.
- Reviewing the design geometry of the detectors mounting structure, in order to minimize the copper surface and to gain efficiency from anticoincidence between closer detectors. We prepared and tested a new holder, which improves this aspect without changing too much the overall configuration (i.e. the thermal and mechanical couplings are similar) (see §3.9.2 and [103]).
- Realizing "clever" bolometers, able to discriminate those events that come from sources different than the absorber bulk. This could be done only by providing bolometers with some sort of spatial recognition.

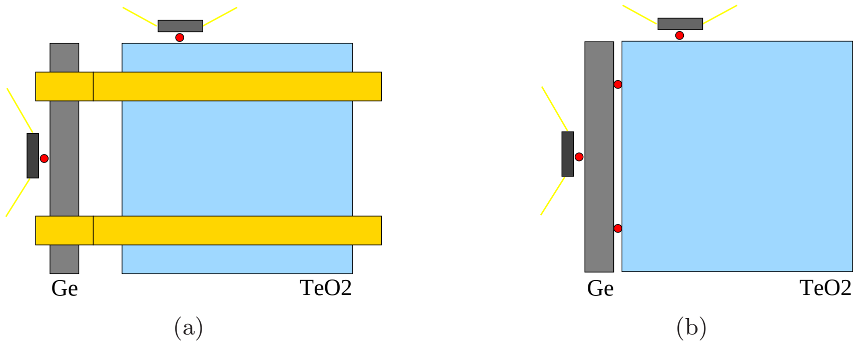


**Figure 7.1** - Model for a bolometer with only one active surface shield. In (a) an external structure holds the shield while in (b) the shield is glued directly on the $TeO_2$ crystal and form a single composite bolometer.

All these attempts are giving positive and interesting results, and it is really a pity that we cannot provide a deeper insight into all of them. In this chapter we will only focus our attention on the third topic, which constitutes the core of this Ph.D. work.

During the last two years, we developed an innovative kind of bolometers which we named *Surface Sensitive Bolometers* (SSB). In the following sections we will introduce their concepts, their behavior, their properties and the experimental results obtained both with small–scale prototypes and with Cuoricino–size detectors.

Parts of the activities and results presented here have been published in several works [18, 75, 104–107].

## 7.2 Working Principle

### The idea

At a first glance, the idea behind the possibility of rejecting external surface events might look rather common and simple. In fact we want to shield our bolometers with other bolometers with a very thin absorber, as illustrated in fig. 7.1(a). From now on, we will name these devices *slab–bolometers* (sometimes abbreviated as 'slabs'). They can be made with an absorber of the same area of the face of the cubic main bolometer, but very thin, with the thickness depending on the material. Six of these slab–bolometers can surround the main bolometer to achieve full coverage. In some sense, this could appear as a common veto–like discriminating system, where anticoincidence techniques are used to identify particles. This solution is however not easily feasible, at least without serious modification of the copper frame structure to hold the shielding bolometers.

Our solution to this problem is to glue the slab–bolometers directly on the absorber of the main bolometer. In this way however, a thermal coupling does exist between the bolometer to be shielded and the slab–bolometers. This new device is therefore a *composite detector* made out of the main absorber plus six slab–bolometers. Our innovation resides in the insight of the behavior of this composite bolometer, which we named *Surface Sensitive Bolometer* (SSB). As we will see soon, the thermal dynamic of a SSB can be exploited to achieve partial spatial resolution through the separation of bulk internal events from those coming from sources external to the main absorber. Therefore, we are able to partially overcome one of the major limitations of classical bolometers operated in the calorimetric mode, namely the lack of information on the events impact point.

**Expected behavior**

The behavior of a SSB is not straightforward, but it can be easily understood from simple considerations. Let us try to explain it from a simple model of a SSB with only one slab–bolometer on one face, as in fig. 7.1(b).

Oversimplifying, we can distinguish two major kinds of possible events: particles coming from external sources and events due to decays inside the main absorber. As an example, degraded $\alpha$ particles from the copper frame surfaces clearly belong to the first class, while $\beta\beta0\nu$ of $^{130}$Te belongs to the second (assuming the main absorber is a $TeO_2$ crystal).

In the first case (fig. 7.2(b)) a particle interacts in the slab–bolometer and releases there all or part of its energy; it could then interact also in the main bolometer. In any case, due to the interconnection of all the SSB parts, two simultaneous temperature signals will be recorded from the two sensors. If the heat capacity of the slab–bolometer absorber is small enough, the temperature read by its sensor will be much higher and faster than that measured by the sensor on the main bolometer.

On the other hand (fig. 7.2(a)) an internal decay is likely to be fully contained in the main absorber. This will lead again to two temperature pulses, which will be however very similar. This time, the small heat capacity of the sheet-bolometer absorber will in fact play a negligible role in the temperature measured by the two sensors.

It is thus clear that the pulse acquired from the two sensors will have a different shape (at least amplitude and rise time), depending on the place of the initial energy release. Pulse Shape Analysis (PSA) will then allow to identify events from different classes.

These considerations looks reasonable, but simulations and experimental tests are needed to confirm them.

In the following, we will speak of *slab pulse* (SP) when referring to the signal read–out by the thermistor on a slab. The *main pulse* (MP) will instead be the signal coming from the thermistor placed on the main absorber. We stress again the fact that for every event, all thermistors detect simultaneously a signal.

**Materials**

A question immediately arises about the material to be used as absorber for the slab–bolometers. Clearly it must satisfy all the requirements stated in §1.2.2, namely to be a dielectric and diamagnetic material. High radiopurity is also welcome, but not strictly required in principle. Given the particular sheet–like shape, mechanical requirements are needed in terms of strength and

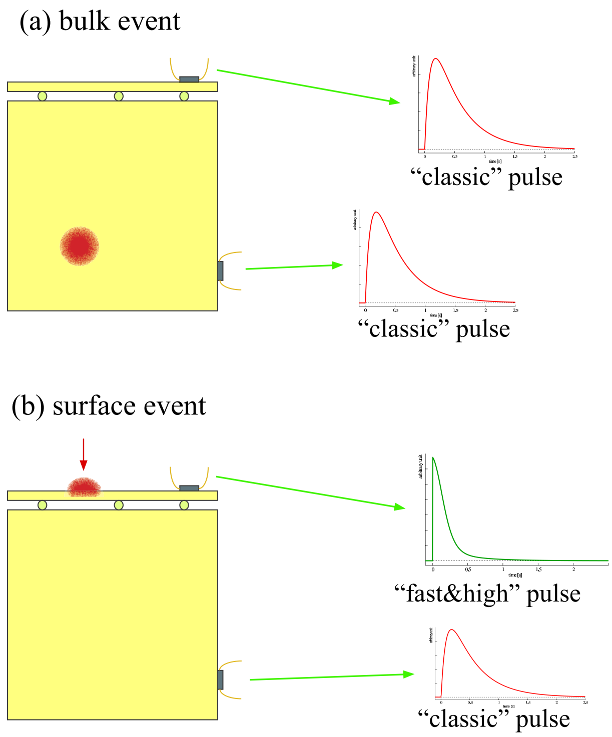


**Figure 7.2** - Working principle of a surface sensitive bolometer with a single slab–bolometer. (a) An event in the main absorber bulk gives rise to two classical and almost identical signals on the two sensors. (b) An external event produces an high and fast pulse on the sensor of the slab–bolometer while the other thermistor give a normal pulse. In both cases, the key parameter is the very small heat capacity of the slab–bolometer.

thermal contractions.

The tests that we will report in this work were designed specifically for the CUORE environment. This means that the main absorber is made of $TeO_2$ and NTD Ge thermistors were used as temperature sensors. Three different materials were tested for the slab–bolometer absorber: high purity Germanium, Silicon (from two different suppliers) and $TeO_2$ . We will come back on this subject later on.

## 7.3 Thermal model and simulations

### Thermal model generalization

As a first step, we simulate SSBs behavior from the knowledge and the properties of usual bolometers, which were already extensively discussed in this work.

The thermal model introduced in §1.3 has been worked out for a specific thermal network with only three nodes. That approach has been a fictitious simplification: in fact it is clear that such a model will perfectly work, after some generalizations, even for a system with any number of nodes. Moreover, the systems of equations (1.18) and (1.24) that describe the static and dynamic

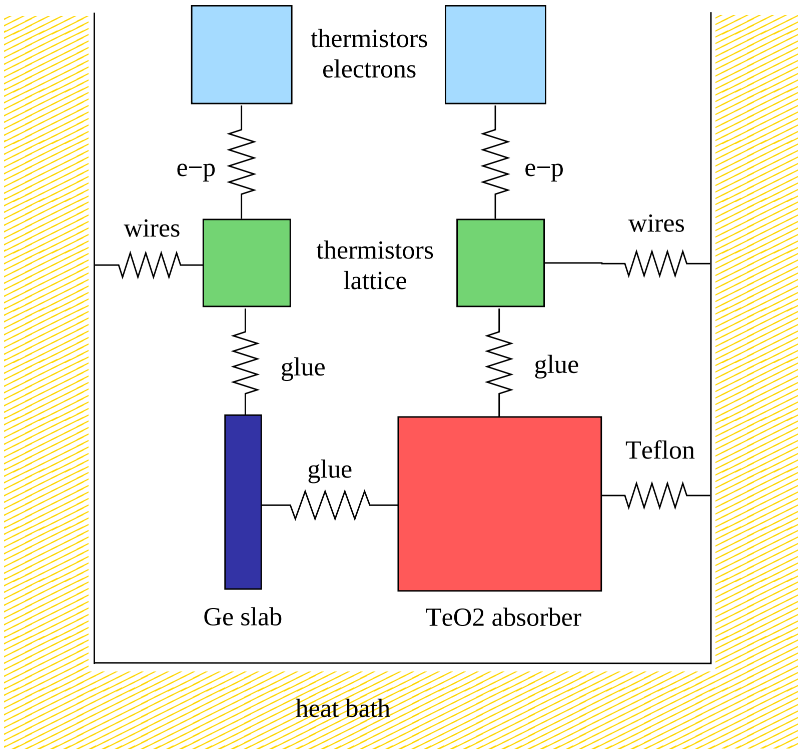


**Figure 7.3** - Thermal network used to simulate the behavior of SSBs.

behavior of the thermal network, have been deduced from very general considerations (e.g. the conservation of energy at each node), and so they could be easily extended for $n$ number of nodes.

The generalization is quite straightforward and consists mainly in a reformulation of the thermal network equations. For more details see [18].

### Thermal network and parameters

In order to reduce the calculation time and point out the main behavior, we started by simulating a SSB with a single slab–bolometer covering only one face of the main, as in fig. 7.1(b). We used a Cuoricino–like main bolometer made of $TeO_2$ with an NTD Ge thermistor (size: $3 \times 3 \times 1$ mm$^3$, series #31) glued on it with 9 glue spots. The slab–bolometer is instead a HPGe absorber of $50 \times 50 \times 0.3$ mm$^3$ coupled to the $TeO_2$ main absorber with only 3 glue spots. A smaller NTD Ge thermistor ($3 \times 1.5 \times 0.4$ mm$^3$, series #31) is glued on the HPGe absorber with 6 glue spots. The thermal network of such composite bolometer is shown in Fig. 7.3.

### Static and dynamic behavior

The load curves of each thermistor are similar to that of a common SSB. The optimal working points can be searched in the same way and the two thermistors appear to behave independently.

Coming to detectors' pulses, we expect to see different behaviors for the two

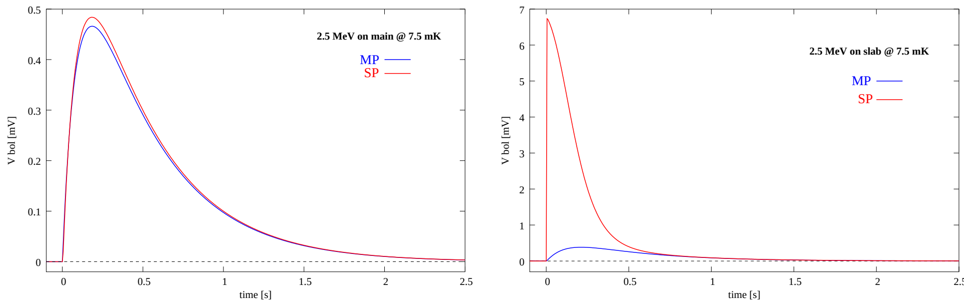


**Figure 7.4** - Simulated voltage signals on the two thermistors of a SSB when the energy is released in the main absorber (left) or in the slab (right). See text for details

thermistors of the bolometer, depending on the event origin.

Figure 7.4 (left) shows the outcome of a simulation where an energy of 2.5 MeV is released in the main absorber crystal. We observe that, given the very small heat capacity of the Ge slab ($\sim$ 1000 smaller than that of the main absorber), the two pulses are almost identical. If the same amount of energy is instead released in the Ge slab, the outcome is completely different, as shown in Fig. 7.4 (right). In this case, the SP is ten times bigger than the MP.

### Scatter plot

The simulated pulses discussed above are clearly different depending on the place where the energy is released. This gives us confidence about the possibility to separate different kind of events. Since the first and most evident difference in the pulses is their amplitude, it is natural to plot this parameter on a graph. A *scatter plot* of the MP amplitude on one axis vs the amplitude of the corresponding SP, for different energy releases in different places (slab/main bolometer absorber) is given in fig. 7.5. We note that the curve obtained by energy deposited in the main crystal is a straight line with slope almost equal to one, i.e. pulses read from the two sensors have almost equal amplitude. On the contrary, when the energy is released in the slab–absorber, the thermistor's read–out easily saturates, due to the fact that the thermistor bias drops to practically zero when the temperature grows high.

Two more comments can be extracted from the plot. First, we supposed here that the particle energy is absorbed in a single place and not shared among both absorbers. We believe that this latter kind of events will be plotted somewhere in the middle between the two bands described above. We will come back later on to this subject.

A second remark is that there is certainly room for detector optimization. For example, it might be interesting to operate the slab–bolometer always in saturated regimes, to simplify its data acquisition and easily tag the external unwanted events. However, we believe that is not worth investigating more in depth the simulation response without previous experimental tests.

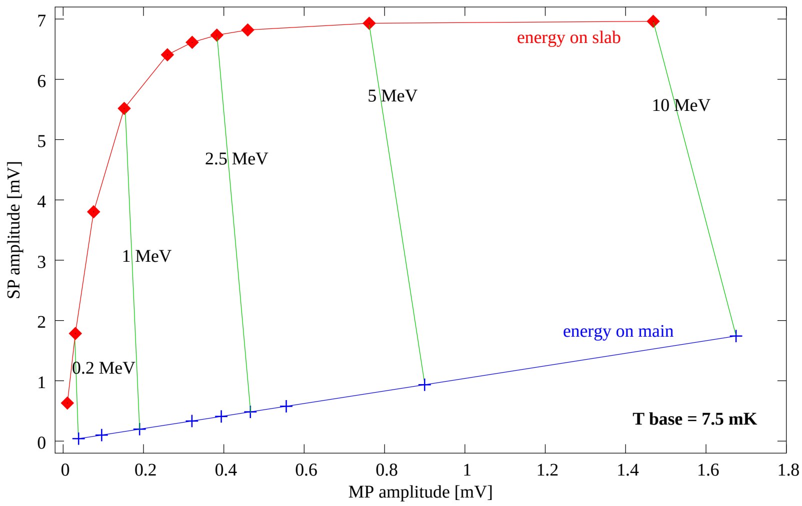


**Figure 7.5** - Simulated scatter plot of coincident SP and MP for different energies released in the main absorber or in the slab absorber. See text for details of the simulation setup and parameters.

## 7.4 Detector design

A surface sensitive bolometer shares all the design and mounting problems of normal bolometers. In addition to the obvious increased complexity of the device itself, we should investigate carefully what is the best material to be used as slab absorber, and how to optimize the thermal couplings.

### 7.4.1 Materials for slabs absorbers

It is clear that good performances in terms of events discrimination are better achieved if the heat capacity of the slab absorbers is much less than that of the main absorber ($TeO_2$ in our case). Since this quantity scales with the volume, slabs absorbers must be very thin.

When the material of the slabs differs from that of the main absorber, the problem of thermal contraction arises. This may have different consequences, including breaking or detachment of the slab itself. This issue must be taken into account also when dealing with crystals that have different contraction coefficient for each crystal axis.

The radiopurity of the materials is not a strict requirement, since we believe that we can discriminate events due to slabs contamination. However, good radiopurity, especially of surfaces, is of course preferred (as we will see in §7.7.4).

We investigated three different possibilities:

**Germanium** was primarily selected because it is available with very high purity level. Unfortunately, it is very expensive.

**Silicon** has been taken into account as a cheap alternative to Ge. Unfortunately, its radiopurity cannot be assured. Two suppliers were used for the slabs used in the tests reported in this dissertation: IET [108] (Poland) and ITC-IRST [72] (Italy).

**$TeO_2$** is the natural candidate because of the good knowledge that we have on this material in terms of radioactivity and thermal behavior. Moreover, in view of a possible implementation of SSBs in CUORE, it prevents the introduction of new untested materials. The drawback of $TeO_2$ is that foils of 0.5 or 0.7 mm thickness are quite fragile, and must be handled with great care.

### 7.4.2 Thermal couplings

We already faced the problem of finding good thermal couplings in chapter 6. In a SSB, the critical couplings are those that involve the slab–bolometers, especially when dealing with differential thermal contractions.

**Slabs to main absorber coupling**

We tried several solutions to couple the slabs to the main absorber. The aim was to keep the slabs firmly in place while allowing some degree of freedom to compensate the differential thermal contractions. We will discuss later each specific attempt. As a general guideline, Araldit glue spots are believed to be elastic enough to compensate small differential contractions. This is especially true if the glue spots are placed close together and in the middle of the face. The spots are made 50 $\mu$m thick using mylar foils as spacers. In other cases, very small Ge stand–off of 50 $\mu$m thickness were used as an additional interface between the two faces.

In the case of all $TeO_2$ absorbers, we do not have to care about thermal contractions, and 4 glue spots are easily placed at the face corners, once the orientation of the slabs' axis matches that of the corresponding main $TeO_2$ face.

**Slabs thermistor coupling**

We have seen that NTD Ge thermistors are usually attached with Araldit glue spots. Our tests showed that this kind of coupling works fine when Si or Ge slab absorbers are used, while problems arise when dealing with thin $TeO_2$ slabs. The usual 6 or 9 spots coupling breaks the $TeO_2$ sheet. Better results were obtained using smaller pedestal thermistors (as in §6.3.3).

## 7.5 General measurements philosophy

In the next sections we will analyze the data collected run by run in our experimental tests on SSBs in the last two years. Before starting, we believe that it might be necessary to point out briefly few general considerations that hold for all measurements. The topics discussed here will then become clearer when dealing with measurements.

### 7.5.1 Measurements methodology

Surface sensitive bolometers are definitely a new kind of bolometers, but they still remain bolometers. As a consequence, the general measurement procedure is almost the same as that of usual bolometers. We must measure load curves, find a good working point, setup the electronics, acquire pulses and baselines and finally analyze them. However, since we had to work and get used with this prototypes, usually load curves were obtained manually and working points found empirically, mostly without the aid of heaters pulses.

We must underline in fact that we mainly focused our attention on the understanding of these devices rather than worrying about the efficiency and performances optimization. This is especially true for the first small–scale prototypes, where the setup was not optimized for high energy resolution.

Concerning the electronic setup, a discussion is needed for what concern the Bessel filter. Usually bolometers signals are filtered by a six–order Bessel with a cutting frequency of 12 Hz. Bolometer pulses shape is generally left almost unchanged by this filter due to the intrinsic slowness of the pulse themselves, at least for big size bolometers. However, we expect (and measured) that signals from the slab–bolometers might be faster, especially on their rise time. Since the effect of a Bessel filter is an integration of the pulse, it might change dramatically the signal shape thus hiding interesting and useful effects. For this reason, we tried different frequencies for the filters. Working with higher cut frequencies on SPs generally led to better results in terms of PSA, even if, unfortunately, it resulted in a general worsening of the noise - which however did not compromise the final result.

Particular care should be devoted to the triggering system, because each detector provides several simultaneous signals, one for each thermistor, every time an event releases energy in the main absorber or in a slab.

### 7.5.2 Analysis tricks

As well as the measurement procedure, also the analysis process of SSB data is similar to that of common bolometers, and it is discussed in §3.5.

As it will be clear soon from the measurements discussion, PSA is very important, and care must be used when producing the OF reference pulse, applying filters and extracting pulse parameters.

The **OF reference pulse** is obtained from a selection (either manual or automatic) of the acquired signals, and after amplitude normalization. The OF reference pulse should usually be a good representative of the shape of the response of that specific bolometer. The quality of the OF depends quite strongly from its reference pulse.

As we have seen when guessing SSBs behavior and as it will became clear with real data, the shape of the signals depends on the event source. In other words, there could be different classes of signals from the same thermistor. Unfortunately, present analysis software does not allow to easily introduce different OF reference pulses. Artifacts and errors might be introduced and results should be double–checked to identify possible mistakes. The **adaptive filter** might be useful in these cases.

The **Wiener filter** [17] is important when dealing with pile–up. In particular, several SSB tests were performed aboveground and thus suffered from a high rate of cosmic rays interactions (about 5–6 Hz above threshold). The samples used aboveground are smaller and arranged to minimize the horizontal

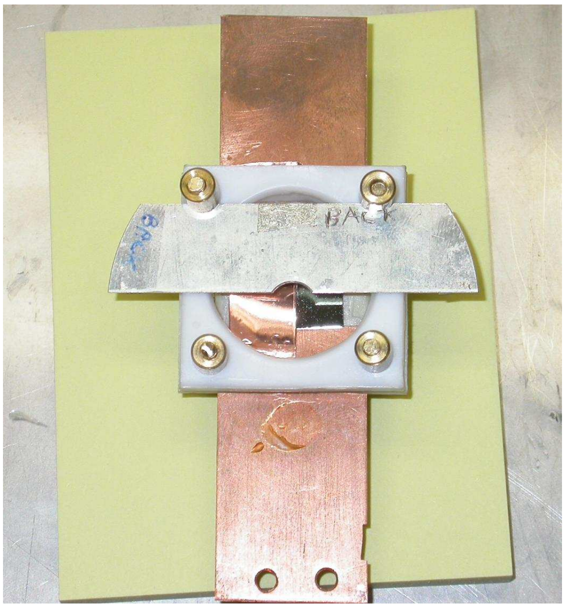


**Figure 7.6** - Picture of the $\alpha$ source. The active area is the small surface close to the circled indentation.

surface area; the duration of their pulses is about 100 ms. Nevertheless, it is not unlikely to have more than one pulse in the same time window. Identification of pile–up pulses is therefore unavoidable.

### 7.5.3 Artificial radioactive sources

In order to prove the SSBs working principle (identification of external events) and to perform energy calibration, we introduced in several occasions an external contamination of $\alpha$ particles. We used two different techniques to contaminate surfaces:

- an $\alpha$ source to implant daughter nuclides (which are $\alpha$ emitters themselves);
- a U–loaded water that can be evaporated on the surface.

**The implanted $\alpha$ source**

We are provided with the $\beta$ emitter source of fig. 7.6. A surface contamination of $^{228}$Ra is in secular equilibrium with its daughter $\alpha$ emitters. The decay chain is the following:

$$^{228}\mathrm{Ra} \xrightarrow{\beta^-} {}^{228}\mathrm{Ac} \xrightarrow{\beta^-} {}^{228}\mathrm{Th} \xrightarrow{\alpha} {}^{224}\mathrm{Ra} \xrightarrow{\alpha} {}^{220}\mathrm{Rn} \xrightarrow{\alpha} {}^{216}\mathrm{Po} \xrightarrow{\alpha} {}^{212}\mathrm{Pb} \xrightarrow{\beta^-} {}^{212}\mathrm{Bi}$$
$$^{212}\mathrm{Bi} \xrightarrow{\beta^-} {}^{212}\mathrm{Po} \xrightarrow{\alpha} {}^{208}\mathrm{Pb}$$
$$^{212}\mathrm{Bi} \xrightarrow{\alpha} {}^{208}\mathrm{Tl} \xrightarrow{\beta^-} {}^{208}\mathrm{Pb}$$

This source can be used to activate external surfaces placed close to its active area in a vacuum chamber. Activation by implantation of $\alpha$-decaying daughter nuclides is possible due to the fact that the $\beta$ contamination in the

| Nuclide | $T_{1/2}$ | $E_\alpha[MeV]$ | B.R. [%] |
|---|---|---|---|
| $^{228}$Th | 1.9131 y | 5.4233 | 72.2 |
| | | 5.3405 | 26.7 |
| $^{224}$Ra | 3.66 d | 5.6855 | 95.0 |
| $^{220}$Rn | 55.6 s | 6.2883 | 99.9 |
| $^{216}$Po | 0.15 s | 6.7785 | 100 |
| $^{212}$Bi | 60.6 m | 6.0901 | 9.8 |
| | | 6.0510 | 25.2 |
| $^{212}$Po | 0.3 $\mu$ s | 8.7844 | 64.0 |

**Table 7.1** - Properties of the $\alpha$ decays produced by the activated $\alpha$ source and involved in its production.

source is superficial. The implanted nuclide is the daughter of the first $\alpha$ decay of the previous chain, namely $^{224}$Ra. Therefore, the activated external surface behaves like a weak $\alpha$ emitter with negligible self–absorption.

Properties of the $^{228}$Th nuclide that produces $^{224}$Ra and of its daughters (which are then emitted by the activated source) are listed in tab. 7.1.

**Uranium loaded water drops**

An Uranium atomic absorption standard solution was acquired from Aldrich Chemical Company, Inc. [109]. It contains 973 $\mu$g/mL of U in a water solution of 1 wt. % of $HNO_3$. A measurement performed with a HPGe detector in the Baradello underground laboratory showed that the secular equilibrium of the $^{238}$U was broken. Moreover, the U source appears to be taken from depleted Uranium, since few decays from $^{235}$U and $^{234}$U and daughters nuclei were observed.

The solution was diluted to reduce the activity to an acceptable rate of about one $\alpha$ emission every 2 minutes from a couple of drops of solution. Few drops where let evaporate on the surfaces of the detector absorbers to contaminate.

We remind the reader that $^{238}$U decays by $\alpha$ emission with a half life of $4.47 \times 10^9$ years. Alpha particles are emitted at 4.15 MeV (b.r. 21%) and 4.20 MeV (b.r. 79%). A weak doublet from $^{234}$U might be observed at 4.77 MeV (b.r. 71.4%) and 4.72 MeV (b.r. 28.4%).

## 7.6 Tests of working principles on small prototypes

### 7.6.1 Goals and objectives

In this section we will report all the tests that have been performed on small–scale surface sensitive detectors. The aims of this work were:

- test the working principle described previously; for this reason the measurements are not optimized for high energy resolution;
- gain experience with SSB assembling, operating, read–out and acquisition;

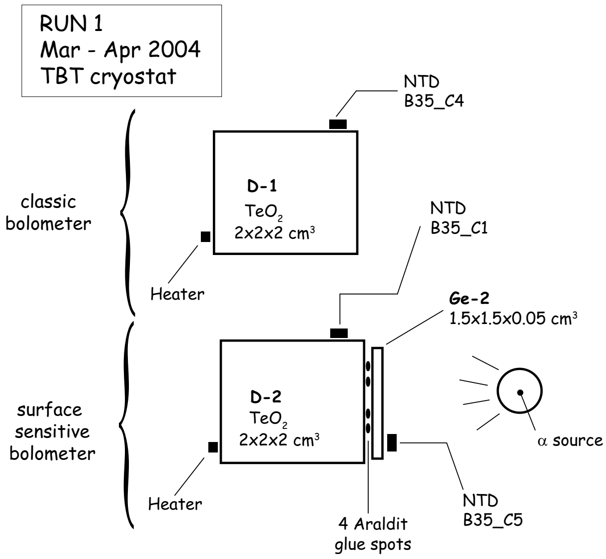


**Figure 7.7** - Scheme and details of the detectors of run 1

· select the best material for the slabs.

Most of the measurements were carried out in the TBT cryostat (§4.3.1) in the Insubria Low Temperature Detectors laboratory. The operating temperature was always around 20–25 mK. Detectors were mounted in the holder described in §4.3.1.2.

We are not going to report here all the details of each measurements. The reason is that we don't want to overwhelm the reader with too much technical information that could hide what is really important. Nevertheless, every single cool–down (also called *run*) will be introduced by a schematic drawing with the main specifications. We hope this will improve readability and comparison between the different setups.

The work reported here has been also the subject of two masters thesis [110, 111] and other useful details can be found there.

### 7.6.2 Run 1: first test!

We realized the very first surface sensitive bolometer in March 2004. The details on the setup and the measurements are summarized in the scheme of fig. 7.7 along with some pictures of the detectors in fig. 7.8.

**Expected events**

Before presenting the results, we will hold your curiosity and try to figure out what kind of events we expected to read–out from this setup. Focusing our attention only on the SSB, we could group all possible event types into three different classes:

1. events due to natural radioactivity or cosmic rays that release all or part of their energy into the main $TeO_2$ absorber; it is also likely that some

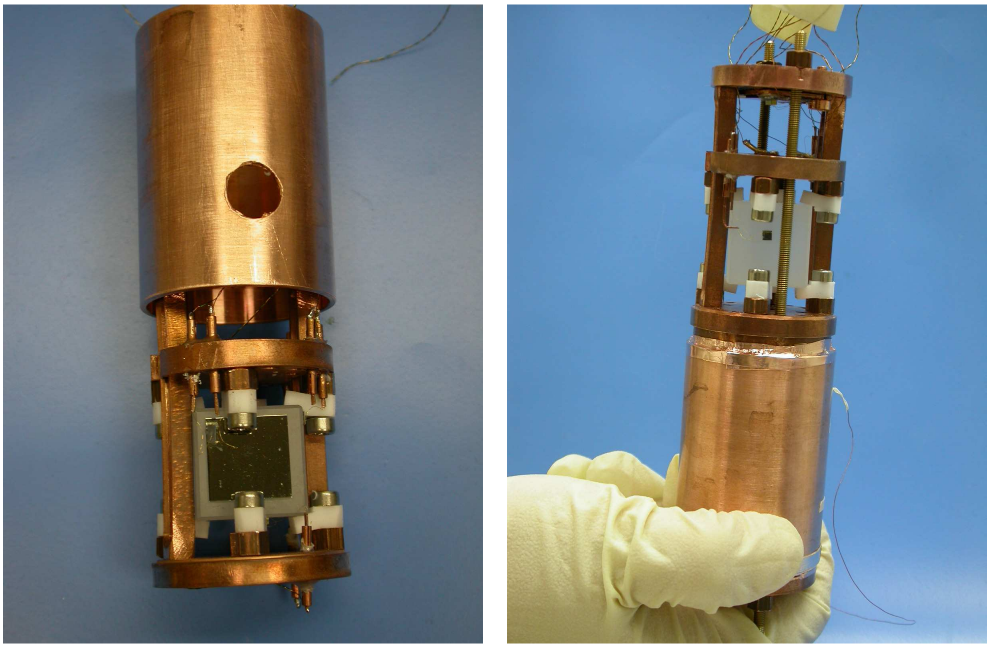

**Figure 7.8** - Picture of the setup used in run 1. The SSB detector with the Ge slab is on the left. The hole in the copper frame is where the radioactive $\alpha$ source is placed. On the right, the SSB detector is enclosed in the bottom holder and a normal bolometer is mounted on the top.

$\alpha$s from the source will fall on the absorber, because the Ge slab size is smaller than the $TeO_2$ face;

2. events due to $\alpha$s from the irradiated copper tape that strike into the Ge slab and leave there all their energy;

3. events due to natural radioactivity or cosmic rays that release energy both in the Ge slab and the $TeO_2$ absorber.

The situation resembles what we depicted in §7.2, when we were trying to predict the behavior of SSBs. In fact, events of the first type are internal bulk events, while type 2 events are those coming from external surface contamination. Therefore, we could say that our test will be successful if we are able to recognize events of type 2 (external contamination) from events of type 1 (bulk events). To be honest, we should be worried by type 3 events, because they are a sort of mixed type events. From the bolometer point of view they are neither completely internal nor fully external, and thus they could mess up everything. This is the sort of thing that only real experiments can tell us.

Before moving to the data, we remind the reader that we also have a classic "naked" bolometer placed just above the SSB. This bolometer could be used as a partial veto to identify cosmic rays events. We will see how in a few paragraphs.

Two measurements were performed in this run. As soon as we started looking at the detectors, it became clear that our experimental setup suffered from both electronic and microphonic noise. The setup of the TBT cryostat was slightly different from the one described in §4.3.1. The sand box was in fact

| **Measurement 1** | | Duration: | 20 h | |
|---|---|---|---|---|
| Detector | Bessel [Hz] | Vbol [mV] | Rbol [MΩ] | Tbol [mK] |
| D-1 | 12 | 9.75 | 75 | 26.46 |
| Ge-2 | 12 | 3.22 | 32.2 | 29.27 |
| D-2 | 12 | 9.3 | 44.08 | 28.17 |

**Table 7.2** - Bessel cut frequency and working points of detectors of measurements 1, run 1.

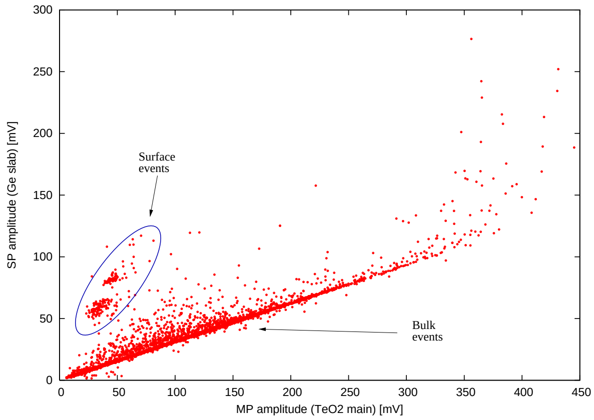


**Figure 7.9** - Scatter plot for the SSB detector of run 1. Data from measurement 1.

missing. Nevertheless, we were able to find reasonable working points for the detectors and to acquire about 24 hours of data.

### Measurement 1

Figure 7.9 reports the scatter plot obtained from the data of the first measurement. Detectors working points are given in tab. 7.6.2.

As already explained, on a scatter plot, MP amplitude is plotted against SP amplitude. To be precise, these are not really "coincident event". They are in fact the same single event which produces simultaneous pulses on each thermistor of the SSB.

In the plot we easily identify two agglomerates of points. The first includes those points that accumulate close to the red straight line, while the points in the blue circle belong to the second. It is straightforward to compare this plot with those introduced and discussed in sections 7.2–7.3. The events on the red line can be identified as events where the energy is released in the main absorber, while the two small groups of events in the blue circle are the $\alpha$s from the source that strikes the Ge slab detector. The first group is due to those $\alpha$ lines at about 6 MeV, while the other arises from the lines at about 9 MeV (see table 7.1). The two groups can be easily separated.

To support the hypothesis that the events on the red line are due to those events that release energy in the main absorber, we perform a coincidence analysis with the the classic bolometer placed above the SSB. By selecting triple coincidence events on the acquired channels, we can get rid of the $\alpha$s that re-

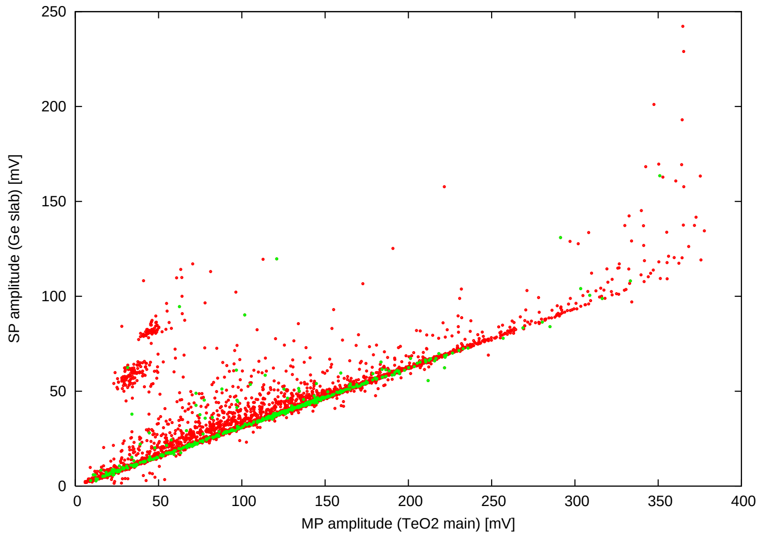


**Figure 7.10** - Scatter plot of data from measurement 1, run 1. The green events are coincidence events with the classic bolometer D-1 place above the SSB.

lease energy only in the Ge shield. In fact, we select only those events that release energy in both detectors (e.g. by muon crossing or multi–compton $\gamma$s) and thus, from the SSB point of view, they look like pure bulk events. This selection is plotted in figure 7.10 as green points.

Most of the coincidence points lie exactly on the bulk events band - thus confirming our hypothesis. However, we must note that some events are someway in the middle between the straight line and the $\alpha$s groups. Our clue is that these events are due to simultaneous release of energy in the main and in the Ge slab absorber (and in the classical detector above). At the beginning of this section we identify them as "type 3" events. In this way, they release energy in both places and so the situation is somehow mixed between the pure bulk and slab event.

This consideration is supported by the fact that only few mixed events are selected from the coincidence analysis with the naked detectors. The probability that a cosmic ray crosses both $TeO_2$ absorbers and the Ge slab is quite low, due to the geometry of the setup (mainly because of the vertical placement of the thin Ge slab).

### Measurement 2

For the second measurements, We report here only the scatter plot of fig. 7.11. In this measurement we changed the Bessel filter of the Ge slab–bolometer read–out from 12 Hz to 120 Hz and the effect of this change is evident from the fact that the slab events are better separated from the bulk ones.

We guessed in §7.2 that slab events should be quite fast. The filter behaves like an integrator on the signal and therefore reduces the signal amplitude while increasing the time constants (the signal integral remains constant). With a 120 Hz filter the pulses from the slab are higher than in the previous 12 Hz measurement. This is the reason for the better separation in the scatter plot,

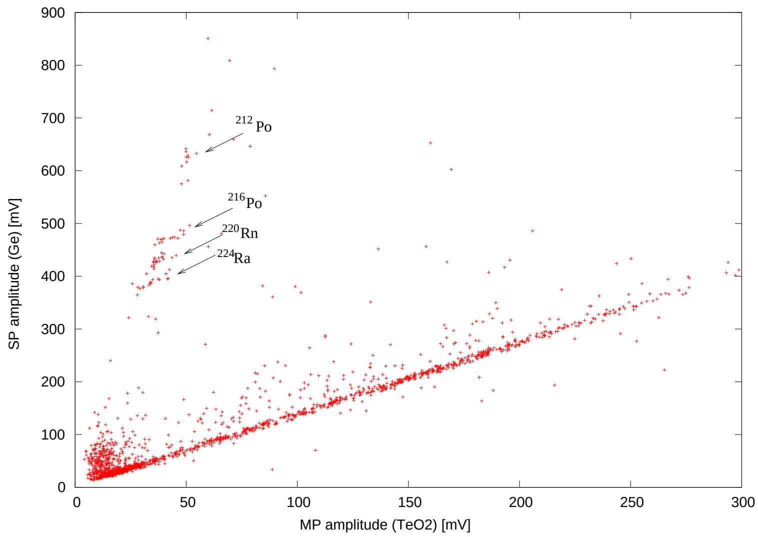


**Figure 7.11** - Scatter plot of measurement 2, run 1. The $\alpha$ peaks of the source are indicated.

and also of the possibility to recognize the main $\alpha$ lines from the source (as shown in the plot).

As a matter of fact, the results of these first tests are very preliminary: we are operating a new kind of detectors in a never tested environment. Later in this chapter we will analyze more and better scatter plots and the evidence on SSB functionality and potentiality will become more clear.

### 7.6.3 Run 2: again with Ge slabs

At the end of April 2004 the TBT cryostat was optimized for vibration as discussed in §4.3.1 and a second run was then performed.

#### 7.6.3.1 Setup

This time the setup was slightly different:

- we prepared a SSB with a smaller main $TeO_2$ absorber in order to reduce the cosmic rays interaction;
- two Ge–slabs (named Ge-A and Ge-C) were glued on opposite sides of the main absorber;
- as before, an irradiated copper tape was placed in front of Ge-A; the other slab Ge-C was irradiated directly on the surface facing outward.

A scheme of the setup with all details is placed in figure 7.12. A picture of the SSB detector is in fig. 7.13.

Unfortunately, during the cool–down, we lost the electrical contact with the thermistor on the Ge-C slab. Moreover, due to a software problem, the acquired baselines are not representative of the real noise conditions. We thus used a white noise spectrum as input for the OF in all the analysis of this run

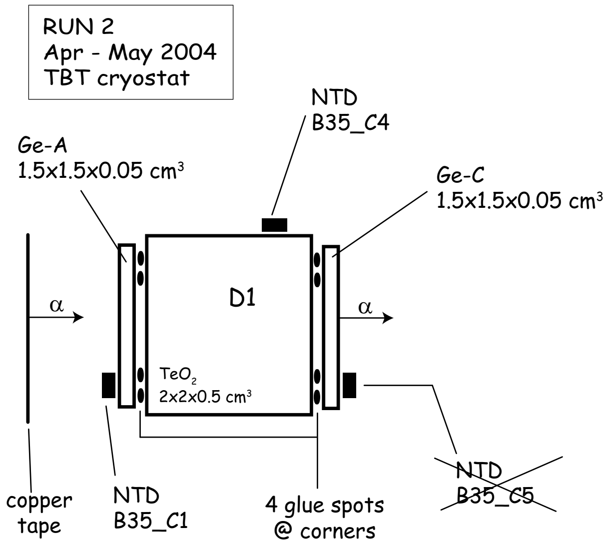


**Figure 7.12** - Scheme and details of the detectors of run 2

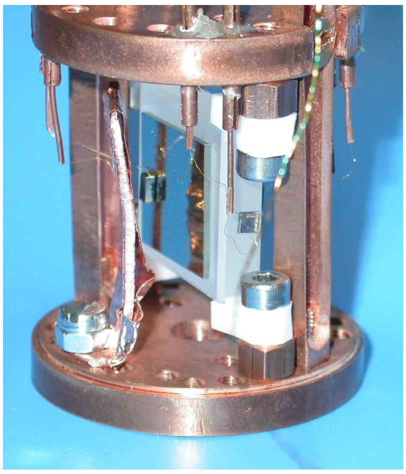

**Figure 7.13** - Picture of the SSB bolometer with two Ge slab–bolometers operated in run 2. On the right side, the irradiated copper tape facing the Ge-A slab–bolometer is visible.

| **Measurement 3, run 2** | | | | |
|---|---|---|---|---|
| Detector | Bessel [Hz] | Vbol [mV] | Rbol [MΩ] | Tbol [mK] |
| D-1 | 12 | 14.6 | 93 | 25.8 |
| Ge-A | 12 | 19.3 | 376 | 22.1 |
| Ge-C | channel dead | | | |

**Table 7.3** - Bessel cut frequency and working points of detectors of measurements 3, run 2.

measurement. The problem was promptly solved at the end of the run and did not affect later measurements.

We will discuss here only the results from measurements number 3 and 7. From the first we will point out some considerations about the data analysis, while the latter gave very encouraging results in terms of scatter plots, pulse shape analysis and energy resolution.

We will skip measurements 4, 5 and 6. They were used to determine the optimal working points for the bolometer, following a procedure similar to that described in 3.2.2. The working point of the thermistor on Ge-A was selected so that its amplitude is close to that of the main absorber when energy is released in the main $TeO_2$ absorber. Measurement 5 has been already discussed in §4.3.1.3 to find out possible noise sources in the TBT cryostat.

#### 7.6.3.2 Measurement 3: pile–up reduction and adaptive filter

As we already discussed, our aboveground setup is not shielded from cosmic rays. As a consequence, our measurements were affected by pile–up (i.e. two or more pulses acquired in the same time span). Pile–up can be recognized and rejected off–line. Secondary pulses which are higher than 10% of the primary pulse are discarded. The necessity of this tool and its effectiveness can be appreciated by comparing figures 7.14(a) and 7.14(b).

We also used data from these measurements to verify if any advantages could come from the implementation of the adaptive filter when dealing with different classes of pulses, as in the case of events from the thermistor of the Ge slab–bolometer. We evaluate the SP amplitude after parsing the signals through OF and an adaptive filter. The resulting comparison show that, for this measurement, no improvement can be seen from the use of the adaptive filter [110].

#### 7.6.3.3 Measurement 7: rise time discrimination and $\alpha$ spectroscopy

This measurement is the result of the working point optimization performed in previous measurements not reported here. The setup and configuration of each channel is given in tab. 7.4

We start reporting in figures 7.15 and 7.16 a comparison of the output of the detector in two different situations. In the first figure (fig. 7.15) the energy is released in the main $TeO_2$ absorber. MP and SP are very similar, especially for what concerns the amplitude. On the contrary, very different pulses are acquired

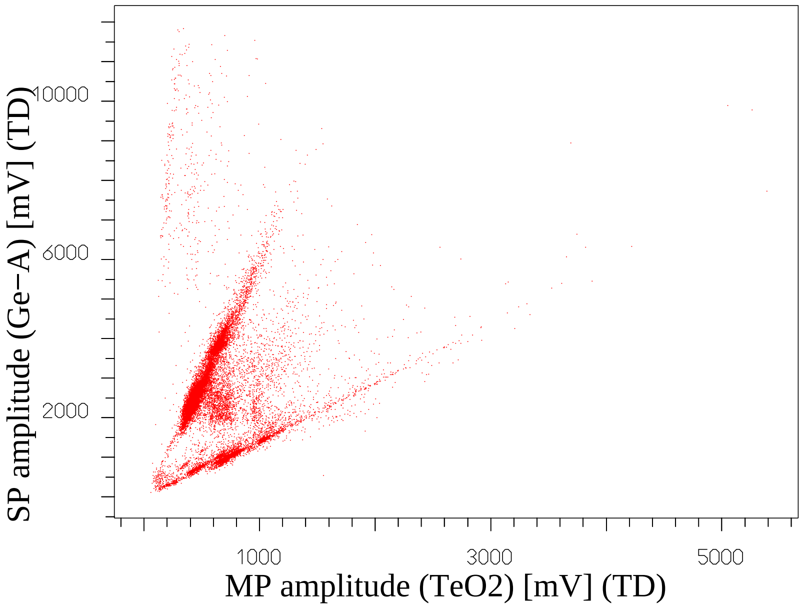


(a) All events.

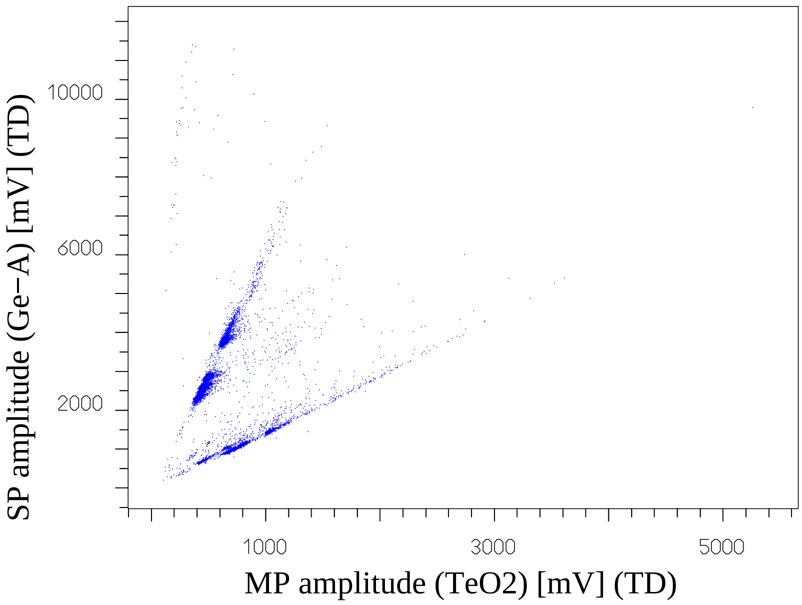


(b) Without pile–up events.

**Figure 7.14** - Scatter plots of measurement 3 data. Pulses processed with white noise and OF.

| **Measurement 7** | | Duration: ∼14 h | | |
|---|---|---|---|---|
| Detector | Bessel [Hz] | Vbol [mV] | Rbol [MΩ] | Tbol [mK] |
| D-1 | 120 | 12.8 | 128 | 24.9 |
| Ge-A | 12 | 23.1 | 234 | 23.3 |
| Ge-C | channel dead | | | |

**Table 7.4** - Bessel cut frequency and working points of detectors of measurements 7, run 2.

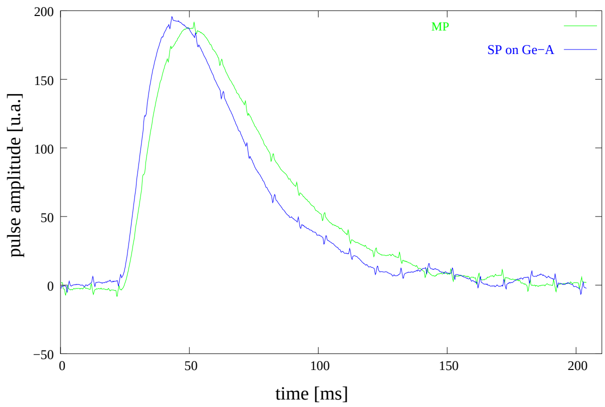


**Figure 7.15** - Measurements 7: a pulse due to an energy release in the main $TeO_2$ absorber.

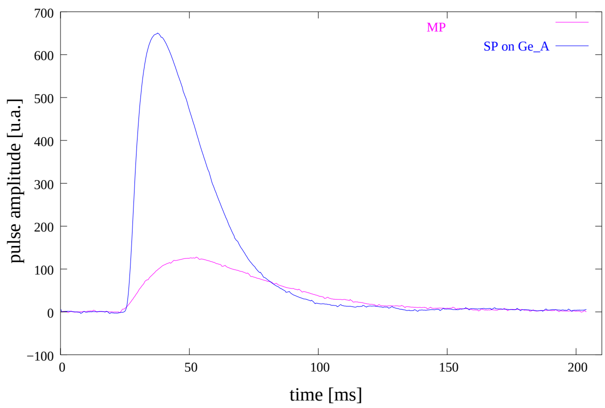


**Figure 7.16** - Measurements 7: a pulse due to an energy release in the Ge-A slab absorber.

when a particle releases the greatest part of its energy in the slab absorber (fig. 7.16). This is an impressive validation of the working principle exposed in §7.2.

The scatter plot obtained after usual analysis (OF, white noise, pile–up rejection) is shown in fig. 7.17.

### Rise time discrimination

Additional evidence supporting the SSB behavior described previously can be deduced from fig. 7.18, where we present the spectrum of the rise time of Ge-A SPs. Two classes of events with different rise times appear clearly around 6.4 ms and 9.6 ms. As shown in the same figure, slower events belong to the bulk event class while faster events are surface events.

### Alfa spectroscopy

Finally, we conclude the analysis of this measurement by plotting the amplitude spectra of the pulses of the two acquired thermistors. The rise time selection performed previously helps selecting for each thermistor only those events that happened in the corresponding absorber.

The spectrum of surface events read by the thermistors on Ge-A is given

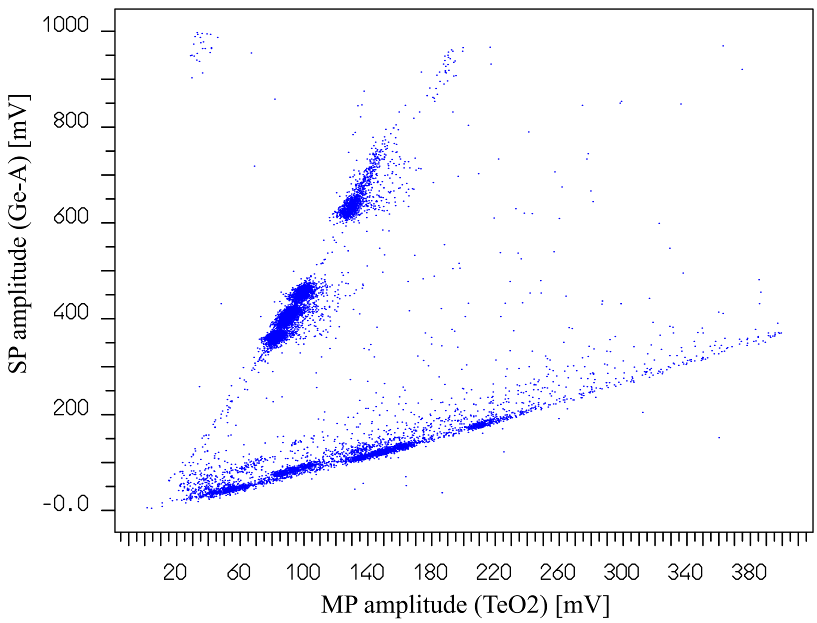


**Figure 7.17** - Final scatter plot of measurements 7.

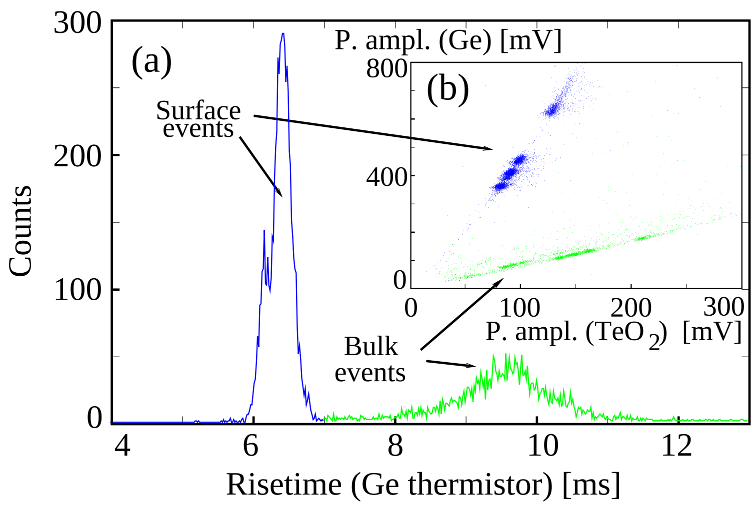


**Figure 7.18** - (a) Rise time distribution for the Ge-A SPs. (b) A detail of the scatter plot reported in fig. 7.17 where fast SPs (left Gaussian in (a)) are reported in blue, while slow SPs (right Gaussian in (a)) in green.

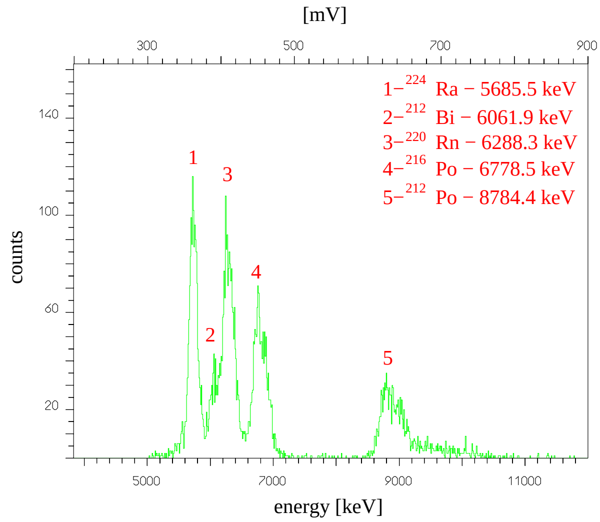


**Figure 7.19** - Energy spectrum of pulses from thermistor on Ge-A obtained by selecting fast rise time events (as in fig. 7.18).

in fig. 7.19. We can recognize the $\alpha$ peaks due to the radioactive source (cfr. §7.5.3): $^{224}$Ra, $^{220}$Rn, $^{216}$Po, $^{212}$Po and $^{212}$Bi. A Gaussian fit on the peaks has been performed [110] to evaluate approximately the resolution which is $\sim$ 150 keV at the $^{224}$Ra peak of 5685.5 keV.

On the other hand, the full spectrum (no rise time cuts) of the main thermistor may be confusing at a first glance. In fact it is the product of the overlap of the spectrum of the events due to $\alpha$s impinging on Ge-A, those of Ge-C and those that fall directly on the main $TeO_2$ absorber plus the cosmic rays and natural radioactivity. Again, events from the Ge-A can be removed from the spectrum by anticoincidence rise time selection with Ge-A SPs as in fig. 7.20. In this way, we can recognize the peaks due to the $\alpha$s on the $TeO_2$ absorber (above 120 mV) and also the imprint of the Ge-C $\alpha$s between 80 and 120 mV. Events at lower amplitudes are due to cosmic rays, natural radioactivity and Ge-A "thermistors events". The latter are due to $\alpha$ particles that release their energy on the Ge-A thermistor itself thus producing very energetic and fast pulses. They are on the top left side of the scatter plot of fig. 7.17.

#### 7.6.3.4 Detector disassembly

As an example of the effect of differential thermal contraction between $TeO_2$ and Ge, we show in fig. 7.21 the detector after it was removed from the cryostat. It is evident that the stresses induced by the Ge through the glue spots result in cracks in the main $TeO_2$ absorber.

### 7.6.4 Run 3: IET Silicon slabs

The encouraging results obtained in the first two runs need to be improved and better understood. We have proved the basic principles: now we need to find a more suitable material than Ge, for the slab absorber. High purity Germa-

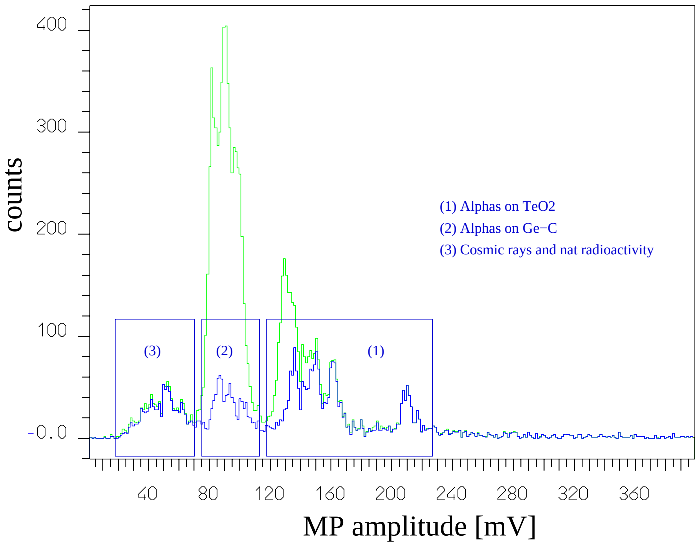


**Figure 7.20** - Spectrum of MPs (no cuts) (green) and spectrum of events after rise time anticoincidence which removes events in Ge-A (blue).

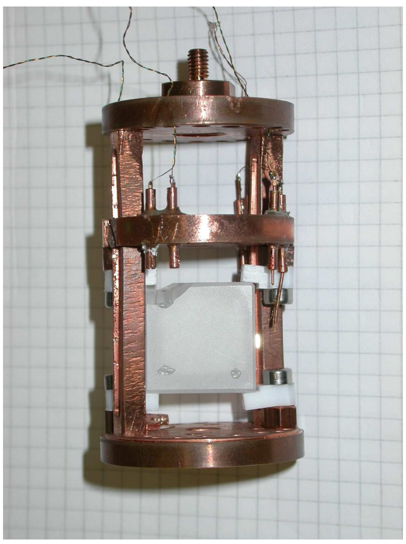

**Figure 7.21** - Picture of the detector of Run2. The face shown is where the Ge-A slab was glued. The cracks are exactly where the glue spots were placed.

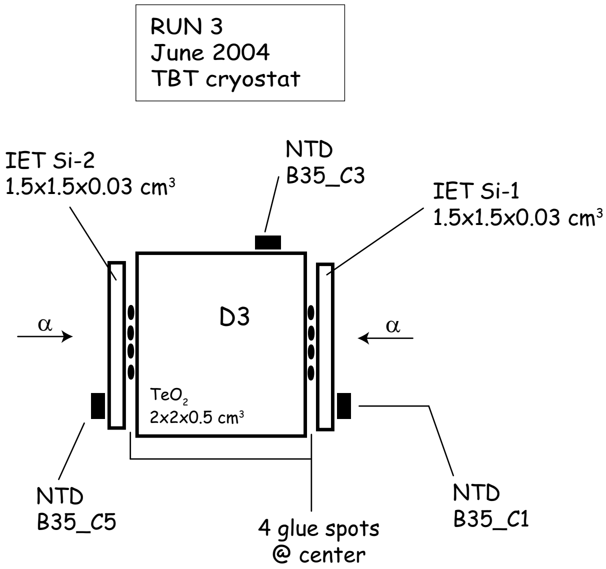


**Figure 7.22** - Scheme and details of the detectors of run 3

| **Measurement 8** | | | | |
|---|---|---|---|---|
| Detector | Bessel [Hz] | Vbol [mV] | Rbol [MΩ] | Tbol [mK] |
| D-3 | 120 | 35.14 | n.a. | n.a. |
| Si-1 | 120 | 25.55 | n.a. | n.a. |
| Si-2 | 120 | 22.20 | n.a. | n.a. |

**Table 7.5** - Bessel cut frequency and working points of detectors of measurements 8, run 3.

nium is too expensive. Silicon appears as a possible replacement. We purchased several thin slabs of Si from the polish company IET [108] that we glued on a $TeO_2$ crystal similar to that used in the previous run.

To prevent $TeO_2$ cracking by the thermal contraction between Ge and $TeO_2$ , the coupling of the slabs was changed. The glue spots were placed in the middle of the face and not at the corners. The overall setup is depicted in fig. 7.22. Working points of the measurement 8 are given in tab. 7.5.

The behavior of the detector is quite good, with similar scatter plots and rise time discrimination as can be appreciated from figures 7.23 and 7.24 respectively. The collected statistic is quite low, but still all the scatter plot features are present.

The data collected in this run show clearly that IET Silicon is a good candidate material for the slab–bolometers. Its performances appear in agreement with those expected.

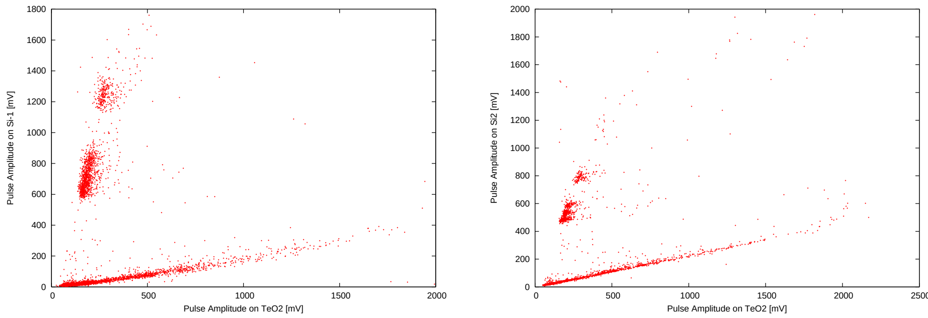


**Figure 7.23** - Scatter plots for the detector of run 3. The amplitude of MPs is plotted against SPs amplitudes of Si-1 (left) and Si-2 (right). Data are from measurement 8, run 3.

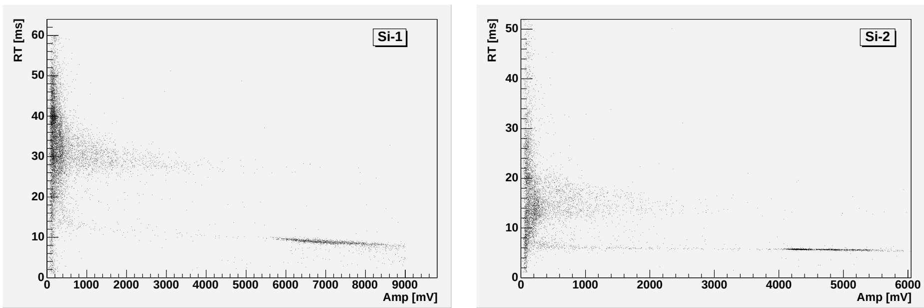


**Figure 7.24** - Plots of the RT vs Amplitudes for the pulses acquired by the thermistors on the two Si slabs. In both cases, faster pulses are mainly due to energetic $\alpha$ events in the slabs. Data are from measurement 8, run 3.

## 7.6.5 Run 8: first test with a $TeO_2$ slab–bolometer

### 7.6.5.1 Setup

After a few cool–down used to investigate other aspects of normal bolometer optimization (see chapter 6), we come back to SSBs. The tests of the previous sections were not conclusive on the research of the better candidate for the slab–bolometer absorber. As already said, $TeO_2$ is in principle the right material. The test reported in this section is the first experimental trial using a $TeO_2$ slab (named T-1). To help comparison, another Si slab–bolometer (named Si-3) was mounted on the opposite face of the $TeO_2$ one (see figure 7.26 for pictures of the final detector and tab. 7.6 for run parameters). We wanted to test not only rejection efficiency, but also the assembly feasibility and the thermal contractions' consequences. The latter should not be a problem for $TeO_2$ slabs on $TeO_2$ main absorber (at least if the axes orientation is taken into account), but it can be problematic when attaching a Ge thermistor on a thin $TeO_2$ slab.

In an effort of facilitating the reproducibility of the connections between Si and $TeO_2$ , we placed small Ge stand–offs ($1 \times 1 \times 0.05$ mm$^3$) in the middle of the crystal face. The same technique was used also for T-1, but with corners placement. The gluing is performed through a thin veil of Araldit® .

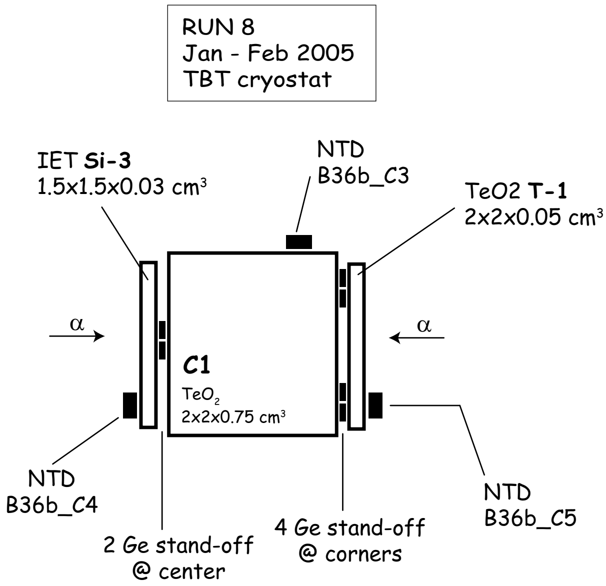


**Figure 7.25** - Scheme and details of the detectors of run 8. The heat capacity of the $TeO_2$ slab is 3.75% of the C-1 crystal.

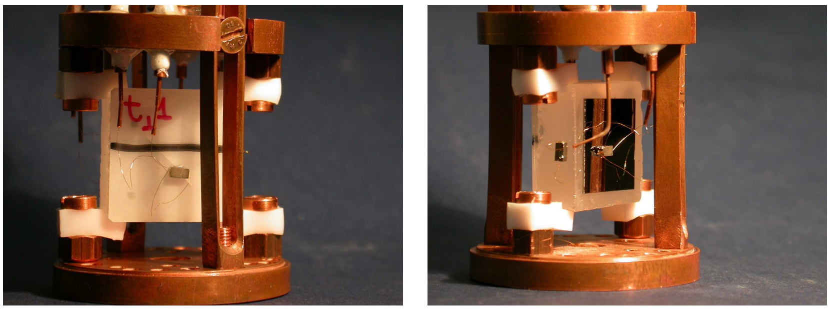

**Figure 7.26** - The SSB detector of run 8 mounted into its copper holder. On one face a $TeO_2$ slab–bolometer is glued (right). On the opposite face a Si one is placed (left).

| Run 8 | | | | |
|---|---|---|---|---|
| Detector | Bessel [Hz] | Vbol [mV] | Rbol [MΩ] | Tbol [mK] |
| C-1 | 120 | 21 | 14 | 24.8 |
| T-1 | 120 | 12.2 | 12.2 | 25.2 |
| Si-3 | 120 | 12 | 12 | 25.3 |

**Table 7.6** - Bessel cut frequency and working points of detectors of run 8.

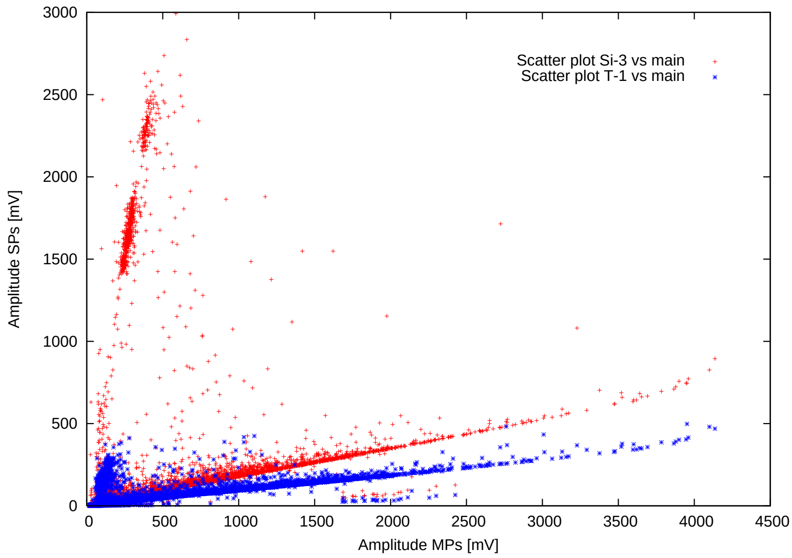


**Figure 7.27** - Overlay plot of the scatter plots from data obtained in run 8.

#### 7.6.5.2 Results

**Scatter plots**

The usual scatter plots of coincident pulses of MPs vs SPs for both channels are superimposed in figure 7.27.

As far as Si-3 is concerned (in red), we observe the usual structure of the two bands we are now familiar with. The $\alpha$ peaks are not well distinguishable, but the slope of the two classes of events (surface and bulk) is different, and separation pretty easy. On the contrary, the scatter plot of T-1 SP vs main amplitudes (in blue) is quite unusual. In fact, it looks like the $\alpha$ events are missing. The *surface band* is populated only in the low energy part by natural radioactivity events.

This strange behavior is supported by a comparison between the pulses of the three thermistors in different situations. A real deposit of energy by an $\alpha$ in the Si-3 absorber produces the pulses reported in fig. 7.28(left). As expected, a fast and high pulse is read by the Si-3 thermistor, while usual longer pulses are recorded by the other two thermistors. The expected situation does not show up when the energy is released in the T-1 absorber (fig. 7.28(right)). It is very likely that the irradiated copper tape was misplaced and the $\alpha$ particles were not able to reach the T-1 absorber. Nevertheless, it could also be that the thermal conductance between T-1 and the main absorber was not good.

#### 7.6.5.3 Conclusions

From the measurements of this run, we may conclude that

- Silicon slab–bolometers proved again to work well;
- no final answer can be given on the performances of $TeO_2$ slab–bolometers due to the impossibility of detect or resolve $\alpha$ particles;

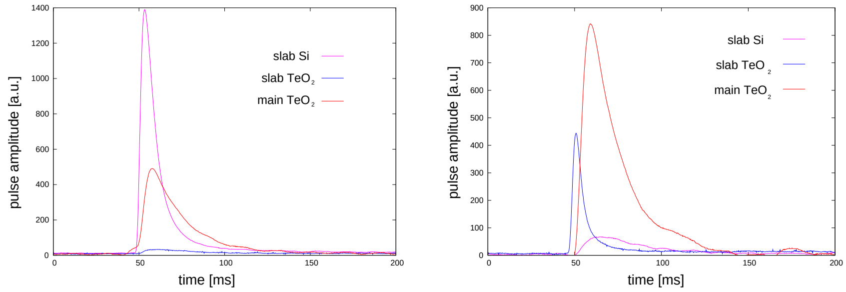


**Figure 7.28** - Real pulses acquired during run 8 for energy released in the Si shield (left) and in the main $TeO_2$ absorber (right).

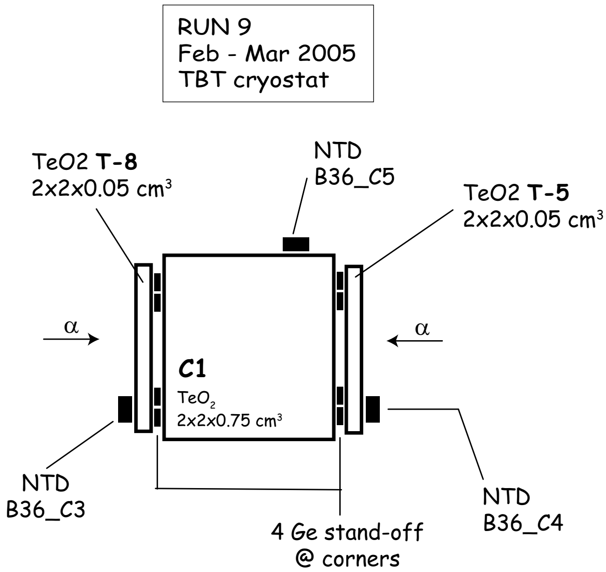


**Figure 7.29** - Scheme and details of the detectors of run 9

- from the mechanical point of view, it turned out that $TeO_2$ slabs are very frail and difficult to handle;
- differential thermal contractions between the $TeO_2$ slab and the thermistor caused the breakage of the slab itself.

We look for more answers and clearer results in the following run.

### 7.6.6 Run 9: more work with $TeO_2$ slabs and parallel read–out

This time we concentrated our efforts only on a full $TeO_2$ SSB.

#### 7.6.6.1 Setup

The detector components and couplings are very similar to those used in the previous run 8 and are presented in fig. 7.29. Here both slab–bolometers are made of $TeO_2$ .

We posed special attention when placing the irradiated copper tape in order to be sure that the $\alpha$ particles reach the two slab–bolometers.

| Run 9 | | | | |
|---|---|---|---|---|
| Detector | Bessel [Hz] | Vbol [mV] | Rbol [MΩ] | Tbol [mK] |
| C1 | 120 | 10.7 | 10.7 | 25.7 |
| T-8 | 120 | 13.9 | 14.0 | 24.8 |
| T-5 | 120 | 10.9 | 10.9 | 25.6 |

**Table 7.7** - Bessel cut frequency and working points of detectors of run 9.

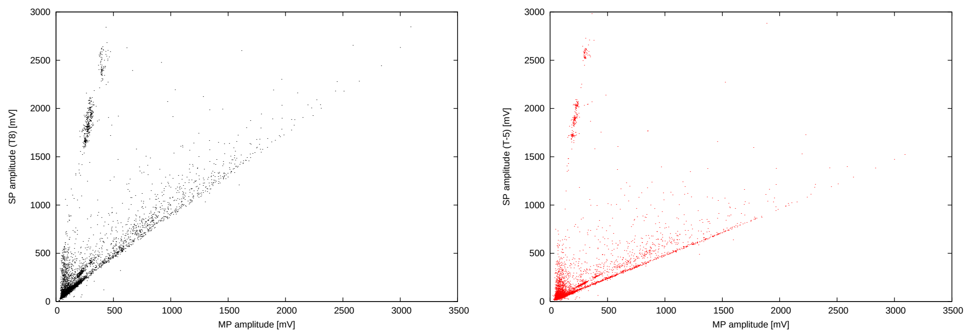


**Figure 7.30** - Scatter plots obtained from the single channel read–out measurement of run 9 for T-8 slab (left) and T-5 slab (right).

### 7.6.6.2 Single channel read–out

We start reporting the results of a measurement with the parameters given in tab. 7.7.

The scatter plots are given in fig. 7.30. An interesting feature appears in both plots. A group of events is clearly visible on a separate line, just above the bulk events band. We could investigate on the origin of these events by analyzing the rise time $\tau_R$ spectrum of the SPs. For example, looking at that of the T-8 thermistor pulses (fig. 7.31(left)), we can select the fast surface $\alpha$ events with 2.5 ms $< \tau_R <$ 3.1 ms. If we select these pulses on the scatter plot of the opposite T-5 pulses, we identify exactly the region above the bulk events line (fig.7.31(right)). The same procedure holds when selecting T-5 surface events and looking for them in the T-8 scatter plot.

In a scatter plot of one slab–bolometer, the line close and parallel to the bulk events band is therefore due to surface energy release in the other slab–bolometer. This behavior could be explained by the fact that the position of an event in the scatter plot does not depend only from the position and the amount of energy release that produces it, but also from the thermal couplings which inevitably shape the pulse evolution. However, we cannot rule out the possibility that this feature is an artifact produced by the analysis software which is not tailored to deal with pulses with different characteristics on the same channel. The reference pulse used in OF is in fact the same for both the fast surface event class and the slow bulk event class. This fact could lead the OF to an incorrect evaluation of the pulses amplitudes.

An important indication that the presence of the slab does modify the shape

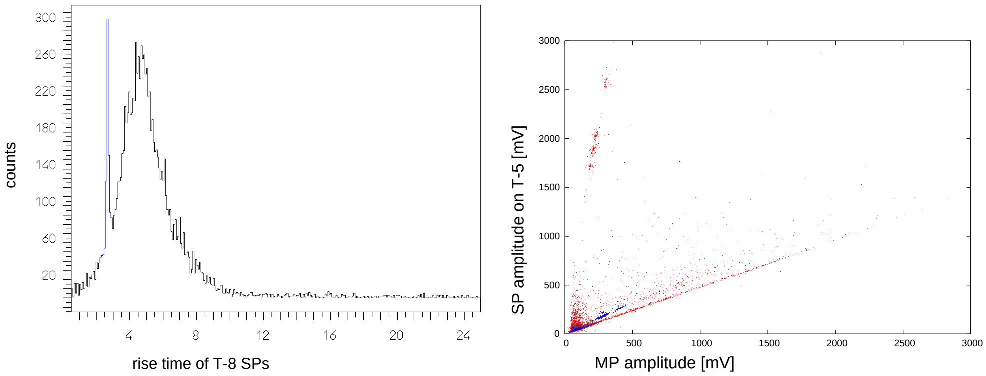


**Figure 7.31** - Rise time spectrum for SP from T-8 (left) and selection of the blue peak in the T-5 scatter plot (right).

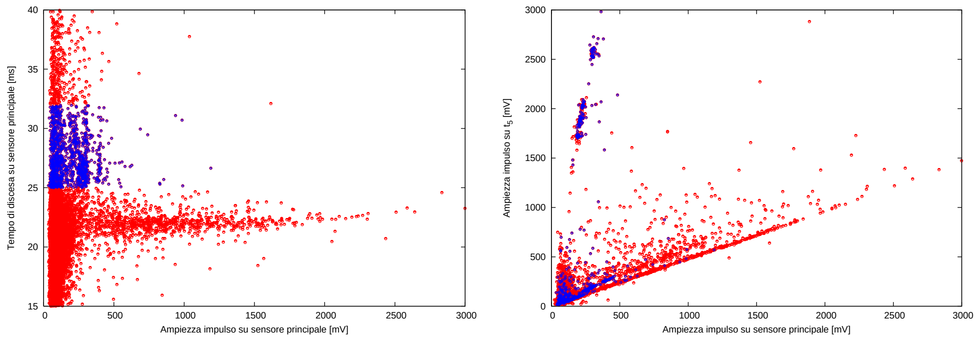


**Figure 7.32** - (left) Plot of decay time vs amplitude for MP. The selected points with (25 ms ¡ $\tau_d$ ¡ 32 ms) correspond to surface events in the scatter plot (right).

of the pulses comes from plots of fig. 7.32. Here we can see that the decay time of surface events is different from that of bulk events when read–out by the thermistor on the main absorber. Up to now PSA was only used for SPs. Here we have a first indication that it can be used also for MPs. We will come back later on this subject because it can have very important consequences.

#### 7.6.6.3 Parallel read–out of the slab–bolometers

In this test, we also tried to read–out the two slab–bolometers thermistors with a single read–out channel as two parallel resistors. In this way we could reduce the number of read–out wires and acquisition channels, therefore greatly simplifying the setup.

The measurements parameters are reported in Tab. 7.8. The working points were extracted from the load curves of fig. 7.33.

The resulting scatter plot in this configuration is given in fig. 7.34. It shows the usual bulk event band and two surface event bands with slightly different slope, which identify the two different thermistors. The slope is different because the couplings and working points are inevitably not the same for the two slab–bolometers.

| **Run 9** | | | | |
|---|---|---|---|---|
| Detector | Bessel [Hz] | Vbol [mV] | Rbol [MΩ] | Tbol [mK] |
| C1 | 120 | 9.67 | 9.7 | 26.0 |
| T-8 ‖ T-5 | 120 | 10.0 | 5.0 | - |

**Table 7.8** - Bessel cut frequency and working points of detectors of run 9 with slabs' parellel read–out.

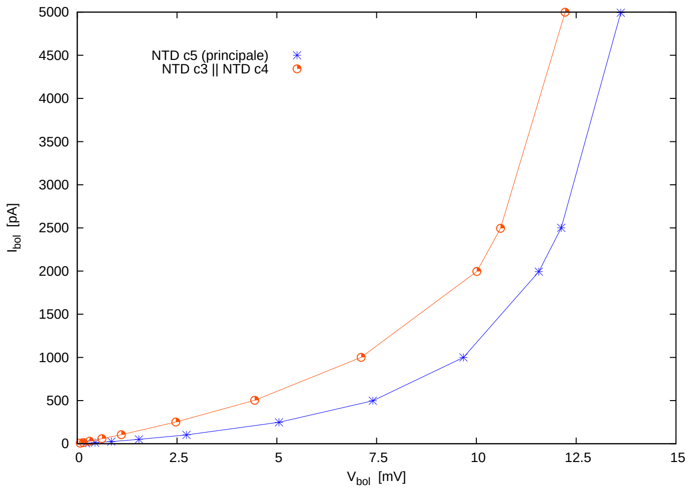


**Figure 7.33** - Load curves for the SSB of run9. The slab–bolometers are read in parallel.

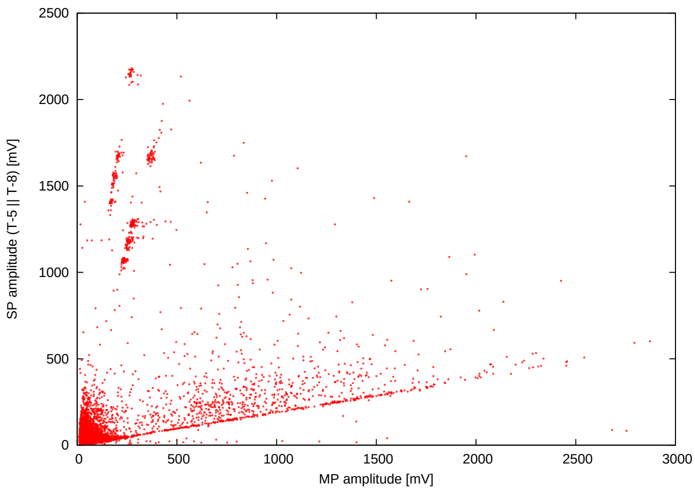


**Figure 7.34** - Scatter plot from run 9 with parallel read–out of the two $TeO_2$ slab–bolometers.

**Figure 7.35** - The T-8 slab–bolometer after the thermal cycle.

#### 7.6.6.4 Conclusions

At the end of this run, we summarize what we learned:

- $TeO_2$ slabs performed very well. However, we must find a better way to couple the thermistor to the slab absorber. In fact, after the thermal cycle, one of the two $TeO_2$ slabs broke apart where the thermistor was glued (see fig. 7.35);

- we got interesting hints that PSA could be used to provide more information, even if performed only on the main absorber thermistor;

- parallel read–out can be implemented to reduce channel proliferation without losing discrimination capabilities.

### 7.6.7 Run 10: IRST Silicon slabs

Unfortunately, due to problems in material procurement, we changed our Si supplier. New Si slabs were purchased from the Italian ITC-IRST [72] and need to be tested.

#### 7.6.7.1 Setup

The configuration of the detector is given in fig. 7.36 and is similar to that used in the previous tests with two Si slab–bolometers (Si-4 and Si-5) glued on the opposite faces of a main $TeO_2$ bolometer.

There are only two main differences with the previous detectors. First, we glued the slabs on the faces parallel to the $< 001 >$ axis, while previously we used the hard faces perpendicular to $< 001 >$. In this direction the thermal contractions are bigger than in the others. Second, we get rid of the Ge stand–offs and the slab absorbers are glued directly on the main $TeO_2$ absorber, with two small spots of glue placed in the middle of the face and aligned along the $< 001 >$ axis.

#### 7.6.7.2 Results

We will not give too many details on this run, because we had two problems that prevent us from reaching final and satisfactory results:

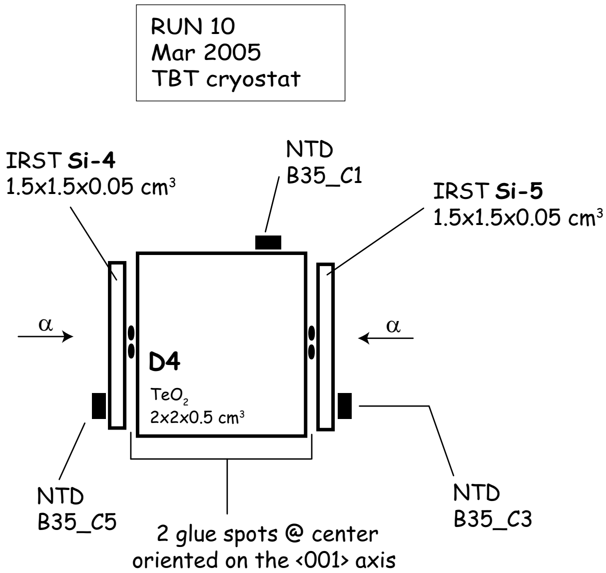


**Figure 7.36** - Scheme and details of the detectors of run 10

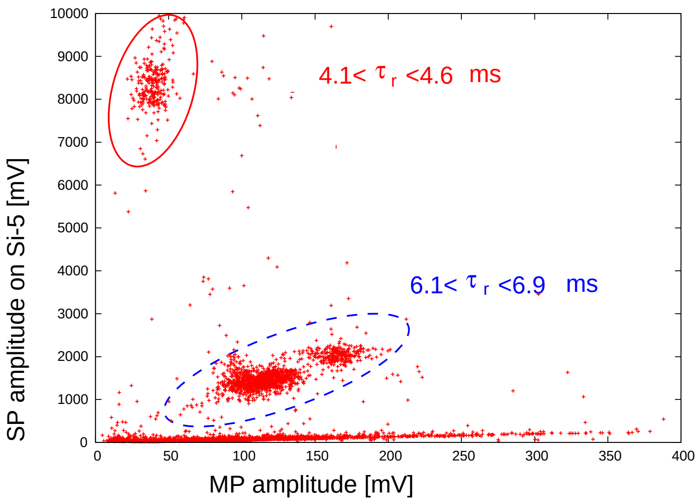


**Figure 7.37** - Run 10: scatter plot of Si-5 vs main with information obtained from the rise time distribution on the same Si-5 thermistor. The origin of the events on the top–left corner is unknown.

- one of the two slab–bolometer (Si-4) partially detached from the main absorber and did not provide good results;

- the scatter plot of the other slab–bolometer (Si-5), shown in fig. 7.37, is quite unusual because of the presence of a family of fast and energetic events of unknown origin. As we will see in the following run, this strange behavior is due to an anomaly of the B35b_c5 thermistor that was mounted on the slab.

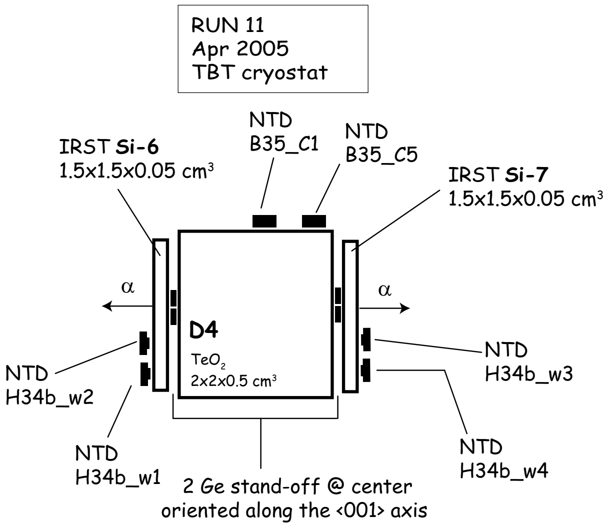


**Figure 7.38** - Scheme and details of the detectors of run 11.

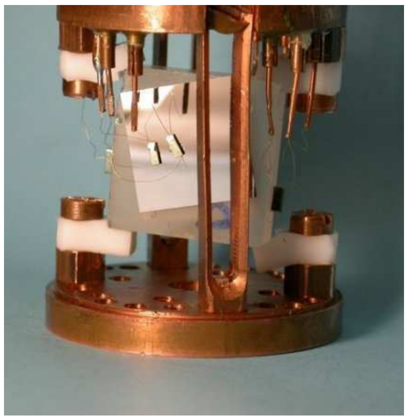

**Figure 7.39** - Picture of run 11 SSB detector. Note the presence of two thermistors on the Si slab.

### 7.6.8 Run 11: again IRST Si slabs

The previous run did not solve the issue on IRST Si slab–bolometers. We therefore set up a new run.

#### 7.6.8.1 Setup

The detector was slightly changed (cfr. fig. 7.38) to take into account the problems of the previous run. The two Si slab–bolometers were glued again on face parallel to the $< 001 >$ axis, but this time we used Ge stand–offs. Another difference is that we irradiate directly the Si slabs with the $\alpha$ source instead of using an irradiated copper tape.

The setup is the same already partially described in §6.3.3. Each element of the detector hosts two thermistors, either of classical shape (on the main absorber) or with pedestal (on the slab–bolometers) (fig. 7.39).

| **Run11 measurement 47** | | Duration: ~11 h | | |
|---|---|---|---|---|
| Detector | Bessel [Hz] | Vbol [mV] | Rbol [MΩ] | Tbol [mK] |
| D-4 (B35b-C5) | 120 | 30.2 | 207 | 23.6 |
| Si-6 (H34b-W1) | 120 | n.a. | | |
| Si-7 (H34b-W4) | 120 | 2.6 | 1.6 | 20.0 |

**Table 7.9** - Bessel cut frequency and working points of detectors of measurements 47, run 11.

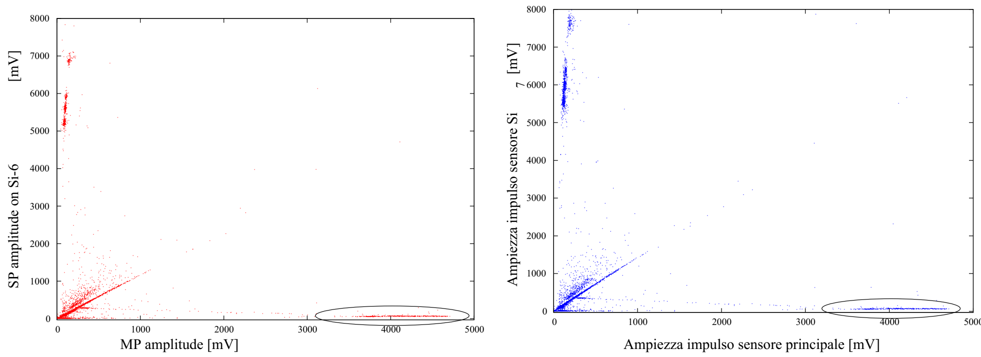


(a) Si-6 vs main (b) Si-7 vs main

**Figure 7.40** - Scatter plots of run 11 detector. The anomaly regions are circled.

#### 7.6.8.2 Results

The scatter plots for measurement number 47 are reported in fig 7.40 with parameters in tab. 7.9.

An anomaly similar to that of fig. 7.37 is present, but this time it is referred to the pulses read by the thermistor on the main. The circled regions enclose fast and energetic events. A crosscheck between the setup of the two runs highlights the fact that the same thermistor B35b_c5 was present. In run 10 it was mounted on a slab–bolometer and the anomaly pulses were seen on the slab absorber, while in this run it is mounted on the main absorber and now the unknown pulses are read by this thermistor. There are therefore good reasons to think that the problem is not in the IRST Si slabs, but in the B35b_c5 thermistor itself, which is probably contaminated. We could thus state that the IRST Si slabs can be positively used as absorbers for SSBs. However, a final test is recommended.

### 7.6.9 Run 12: couplings optimization of $TeO_2$ slab–bolometer (with a surprise)

A point still open after this sequence of tests is related to the thermal couplings of $TeO_2$ slabs with NTD Ge thermistors. Two of the three $TeO_2$ slab–bolometers used in the previous tests got broken by their thermistor. This is probably due to the fact that the Araldit glue is not sufficiently elastic at low temperature to compensate the differential thermal contractions. A new run was thus prepared

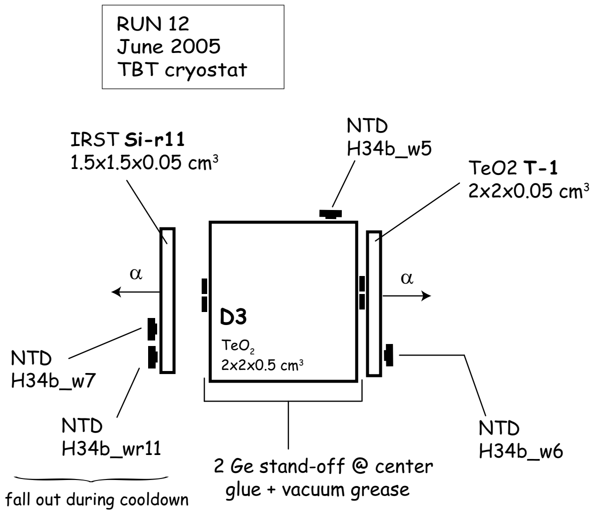


**Figure 7.41** - Scheme and details of the detectors of run 12.

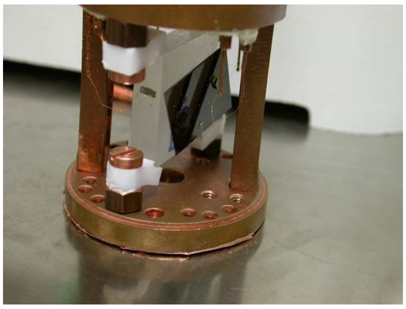

**Figure 7.42** - The detector used in run 12 after the measurements. The Si slab fell out spontaneously during the cool–down.

to test whether it is possible to replace the glue with vacuum grease (from Dow Corning [112]). We reported the details and the results of these measurements in §6.3.4.

Here we want to analyze the possible use of the same vacuum grease to attach the slab–bolometer to the main absorber. This solution could solve the problems of thermal contraction when using Si slabs, and greatly simplify the mounting procedure.

#### 7.6.9.1 Setup

As shown in fig. 7.41, the detector was designed to have two slab–bolometers, one made of Si and the other of $TeO_2$ . Unfortunately, the Si slab fell out during the cool down (as shown in fig. 7.42) and so we remain with only one $TeO_2$ slab–bolometer.

#### 7.6.9.2 Results

As usual, let us start our analysis from the scatter plot of the amplitudes of T-1 pulses vs main pulses (fig. 7.43). The two bands of surface and bulk events are

| **Run12** | | | | |
|---|---|---|---|---|
| Detector | Bessel [Hz] | Vbol [mV] | Rbol [MΩ] | Tbol [mK] |
| D-3 | 120 | 3.9 | 384 | 25.6 |
| T-1 | 120 | 2.56 | 101.6 | 33.1 |
| Si-r11 | detached | | | |

**Table 7.10** - Bessel cut frequency and working points of detectors of run 12.

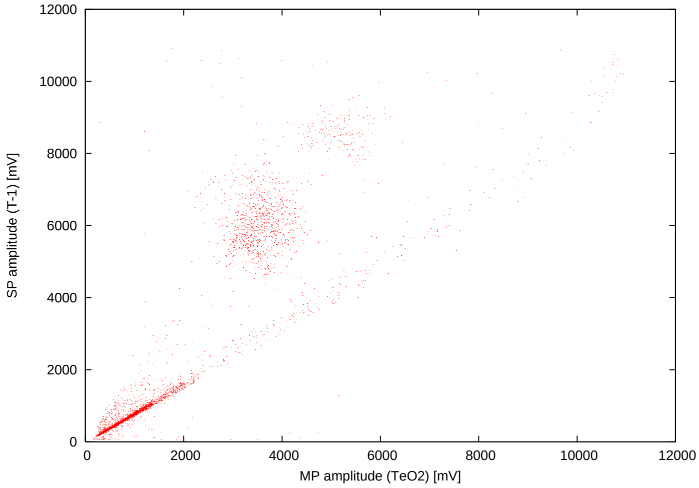


**Figure 7.43** - Scatter plot of run 12. The surface event band is present, but it is unusually broad.

recognizable even if the surface events are quite spread over a range of values. It is however clear that, as far as the discrimination capabilities are concerned, the detector performed well.

The rise time discrimination is very effective, as shown in fig. 7.44. Instead of the usual $\tau_R$ spectrum, we plot the rise time vs the amplitude for T-1 SPs, which is a clearer graph and allows smarter cuts.

An important and unexpected result has been obtained in this run and

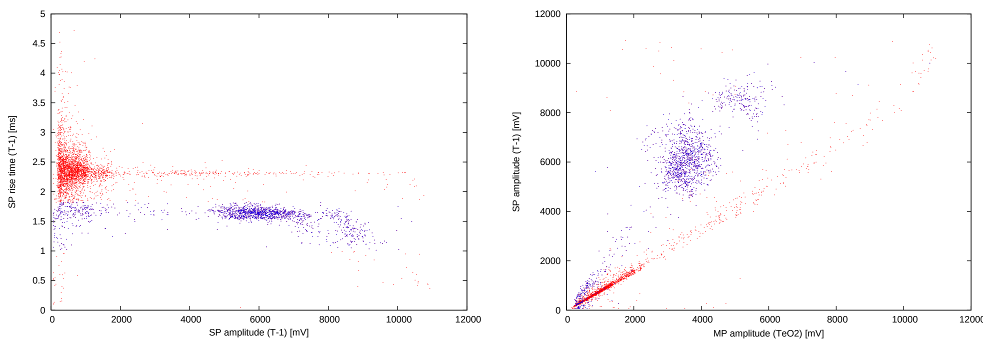


**Figure 7.44** - Rise time selection on run 12 data. The rise time vs amplitude of T-1 pulses (left) allows to select 1 ms ¡ $\tau_R$ ¡ 1.82 ms, which correspond to the surface events in the scatter plot (right).

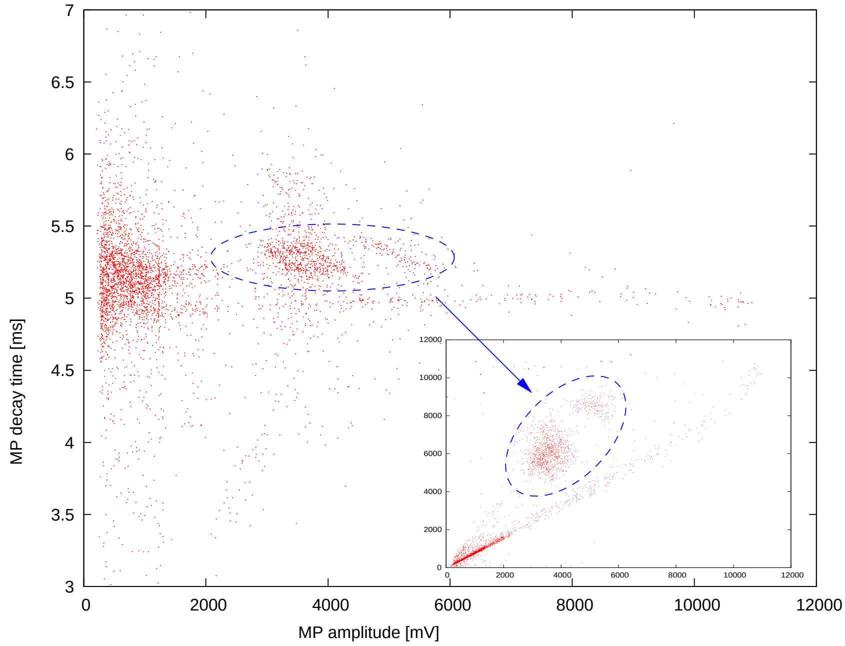


**Figure 7.45** - Run 12: discrimination of events based on decay time of pulses from the main bolometer.

is related to what anticipated in §7.6.6.2 about the possible identification of surface events using PSA on the pulses from the main bolometer. The effect is shown in fig. 7.45. This result is very important and leads the way to what will be much more evident on large–size prototypes, as we will see soon in the next section.

## 7.7 Tests of rejection efficiency at underground site

### 7.7.1 Goals and objectives

The experiments carried out during the year 2004 and documented in the previous section gave indeed very promising and encouraging results on the application of the SSB technique. The working principle was proved and different kinds of PSA were devised for the discrimination of surface events.

The next step clearly involves the application of this technique to large–size CUORE–like bolometer. A final validation of the SSB technique requires

- test on large–size crystals ($5 \times 5 \times 5$ cm$^3$): the extrapolation from small–scale prototypes is not always safe; moreover, there might be thermal, mechanical or assembly problems which do not show up in smaller detectors;
- complete coverage: up to now, only one or two slab–bolometers were used on each SSB;

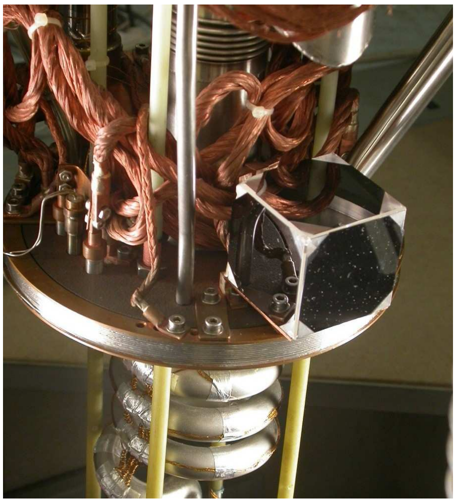

**Figure 7.46** - A $5 \times 5 \times 5$ cm$^3$ SSB with Si slabs placed on the 70 K flange of the AL cryostat for a thermal cycle test.

· quantitative evaluation of the background reduction: this goal can be achieved only in underground tests, were we have good control on the radioactive level; as discussed in §3.9.1, we will be especially interested at the 3–4 MeV region of the spectrum.

To address this item, a one year R&D program was pursued from Spring 2005 to September 2006. The Hall C cryostat at LNGS (see §4.4) is the natural environment for these tests.

### 7.7.2 Run SSB–LNGS–1

#### 7.7.2.1 Setup

The first run was shared with a test of the new design of the CUORE assembly. A 3–planes tower was prepared to host 8 normal bolometers and 4 SSBs (in the bottom plane).

Due to a delay in the delivery of the $TeO_2$ slabs, the four detectors were realized gluing a Si slab ($50 \times 50 \times 0.3$ mm$^3$) on each face of the $5 \times 5 \times 5$ cm$^3$ crystals. The coupling of the Si slabs was made with two Ge stand-offs oriented along the $< 001 >$ axis, glued with a veil of Araldit® as in §7.6.8. Small amounts of vacuum grease were added to help holding together those slabs which fell out during the assembly.

Several gluing tests has been previously performed in Como, to evaluate the mechanical stability. One prototype underwent a thermal cycle at $LN_2$ temperature, to test the effect of thermal contractions. The AL cryostat (see §4.3.2) was particularly useful for such test. We used the pulse tube to cool down the 70 K and 4 K flanges where some space is available to host a $5 \times 5 \times 5$ cm$^3$ detector as shown in fig. 7.46

The coverage of three crystals (fig. 7.47(left)) was not complete: a roughly triangular area on each vertex was not faced by the slab, being then partially

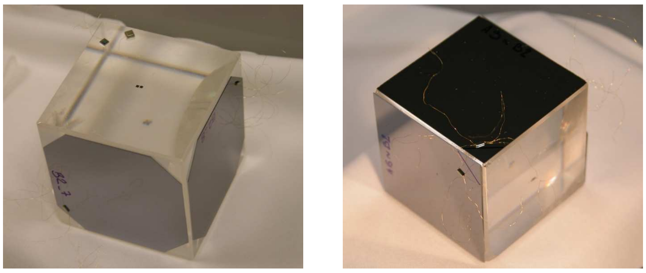

**Figure 7.47** - SSB with Si slabs with partial (left) and full coverage (right). The pictures were taken during the slabs assembly when some slabs were still to be glued.

covered by the PTFE pieces used to held the crystal in the copper frame; the Si slabs covered the fourth crystal almost completely (fig. 7.47(right)), and the Teflon tips were positioned on the slabs themselves. This was the smallest crystal: its dimensions were much smaller that those foreseen for this mounting system, and the interposition of the slabs between the crystal and the PTFE tips increased the size of the detector, helping to hold the crystal firmly in the mounting. Unfortunately, this was not enough: this crystal, as well as the other with particularly small dimensions, resulted loosely held in the mounting, with a consequent deterioration of their performances.

Each slab was provided with its own NTD Ge thermistor used to read–out the thermal signal. Thermistors of the series #31 were used for the $TeO_2$ absorbers, while the Si slabs host pedestal thermistors (see §6.3.3) belonging to series #34. The latter are attached to the Si slabs with a small amount of vacuum grease. During the wiring, we broke few slabs–thermistors, and new ones had to be added. The six thermistors of the slab–bolometers were connected in parallel (cfr. §7.6.6). In this way, for each detector, only two channels were acquired: the main and the parallel of the slabs.

The final 4-detectors plane is shown in figure 7.48.

We emphasize that no special cleaning procedure was performed on the detectors.

#### 7.7.2.2 Results

The two detectors with smaller dimensions showed rather poor performances, responsible for the excess noise due to their vibrations, while for the other two (named B21 and B33) a good energy resolution, compatible with that of Cuoricino detectors, was measured. Their working points are given in table 7.11.

The performances can be appreciated from fig. 7.49, where a fit of the $^{40}$K peak is done on the spectrum of the thermistor on the main absorber of the two good detectors. The FWHM is 5.5 keV for the B21 and 6.53 keV for the B33 at $\sim 1.46$ MeV ($^{40}$K decay).

The slab–bolometers could be read-out only for the B21 detector due to a wire problem during the cool–down. Our analysis will therefore concentrate only on this SSB.

Signals were acquired on both main and slab (we mean the parallel of the

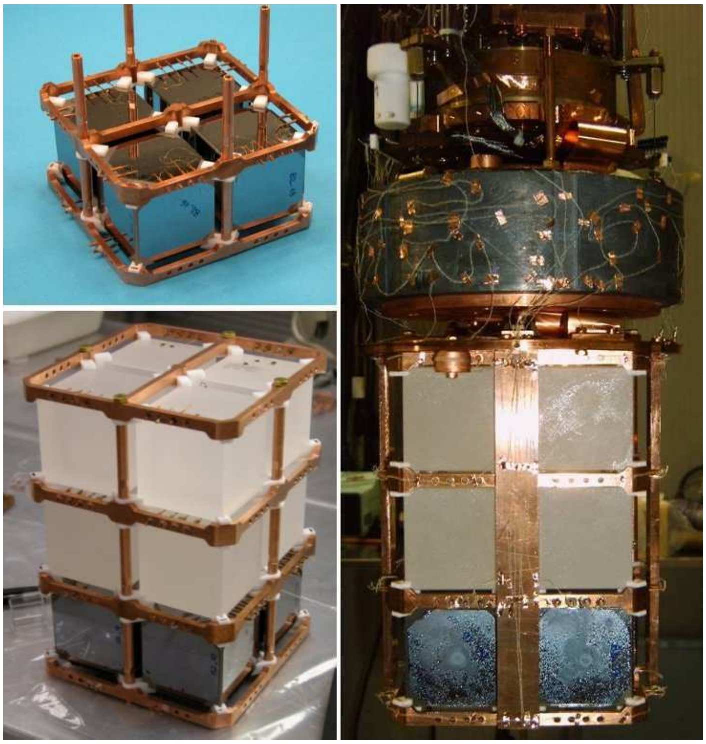

**Figure 7.48** - Top left: The plane with the 4 SSBs. Bottom left: the full 3-planes tower. Right: the tower mounted below the Hall C cryostat.

| **Measurements: 1018–1030 + 1039–1065**<br>Duration: 540.31 h | | | | |
|---|---|---|---|---|
| Detector | Bessel [Hz] | Vbol [mV] | Rbol [MΩ] | Tbol [mK] |
| B21 main | 12 | 6,295 | 95,5 | |
| B21 slabs | 20 | 2,590 | 15,6 | |
| B33 main | 12 | 3,103 | 35,1 | |
| B33 slabs | lost during cooldown | | | |

**Table 7.11** - Bessel cut frequency and working points of SSB detectors of SSB–LNGS–1 run.

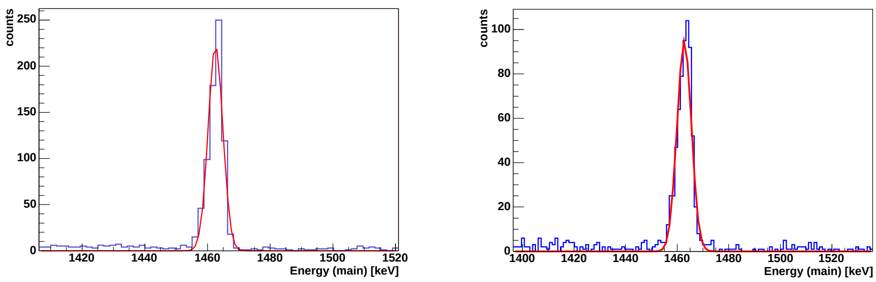


**Figure 7.49** - Fit of the $^{40}$K peak for the B21 (left) and B33 (right) SSB detectors

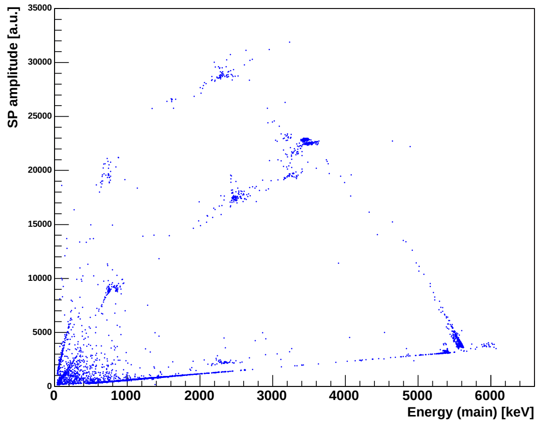


**Figure 7.50** - Scatter plot of SSB–LNGS–1 run, detector B21.

6 slabs) channels with an independent trigger and trigger threshold. Once only signals above the common maximum threshold are considered, only coincident events are observed. The amplitude measured on the main was calibrated in energy exposing the detector to a gamma source: this provides a correct conversion of the MP amplitude, which is meaningful only for those signals due to pure interaction in the main $TeO_2$ absorber. A similar calibration was not possible for signals produced in the slab–bolometers.

**Scatter plot**

The scatter plot of coincident events is shown in fig. 7.50. We can easily recognize the familiar band of *bulk events* in the lower part of the plot and the *surface events* band which is composed by multiple lines, because we have 6 different slab–bolometers. The graph is very similar to that observed in fig. 7.34 for a small prototype.

Mixed events are ascribed to surface alpha contamination. In the scatter plot they appear as a line connecting the bulk and the surface events band. The contamination is probably due to $^{210}$Po. A peak at about 5.3 MeV is in fact present in the main absorber spectrum. However, the peak is not exactly at the expected energy value for the $^{210}$Po decay.

A comparison with MonteCarlo simulations (see figures 7.51 and 7.52) performed by O. Cremonesi shows that the contamination is probably on the slabs surfaces. The presence of the gap between the mixed event line and the bulk event band is due to the recoil energy of the $\alpha$-decaying nuclide. On the contrary, a surface contamination on the main absorber should produce a mixed event line that starts from the bulk band. These considerations are very positive hints that SSB are able to identify also surface contamination between the main absorber and the slab, which is dangerous because it can give rise to that continuum background which extends down to the $\beta\beta0\nu$ region, and which we are trying to avoid. Events from $TeO_2$ or slab surface contamination are moved into the mixed event region of the scatter plot and thus removed from the main

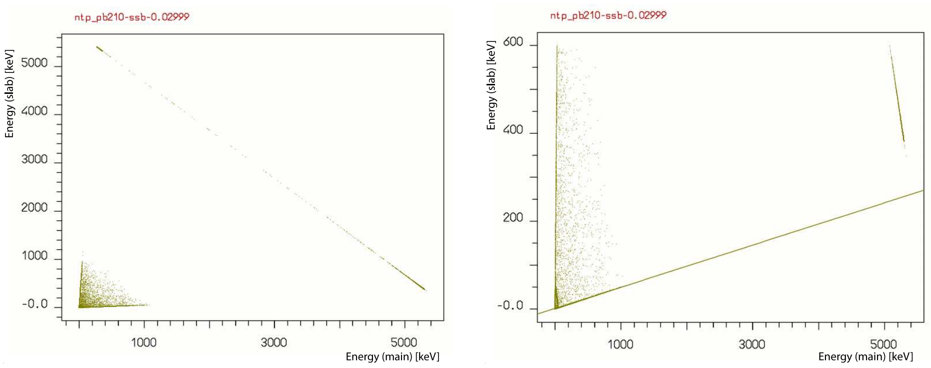


**Figure 7.51** - Scatter plot from MonteCarlo simulation of a $^{210}$Pb contamination on the slab at 1 $\mu$m depth. Full plot (left) and zoom of the alpha region close to the bulk event band (right). The gap is due to the recoil energy.

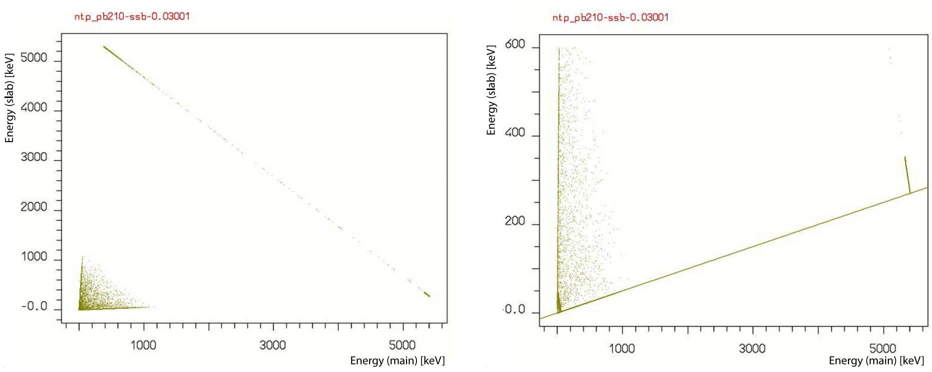


**Figure 7.52** - Scatter plot from MonteCarlo simulation of a $^{210}$Pb contamination on the main absorber at 1 $\mu$m depth. Full plot (left) and zoom of the alpha region close to the bulk event band (right)

event band.

A final comment on the scatter plot of fig. 7.50, which is also linked to the arguments just mentioned, is the high contamination level of the detector elements. We remind the reader that no external radioactive source was introduced in the setup. Nevertheless, it is clear that both the slabs and the main absorber are contaminated. However, few untested elements were used, namely the vacuum grease and the ink of a pen used to mark the slabs. The contamination could also be in the slabs themselves. The worst thing is that the region of the bulk event band between the $^{210}$Po peak and the gamma region is not empty as we expected. We will come back later on this subject, but, as a first hypothesis, we could guess that these events arise from surface contamination of the main absorber in places that are not covered by the slabs ($\sim 5\%$).

### SP rise times analysis

We are now familiar with the use of the SP rise time to recognize the surface events band, and these large–size bolometers are not an exception, as shown in fig. 7.53. In this plot, we can also see that we are able to identify all the six slabs that are read in parallel.

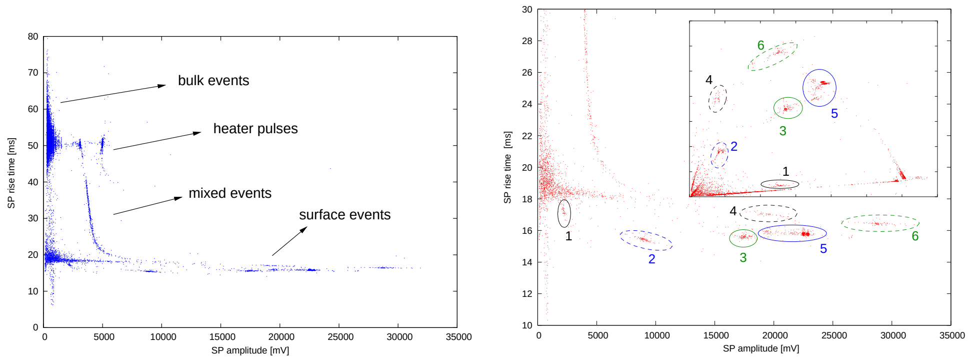


**Figure 7.53** - (left) Rise time vs amplitude for SP for B21 detector. (right) SP rise time discrimination of surface events and identification of the six slabs (that are read in parallel).

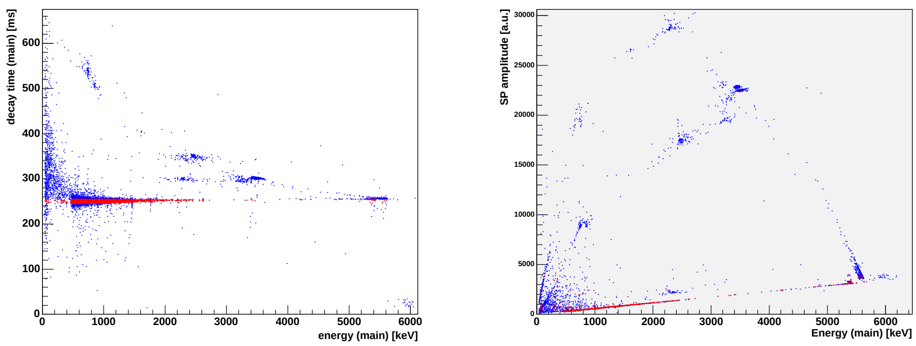


**Figure 7.54** - MP decay time discrimination for the B21 detector of the SSB–LNGS–1 run.

We must also note that the events grouped inside the circle labeled '1' (fig. 7.53(right)) are too close to the bulk event band, when reported in the scatter plot. The reason for this behavior could be that the coupling of the slab (to which these events belong) with the main absorber is too high. Another possibility is that the slab was not electrically connected, and therefore surface events are not recognized as such in the scatter plot. This explanation will be better investigated in the next run. In a parallel readout it is indeed not easy to check that all six thermistors are really acquired.

Similar results on pulse classes recognition can be obtained from SP decay times analysis.

### MP decay times analysis

Figure 7.54 (left) shows a plot of the MP decay time vs amplitude for the B21 SSB. What is clearly evident is that the events belonging to the main band have the usual distribution observed in normal bolometers, while surface or mixed events are well distinguishable because of their slower decay time. The conclusion is that the presence of the slabs thermally connected on the $TeO_2$ crystal modifies the response of the bolometer in such a way that bulk events are distinguishable from surface events just looking at their decay time. The effect of the DT selection is shown in fig. 7.54 (right).

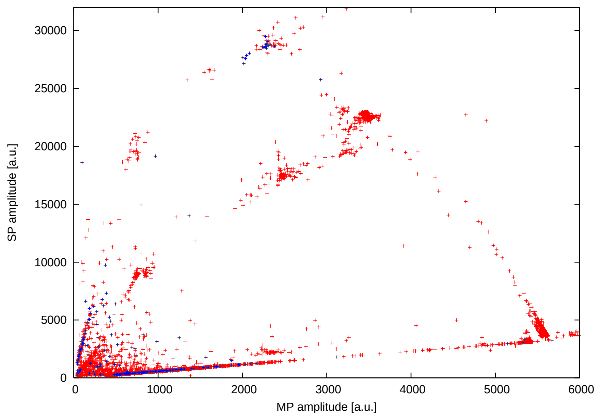


**Figure 7.55** - Scatter plot of SSB–LNGS–1 run for detector B21. The blue points are selected by coincidence with the above B64 detector.

A similar figure is obtained for the other B33 detector (the one with the SSB electrical contact disconnected), proving that this is a characteristic feature of these composite bolometers. The rejection efficiency for alpha events, in the region of the $\beta\beta 0\nu$ signal, appears to be in both cases quite high.

It is useless to underline the importance of this result, that confirms what was already seen with the small prototypes in Como. We must note however that this effect, at this point, is not completely clear, and the parallel read–out surely does not help understanding the underlying physics.

### Coincidence analysis with a normal bolometer

The presence of two planes of normal bolometers is very important for background comparison. Before that, we analyze the coincidence events between the B21 SSB detector and the normal bolometer placed above it (named B64). The selected points are plotted in fig. 7.55. A slab line is evidenced and is related to the top slab that faces the B64 detector. Several classes of events appear. Their origin can be recognized by looking at their position in the scatter plot and then at the energy released in the B64 detector:

- high energy surface events: they are probably due to an $\alpha$ contamination (probably $^{210}$Po) on the surface of the B64 bolometer, where the energy released is only $\sim 100keV$ corresponding to the nuclear recoil;

- high energy bulk events: similarly to the previous situation, since the slab coverage is not full, part of the $\alpha$ from the B64 surface are able to strike directly onto the main absorber of the B21 SSB and release there their energy (again very close to $^{210}$Po $\alpha$s); the recoil is observed in the B64 spectrum;

- low energy bulk events: they are due to $\gamma$ events that interact in both main absorbers; a plot of the sum energy shows clearly the presence of a peak at the energy of $^{40}$K (fig. 7.56);

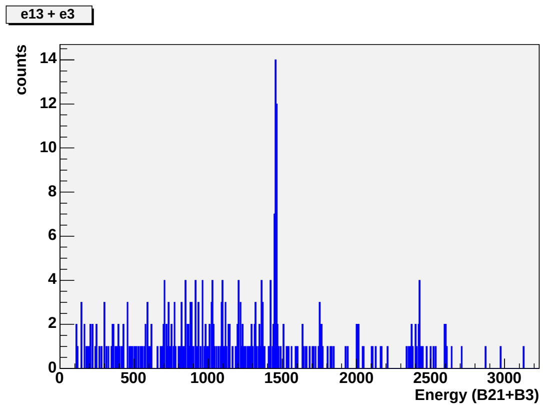


**Figure 7.56** - Energy spectrum of the sum of coincident events in the main absorber of the B21 SSB and in the above B64 normal bolometer. A peak at the $^{210}$Po $\gamma$-decay energy appears clearly.

| | energy regions | | |
|---|---|---|---|
| | 2.9–3.2 [MeV] | 3.2–3.4 [MeV] | 3.4–3.9 [MeV] |
| normal bolometer anti-coincidence average | $0.44 \pm 0.06$ | $0.58 \pm 0.09$ | $0.41 \pm 0.05$ |
| B21+B33 SSB average (decay time cuts) | $0.17 \pm 0.08$ | $0.51 \pm 0.16$ | $0.29 \pm 0.08$ |

**Table 7.12** - Comparison of the background in the region above natural radioactivity for normal bolometers and SSB bolometers with cuts on MPs decay time for the SSB–LNGS–1 run. Values are expressed in counts/keV/kg/y.

- low energy surface events: among these events we found 7 that are due to nuclear recoil of $\alpha$ contamination, in the slab that faces the B64 detector where the $\alpha$ releases about 5.3 MeV (again $^{210}$Po); highly degraded $\alpha$ particles will also fall in this region along with low energy photons;

- low energy mixed events: these are events due to multiple interaction of photons in each of the selected elements: the SSB B21 main absorber, its upper slab and the B64 absorber.

### Background reduction

In spite of the absence of special cleaning procedures for the detector and mounting structure, we tried to quantify the background reduction achievable by selecting only bulk events by means of a cut on the decay time of the MPs, as in fig. 7.54. A comparison can be easily made with the other normal bolometers that were measured in the same setup. The background spectrum integrals in the $\alpha$ regions are given in tab. 7.12.

The result is very encouraging, because the values in the 2.9–3.2 MeV region is very close to that of Cuoricino, even with an high contamination level.

We have checked what happened to a normal peak, when the cuts on the MPs decay time are applied. We used the huge $^{40}$K peak for both B21 and B33 detectors. The result is that the decay time cuts leave practically unchanged (of the order of 0.1%) the “normal” events in the 1–2 MeV region.

**Open questions**

The results reported up to now are very promising and confirm the great possibility of the SSBs. However, some aspects of this test are not fully understood:

· what is the $\alpha$ contamination source and where is it placed? Our analysis is consistent with $^{210}$Po, but the energy is 100 keV too high. Is it only a problem of calibration?

· where is the missing 5.4 MeV line of $^{210}$Po which is common to all our bolometers?

· do we really read all the six slabs thermistors?

The parallel read–out does not help understanding the SSB behavior: it is difficult to separate each slab contribution or, even worse, to know if a slab is missing. At the end of the experiment we found out that three slabs were weakly coupled, therefore affecting the behavior of the SSB.

In an effort to answer these questions, we prepared a new run.

### 7.7.3 Run SSB–LNGS–2

The aim of this test if to verify how contaminations in different points of the detector contribute to scatter plots. From the analysis of the previous test, some unclear points were still present due to the complication induced by the large contamination and the parallel read–out of the slabs. This run is not a background test: it is somehow more technical, more similar to those of §7.6.

#### 7.7.3.1 Setup

The setup for this run was very similar to that used in Como during run 9 (see §7.6.6 and fig. 7.29), where two $TeO_2$ slab–bolometers (S1 and S2) are glued on a $TeO_2$ main absorber of $2 \times 2 \times 0.5$ cm$^3$. As indicated in this figure, the peculiarity of this setup is the Uranium contamination (see 7.5.3) location. In fact, few drops of U loaded water evaporated on the side of S1 that faced the main absorber. The face of the main on which S2 is glued is contaminated as well. In this way we will be able to check whether we can identify events coming from the surfaces of the absorbers.

The Araldit glue was used to place the slabs, while the slabs thermistors were attached with small amounts of vacuum grease.

Each thermistor was acquired separately to gain all possible information on the detector.

The detector was mounted on the cold finger linked to the first decoupling stage of the Hall C cryostat. As a consequence, the detector setup was not optimal from the microphonic point of view, and this situation affected the measurement quality - but not the main results, as we will see soon.

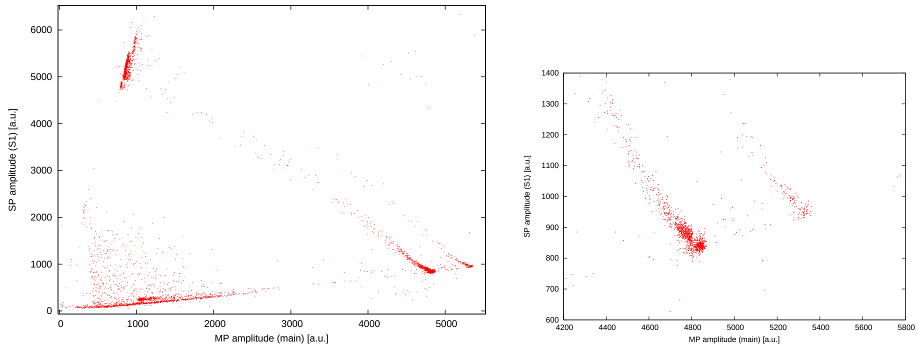


**Figure 7.57** - Scatter plot of the contaminated S1 slab (right) and zoom of the $\alpha$ region close to the bulk event band (left).

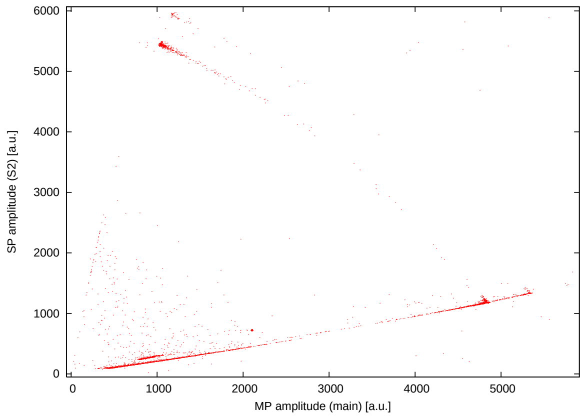


**Figure 7.58** - Scatter plot of the S2 slab that faces the contaminated face of the main absorber.

### 7.7.3.2 Results

We report here only the statistics acquired with one single measurement of only 15 hours. Nevertheless, the scatter plots are very interesting and features–rich. They are shown in fig. 7.57 and 7.58. The working points are provided in tab. 7.13.

Both plots confirm the simulated and expected behavior shown in fig. 7.52 and 7.51, and previously discussed. When the contamination is on the slab, the mixed events are very close to the bulk event ($\alpha$s very close to surface with only

| **Measurement 1093** | | Duration: 15 h | | |
|---|---|---|---|---|
| Detector | Bessel [Hz] | Vbol [mV] | Rbol [MΩ] | Tbol [mK] |
| $TeO_2$ main | 20 | n.a. | 9.45 | |
| S1 slab | - | n.a. | 12 | |
| S2 slab | - | n.a. | 2.4 | |

**Table 7.13** - Bessel cut frequency and working points of detectors of measurements 1093, run SSB–LNGS–2.

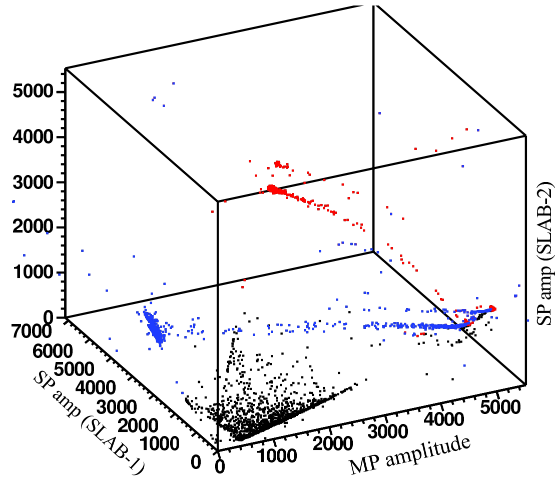


**Figure 7.59** - 3D scatter plot of the MP amplitude vs the SP amplitude on both S1 and S2 slabs. Events due to the $\alpha$ contaminations in the two different parts of the detector are highlighted. Blue: contamination on S1. Red: contamination facing S2.

nuclear recoil left in the slab), while events due to contaminations in the main absorber appear close to the surface events band. The presence of a gap due to the energy of nuclei recoils is evidenced in fig.7.57 (right).

Interesting considerations can be drawn by looking at a simultaneous 3D scatter plot of both plots, like the one reported in fig. 7.59. In that graph we selected in different color the $\alpha$ events on the two slabs: in blue those due to $\alpha$ particle from the S1 contamination, and in red those coming from the main absorber contamination facing S-2. When this plot is converted into the usual bidimensional scatter plots as in figures 7.60 and 7.61, an important feature is unveiled. In fact, on a scatter plot, surface events on the other slab appear as bulk events. In this way, we could explain the origin of the second short line at low energy that is parallel to the bulk event line.

What is dangerous here it's those mixed events that leave most of their energy in the main absorber, because they fall in the $\beta\beta0\nu$ region of the main absorber energy spectrum, if they are not properly recognized as mixed events on the opposite slab. The rejection method based on the scatter plot analysis is therefore very powerful, but it might dramatically worsen the background if any slab is missing (e.g. thermally connected but not electrically read–out).

### 7.7.4 Run SSB–LNGS–3

In the hope of setting up the "final test" on SSB, we worked on a new experiment. The goal is to evaluate the background reduction in a setup that resembles, as close as possible, the CUORE one, at least for what concerns material cleaning and mechanical structure.

The test aims also at looking for a confirmation of the possibility of avoiding the use of the thermistors on the slabs, and therefore selecting the surface events only by looking at the decay time of the pulses recorded by the thermistor on

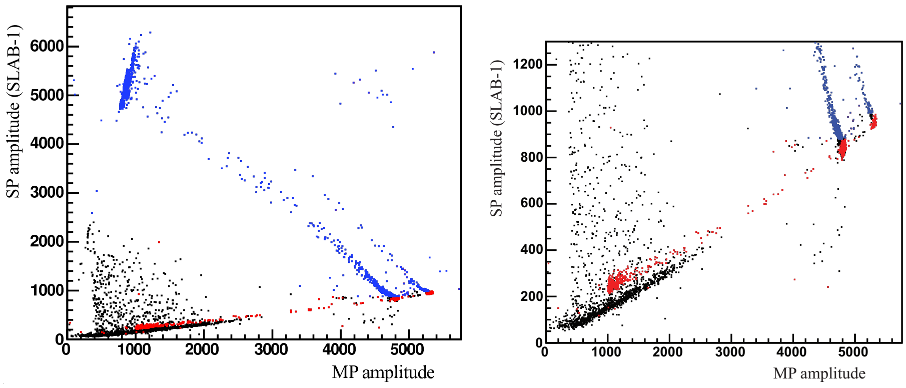


**Figure 7.60** - Scatter plot of the MP amplitude vs the SP amplitude of S1 and zoom of the $\alpha$ region (left). Events due to the $\alpha$ contaminations in the two different parts of the detector are highlighted. Blue: contamination on S1. Red: contamination facing S2.

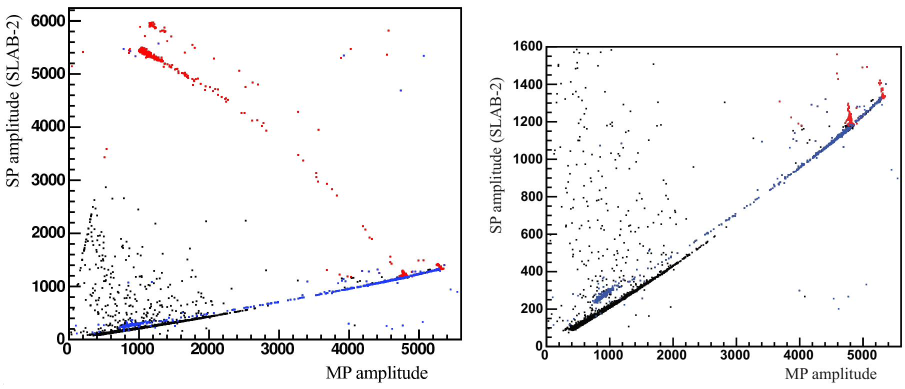


**Figure 7.61** - Scatter plot of the MP amplitude vs the SP amplitude of S2 and zoom of the $\alpha$ region (left). Events due to the $\alpha$ contaminations in the two different parts of the detector are highlighted. Blue: contamination on S1. Red: contamination facing S2.

the main absorber.

#### 7.7.4.1 Setup

As in the first SSB run at LNGS, an array of 12 crystals was prepared during the first months of 2006, where the bottom plane hosts 4 SSBs. This time we used $TeO_2$ slabs (like those of fig. 7.62) and the same cleaning procedure used for the RAD array (crystal and copper etching, clean room assembly, ...- see §3.9.1). Only the $TeO_2$ slabs were not cleaned specifically due to their fragility.

The dimensions of the main bolometers were requested to fit exactly in the holder - as we learned from the first run at LNGS, detectors work better if they are well tightened in their position!

To reduce the time required to prepare the detector and because of the limited number of wires available in the cryostat, two SSBs have 5 *passive* slabs and only one *active* slab. We speak about *passive* slabs when the thermistor of the slab–bolometer is missing, i.e. we do not have a real slab–bolometer, but

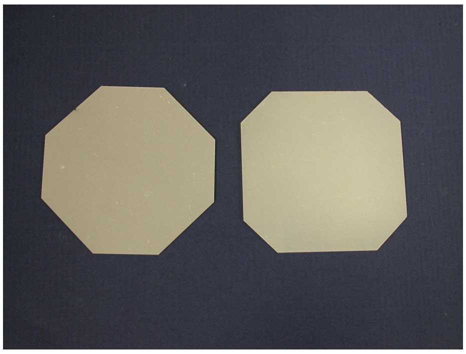

**Figure 7.62** - Two different kind of $TeO_2$ slabs used in the SSB–LNGS–3 run.

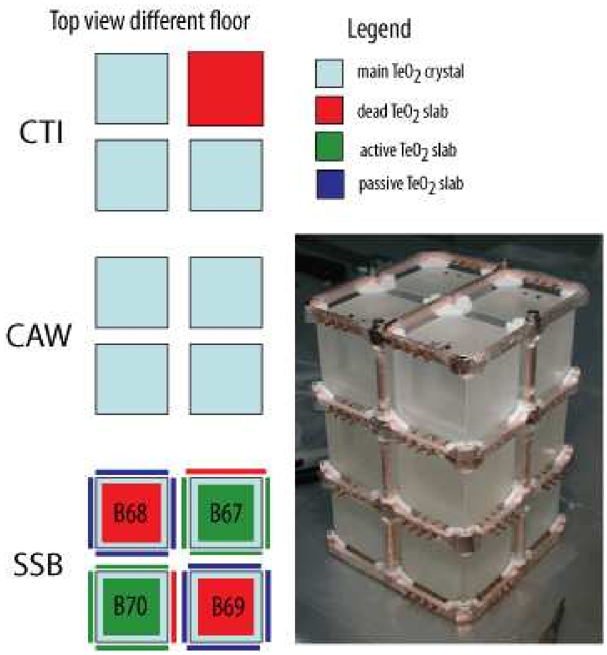


**Figure 7.63** - Scheme and picture of the detectors of Run SSB–LNGS–3.

only a $TeO_2$ slab. An *active* slab is instead a usual slab–bolometer where the thermistor is read–out. The other two SSBs have full independent read–out as shown in figure 7.63. Detectors' names are stated in the same figure. Unfortunately, during the cool–down, we lost the connection with 3 active shields on 3 different detectors. Moreover, on the fourth SSB, the only active shield had a strange behavior (very small pulses without clear coincidence with the rest of the detector), that made it unusable. Summarizing, we have two detectors with five active slab–bolometers plus a passive slab, one detector with six passive slabs, and the last detector with five passive slabs plus an unusable slab (that might even be thermally disconnected from the main, and thus cannot be classified as *passive*).

#### 7.7.4.2 Results

Two measurements sets were acquired and analyzed for a total of about 950 h of statistics. We will report here only the results of the second set, but these are fully compatible with those of the first set. Between the two sets, few hardware changes were performed, namely concerning the trigger method and channel gain. Unfortunately, also a general worsening of the quality of the measurements did occur, and therefore the resolution of the detector was not as high as expected.

The prototype nature of these detectors forced us to follow different paths for data analysis. First, we investigated the parameters space to find out if there is any correlations that might be useful to discriminate between bulk and surface events. Comparison with scatter plots and information from slab–bolometers is very useful in this process. A calibration measurement (like those performed in Cuoricino with $^{232}$Th source) is also useful. Surface $\alpha$ contaminations are too weak to give significant contributions, while bulk events from $^{232}$Th gamma events can be used to look at their pulse parameters (decay/rise time, TVR, TVL, ...).

Here, we divide our analysis in two steps:

1. pretend we do not have the read–out of the active slab–bolometers and perform a blind analysis using only the information provided by the MPs to select the events and evaluate the counting rate in the 3–4 MeV region;

2. cross–check the results and the selection efficiency by adding the information from the SPs.

We underline that this analysis and the results are only preliminary, because the run was stopped only very recently in September 2006. For this reason, we concentrate our efforts only on the 3–4 MeV region of the bolometers spectra.

The working points of the detectors are in tab. 7.14

**Blind analysis on MP decay times**

Let's start by looking at the resolution of the detectors reported in fig. 7.64. They were deducted on the $^{40}$K from the sum of the background measurements of the 2nd dataset. As already anticipated, the resolution is not very high, especially for the detectors with active slabs, due to high microphonic noise.

Calibration measurements were used to convert MP amplitude into energy. Energy calibration was not possible for slabs.

After a general clean-up of the background measurements (noise, 2nd pulses, double triggers, ...), we plotted the decay time vs amplitude of the MPs for all the detectors, as in fig. 7.65. It is evident that, despite the precaution on detector contaminations, there is an unwanted high level of $\alpha$ contamination coming from the slabs.

Our challenge is to find out if we are able to discriminate these events. Let us look at the B70 detector, for which we have 5 active slabs that we will use later to cross–check the results. We performed the following cuts in the decay time vs amplitude plot (see fig. 7.66):

| Measurement 1292–1333 | | |
|---|---|---|
| | | Duration: ∼758 h |
| Detector | Bessel [Hz] | Rbol [MΩ] |
| B67 | 8 | 2.35 |
| B67 slab 1 | 12 | 114 |
| B67 slab 2 | 12 | 88.6 |
| B67 slab 3 | 12 | 140 |
| B67 slab 4 | 12 | 52 |
| B67 slab 5 | 12 | 61 |
| B67 slab 6 | lost wire connection | |
| B68 | 8 | 144 |
| B68 slab top | lost wire connection | |
| B69 | 12 | 48.6 |
| B69 slab top | not usable | |
| B70 | 12 | 25.5 |
| B70 slab 1 | 80 | 135 |
| B70 slab 2 | 80 | 305 |
| B70 slab 3 | 80 | 242 |
| B70 slab 4 | 80 | 99 |
| B70 slab 5 | 80 | 87 |
| B70 slab 6 | lost wire connection | |

**Table 7.14** - Bessel cut frequency and working points of detectors of run SSB–LNGS–3 in the second set of measurements.

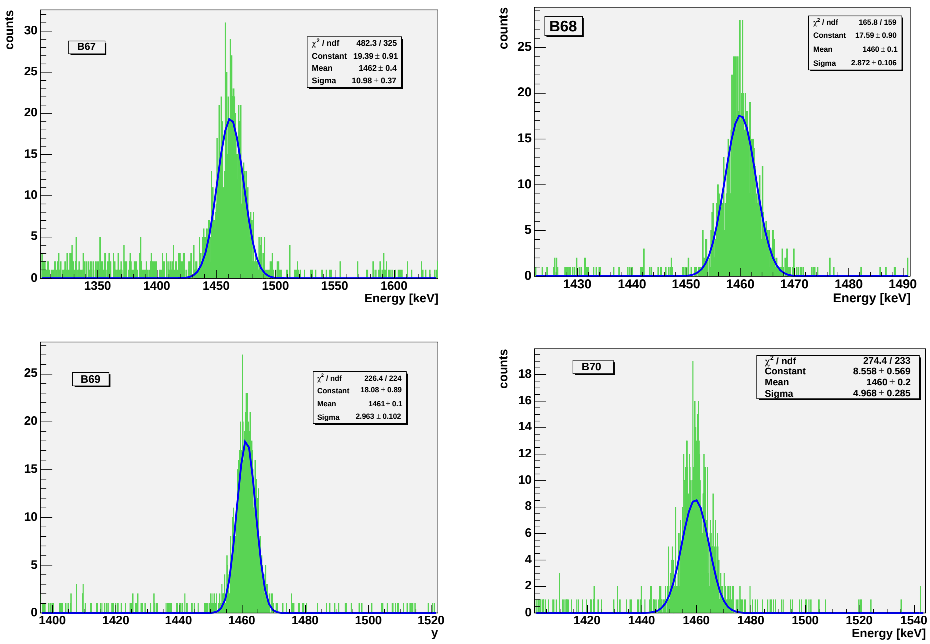


**Figure 7.64** - Fit of the $^{40}$K peak at 1460 KeV for the four SSBs from the background measurements of set2. The FWHM are: B67: 25.8 KeV; B68: 6.7 KeV; B69: 7.0 KeV; B70: 11.6 keV.

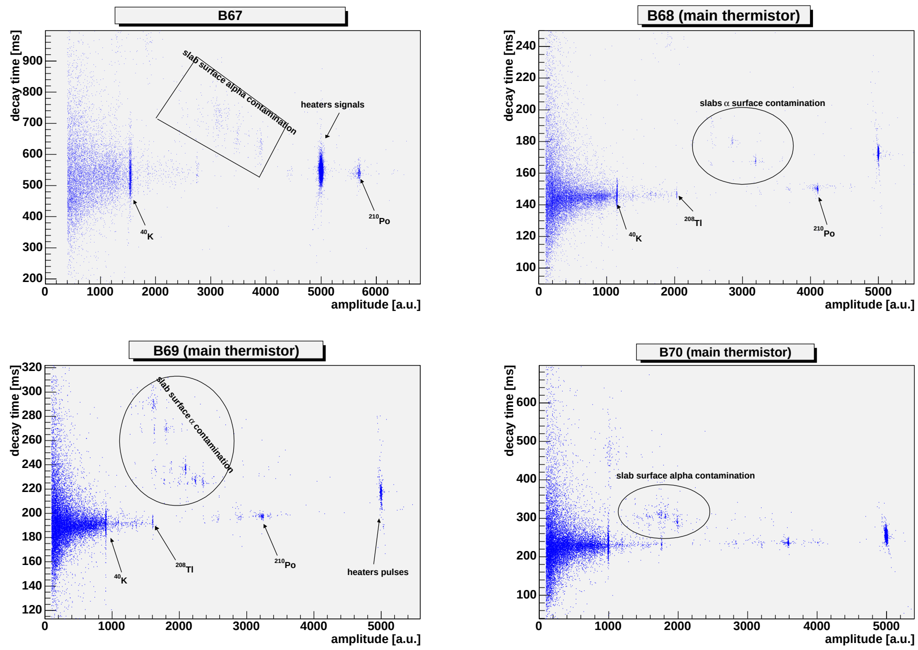


**Figure 7.65** - Plots of the decay time vs amplitude of the pulses recorded by the thermistor on the main absorber for all SSBs.

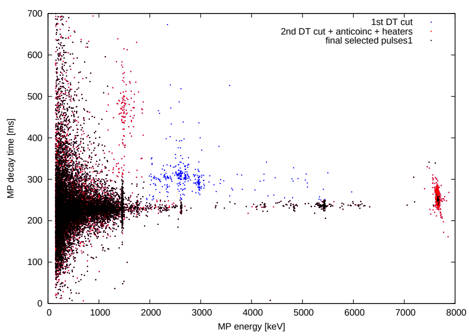


**Figure 7.66** - DT cuts for the B70 SSB. See text for cuts details.

- 1st cut of the events in this range:

$$1900 < \text{amplitude [keV]} < 6000 \quad \text{AND} \quad 250 < \text{decay time [ms]} < 1000;$$

- remove all events that have a 0.2 s coincidence with another detector in the whole array (global anticoincidence);

- 2nd cuts of those events in this range:

$$1200 < \text{amplitude [keV]} < 1900 \quad \text{AND} \quad 300 < \text{decay time [ms]} < 1000;$$

The spectrum of the remaining events is given in 7.67. A handful of events is still present in the region above 2.6 MeV.

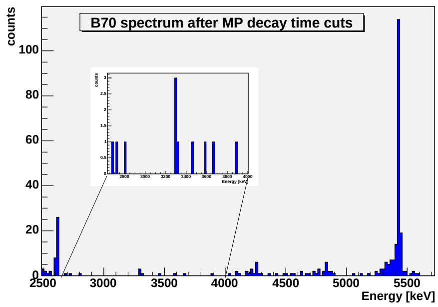


**Figure 7.67** - Spectrum of the events on the B70 SSB detector after MP decay time cuts. In the inset, a zoom of the region of interest for our analysis.

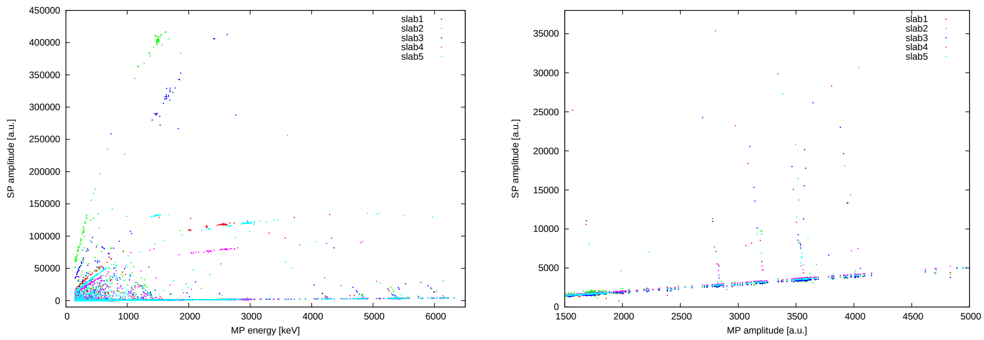


**Figure 7.68** - Superimposition of the scatter plots of all the slab–bolometers of the B70 detector and a zoom of the $\alpha$ region (right).

### Check of the results

We are now interested to verify the followed procedure by looking at the scatter plots. In fig. 7.68 a superimposition of the scatter plots of all the slabs is shown. We remind the reader that, unfortunately, a slab is missing. The figure is very nice because the $\alpha$ contamination of the slabs is clearly visible. It is also clear that part of the contamination is on the slabs surfaces, and therefore produces lines of mixed events that go down toward the bulk events line, as we learned in the previous runs. Four $\alpha$ lines can be recognized.

From each scatter plot it is easy to select only surface events by applying proper cuts[1], as, for example, in fig. 7.69. The events selected in this way can be reported on the plot of the MP decay time vs amplitude as in figure 7.70. From this plot we can deduce that decay time selection can recognize the surface events from the "missing" slab, that obviously cannot be done in other ways.

On the other side, MP decay times selection is not particularly effective for mixed events that lay close to the bulk event line (as it is evident in fig. 7.71). This is not a problem because their energy in the main absorber spectrum is close to those of the bulk $\alpha$ line they tend to. Therefore, they should be far away from the expected $\beta\beta0\nu$ region. However, mixed events at lower energy might constitute a serious problem if not properly discriminated.

What might be crucial here, is the detector noise. In fact, the decay time is

[1] Presently cuts can be performed only by fixing the range of each parameter.

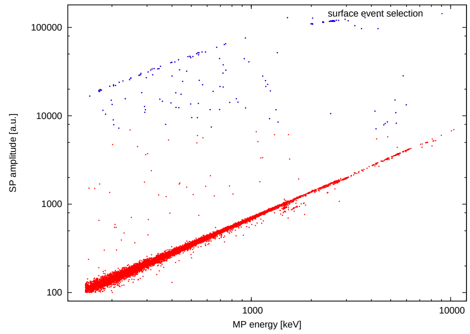


**Figure 7.69** - Selection of surface events by scatter plot cuts on a slab of the B70 SSB.

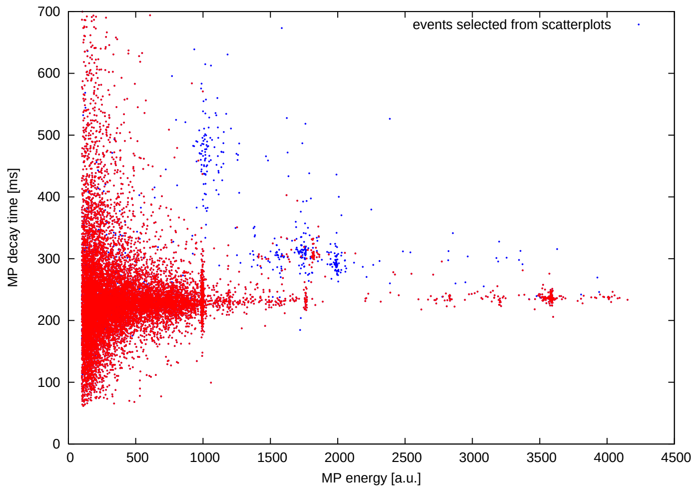


**Figure 7.70** - Plot of the decay time vs amplitude for the main absorber of the B70 SSB. The events in red are selected by means of cuts on the scatter plots.

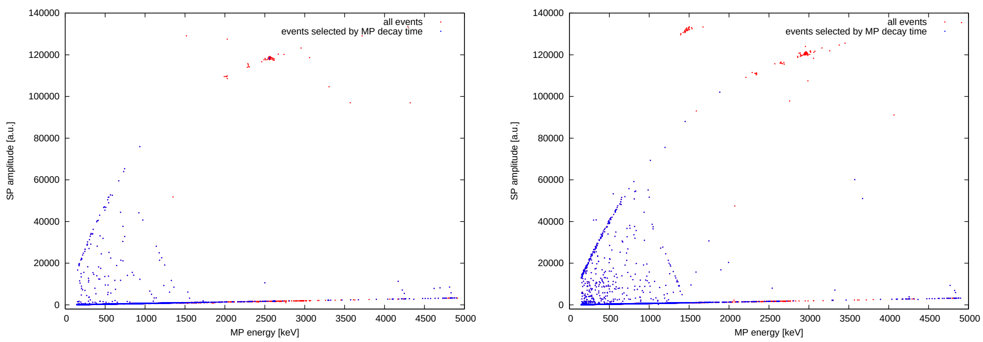


**Figure 7.71** - Scatter plot of two different slab–bolometers of the B70 SSB. Red dots are the scatter plot before any cut on pulse shape, while blue dots are those selected by applying cuts on the MP decay time. Note that mixed events close to the bulk event line are not discarded.

| | counts/keV/kg/y | |
|---|---|---|
| | 2.7–3.2 [MeV] | 3.4–3.9 [MeV] |
| CAW2 | $0.16 \pm 0.04$ | $0.11 \pm 0.03$ |
| SSB (as passive) | $0.11 \pm 0.03$ | $0.14 \pm 0.03$ |
| SSB (as active) | $0.07 \pm 0.02$ | $0.04 \pm 0.02$ |
| RAD | $0.06 \pm 0.01$ | $0.08 \pm 0.02$ |

**Table 7.15** - Preliminary comparison of the background in the region above the natural radioactivity for bolometers in the SSB–LNGS–3 run. Values are expressed in counts/keV/kg/y. The values of the CAW2 bolometers may be affected by the fact that they face contaminated slabs. We underline that we are dealing with an incredible small number of events in the region of interest: the number of background events that are not rejected is less than 10.

evaluated on the acquired pulse without any filtering (except for the baseline, which value is computed after the OF). Better discrimination might possibly be achieved by looking at other parameters, like *Test Value Right/Left*, that are obtained by parsing the acquired pulse through the OF.

The procedure illustrated here for the B70 SSB could be followed similarly for the other detector with active slabs (B67), and we obtained similar results. On the other hand, the analysis for B68 and B69 could only be performed on the MP decay times, because all slabs are passive.

**Conclusions**

Despite the fact that this test underwent a series of misfortunes, our efforts in the analysis are repaid by very encouraging results.

Comparison with other detectors in the same array and previous RAD measurements give the preliminary results summarized in tab. 7.15.

This test also showed the presence of U and Th shallow radioactivity in slabs. SSBs are able to discriminate this kind of contamination and therefore this is not a serious issue, especially when the contamination level is low. However, a procedure for cleaning $TeO_2$ slabs should be investigated in the future.

## 7.8 Comments and remarks

### 7.8.1 Summary of rejection possibilities

**Scatter plot**

The scatter plot of the amplitude of coincident events between the slab–bolometers and the main bolometer is the simplest and most efficient way to discriminate surface events. If all the slab–bolometers are read–out, the discrimination is very close to 100% for detectors with good resolution.

**SP rise time selection**

Surface events are characterized by faster rise time compared to bulk events. We expected to observe this behavior and indeed we see it clearly. Cuts in the rise time vs amplitude for slab–bolometers pulses can be easily done to select surface events. Unfortunately, the selection is not always complete, especially for mixed events. Moreover, as for the scatter plot method, we have the drawback of 6 more channels for each detector to acquire and read–out.

**MP decay time selection**
The possibility of selecting surface events by using only the thermistor of the main bolometer was somehow unexpected but not undesired. In fact, in this way we could greatly simplify the mounting and assembly procedure without increasing the read–out channels.

At present, we can only formulate hypothesis on the physical origin of this effect. Simulations (and tests) are currently going on to understand what is the critical parameter that controls the pulse development for events in the slabs. We believe that the heat capacity of the slab–bolometers could make the difference. We are also trying to figure out if there is a way to enhance this effect, and therefore increase the power of this technique.

However, decay-time method is still weaker at this development stage (as said, there is evidence for surface events not identified as such by decay time, especially for mixed events), and cannot be considered reliable for use in a final experiment.

### 7.8.2 Detector complexity

One of the major drawbacks of this new technique is that the detector is far from being simple. Basic bolometers are very simple detectors, relatively easy to build and assembly. Their operation principle is quite straightforward and their operation and behavior are well known. On the contrary, at every level, SSBs are not so simple:

· slab fragility;

· difficult coupling of the thermistors of the slabs;

· overall handling not easy;

· increased number of wires;

· analysis tool needs to be adjusted to address the needs of the new technique.

As a result, assembling an SSB would require much more work, time, and patience.

However, we believe that the complexity of the SSBs is counterbalanced by their great potentiality in background rejection. This means, for example, that the cleaning and handling procedures of materials can be simplified. Moreover, if the MP discrimination will prove to be really successful and reliable, we could get rid of six thermistors, which means less gluing, less wiring, and much less troubles. An intermediate possibility is the parallel read–out of the slab–bolometers.

### 7.8.3 What's next?

After these two years of R&D on SSBs, the technique has been mastered, but it is not yet mature enough to be implemented in a production experiment. There is however plenty of room for improvements under many points of view. At the current status, we believe that SSBs best application enviroenment is the study and diagnostic of background contaminations. This role can be enhanced by improving the slab radio–purity, the comprehension of the decay–time discrimination method and developing specific mounting structure for SSB, even if different from the CUORE one.

From this point of view, it seems iteresting to try to setup a fully shielded SSB where the PTFE pieces hold the bolometer through the slabs instead that keeping it from the main crystal. The thermal behaviour might change but this solution has the advantages of providing real full coverage of the main bolometer, with no point of sight from outside.

In the framework of CUORE, other methods are proving to be effective in background reduction and their impact on the CUORE design is more limited than in the case of SSB. However, the SSB option has not yet been completely discarded and we are evaluating the possibility of having a small SSB section inside the CUORE array that might help to disentagle contamination problems that might arise.

The R&D work on SSB is therefore not yet finished. A new run is currently being designed and prepared in HallC at LNGS. One or more full $TeO_2$ SSBs will be prepared with full read–out (all slab–bolometers read–out independetely) and with clean slabs. Special care will be devoted to ensure no wire will be lost during cool–down.

# · Chapter 8 ·

# Scintillating bolometers

## 8.1 Introduction and motivations

We already underlined many times the importance of reducing the background in $\beta\beta0\nu$ experiment, in particular in CUORE where degraded surface $\alpha$ contamination is considered the crucial limiting element.

In the previous chapter, we introduced a new technique that can be used to discriminate external surface events from bulk ones. The new composite bolometers, named *Surface Sensitive Bolometers* (SSB), respond to particle interactions with different class of pulses depending on the event origin.

Another method to obtain similar discrimination is to couple the light signal of a scintillator to the phonon signal of a normal bolometer. In this way, a double independent read–out (heat and scintillation) will allow the required suppression of the background thanks to the different Quenching Factor (QF) between $\alpha$ and $\gamma$.

The idea of using a scintillating bolometer is not new and dates back to 1989 [113]. Members of the Cuoricino collaboration performed a measurement with a thermal bolometer and a silicon photodiode [114] but the attempt was not carried on due to problems in operating photodiode at 10 mK. A different approach was proposed [115] to use bolometers as light detectors and was followed successfully by many groups, especially for Dark Matter searches [116].

This technique was also tested as an R&D activity for CUORE by S. Pirro and others. [117]. Several Mo and Cd based crystals were tested with the bolometric technique. The scintillation light was measured through a second independent bolometer made of a thin pure Ge absorber. The results of these tests demonstrate clearly the feasibility of this technique.

Starting from this work, in this last chapter we will present a measurement we performed in the Low Temperature Detectors Laboratory of the Insubria University during summer 2006. The experiment was meant to verify the possibility of operating doped $TeO_2$ crystals [118] as bolometers and check their scintillating properties (if any). In particular, we want to test the results reported by Coron and others [119] on the scintillation of pure $TeO_2$ .

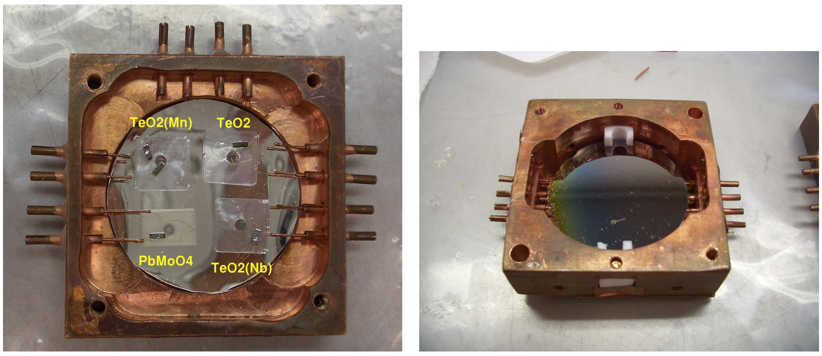


**Figure 8.1** - (left) Pictures of the bolometers placed in their holder with the reflecting foil below them. (right) Picture of the Ge disk that acts as a light detector.

**Figure 8.2** - Scheme of the setup of the detectors.

## 8.2 Bolometric light detectors

In this section, we will briefly review the basic concept of scintillation and light detection in the bolometers case.

We know that a small bolometer, with small heat capacity, can reach very high sensitivity (few tenths of eV); therefore a "dark" thin bolometer can absorb scintillation photons and five a measurable thermal signal. The bolometer is operated as a light detector and has the characteristic time constant of bolometers (20 – 500 ms). Obviously, it is also sensitive to every energy release ($\alpha, \beta$ and $\gamma$ particles).

It is clear that such a light detector cannot easily reach the threshold of PMTs ($\sim 1$ photoelectron i.e. 3–7 photons considering their quantum efficiency), but they have two important advantages. First, they are sensitive over an extremely large band of photon wavelenght (depending on the absorber material) and second, the overall quantum efficiency can be as good as that of photodiodes and allow to obtain, above threshold, better energy resolution with respect to PMTs.

## 8.3 Experimental setup

Our setup was derived from the one developed by S. Pirro [117].

Four small bolometers were placed in the setup sketched in fig. 8.2. The bolometers are pictured in 8.1 along with the Ge disk that act as light detector. On of the four bolometer is a $PbMoO_4$ kindly lended by S. Pirro. It will act as

| Detectors for scintillation test | |
|---|---|
| Detector | size |
| Nb–doped $TeO_2$ | $1 \times 1 \times 0.1$ cm$^3$ |
| Mn–doped $TeO_2$ | $1 \times 1 \times 0.1$ cm$^3$ |
| pure $TeO_2$ | $1 \times 1 \times 0.1$ cm$^3$ |
| $PbMoO_4$ | $1.4 \times 6.8 \times 10.1$ mm$^3$ |
| Ge light detect | 35 mm dia, 1 mm thick |

**Table 8.1** - Charactheristics of the bolometers used in the scintillation test measurements.

a known bolometer with proved scintillating properties and will help to make comparison with the measurements performed in Hall C. A scintillation signal in a $TeO_2$ bolometer operated at 20 mK is reported in literature [119] and therefore we placed a pure $TeO_2$ crystal plus two other $TeO_2$ bolometers provided by I. Dafinei that are doped in Mn and Nb. This materials should act as activators and improve the light output. Details of the bolometers properties are given in tab. 8.1.

The detectors are attached directly to the copper by means of an Araldit spot and are enclosed in a housing of highly reflective polymeric multilayer foil [120]. One side of the foil is itself scintillating at low temperatures. However, we didn't use this feature because the high rate of events of our enviroenment would probably blind the light detector. Therefore, we mounted the reflector with the scintillating side facing outward.

The light detector is a large pure Ge disk absorber able to read several scintillanting crystal at the same time. One side of the disk (the one facing the scintillator) is coated with a layer of 60 nm of $SiO_2$ in order to increase the absorption of the scintillating photons. The disk is held by two PTFE supports compressed togheter by a screw at two opposite sides.

Finally, two Si slab–bolometers and two $TeO_2$ slab–bolometers acts were placed to act as a muon veto as shown in fig. 8.3. The whole setup was mounted with the Ge disk in the vertical plane in order to minimize the cosmic rays interactions.

An external $\alpha$ source was introduced in the setup by evaporating few drop of $^{238}$U solution as described in §7.5.3. The $PbMoO_4$ was not contaminated due to the presence of $^{210}$Pb that produce an $\alpha$ line at 5407 due to the decay of $^{210}$Po.

## 8.4 Data analysis and results

Several measurements were performed. Due to limitation in the number of available DAQ channels, we were unable to acquire all the detectors simultaneously. We report here only the data from measurements number 63 (for the doped $TeO_2$ bolometers) and number 70 (for the $PbMoO_4$ and the pure $TeO_2$ ). The parameters are in tab. 8.2 and 8.3 respectively.

The first relevant information is that we were able to see pulse events on all the detectors. In particular, doped $TeO_2$ was never tested before as absorber for

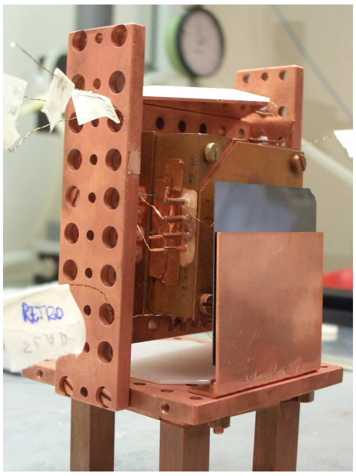

**Figure 8.3** - Picture of the final detector before placing the external copper coverage. Two $TeO_2$ slabs are placed above and below of the scintillanting bolometers structure and two Si slabs on the sides to be used as cosmic rays veto.

| **Measurement 63** | | Duration: | 13.3 h | |
|---|---|---|---|---|
| Detector | Bessel [Hz] | Vbol [mV] | Rbol [MΩ] | Tbol [mK] |
| Nb–doped $TeO_2$ | 31 Hz | 6.43 | 5.2 | 16.7 |
| Mn–doped $TeO_2$ | 31 Hz | 2.40 | 3.8 | 17.5 |
| Ge light detect | 31 Hz | 3.49 | 5.6 | 17.9 |

**Table 8.2** - Bessel cut frequency and working points of detectors of measurements 63.

| **Measurement 70** | | Duration: | 14.0 h | |
|---|---|---|---|---|
| Detector | Bessel [Hz] | Vbol [mV] | Rbol [MΩ] | Tbol [mK] |
| $PbMoO_4$ | 120 Hz | 1.55 | 12.4 | 14.8 |
| undoped $TeO_2$ | 120 Hz | 7.47 | 36.5 | 12. 81 |
| Ge light detect | 120 Hz | 3.49 | 5.6 | 17.9 |

**Table 8.3** - Bessel cut frequency and working points of detectors of measurements 70.

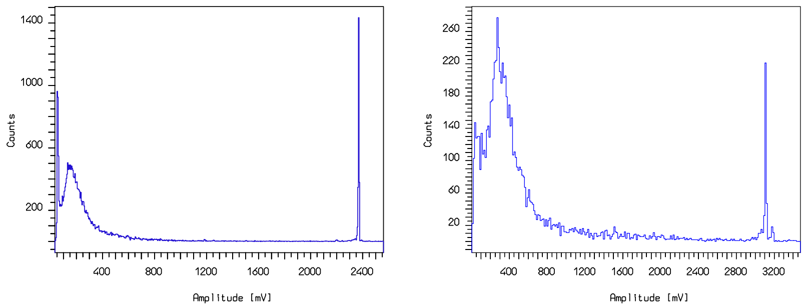


**Figure 8.4** - Pulse amplitude spectra for the $PbMoO_4$ (left) and the $TeO_2$ (Nb) (right) detectors.

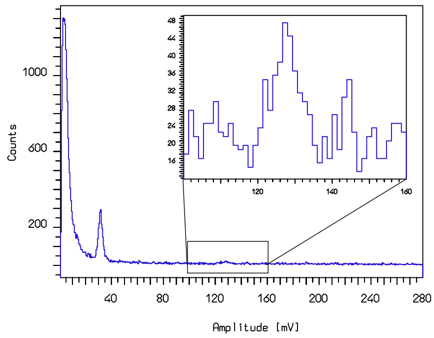


**Figure 8.5** - Spectrum of the Ge detector and zoom of the peak ascribed to $^{210}$Pb $\gamma$ events.

bolometers. Figure 8.4 show the amplitudes spectra for the $PbMoO_4$ and the Nb–doped detectors. The peak from the $^{210}$Pb is clearly visible in the first detector while the $\alpha$s from $^{238}$U and $^{234}$U are visible in the latter. The amplitudes spectrum for the Mn–doped detector is similar. Unfortunately, the resolution is quite low and we are unable to resolve the U doublets. No $\gamma$ peak is observed due to the small dimensions of the crystals. The small size is also responsible for the strong nonlinearity of their energy response at high values. The $^{210}$Po peak allow to convert the spectrum into energy values but this is likely to be not partially unreliable.

The spectrum of the Ge disk shown in fig.8.5(left) is, on the contrary, even more difficult to calibrate because no peak is observed and the detector was very noisy. However, a closer look (fig. 8.5(right)) show the presence of a small peak that can be probably be assigned to the 46.5 keV $\gamma$ emitted following the $\beta$ decay of $^{210}$Pb. As we will see later, this interpretation looks reasonable because it allows to extract similar results of those obtained in Hall C.

Moving to the scintillating data, we report the scatter plot of heat vs light for coincident events between $PbMoO_4$ and Ge in fig. 8.6. The plot is compared with that of S. Pirro obtained with the same detectors.

Before commenting the plots, we underline that the sensitivity of the light detector was quite low and the channel quite noisy (about 4 keV peak-to-peak). Moreover, to understand the plot, we have to point out that the two channels (Ge and $PbMoO_4$) are triggered simultaneously, the trigger being set on the heat ($PbMoO_4$) channel. Another problem is related to the presence of a cross–

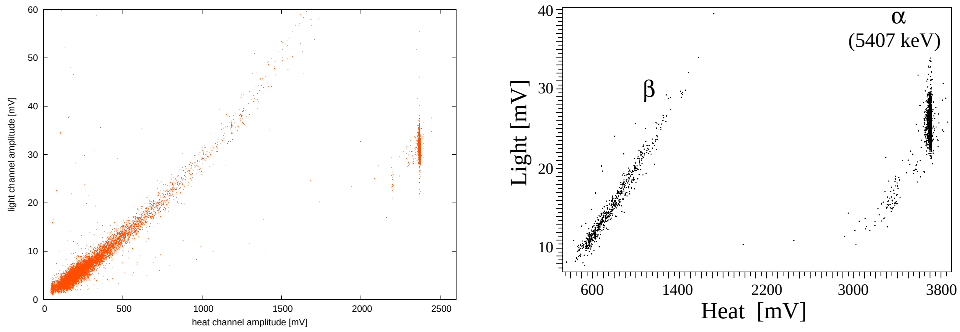


**Figure 8.6** - Comparison between the scatter plot of the heat vs light signals amplitudes for the $PbMoO_4$ obtained from our measurement (left) and in Hall C [117] (right).

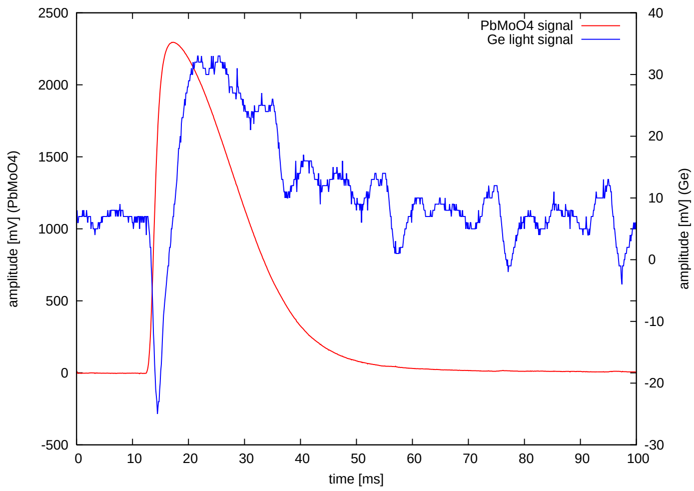


**Figure 8.7** - Example of a cross–talk signal induced on the Ge detector (blue) by an event on the $PbMoO_4$ (red).

talk between the two channel as it can be seen in fig. 8.7.

In spite of these issues, interesting considerations can be extracted from the scatter plots:

- the scintillation light is clearly visibile, in particular the different QF between the $\alpha$ and the electron–like events;
- the electron–like events band extends up to the energy of alpha events due to the interaction of cosmic rays (which are instead not present in the Hall C measurement).

No light signals is seen neither on the undoped $TeO_2$ crystal nor on the doped ones. An analysis of the pulses reveal the presence of a cross–talk with the Ge light detector channel. Moreover the relationship between light and heat is linear as can be seen in fig. 8.8. In this figure we made a tempatively energy calibration of the detectors so that we can superimpose all the bolometers data.

In conclusion, in this run we were able to see the scintillating light of the $PbMoO_4$ crystal while our sensitivity does not allow us to check the results of

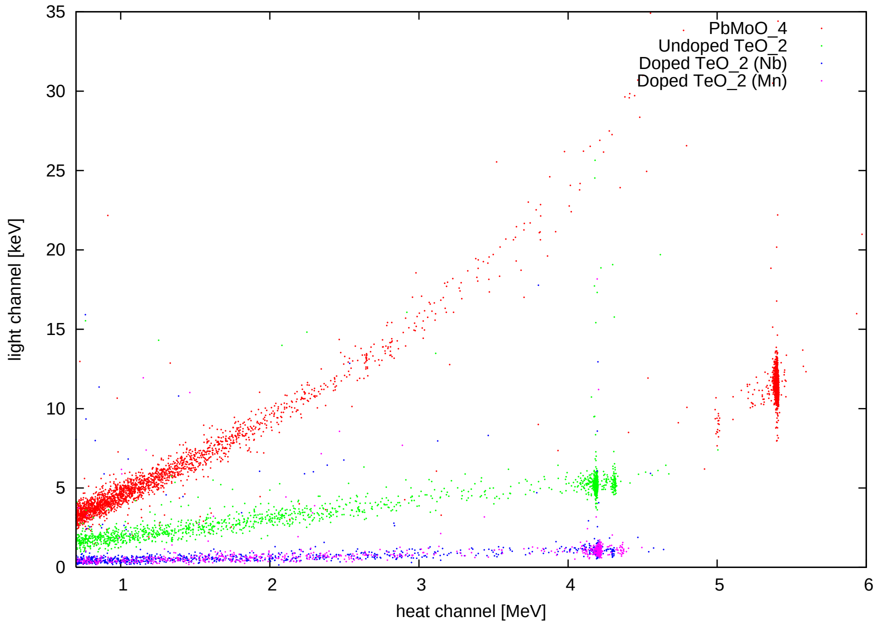


**Figure 8.8** - Comparison, among all the tested detectors, of the light-vs-heat scatter plots. The response is (roughly) energy calibrated (see text).

| | $PbMoO_4$ | $TeO_2$ | $TeO_2$ (Nb) | $TeO_2$ (Mn) |
|---|---|---|---|---|
| $\alpha$ LY | $2.16/\eta$ | $\lesssim 1/\eta$ | $\lesssim 0.2/\eta$ | $\lesssim 0.2/\eta$ |
| $\gamma$ LY | $8.32/\eta$ | n.a. | | |
| $\alpha/\gamma$ QF | 26% | n.a. | | |

**Table 8.4** - Summary of the results on the Light Yeld (LY) and Quenching Factor (QF) obtained in our test. For the $TeO_2$ crystals only weak limit on the $\alpha$ LY could be extracted. The LY is expressed in [keV/MeV]. $\eta < 1$ is the light efficiency.

Coron et al. [119] on $TeO_2$ scintillation They light yeld they reported for pure $TeO_2$ is about 0.05 keV/MeV for $\gamma$ and $\sim$ 0.002 for $\alpha$ which is indeed very small. We were able only to put limits on the light yeld as summurized in table 8.4.

Future tests will be devoted to improve the overall quality of the measurements (underground measurements, strong noise reduction, . . . ) to achieve the required sensitivity.

# Acknowledgments

At the end of this work, I would like to thank all the people who, at different levels and in different ways, have contributed to make this experience so fascinating.

I have always believed that what makes things interesting is the people who face them in a different and original way, according to their specific personality, with passion and determination. This idea guided me also in the choice of a university and of the master thesis, which then led to this doctoral research.

I therefore start with thanking Prof. Andrea Giuliani, who patiently supervised my activity, stimulating and guiding my work. I thank him for his deep understanding of Physics (which I am afraid I did not sufficiently take advantage of) and his passion for research.

I thank Dr. Marisa Pedretti for teaching me how to work with passion, committment, and tenacity, and for the everyday experimental work. I thank her for helping me "above and beyond the call of duty".

Among the Como collaborators, I thank Luca, Claudia, Erica, Monica e Chiara for making work interesting and fun. I am afraid I have often been "heavy", but I'm glad you tolerated me! Thank you because from each of you I had occasion to learn and grow.

One of the most stimulating aspects of these years was certainly the possibility to work within a young and dynamic international collaboration. My esteem goes first of all to Prof. Ettore Fiorini for his incredible tenacity and passion for the CUORE experiment. I also thank the many people I had the pleasure to work with, and who contributed to my professional development. In the Milano group I especially thank Dr. Oliviero Cremonesi and Dr. Maura Pavan, for introducing me to bolometer analysis. My shifts at Gran Sasso were always an important occasion to learn, also thank to the precious help of Dr. Carlo Bucci, Dr. Stefano Pirro and Dr. Paolo Gorla.

Finally, I wish to thank those who most of all have supported my work, because this is only a part of a much bigger adventure. I thank my parents, Caterina, my brothers and sisters and all my friends for their company and support along the way.

# Bibliography


[1] S. Simon, Nature **135**, 763 (1935).

[2] N. E. Booth, B. Cabrera, and E. Fiorini, Ann. Rev. Nucl. Part. Sci. **46**, 471 (1996).

[3] K. Pretzl, Nucl. Instrum. Meth. **A454**, 114 (2000), hep-ex/9911028.

[4] A. Giuliani, Physica B **280**, 501 (2000).

[5] C. W. Fabjan and F. Gianotti, Rev. Mod. Phys. **75**, 1243 (2003).

[6] M. Ohkubo, K. Mitsuda, and H. Takahashi, editors, *Proceedings of the 11th International Workshop On Low Temperature Detectors (LTD-11)*, Nucl. Instrum. Methods A 559, Amsterdam, 2006, Elsevier.

[7] F. Gatti, editor, *Proceedings of the 10th International Workshop On Low Temperature Detectors (LTD-10)*, Nucl. Instrum. Methods A 520, Amsterdam, 2004, Elsevier.

[8] Y. B. Levinson, Phonon propagation with frequency down-conversion, in *Nonequilibrium Phonons in Nonmetallic Crystals*, edited by W. Eisenmenger and A. Kaplyanskii, chap. 3, pp. 91–143, Elsevier Science Publisher B.V., Amsterdam, 1986.

[9] B. Taylor, H. Maris, and C. Elbrum, Phys. Rev. Lett. **49**, 416 (1969).

[10] K. Irwin *et al.*, Rev. Sci. Instr. **66**, 5322 (1995).

[11] C. Cozzini *et al.*, LTD9 conference proceedings **605**, 481 (2001).

[12] N. Mott and J. Davis, Phil.Mag. **B42**, 845 (1980).

[13] A. Giuliani and S. Sanguinetti, Mater. Sci. Eng. **R 11**, 1 (1993).

[14] P. Richards, J. Appl. Phys. **76**, 1 (1994).

[15] S. Moseley, J. Mather, and D. McCammon, J. Appl. Phys. **56**, 1257 (1984).

[16] M. Galeazzi and D. McCammon, (2003), astro-ph/0304397.

[17] W. H. Press *et al.*, *Numerical Recipes in C : The Art of Scientific Computing*, 2nd ed. (Cambridge University Press, Cambridge, England, 1992).

[18] S. Sangiorgio, *Modellizzazione e ottimizzazione di rivelatori bolometrici per la ricerca del decadimento $\beta\beta0\nu$ del $^{130}$Te*, Master's project, Università degli Studi di Milano, Faculty of Mathematical, Physical and Natural Sciences, 2003.

[19] APS Multidivisional Neutrino Study, S. J. Freedman and B. Kayser, (2004), physics/0411216.

[20] E. Fermi, Z. Phys. **88**, 161 (1934).

[21] B. Pontecorvo, Zh. Eksp. Teor. Fiz. **33**, 549 (1957).

[22] B. Pontecorvo, Zh. Eksp. Teor. Fiz. **53**, 1717 (1967).

[23] Z. Maki, M. Nakagawa, and S. Sakata, Progr. Theor. Phys. **28**, 870 (1962).

[24] T. Schwetz, Phys. Scripta **T127**, 1 (2006), hep-ph/0606060.

[25] E. Majorana, Nuovo Cimento **14**, 171 (1937).

[26] R. N. Mohapatra and G. Senjanović, Phys. Rev. D **23**, 165 (1981).

[27] C. Aalseth *et al.*, (2004), hep-ph/0412300.

[28] W. M. Alberico and S. M. Bilenky, (2003), hep-ph/0306239.

[29] S. R. Elliott, (2006), nucl-ex/0609024.

[30] M. Goeppert-Mayer, Physics Rev. Lett. **59**, 512 (1987).

[31] M. K. Moe, Nucl. Phys. Proc. Suppl. **38**, 36 (1995).

[32] S. R. Elliott and P. Vogel, Ann. Rev. Nucl. Part. Sci. **52**, 115 (2002), hep-ph/0202264.

[33] CHOOZ, M. Apollonio *et al.*, Phys. Lett. **B466**, 415 (1999), hep-ex/9907037.

[34] F. Boehm *et al.*, Phys. Rev. **D64**, 112001 (2001), hep-ex/0107009.

[35] A. Strumia and F. Vissani, Nucl. Phys. **B726**, 294 (2005), hep-ph/0503246.

[36] S. Petcov, 2006, private communication.

[37] S. Pascoli and S. T. Petcov, Phys. Lett. **B544**, 239 (2002), hep-ph/0205022.

[38] J. Suhonen and O. Civitarese, Phys. Rept. **300**, 123 (1998).

[39] V. A. Rodin, A. Faessler, F. Simkovic, and P. Vogel, Nucl. Phys. **A766**, 107 (2006).

[40] H. V. Klapdor-Kleingrothaus *et al.*, Eur. Phys. J. A **12**, 147 (2001).

[41] IGEX, C. E. Aalseth *et al.*, Phys. Rev. **D65**, 092007 (2002), hep-ex/0202026.

[42] H. V. Klapdor-Kleingrothaus, A. Dietz, H. L. Harney, and I. V. Krivosheina, Mod. Phys. Lett. **A16**, 2409 (2001), hep-ph/0201231.

[43] C. E. Aalseth *et al.*, Mod. Phys. Lett. **A17**, 1475 (2002), hep-ex/0202018.

[44] H. V. Klapdor-Kleingrothaus, (2002), hep-ph/0205228.

[45] H. V. Klapdor-Kleingrothaus, A. Dietz, I. V. Krivosheina, C. Dorr, and C. Tomei, Nucl. Instrum. Meth. **A510**, 281 (2003), hep-ph/0308275.

[46] H. V. Klapdor-Kleingrothaus, O. Chkvorez, I. V. Krivosheina, and C. Tomei, Nucl. Instrum. Meth. **A511**, 335 (2003), hep-ph/0309157.

[47] H. V. Klapdor-Kleingrothaus, A. Dietz, I. V. Krivosheina, C. Dorr, and C. Tomei, Phys. Lett. **B578**, 54 (2004), hep-ph/0312171.

[48] Y. G. Zdesenko, F. A. Danevich, and V. I. Tretyak, Phys. Lett. **B546**, 206 (2002).

[49] F. Feruglio, A. Strumia, and F. Vissani, Nucl. Phys. **B637**, 345 (2002), hep-ph/0201291.

[50] A. Giuliani, Nucl. Phys. Proc. Suppl. **138**, 267 (2005).

[51] E. Fiorini and T. O. Niinikoski, Nucl. Instrum. Meth. **A 224**, 83 (1984).

[52] A. Alessandrello *et al.*, Nucl. Instrum. Meth. **A 440**, 397 (2000).

[53] C. Arnaboldi *et al.*, Nucl. Instrum. Meth. **A554**, 300 (2005).

[54] R. Arnold *et al.*, Nucl. Instrum. Meth. **A536**, 79 (2005), physics/0402115.

[55] NEMO, R. Arnold *et al.*, Phys. Rev. Lett. **95**, 182302 (2005), hep-ex/0507083.

[56] GERDA, S. Schonert *et al.*, Nucl. Phys. Proc. Suppl. **145**, 242 (2005).

[57] GERDA, I. Abt *et al.*, LNGS-EXP **33/05 add. 3/06** (2006), `http://www.mpi-hd.mpg.de/ge76/gerda-lngs-sc-oct06.pdf`.

[58] CUORE, C. Arnaboldi *et al.*, Nucl. Instrum. Meth. **A518**, 775 (2004), hep-ex/0212053.

[59] Majorana, C. E. Aalseth *et al.*, Nucl. Phys. Proc. Suppl. **138**, 217 (2005).

[60] R. Ardito *et al.*, (2005), hep-ex/0501010.

[61] G. White, S. J. Collocott, and J. G. Collins, Journal of Physics: Condensed Matter **2**, 7715 (1990).

[62] M. Barucci *et al.*, J. Low Temp. Phys. **123**, 303 (2001).

[63] A. Woodcraft, R. Sudiwala, E. Wakui, and C. Paine, J. Low Temp. Phys. **134**, 925 (2004).

[64] A. Alessandrello *et al.*, Czechoslovak J. Phys. **46-S5**, 2893 (1996).

[65] E. Olivieri, M. Barucci, J. Beeman, L. Risegari, and G. Ventura, Journal of Low Temperature Physics **143**, 153 (2006).

[66] C. Arnaboldi *et al.*, Phys. Lett. B **584**, 260 (2004).

[67] S. Di Domizio, *Ottimizzazione del rivelatore CUORE per la misura del doppio decadimento beta con tecniche bolometriche*, Master's project, Università degli Studi di Roma "La Sapienza", Faculty of Mathematical, Physical and Natural Sciences, 2004–2005.

[68] S. Baker and P. Cousins, Nucl. Instrum. Meth. **224**, 437 (1984).

[69] PDG, R. Barnett *et al.*, Phys. Rev. D **54**, 1 (1996).

[70] H. V. Klapdor-Kleingrothaus *et al.*, Nucl. Instrum. Meth. **A522**, 367 (2004).

[71] E. Gatti and P. Manfredi, Rivista Nuovo Cimento **9**, 1 (1986).

[72] Istituto Trentino di Cultura - Centro per la ricerca scientifica e tecnologica, via Sommarive 18, Povo, TN, Italy `http://www.itc.it/irst`.

[73] A. Alessandrello *et al.*, Nucl. Instrum. Meth. **A412**, 454 (1998).

[74] M. Pedretti *et al.*, Large mass bolometers for neutrinoless double beta decay detection: model and last results, in *Proc. SPIE*, edited by L. A. Franks, A. Burger, R. B. James, and P. L. Hink, , Hard X-Ray and Gamma-Ray Detector Physics V No. 5198, pp. 92–102, SPIE, 2004.

[75] M. Pedretti, *The single module for Cuoricino and CUORE detectors: tests, construction and modelling*, PhD dissertation, University of Insubria, Department of Chemical, Physical and Mathematical Sciences, 2004.

[76] S. Sangiorgio, GraMiKo radioactivity measurements database `http://crio.mib.infn.it/cuore/db_rad/`.

[77] G. K. White and P. J. Meeson, *Experimental Techniques in Low–Temperature Physics*, 4th ed. (Oxford University Press, Great Calrendon Street, Oxford, 2002).

[78] F. Pobell, *Matter and Methods at Low Temperatures*, 2nd ed. (Springer–Verlag Berlin Heidelberg New York, 1996).

[79] L. G. Foggetta, *Sviluppo di un sistema di acquisizione per rivelatori criogenici innovativi*, Master's project, Università degli Studi dell'Insubria, Faculty of Mathematical, Physical and Natural Sciences, 2004.

[80] Bondolier, - epoxy tape with fast polimeritation produced by Dyna Systems, NCH Italia.

[81] Air Liquide Advanced Technology Division, Les Engenieres, 38360 Sassenage, FR `http://www.dta.airliquide.com`.

[82] K. Uhlig, Cryogenics **42**, 73 (2002).

[83] K. Uhlig, Cryogenics **44**, 53 (2004).

[84] Mykrolis Corporation, Gas Microcontamination Business Unit 6975 Flanders Drive San Diego, CA 92121 `http://www.aeronex.com`.

[85] R. N. Richardson and B. E. Evans, International Journal of Refrigeration **20**, 367 (1997).

[86] G. Popescu, V. Radcenco, E. Gargalian, and P. Ramany Bala, International Journal of Refrigeration **24**, 230 (2001).

[87] P. Kittel, A. Kashani, J. Lee, and P. Roach, Cryogenics **36**, 849 (1996).

[88] Cryomech, Inc., 113 Falso Drive, Syracuse, New York USA 13211, `http://www.cryomech.com`.

[89] T. Tomaru *et al.*, Cryogenics **44**, 309 (2004).

[90] S. Caparrelli *et al.*, Review of Scientific Instruments **77**, 095102 (2006).

[91] C. Arnaboldi *et al.*, IEEE Tran. Nucl. Sci. **44**, 416 (1997).

[92] C. Arnaboldi *et al.*, Nucl. Instrum. Meth. **A520**, 578 (2004).

[93] C. Arnaboldi *et al.*, IEEE Tran. Nucl. Sci. **49**, 2440 (2002).

[94] E. Pasca, *Low temperature properties of Neutron Transmutation Doped Germanium*, PhD dissertation, University of Florence, Department of Physics, 2005.

[95] J. Beeman, 2006, private communication.

[96] J. C. Mather, Appl. Opt. 21 **6**, 1125 (1982).

[97] W. A. Phillips, Rep. Prog. Phys. **50**, 1657 (1987).

[98] C. C. Yu and A. J. Leggett, Comments Cond. Mat. Phys. **14**, 231 (1988).

[99] J. M. B. Lopes dos Santos *et al.*, Phys. Rev. **B 61**, 8053 (2000).

[100] P. Strehlow and M. Meissner, Physica **B 263-264**, 273 (1999).

[101] P. J. Reijntjis *et al.*, Rev. Sci. Instrum. **57**, 1413 (1986).

[102] S. A. J. Wiegers, R. Jochemsen, C. C. Kranenburg, and G. Frossati, Rev. Sci. Instrum. **58**, 2274 (1987).

[103] P. Gorla, *Optimization of the detector performances*, PhD dissertation, Università di Milano–Bicocca, 2005.

[104] S. Sangiorgio *et al.*, Innovations in low-temperature calorimeters: surface sensitive bolometers for background rejection and capacitive bolometers for higher energy resolution, in *Proc. SPIE*, edited by A. Burger, R. B. James, and L. A. Franks, volume 5540 of *Hard X-Ray and Gamma-Ray Detector Physics VI*, pp. 165–176, 2004.

[105] L. Foggetta, A. Giuliani, C. Nones, M. Pedretti, and S. Sangiorgio, Applied Physics Letters **86**, 134106 (2005).

[106] C. Nones *et al.*, Nucl. Instrum. Meth. **A559**, 355 (2006).

[107] C. Nones *et al.*, Prog. Part. Nucl. Phys. **57**, 269 (2006).

[108] Institute of Electron Technology, Al. Lotników 32/46, 02-668 Warsaw, Poland `http://www.ite.waw.pl/`.

[109] Aldrich Chemical Company, Inc., Aldrich MSDS 1, 1826:A / Corp MSDS 1 (2), 3577:D.

[110] C. Nones, *Sviluppo di bolometri innovativi per la fisica del neutrino con discriminazione attiva del fondo*, Master's project, Università degli Studi di Milano, Faculty of Mathematical, Physical and Natural Sciences, 2003–2004.

[111] C. Salvioni, *Discriminazione attiva del fondo in esperimenti bolometrici per la ricerca del doppio decadimento beta*, Master's project, Università degli Studi dell'Insubria, Faculty of Mathematical, Physical and Natural Sciences, 2004–2005.

[112] Dow Corning Corporation, PO box 994, MIDLAND MI 48686-0994, USA `http://www.dowcorning.com/`.

[113] L. Gonzalez-Mestre and D. Perret-Gallix, Nucl. Instrum. Meth. A **279**, 382 (1989).

[114] A. Alessandrello *et al.*, Nucl. Phys. Proc. Suppl. **28A**, 233 (1992).

[115] C. Bobin *et al.*, Nucl. Instr. and Meth. A **386**, 453 (1994).

[116] S. Cebrian *et al.*, Phys. Lett. **B563**, 48 (2003).

[117] S. Pirro *et al.*, (2005), nucl-ex/0510074.

[118] I. Dafinei, M. Diemoz, E. Longo, A. Peter, and I. Foldvari, Nucl. Instrum. Meth. **A554**, 195 (2005).

[119] N. Coron *et al.*, Nucl. Instrum. Meth. **A520**, 159 (2004).

[120] M. F. Weber, C. Stover, L. Gilbert, T. Nevitt, and A. Ouderkirk, Scienze **287**, 2451 (2000).